

# UC Berkeley

## UC Berkeley Electronic Theses and Dissertations

### Title

Ablation on Taylor Glacier, Antarctica

### Permalink

<https://escholarship.org/uc/item/1x61202d>

### Author

Bliss, Andrew Knisely

### Publication Date

2011

Peer reviewed|Thesis/dissertation

**Ablation on Taylor Glacier, Antarctica**

by

Andrew Knisely Bliss

A dissertation submitted in partial satisfaction  
of the requirements for the degree of

Doctor of Philosophy

in

Geography

in the

Graduate Division

of the

University of California, Berkeley

Committee in charge:

Professor Kurt M. Cuffey, Chair

Professor John C. H. Chiang

Professor Inez Y. Fung

Spring 2011

Ablation on Taylor Glacier, Antarctica

Copyright © 2011

by

Andrew Knisely Bliss

## Abstract

Ablation on Taylor Glacier, Antarctica

by

Andrew Knisely Bliss

Doctor of Philosophy in Geography

University of California, Berkeley

Professor Kurt M. Cuffey, Chair

Taylor Glacier, an outlet of the East Antarctic Ice Sheet, flows through the Transantarctic Mountains and terminates in the Dry Valleys. Understanding how this glacier fluctuates is important for studies of glacial geology, paleoclimate, ice dynamics, and ecology. Sublimation is the primary mass-loss process for most of the glacier. Four years of specific balance measurements from the ablation zone show sublimation rates up to 40 cm per year. We used data from an array of weather stations as inputs to a model for latent heat flux and hence sublimation rate. Calculated and measured ablation rates agree to within uncertainties, indicating that wind speed and vapor pressure gradient (a function of temperature and humidity) are the governing variables, as expected from theory. Measurements and model results together allowed us to examine the spatial and temporal variations of sublimation on the glacier. On average, sublimation is about two times faster in summer than winter. Rapid sublimation occurs during storms and katabatic wind events, but such periods contribute less to the annual total than do slow, persistent losses. Spatially, sublimation reaches a maximum midway along the glacier, where descending surface air currents are focused by the topography of the aptly-named tributary, Windy Gully.



# Contents

<b>Contents</b>	<b>i</b>
<b>List of Figures</b>	<b>v</b>
<b>List of Tables</b>	<b>xviii</b>
<b>Acknowledgements</b>	<b>xxi</b>
<b>1 Overview</b>	<b>1</b>
1.1 Introduction . . . . .	1
1.2 Field Site . . . . .	2
1.3 Ablation Data . . . . .	3
1.3.1 Ablation Measurement Technique . . . . .	3
1.3.2 Uncertainties in Ablation Measurements . . . . .	3
1.3.3 Measured Ablation Rates . . . . .	9
1.4 Weather Data . . . . .	9
1.4.1 Weather Station Setup . . . . .	9
1.4.2 Weather Station Data . . . . .	11
1.4.3 Derived Parameters . . . . .	15
1.5 Sublimation Models . . . . .	17
1.5.1 Predicted Sublimation . . . . .	18
1.5.2 Sensitivity of Predictions to Input Values . . . . .	18
1.6 Energy Budget . . . . .	19
1.6.1 Energy Budget Data . . . . .	21
1.7 Relation of Sublimation to Weather Modes . . . . .	21
1.7.1 Example Time Period . . . . .	23

1.7.2	Magnitude versus frequency of sublimation . . . . .	25
1.8	Discussion . . . . .	26
1.8.1	Measured Ablation Rates . . . . .	26
1.8.2	Weather Data . . . . .	27
1.8.3	Modeled Ablation Rates . . . . .	27
1.8.4	Energy Budget . . . . .	27
1.9	Conclusion . . . . .	28
1.10	Appendix: Outliers and Gap Filling . . . . .	29
1.11	Appendix: Surface Temperature . . . . .	29
1.11.1	Parameterized . . . . .	29
1.11.2	Adjusted for Energy Balance . . . . .	30
1.12	Appendix: Roughness Length . . . . .	30
<b>2</b>	<b>Ablation Data</b>	<b>32</b>
2.1	Field Site . . . . .	32
2.2	Fieldwork Anecdotes . . . . .	32
2.3	Ablation Measurement Technique . . . . .	38
2.4	Uncertainties in Ablation Measurements . . . . .	40
2.5	Measured Ablation Rates . . . . .	42
2.5.1	Large-Scale Spatial Variability of Ablation . . . . .	42
2.5.2	Spatial Extrapolation of Ablation . . . . .	42
2.5.3	Temporal Variability of Ablation . . . . .	43
2.6	Discussion . . . . .	47
2.6.1	Measured Ablation Rates . . . . .	47
<b>3</b>	<b>Weather Data</b>	<b>49</b>
3.1	Weather Station Setup . . . . .	49
3.1.1	Setup Anecdotes . . . . .	49
3.1.2	Instrumentation . . . . .	50
3.1.3	Data Properties . . . . .	52
3.2	Weather Station Data . . . . .	55
3.2.1	Winds . . . . .	70

3.2.2	Air Temperature . . . . .	73
3.2.3	Relative Humidity . . . . .	73
3.2.4	Shortwave Radiation . . . . .	73
3.2.5	Longwave Radiation . . . . .	81
3.2.6	Air Pressure . . . . .	81
3.2.7	Snowfall . . . . .	81
3.2.8	Effects of Windy Gully . . . . .	84
3.2.9	Correlations between stations and Autocorrelations . . . . .	84
3.3	Derived Parameters . . . . .	86
3.3.1	Surface Temperature . . . . .	86
3.3.2	Vapor Pressure . . . . .	94
3.3.3	Subsurface Temperature . . . . .	94
3.3.4	Roughness Lengths . . . . .	97
3.3.5	Lapse Rates . . . . .	102
3.3.6	Inversions . . . . .	105
3.3.7	Cloudiness . . . . .	108
3.4	Modes of Weather Variability . . . . .	110
3.4.1	Characteristics of the Storm Mode . . . . .	111
3.4.2	Characteristics of the Katabatic/Foehn Mode . . . . .	117
3.4.3	Characteristics of the Diurnal Mode . . . . .	117
3.4.4	Characteristics of the Calm Mode . . . . .	117
3.4.5	Frequency of Modes . . . . .	118
<b>4</b>	<b>Sublimation Models</b>	<b>119</b>
4.1	Predicted Sublimation . . . . .	120
4.2	Sensitivity of Predictions to Input Values . . . . .	122
4.3	Discussion of Modeled Ablation Rates . . . . .	125
<b>5</b>	<b>Energy Budget</b>	<b>126</b>
5.1	Energy Budget Data . . . . .	126
5.2	Discussion of the Energy Budget . . . . .	137
<b>6</b>	<b>Sublimation Variability, Analyzed</b>	<b>138</b>

6.1	Magnitude versus frequency of sublimation . . . . .	138
6.2	Example Time Periods . . . . .	142
6.2.1	March 2006: katabatic/foehn and then a storm . . . . .	142
6.2.2	September 2005: katabatic/foehn . . . . .	154
<b>7</b>	<b>Conclusions and Future Work</b>	<b>156</b>
7.1	Concluding Remarks . . . . .	156
7.2	Future Work . . . . .	156
	<b>Bibliography</b>	<b>159</b>

# List of Figures

0.1	The author, looking geeky, getting ready to carry a set of solar panels up a hill for a GPS base station. . . . .	xxii
1.1	A digital elevation and bathymetric model of Antarctica from BEDMAP [Lythe and Vaughan the BEDMAP Consortium, 2001], in meters above sea level. The red circle is the location of Taylor Glacier. The center of the plot is South Pole and the outer edge is 60° S. The black arrow indicates the most common storm track for storms that reach Taylor Glacier [Morse <i>et al.</i> , 1998].	4
1.2	A satellite image showing the configuration of land, ocean, and ice in the region surrounding Taylor Glacier. The March 3rd, 2006 MODIS image came from <a href="http://rapidfire.sci.gsfc.nasa.gov/subsets/?subset=RossSea.2006062.aqua.500m">http://rapidfire.sci.gsfc.nasa.gov/subsets/?subset=RossSea.2006062.aqua.500m</a>	5
1.3	A SPOT image of Taylor Glacier, Antarctica showing this study's weather station locations (numbered by elevation), and LTER weather stations at Lake Bonney (Bo), Taylor Glacier (T), and Beacon Valley (Be). Station 1 started at 1a and moved less than 2 months later to 1. Black dots represent ablation poles. The patchy snow line is near Wx 5; the glacier surface to the east is blue ice. Image credit: SPIRIT Program ©CNES 2009 and Spot Image 2008 all rights reserved. . . . .	6
1.4	A digital elevation model of the Taylor Glacier region derived from satellite imagery. Ice velocity vectors, measured with GPS, show the flow direction. The velocities shown are the average of 4-6 clustered poles. The fastest velocities are about 20 m/yr. Elevation data courtesy of the SPIRIT Program ©CNES 2009 and Spot Image 2008 all rights reserved. . . . .	7
1.5	The measured ablation rates in the <b>3:4</b> interval were highest (about 0.4 m/yr) at the base of the steeply-sloping Windy Gully where the wind speeds, and hence the latent heat flux, were the highest. This plot also shows 250 m topographic contours generated from the RAMP digital elevation model Liu <i>et al.</i> [2001]. TV is Turnabout Valley and AV is Arena Valley. . . . .	8

1.6	Measured ablation rates for intervals with weather station measurements. Summertime ablation rates were a factor of two faster than whole-year rates. For each set of 4 or 6 ablation poles (see map in figure 1.3), one symbol is plotted on the graph at the mean value of that group. The 25th and 75th percentile within the group is plotted as the bottom and top of the gray error bar associated with the mean symbol. Symbols without error bars represent single ablation poles, so statistics could not be calculated. The set of single dots near Wx 5 in the upper graph are long-term ablation rates from 1993-2003 (personal communication from E.D. Waddington, 2005). The stars are measurements done by <i>Robinson</i> [1984] from November 1976-November 1977. The left-pointing triangle is from <i>Hoffman et al.</i> [2008] for ablation from 1995-2006. The weather station locations are plotted as text (e.g. Wx 1).	10
1.7	Measured weather variables from Wx 1: temperature ( $^{\circ}\text{C}$ ), wind speed (m/s), relative humidity (%), shortwave radiation ( $\text{W}/\text{m}^2$ ), and longwave radiation ( $\text{W}/\text{m}^2$ ). Data were smoothed with a triangular filter that assigned the highest weight to the central point and the lowest weight to points 15 days prior to and 15 days after the central point. See section 3.2 for comparable data from other stations. . . . .	12
1.8	Unsmoothed 20-minute temperature and wind speed data for Wx 1, plotted with the glacier-wide timeseries of the katabatic and storm modes. Section 3.4 has comparable plots for other stations and a discussion of the modes. . .	13
1.9	The measured air temperature (K) is usually higher than the modeled surface temperature (adjusted to make the energy budget go to zero). The measured vapor pressure (mbar) at screen height is usually lower than the surface vapor pressure calculated from the surface temperature assuming saturation. The vapor pressure difference (mbar) is much larger in summer than winter. All data from Wx 1. Data were smoothed with a 30-day triangular filter. See section 3.3 for comparable data from other stations. . . . .	16
1.10	Modeled sublimation rates are linearly related to the ablation rates measured at ablation stakes close to the weather stations. The symbol shapes are the same as in figure 1.6. The width of the horizontal error bar depends on the measured variability in ablation, as in figure 1.6. The height of the vertical error bar is $\pm$ one standard deviation away from the mean of the Monte Carlo simulation explained in the text. . . . .	19

1.11	Histograms of modeled sublimation after perturbations to one or more input variables from a Monte Carlo simulation. The x-axis shows the total sublimation for the period of record at station 1 in cm. The text discusses the method of perturbation. The solid vertical line in each plot is the sublimation predicted by the unperturbed model. The dotted line is the model result using the (+) uncertainty and the dashed line is using the (-) uncertainty. The total number of points in each simulation was 1000 and each of the 81 histogram bins is 0.5 cm wide. The sublimation model is more sensitive to the uncertainties in surface temperature and roughness than to the instrument uncertainties associated with the measurements of temperature, relative humidity, and wind speed. See section 4.2 for comparable data from other stations. . . . .	20
1.12	Relative magnitudes of the terms in the energy budget for station 1 (all units: $\text{W/m}^2$ ). Data were smoothed with a 30-day triangular filter. Fluxes that added energy to the glacier surface were defined to be positive and fluxes that removed energy from the surface were negative. The modeled sublimation rates for all 5 stations exhibit maxima in the summer months. In summer, the warmer temperatures allow for higher vapor pressure differences so despite calmer winds and higher relative humidity, the sublimation rates are higher than in winter. Winter sublimation is quite variable because of storms. Similar plots for other stations are in section 5.1. . . . .	22
1.13	Weather patterns at Wx 1 are distinctly different during katabatic, calm, and stormy periods. Panels show sublimation (mm per 20-minute interval), wind speed (m/s), vapor pressure difference between the measurement height and the surface (mbar), temperature ( $^{\circ}\text{C}$ ), and relative humidity (%) for late February and early March 2006. When the vapor pressure difference and wind speed are large, the ablation is high. When the vapor pressure difference or the wind speeds are low, so is ablation. See 6.2 for comparable data from other stations. . . . .	24
1.14	The relationship between the frequency and magnitude of sublimation at Wx 1 indicates that frequent, small events ( $<0.025$ mm/interval) contribute more to the total sublimation than infrequent, large events ( $>0.05$ mm/interval). Storms and katabatic wind periods have the largest sublimation rates while the high frequency of calm periods mean they are important too. See section 6.1 for comparable data from other stations. . . . .	25
2.1	A SPOT image of Taylor Glacier, Antarctica showing this study's weather station locations (numbered by elevation), and LTER weather stations at Lake Bonney (Bo), Taylor Glacier (T), and Beacon Valley (Be). Station 1 started at 1a and moved less than 2 months later to 1. Black dots represent ablation poles. The patchy snow line is near Wx 5; the glacier surface to the east is blue ice. Image credit: SPIRIT Program ©CNES 2009 and Spot Image 2008 all rights reserved. . . . .	33

2.2	The measured ablation rates in the <b>3:4</b> interval were highest (about 0.4 m/yr) at the base of the steeply-sloping Windy Gully where the wind speeds, and hence the latent heat flux, were the highest. This plot also shows 250 m topographic contours generated from the RAMP digital elevation model <i>Liu et al.</i> [2001]. TV is Turnabout Valley and AV is Arena Valley. . . . .	34
2.3	The terminus of Taylor Glacier, looking up-glacier to the west. Picture taken from a helicopter by Andy Bliss. . . . .	35
2.4	Mount Erebus and Castle Rock from the southern tip of Ross Island near McMurdo station. Sir James Clark Ross named Mount Erebus after one of his ships on an early expedition to Antarctica. It is the southernmost active volcano in the world and has an active lava lake in its summit crater. The mountain is 3794 m tall, though it does not look that tall from sea level. Photo by Andy Bliss. . . . .	36
2.5	Camp 1 with Johnny, Sarah, and Jeff. The multicolored tent was our kitchen tent. The yellow tents were double-walled canvas tents, state-of-the-art technology in 1912 when Sir Robert Falcon Scott died in one returning from South Pole. A quote, from just after he reached the pole and found that Roald Amundsen had beaten him to it, “Great god! This is an awful place.” Photo by Andy Bliss. . . . .	37
2.6	Northwest Mountain. Photo by Andy Bliss. . . . .	38
2.7	A typical ablation pole installation. Here Jeff and Kurt were measuring the pole’s position with GPS, and making notes about the character of the glacier surface. Picture by Andy Bliss. . . . .	39
2.8	The timeline shows when ablation pole and weather station measurements were made. The numbers in parentheses refer to different intervals of time in subsequent figures and in the text. . . . .	40
2.9	Histogram of the difference between north- and south-side pole heights. When installed there was no difference; after a year, the north sides had ablated more and this persisted to the three year mark. Also noted: mean, standard deviation, number of points, and standard error of the mean. . . . .	41
2.10	Interpolated ablation field for the <b>3:7</b> interval, in m/yr. . . . .	42



2.11	Measured ablation rates for intervals with weather station measurements. Summertime ablation rates were a factor of two faster than whole-year rates. For each set of 4 or 6 ablation poles (see map in figure 2.1), one symbol is plotted on the graph at the mean value of that group. The 25th and 75th percentile within the group is plotted as the bottom and top of the gray error bar associated with the mean symbol. Symbols without error bars represent single ablation poles, so statistics could not be calculated. The set of single dots near Wx 5 in the upper graph are long-term ablation rates from 1993-2003 (personal communication from E.D. Waddington, 2005). The stars are measurements done by <i>Robinson</i> [1984] from November 1976-November 1977. The left-pointing triangle is from <i>Hoffman et al.</i> [2008] for ablation from 1995-2006. Along-flow distance was measured down the centerline of the glacier from the western side of the study area. The weather station locations are plotted as text (e.g. Wx 1).	43
2.12	Ablation Rates for the <b>3:L</b> interval.	44
2.13	Ablation Rates for the <b>2:7</b> interval.	44
2.14	Ablation Rates for the <b>2:7</b> interval, extrapolated from the measured points (figure 2.13) to all ablation poles.	45
2.15	Ablation Rates for the <b>3:7</b> interval.	45
2.16	Ablation Rates for the <b>3:7</b> interval, extrapolated from the measured points (figure 2.15) to all ablation poles.	46
2.17	Ablation Rates for the <b>2:10</b> interval.	46
2.18	Ablation Rates for the <b>2:10</b> interval, extrapolated from the measured points (figure 2.17) to all ablation poles.	47
3.1	Wx 4 was located upglacier from Windy Gully (white sloping ice directly behind the weather station). Photo by Andy Bliss.	50
3.2	Battery voltage was above 13 V when the batteries were being charged by the solar panels. In the winter it remained above 12 V because we had plenty of batteries. Station 3's solar panel failed in early October 2005.	53
3.3	Outlier points remaining in the dataset after running the outlier detection routine with different window widths and ratio factors. The dataset shown is temperature from Wx 4, mid-November 2003 to the end of January 2004.	54
3.4	Weather variables timeseries, measured by Wx 1: temperature ( $^{\circ}\text{C}$ ), wind speed (m/s), relative humidity (%), shortwave radiation ( $\text{W}/\text{m}^2$ ), and long-wave radiation ( $\text{W}/\text{m}^2$ ). Data were smoothed with a triangular filter that assigned the highest weight to the central point and the lowest weight to points 15 days prior to and 15 days after the central point.	61
3.5	Weather variables timeseries – Wx Bo.	62

3.6	Weather variables timeseries – Wx T. . . . .	63
3.7	Weather variables timeseries – Wx 2. . . . .	64
3.8	Weather variables timeseries – Wx 3. . . . .	65
3.9	Weather variables timeseries – Wx 4. . . . .	66
3.10	Weather variables timeseries – Wx 5. . . . .	67
3.11	Weather variables timeseries – Wx 6. . . . .	68
3.12	Weather variables timeseries – Wx Be. . . . .	69
3.13	Wind Directions for the entire record. The background image is from Landsat. . . . .	70
3.14	Wind Directions for Summer. . . . .	71
3.15	Wind Directions for Winter. . . . .	71
3.16	Wx 3 wind direction, showing the sensor rotation over time. . . . .	72
3.17	Incoming shortwave radiation at Wx 1. Day of the year was plotted along the x-axis and time of day along the y-axis, with the incoming shortwave as the colors ( $\text{W/m}^2$ ). Local noon was 01:00 UTC. These were 5-minute data instead of the usual 20-minute data. Faint dark lines (e.g. close to 06:00) were caused by shading of the sensor by parts of the station. Again, note that the station moved in early January 2004. . . . .	74
3.18	Incoming shortwave radiation at Wx 2. Axes as in figure 3.17. . . . .	75
3.19	Incoming shortwave radiation at Wx 4. Axes as in figure 3.17. . . . .	76
3.20	Incoming shortwave radiation at Wx T. Axes as in figure 3.17. These were 20-minute data. . . . .	77
3.21	The skyview factor plotted here measures the percentage of the sky visible from a grid cell of a DEM. A flat plain would have a skyview factor of 1 and a slot canyon would have a skyview factor close to 0. . . . .	78
3.22	Timeseries of albedo showed snowfall events (albedo increased rapidly to $>0.7$ ) as well as a subtle trend of the baseline (non-snow) albedo over each summer. Data were smoothed with a running median filter with a window width of 3 days. . . . .	79
3.23	A hollow crust, such as the one pictured, can form near the surface of the ice, causing higher albedo. The black scale bar in the lower right represents 10 cm. Photo by Andy Bliss. . . . .	80
3.24	Pressure differences between stations. Station 1’s pressure sensor drifted about 6.5 mbar/year compared to the other two stations. The jump in January 2004 was from station 1’s move to a new location. Blue: Wx 1 - 4, red: Wx 1 - 2, green: Wx 2 - 4. . . . .	82
3.25	The air pressure difference between Wx 2 and 4 (mbar) affects the wind speed ( $\text{m/s}$ ) at both stations. . . . .	83

3.26	Windy Gully (upper center) is a steep tributary of Taylor Glacier. Cavendish Rocks is a nunatak in the middle of Taylor Glacier. Photo taken from a helicopter by Andy Bliss. . . . .	84
3.27	Autocorrelations of wind speed, temperature, and relative humidity for the whole year, summer, and winter. . . . .	87
3.28	The measured air temperature (K) is usually higher than the modeled surface temperature (adjusted to make the energy budget go to zero). The measured vapor pressure (mbar) at screen height is usually lower than the surface vapor pressure calculated from the surface temperature assuming saturation. The vapor pressure difference (mbar) is much larger in summer than winter. All data from Wx 1. Data were smoothed with a 30-day triangular filter. . . . .	88
3.29	Derived variables timeseries – Wx Bo. . . . .	88
3.30	Derived variables timeseries – Wx T. . . . .	89
3.31	Derived variables timeseries – Wx 2. . . . .	89
3.32	Derived variables timeseries – Wx 3. . . . .	90
3.33	Derived variables timeseries – Wx 4. . . . .	90
3.34	Derived variables timeseries – Wx 5. . . . .	91
3.35	Derived variables timeseries – Wx 6. . . . .	91
3.36	Derived variables timeseries – Wx Be. . . . .	92
3.37	Temperature with depth for Wx 1. Scale: Kelvin. . . . .	95
3.38	Subsurface temperature profiles for Wx 1. In summer (far left panel) the surface temperature was warmer than the rest of the ice. By fall (left), the surface temperature was close to the mean annual surface temperature (colder than the mean annual air temperature). A warm layer of ice, a vestige of the previous summer’s heat remained in the subsurface with a temperature peak at about 5 m depth. In winter (right panel), the surface temperature was about 15 K colder than the temperature at depth, and the previous summer’s warmth had been wiped out. When spring rolled around (far right), the surface temperature had increased back to the mean and a layer of cold ice remained below. . . . .	96
3.39	$Z_o$ timeseries for Wx 1. The green dots plot unsmoothed data. The black line shows data smoothed with a triangular filter with a width of 30 days. The blue line shows a running median, again with 30 days of data. . . . .	98
3.40	$Z_o$ timeseries for Wx 2. . . . .	98
3.41	$Z_o$ timeseries for Wx 4. . . . .	99

3.42	$Z_o$ timeseries for times with the upper wind speed $>10$ m/s. The $Z_o$ calculation was better behaved when considering fast wind speeds. The black lines are the same data smoothed with a 5-day triangular filter (with gaps removed). Blue: Wx 1, red: Wx 4, green: Wx 2. . . . .	99
3.43	Surface sinuosity (top) and ablation rates (bottom with <b>4:L</b> in black and <b>4:7</b> in gray). The sinuosity measurement closest to the terminus (distance of 64 km) was 1.26. Sinuosity generally increases and decreases in a manner similar to ablation rates. . . . .	101
3.44	A perspective view of the 4 cm parabolic egg carton. No vertical exaggeration, units are meters, colors are height. . . . .	102
3.45	Profiles from the 4 cm parabolic egg carton have sinuosities close to 1.03. Exaggerated vertical scale, units are meters. Subplot titles indicate the sinuosity for that profile, as well as the angle from which the profile was taken (0 was an edge of the domain). . . . .	103
3.46	Sinuosity versus surface height amplitude. By varying the vertical scale of the parabolic egg carton, and then taking 100 random profiles, and averaging their sinuosities, we arrive at a relationship between sinuosity and amplitude. . . . .	103
3.47	Lapse rate with time. The gray dots are all the data, calculated from our 6 stations. The black line is the same data smoothed with a triangular filter with a width of 60 days. . . . .	104
3.48	Weekly-mean temperatures at each station, plotted against station elevation (y-axis) and time (x-axis). For each week, the temperature of the lowest-elevation station (Wx Bo) was plotted on the x-axis based on the date. Higher-elevation stations tended to be colder and thus plot above and left of the lowest station. During inversions, the higher-elevation stations were warmer and thus plotted above and right from Wx Bo. The legend on the left side of the middle panel shows the dry and saturated adiabatic lapse rates, for scale. The temperature drop with elevation was usually close to linear in summer. Inversions were common in the winter months, March-September, especially at Wx Bo in Taylor Valley where the surface slope is flat and the cold air was able to pool. . . . .	104
3.49	Lapse rate and wind speed. Fast winds on the glacier meant the lapse rate was close to adiabatic. Slow winds allowed a wider range of lapse rates, which were sometimes affected by inversions, as can be seen in figure 3.48. . . . .	105
3.50	Weekly-mean relative humidity at each station, plotted against station elevation (y-axis) and time (x-axis). For each week, the relative humidity of the lowest-elevation station (Wx Bo) was plotted on the x-axis based on the date. Higher-elevation stations which had lower (higher) relative humidity plot above and left (right) of the lowest station. Since relative humidity depends on temperature, it is difficult to interpret this plot, but it clearly shows the dry air emanating from Windy Gully at 860 m. . . . .	106

3.51	Weekly-mean vapor pressure at each station, plotted against station elevation (y-axis) and time (x-axis). For each week, the vapor pressure of the lowest-elevation station (Wx Bo) was plotted on the x-axis based on the date. Higher-elevation stations which had lower vapor pressure plot above and left of the lowest station. Vapor pressure lapse rates were strongest in summer, when the air temperatures were warmer and hence the saturation vapor pressure was higher. Air from Windy Gully (860 m) tends to be dry relative to the air nearby because it descends rapidly down the Gully before reaching the weather station and the air does not have time to gather much moisture from the glacier surface. . . . .	107
3.52	Example timeseries of $SW_{in}$ (dots: blue=Wx 1, green=Wx 2, red=Wx 4) and $SW_{pot}$ (lines, same colors) for December 2004. The match was good on clear days (e.g. 12/5), cloudy days stand out (e.g. 12/8), and the model often overpredicted the measured at night when the sun went behind mountains. Time plotted in UTC, local time is UTC+13. . . . .	109
3.53	$SW_{in}$ and $SW_{pot}$ for March 2005. At the daily maximum value, the potential was higher than the actual by a significant margin (about 25 W/m <sup>2</sup> ). This was partly due to the fact that the simple model did not include attenuation in the atmosphere, which would be most important when the sun was close to the horizon, like it was in March. Note the scale is different from figure 3.52.	109
3.54	Cloud fraction (percentage of the sky covered with clouds) decreases as the measured incoming shortwave radiation approaches the potential shortwave radiation. . . . .	110
3.55	Cloudy periods showed up clearly in the longwave radiation data for December 2004. The plot shows $R_{tov}$ , defined in the text. For this example, when the values were in the range -100 to -150 W/m <sup>2</sup> , the sky was clear. From 0 to -100 W/m <sup>2</sup> , the sky was cloudy. Compare to shortwave radiation depicted in figure 3.52. . . . .	111
3.56	Example of the expectation and weighting process. In this case, the expected wind direction for the katabatic/foehn mode at Wx 4 was 195°. The top panel shows the wind direction timeseries (data minus expectation). The middle-left panel shows a histogram of the top panel. The katabatic/foehn wind direction shows up as a clear peak. The middle-center panel shows the weighting function, with 195 weighted 1. The middle-right panel shows a histogram of the bottom panel. The bottom panel shows the timeseries of the weights. When this and other stations highly weight the katabatic mode, it becomes the dominant one. . . . .	112
3.57	Temperature and wind speed for Wx Bo, plotted with the glacier-wide timeseries of the katabatic and storm modes. These are 20-minute data. . . . .	112
3.58	Temperature and wind speed for Wx T, plotted with the glacier-wide timeseries of the katabatic and storm modes. These are 20-minute data. . . . .	113

3.59	Temperature and wind speed for Wx 1, plotted with the glacier-wide time-series of the katabatic and storm modes. These are 20-minute data. . . . .	113
3.60	Temperature and wind speed for Wx 2, plotted with the glacier-wide time-series of the katabatic and storm modes. These are 20-minute data. . . . .	114
3.61	Temperature and wind speed for Wx 3, plotted with the glacier-wide time-series of the katabatic and storm modes. These are 20-minute data. . . . .	114
3.62	Temperature and wind speed for Wx 4, plotted with the glacier-wide time-series of the katabatic and storm modes. These are 20-minute data. . . . .	115
3.63	Temperature and wind speed for Wx 5, plotted with the glacier-wide time-series of the katabatic and storm modes. These are 20-minute data. . . . .	115
3.64	Temperature and wind speed for Wx 6, plotted with the glacier-wide time-series of the katabatic and storm modes. These are 20-minute data. . . . .	116
3.65	Temperature and wind speed for Wx Be, plotted with the glacier-wide time-series of the katabatic and storm modes. These are 20-minute data. . . . .	116
4.1	Modeled sublimation rates are linearly related to the ablation rates measured at ablation stakes close to the weather stations. The modeled sublimation in the left (right) panel does not (does) include a stability correction; the correction is small. The symbol shapes are the same as in figure 2.11 and colors correspond to stations: Wx 1 blue, Wx 2 green, Wx 3 yellow, Wx 4 red, Wx 5 cyan. Note that ablation is not directly comparable to sublimation. The two points with the lowest measured ablation rates probably had significant snowfall which decreased the measured ablation, leading to a mismatch. The rest of the glacier received little snowfall. The width of the horizontal error bar depends on the measured variability in ablation, as in figure 2.11. The height of the vertical error bar is $\pm$ one standard deviation away from the mean of the Monte Carlo simulation explained in the text. . . . .	121
4.2	The upper line (red) shows modeled sublimation at Wx T (in cm). The lower line (blue) shows measured ablation at the same location. The measurements were noisy due to the sensor used. The occasional spikes and dips were due to snowfall of a few centimeters. The instrument was reset at the beginning of 2007. . . . .	121
4.3	Monthly measurements of surface height change (blue includes snow; red without snow) and modeled sublimation for 2004-6. The correspondence was good, except in summer when the model prediction was low. Compare to figure 5 of <i>Hoffman et al.</i> [2008]. . . . .	122

4.4	Histograms of modeled sublimation after perturbations to one or more input variables from a Monte Carlo simulation. The x-axis shows the total sublimation for the period of record at station 1 in cm. The text discusses the method of perturbation. The solid vertical line in each plot is the sublimation predicted by the unperturbed model. The dotted line is the model result using the (+) uncertainty and the dashed line is using the (-) uncertainty. The total number of points in each simulation was 1000 and each of the 81 histogram bins is 0.5 cm wide. The sublimation model is more sensitive to the uncertainties in surface temperature and roughness than to the instrument uncertainties associated with the measurements of temperature, relative humidity, and wind speed. . . . .	123
4.5	Constant Offset Uncertainty Test – Wx 2. . . . .	123
4.6	Constant Offset Uncertainty Test – Wx 3. . . . .	124
4.7	Constant Offset Uncertainty Test – Wx 4. . . . .	124
4.8	Constant Offset Uncertainty Test – Wx 5. . . . .	124
5.1	Relative magnitudes of the terms in the energy budget for station 1 (all units: $W/m^2$ ). Data were smoothed with a 30-day triangular filter. Fluxes that added energy to the glacier surface were defined to be positive and fluxes that removed energy from the surface were negative. The modeled sublimation rates for all 5 stations exhibit maxima in the summer months. In summer, the warmer temperatures allow for higher vapor pressure differences so despite calmer winds and higher relative humidity, the sublimation rates are higher than in winter. Winter sublimation is quite variable because of storms. . . .	127
5.2	Energy budget timeseries – Wx T. . . . .	128
5.3	Energy budget timeseries – Wx 2. . . . .	128
5.4	Energy budget timeseries – Wx 3. . . . .	129
5.5	Energy budget timeseries – Wx 4. . . . .	129
5.6	Energy budget timeseries – Wx 5. . . . .	130
6.1	The relationship between the frequency and magnitude of sublimation at Wx 1 indicates that frequent, small events ( $<0.025$ mm/interval) contribute more to the total sublimation than infrequent, large events ( $>0.05$ mm/interval). Storms and katabatic wind periods have the largest sublimation rates while the high frequency of calm periods mean they are important too. . . . .	139
6.2	Magnitude-frequency of sublimation with modes – Wx T. . . . .	139
6.3	Magnitude-frequency of sublimation with modes – Wx 2. . . . .	140
6.4	Magnitude-frequency of sublimation with modes – Wx 3. . . . .	140
6.5	Magnitude-frequency of sublimation with modes – Wx 4. . . . .	140

6.6	Magnitude-frequency of sublimation with modes – Wx 5. . . . .	141
6.7	Cumulative sum of modeled sublimation for different modes of weather variability. Refer to table 3.2 to convert between the ‘Met’ and ‘Wx’ notation. Ignore Met 5: it was on rock, not ice. . . . .	141
6.8	Weather patterns at Wx 1 are distinctly different during katabatic, calm, and stormy periods. Panels show sublimation (mm per 20-minute interval), wind speed (m/s), vapor pressure difference between the measurement height and the surface (mbar), temperature (°C), and relative humidity (%) for late February and early March 2006. When the vapor pressure difference and wind speed are large, the ablation is high. When the vapor pressure difference or the wind speeds are low, so is ablation. . . . .	143
6.9	Advanced Very High Resolution Radiometer (AVHRR) image of the Taylor Glacier region on March 4th, 2006. The dark (warm) trace of the katabatic/foehn wind can be seen emanating from Skelton Glacier, just south of Taylor Glacier. White (cold) cloud streaks are also visible, indicating fast winds aloft. From <a href="http://avhrr.acecrc.org.au/">http://avhrr.acecrc.org.au/</a> . . . . .	144
6.10	This AVHRR image was taken March 12th, 2006 when Taylor Glacier was in the midst of the storm. A comma cloud is clearly visible and Taylor Glacier is under thick clouds. . . . .	145
6.11	NOAA-NCEP reanalysis for March 4th, 2006 during a katabatic/foehn event. The blue star and box show the approximate locations of Taylor Glacier and the AVHRR images respectively. Data from <a href="http://iridl.ldeo.columbia.edu/">http://iridl.ldeo.columbia.edu/</a> . . . . .	146
6.12	NOAA-NCEP reanalysis for March 12th, 2006 during a storm. . . . .	147
6.13	Ablation variables example for All Stations. Axes are the same as in figure 6.8. Refer to figure 6.19 for an index map with the station color coding. . . .	147
6.14	Ablation variables example – Wx T. . . . .	148
6.15	Ablation variables example – Wx 2. . . . .	149
6.16	Ablation variables example – Wx 3. . . . .	150
6.17	Ablation variables example – Wx 4. . . . .	151
6.18	Ablation variables example – Wx 5. . . . .	152
6.19	Another way of looking at the data from the March 2006 storm plotted above. All stations are on the same axes and are coded by color, as shown on the index map. . . . .	153
6.20	AVHRR image of a katabatic event at 16:08 UTC on September 18th, 2005. Dark areas were warm (the Dry Valleys and Transantarctic Mountains along the left side of the image. Drainage winds from the continent were evident by the sea ice they cleared from Terra Nova Bay (dark spot of ocean in the left center). . . . .	154



6.21	Ablation variables example for All Stations – September 17-20, 2005. Refer to figure 6.19 for an index map with the station color coding. . . . .	155
7.1	A cliff above Plummet Glacier in the Kukri Hills. Plummet Glacier is a minor tributary to Taylor Glacier. Photo by Andy Bliss. . . . .	158

# List of Tables

1.1	Summer averages of temperature, relative humidity, wind speed, vapor pressure of the air, vapor pressure difference between the air and surface, calculated sublimation rate (mm/20-min interval), and elevation for reference. Data from NDJ 2005/6. See section 3.2 for comparable data from other years.	11
1.2	Winter averages of weather variables. Data from MJJ 2006.	13
1.3	Summertime components of the energy budget for NDJ 2005/6. Abbreviations defined in equation 1.4, and $R$ stands for net radiation. See section 5.1 for comparable data from other years.	22
1.4	Wintertime components of the energy budget for MJJ 2006. Abbreviations defined in equation 1.4, and $R$ stands for net radiation.	23
3.1	Weather Station Instrumentation. The table shows the height at instrument installation. Ablation of the ice surface increased the distance between the sensors and the surface over time. Instrument accuracies were taken from the manufacturer’s literature. The Monte Carlo column shows the range of values used in the simulation described in section 4.2.	51
3.2	Weather station name lookup table. ‘Wx’ names are used throughout the text. Our stations (numbered) are organized by elevation. ‘Met’ names were used in my computer code, and may inadvertently appear in figures.	52
3.3	Summer averages of temperature ( $^{\circ}\text{C}$ ), relative humidity (%), wind speed ( $\text{m s}^{-1}$ ), vapor pressure of the air (mbar), vapor pressure difference between the air and surface (mbar), calculated sublimation rate (mm per 20-min interval), and elevation (m.a.s.l.) for reference. Data from NDJ 2005/6.	56
3.4	Weather Variables Table – MJJ 2006.	56
3.5	Weather Variables Table – Winter 2004	56
3.6	Weather Variables Table – Summer 2004/5	57
3.7	Weather Variables Table – Winter 2005	57
3.8	Weather Variables Table – NDJF	57
3.9	Weather Variables Table – MAMJJASO	58

3.10	Weather Variables Table – December 21, 2003 - January 21, 2004 for comparison to <i>Lewis et al.</i> [1998]. . . . .	58
3.11	Weather Variables Table – December 21, 2004 - January 21, 2005. . . . .	58
3.12	Weather Variables Table – December 21, 2005 - January 21, 2006. . . . .	59
3.13	Weather Variables Table – Summer, All Years. . . . .	59
3.14	Weather Variables Table – Winter, All Years. . . . .	59
3.15	Weather Variables Table – Three Whole Years, December 2003 – November 2006. . . . .	60
3.16	Directional constancy of the wind at each station. . . . .	72
3.17	Wind Speed correlations between stations. . . . .	85
3.18	Temperature correlations between stations. . . . .	85
3.19	Relative Humidity correlations between stations. . . . .	86
3.20	Mean and median roughness calculated from the Law of the Wall. The %>0.03 column refers to the figures below, where I cut off a portion of the data to show the result more effectively. . . . .	98
3.21	Percent time a station had the warmest temperature in the network. The second row shows station elevations in meters. . . . .	106
3.22	Inversions: frequency of occurrence (in percent) for different seasons and modes. See section 3.4 for a description of the modes. . . . .	108
3.23	Modes: frequency of occurrence (in percent) for different seasons. . . . .	118
5.1	Summertime components of the energy budget for NDJ 2005/6. Abbreviations defined in equation 1.4, and $R$ stands for net radiation. . . . .	130
5.2	Wintertime components of the energy budget for MJJ 2006. Abbreviations defined in equation 1.4, and $R$ stands for net radiation. . . . .	131
5.3	Energy Balance Table – Winter 2004 . . . . .	131
5.4	Energy Balance Table – Summer 2004/5 . . . . .	132
5.5	Energy Balance Table – Winter 2005 . . . . .	132
5.6	Energy Balance Table – NDJF for comparison to other authors' work. . . . .	133
5.7	Energy Balance Table – MAMJJASO for comparison to other authors' work. . . . .	133
5.8	Energy Balance Table – December 21, 2003 – January 21, 2004 for comparison to <i>Lewis et al.</i> [1998]. . . . .	134
5.9	Energy Balance Table – December 21, 2004 – January 21, 2005 for comparison to <i>Lewis et al.</i> [1998]. . . . .	134

5.10	Energy Balance Table – December 21, 2005 – January 21, 2006 for comparison to <i>Lewis et al.</i> [1998]. . . . .	135
5.11	Energy Balance Table – Summer, All Years . . . . .	135
5.12	Energy Balance Table – Winter, All Years . . . . .	136
5.13	Energy Balance Table – Three Whole Years, December 2003 – November 2006.	136

## Acknowledgements

Thanks to Kurt Cuffey for all of his support through this behemoth of a dissertation. Thanks to fellow scientists who helped in the field: Johnny Sanders, Jonathan Thom, Howard Conway, Dave Morse, Jeff Kavanaugh, Sarah Aciego, and Hassan Basagic. Thanks to the support staff who made the Antarctic fieldwork possible. The McMurdo Dry Valleys LTER project graciously provided their weather station and ablation data. The National Science Foundation and the University of California provided funding, without which none of this would have been possible, so thanks to them too.

Thanks to my other committee members, John Chiang and Inez Fung for their helpful comments and encouragement. Thanks to Rob Rhew, the other physical geographer at Berkeley. Thanks to the staff of Berkeley Geography for their help with a myriad of things over the years.

Thanks to Dad and Mom for taking me places, encouraging me to look out the window and be curious about what was out there. Thanks to Maynard Miller for sparking my interest in glaciers, and teaching me how to “see” the landscape with a scientific eye. Thanks to Doug MacAyeal for introducing me to Antarctica, being a great example of a field team leader, and teaching me my first Matlab.

Finally, thanks to Taryn for her all-around awesomeness, for keeping me well-fed for long nights of coding, for her endless patience, for making me eat my vegetables so I can live forever, and for making said vegetables actually taste good.

I feel like I just won an Oscar, considering this page...



# Curriculum Vitæ

Andrew Knisely Bliss

## Education

2001	University of Chicago B.S., Geophysical Sciences
2004	University of California Berkeley M.S., Geography
2011	University of California Berkeley Ph.D., Geography



Figure 0.1. The author, looking geeky, getting ready to carry a set of solar panels up a hill for a GPS base station.



# Chapter 1

## Overview

### 1.1 Introduction

Taylor Glacier originates at the edge of the East Antarctic plateau, on Taylor Dome. It follows a tortuous path through the Transantarctic Mountains, and terminates in several lobes in the McMurdo Dry Valleys. Sublimation dominates the surface mass balance on most of the 80 km-long ablation zone. Although Taylor Glacier accounts for a trivial fraction of the outflow from the ice sheet, several aspects make it a feature of primary importance and motivate our investigation of its ablation. The glacier connects the site of a 100,000-year ice core climate history with an extensive glacial geological record in the terminal valleys [*Steig et al.*, 2000; *Brook*, 1993; *Higgins et al.*, 2000a, b; *Marchant et al.*, 1993]. The ablation zone itself exposes late Pleistocene ice that is a resource for paleoclimate studies [*Aciego et al.*, 2007]. The main terminus lies in Taylor Valley, the location of Antarctica’s premier Long Term Ecological Research site [*Prisco*, 1999; *Doran et al.*, 2002]. In all of these contexts, it is essential to understand how Taylor Glacier waxes and wanes over time.

In addition to these specific regional issues, Taylor Glacier is a useful laboratory for general studies of sublimation. In Antarctica, about 1% of the total ice sheet area comprises “blue-ice” zones [*Bintanja*, 1999]. Of such zones, Taylor Glacier has been the most intensively studied for ice dynamics [*Kavanaugh and Cuffey*, 2009]. All across Antarctica, net surface balance rates depend primarily on accumulation minus sublimation and wind scour [*Van de Berg et al.*, 2005]. Though small in magnitude, sublimation can amount to 10-15% of accumulation [*van den Broeke*, 1997; *Lenaerts et al.*, 2010]. Less significant but still non-negligible are sublimation losses in central Greenland [*Box and Steffen*, 2001]. In contrast to these cases, accumulation is essentially absent from much of Taylor Glacier [*Fountain et al.*, 2006]; this provides an opportunity to study sublimation with a minimum of confounding factors.

Previous studies at Taylor Glacier have elucidated ice dynamics of both the accumulation and ablation zones [*Robinson*, 1984; *Hubbard et al.*, 2004; *Morse et al.*, 2007; *Kavanaugh et al.*, 2009b; *Kavanaugh and Cuffey*, 2009], connections to geomorphology [*Higgins et al.*, 2000a], basal properties [*Hubbard et al.*, 2004; *Holt et al.*, 2006], and the overall state of mass



balance [Kavanaugh *et al.*, 2009a]. Most relevant to the present study are Robinson’s work from the mid-1970’s and the extensive recent investigations by A. Fountain and colleagues of ablation and energy balance on the lowest part of the ablation zone. Robinson [1984] found that ablation rates for 1976-77 varied linearly from about 0.45 m/yr water equivalent (w.e.) at the terminus to 0.16 at about 1040 m.a.s.l. He also determined (by measuring crevasse temperatures) that the mean annual temperature at the terminus was  $-17^{\circ}\text{C}$ . From shallow drill holes, he established a lapse rate on the glacier of  $4.0 \pm 0.5$  degrees/km. Fountain *et al.* [2006, fig. 8] found ablation rates at the terminus of Taylor Glacier (averaged over a 7-year period from 1994 to 2001) to be 0.34 m/yr w.e. Ablation rates linearly decreased to 0.12 m/yr w.e. at the top of their survey, 11 km from the terminus at an elevation of 500 m. They found no significant temporal trend in the data. Using 11 years of data from a weather station 4 km up from the terminus, Hoffman *et al.* [2008] found that melt occurred on only 42 days and most of the 0.18 m/yr w.e. ablation occurred via sublimation. They also found that subsurface melt occurred more frequently than surface melt (with an energy balance model that included solar radiation penetration into the ice). Johnston *et al.* [2005] used an energy balance model to understand the melt channels at the terminus of Taylor Glacier. The microclimate within the channel walls was more conducive to melt than the flat surface surrounding the channels.

Compared to this previous work, our study significantly expands the spatial scope and resolution of mass balance measurements and advances understanding of the factors controlling sublimation on a large portion of this glacier. Our paper addresses the following questions, specifically. What are the spatial and temporal patterns of ablation, temperature, wind speed, humidity, and energy fluxes on Taylor Glacier? What is the simplest model that can accurately predict sublimation from weather station data? Which weather variables are most important for that prediction? Under what synoptic conditions do fast sublimation events occur? How important are such events compared to the “background” levels of sublimation?

## 1.2 Field Site

Taylor Glacier is in the Transantarctic Mountains, west of the main United States base in Antarctica, McMurdo Station, and south of New Zealand. The red circle in figure 1.1 shows Taylor Glacier’s location, in the vicinity of  $77.75^{\circ}$  S,  $161.0^{\circ}$  E. Figures 1.2, 1.3, 1.4, and 1.5 map the main features of the study region. Taylor Glacier’s source on Taylor Dome (2365 m.a.s.l.) is located about 30 km west of the boundary of the figure. Ice flowing from the dome converges into Taylor Glacier proper at Taylor Mouth (1700 m.a.s.l.). Between Taylor Mouth and about 1100 m.a.s.l., the glacier surface consists of patchy areas of blue ice and firn. It is heavily crevassed because of flow over bedrock steps and bumps. Our study focused on the main part of the ablation zone (i.e., from which most mass loss occurs), which begins in a broad and gently-sloping area north of Beacon Valley (about 1300 m.a.s.l.) and extends to the main terminus in Taylor Valley (50 m.a.s.l.). The glacier has a number of tributaries and distributary lobes. Significant tributaries include Cassidy Glacier and Windy Gully. Significant distributaries flow into Beacon Valley (and Turnabout Valley), Arena Valley, and

the upper and lower ends of Pearse Valley and Simmons Basin. Taylor Glacier also has a wide confluence with Ferrar Glacier but does not receive much mass from it [Kavanaugh *et al.*, 2009a]. The mountains around the glacier rise up to 1500 meters above the glacier; these features strongly affect the pattern of winds.

## 1.3 Ablation Data

### 1.3.1 Ablation Measurement Technique

We assessed ablation rates at a network of survey sites (Figure 1.3), using the standard technique of repeated pole-height measurements. The 3m-long aluminum conduit poles were initially placed 2 m into the ice or firn. Exposed heights were determined as the average of measurements on the north and south sides of each pole (more details in section 2.3). We also estimated depths of undulations on the surface; ice surfaces undulate at horizontal and vertical scales of order 10 cm and 1-10 cm, respectively. The configuration of the survey grid was primarily determined by the requirements of an ice dynamics study. Consequently, the density and spatial coverage are unusually large for a mass balance program. The entire network was used in the first year of the study. Because of logistical constraints, subsequent measurements were obtained only at subsets of locations.

Measurements span a 4 year period, from November 2002 to January 2007. In the 2002-3 summer field season (abbreviated as **3**), we installed 273 poles and measured initial heights. We revisited the entire network of poles in the 2003-2004 season (**4**) and also visited 73 poles along a flowline at season’s end on January 26th, 2004 (**L** for late-season). Four poles near three of the weather stations were visited on February 1st, 2006 (**6**), by H. Basagic of Portland State University. Finally, 163 poles were measured again within one week of January 1st, 2007 (**7**), again by H. Basagic.

### 1.3.2 Uncertainties in Ablation Measurements

For each pole height measurement, surface undulations introduce an uncertainty of one to a few centimeters (estimated as 25% of the undulation depth). More significant for our analyses is that local spatial variability – differences between nearby poles – shows that a single pole might do a poor job of representing the mean ablation of the local region. Fortunately, the local spatial variability tended to average itself out when considering longer time periods. For the **4:L** interval (one to two months), the average pole height change was 3.2 cm and the average standard deviation of measurements among clustered poles was 36.0% of the ablation. For **3:4**, the numbers were 19.2 cm and 15.6%. For **3:7**, they were 67.7 cm and 8.0%. Sources of local variability included both measurement errors and sublimation variations, the latter related to microtopography, temporary coverage by snow dunes, and perhaps micrometeorological effects. The sublimation from the ice surface was greatly reduced when covered by a snow dune. After a snow dune was removed via

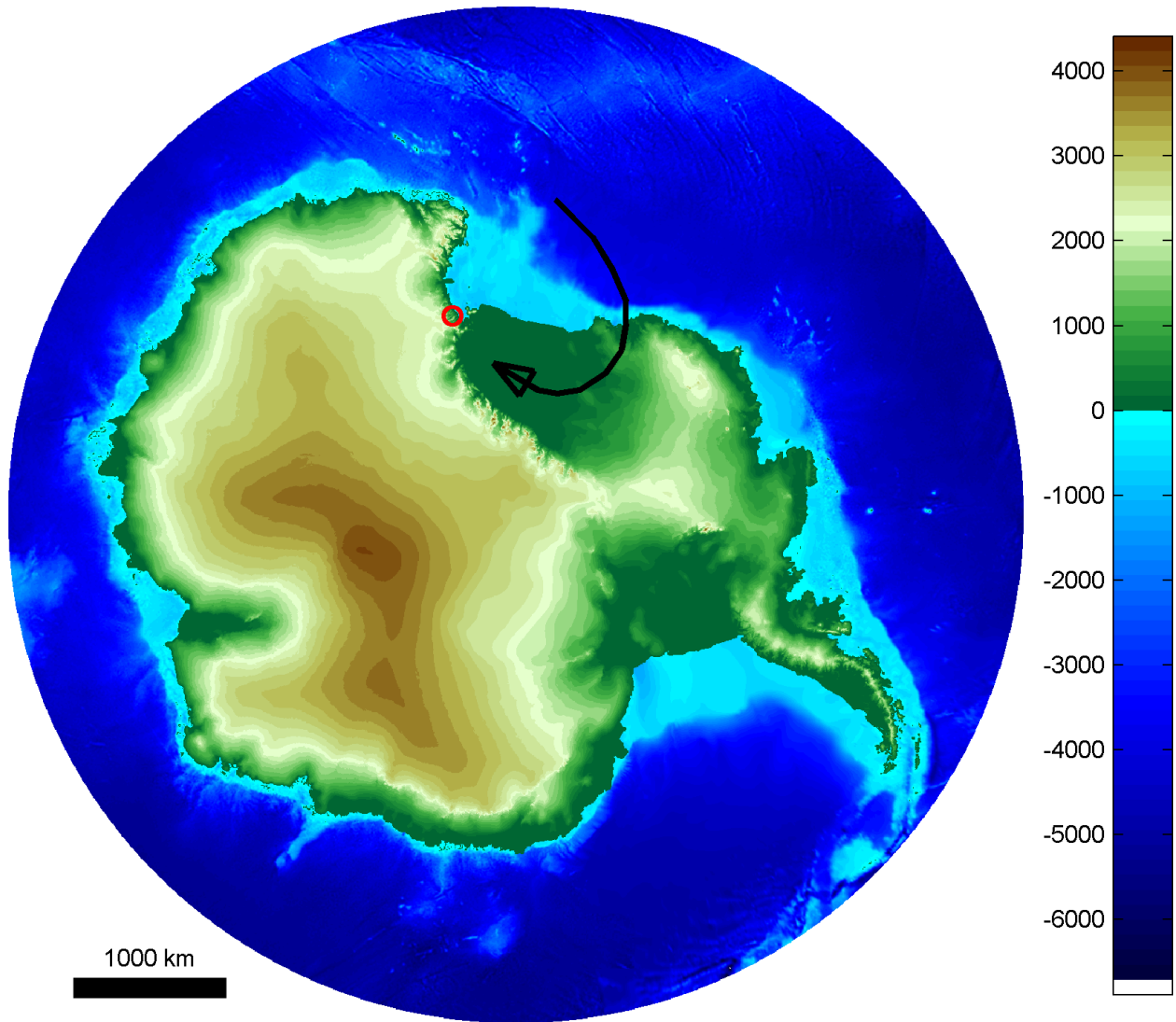


Figure 1.1. A digital elevation and bathymetric model of Antarctica from BEDMAP [Lythe and Vaughan the BEDMAP Consortium, 2001], in meters above sea level. The red circle is the location of Taylor Glacier. The center of the plot is South Pole and the outer edge is  $60^\circ$  S. The black arrow indicates the most common storm track for storms that reach Taylor Glacier [Morse *et al.*, 1998].



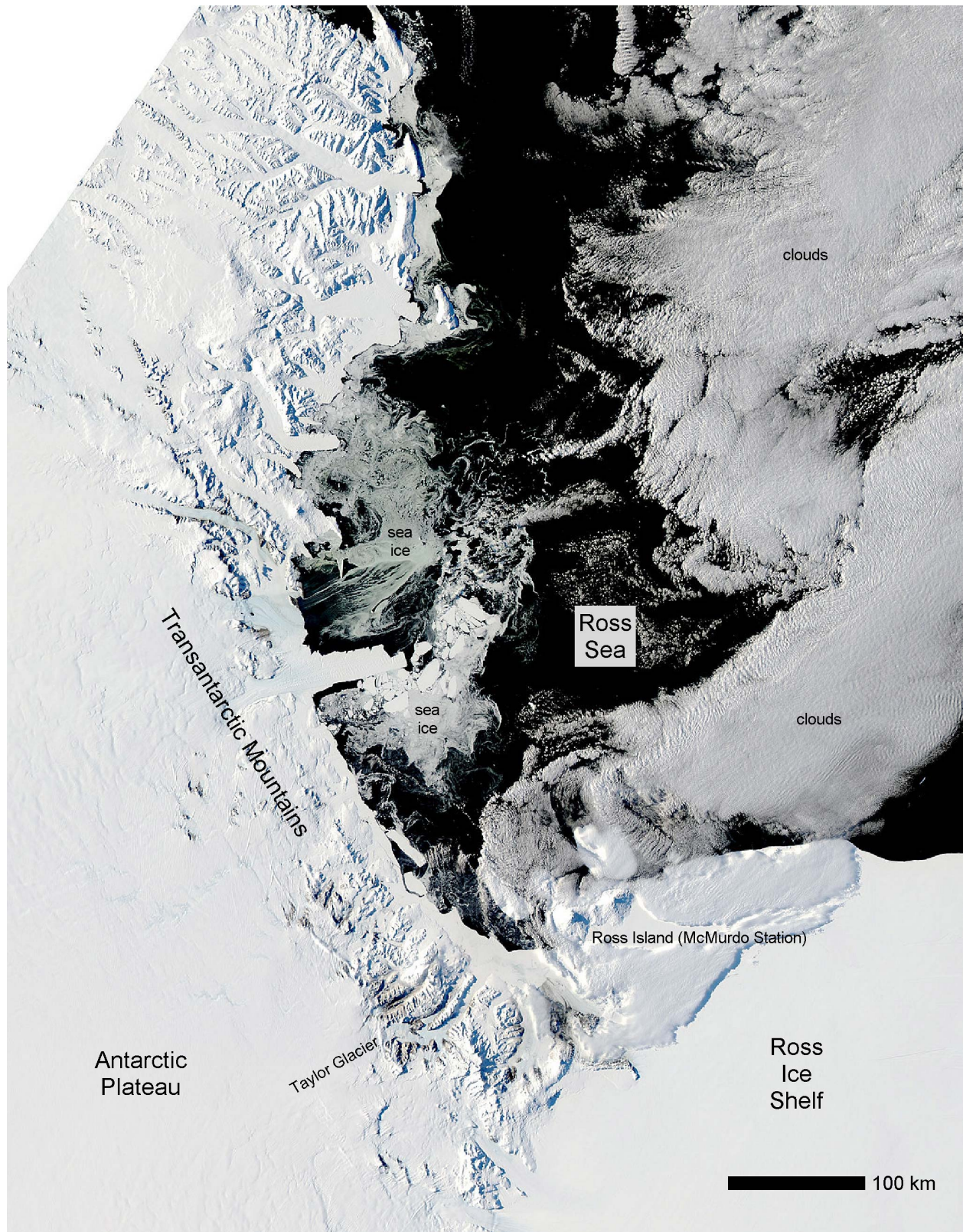


Figure 1.2. A satellite image showing the configuration of land, ocean, and ice in the region surrounding Taylor Glacier. The March 3rd, 2006 MODIS image came from <http://rapidfire.sci.gsfc.nasa.gov/subsets/?subset=RossSea.2006062.aqua.500m>

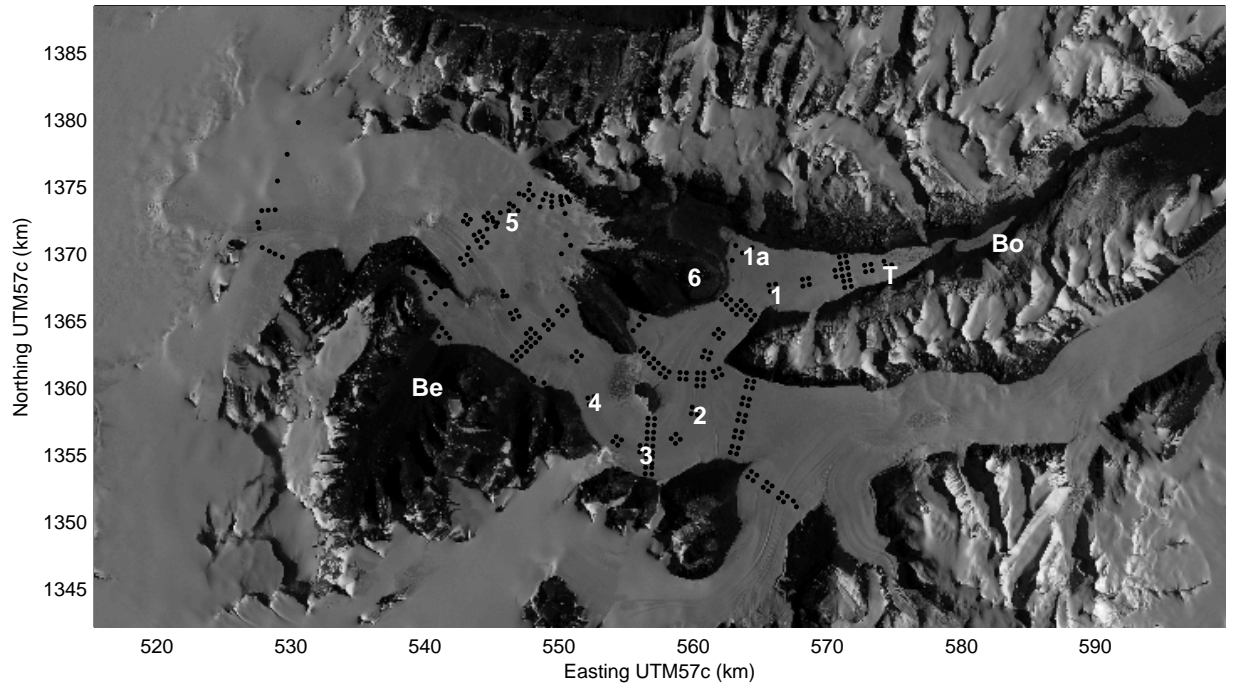


Figure 1.3. A SPOT image of Taylor Glacier, Antarctica showing this study's weather station locations (numbered by elevation), and LTER weather stations at Lake Bonney (Bo), Taylor Glacier (T), and Beacon Valley (Be). Station 1 started at 1a and moved less than 2 months later to 1. Black dots represent ablation poles. The patchy snow line is near Wx 5; the glacier surface to the east is blue ice. Image credit: SPIRIT Program ©CNES 2009 and Spot Image 2008 all rights reserved.



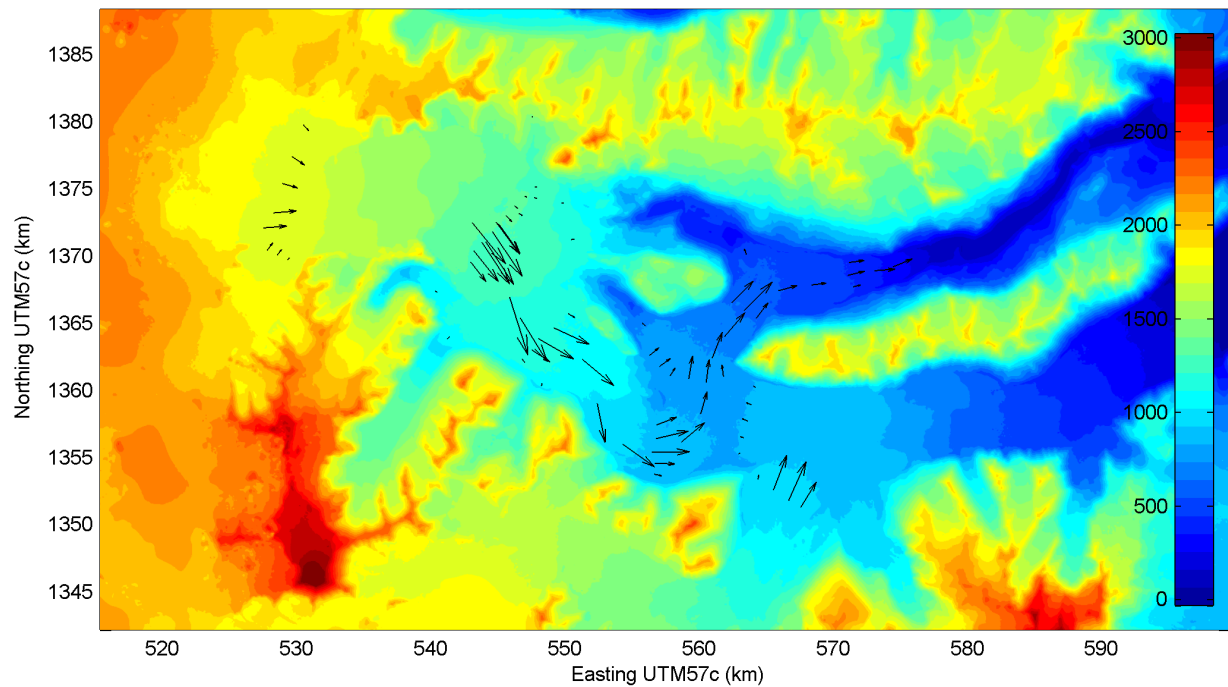


Figure 1.4. A digital elevation model of the Taylor Glacier region derived from satellite imagery. Ice velocity vectors, measured with GPS, show the flow direction. The velocities shown are the average of 4-6 clustered poles. The fastest velocities are about 20 m/yr. Elevation data courtesy of the SPIRIT Program ©CNES 2009 and Spot Image 2008 all rights reserved.

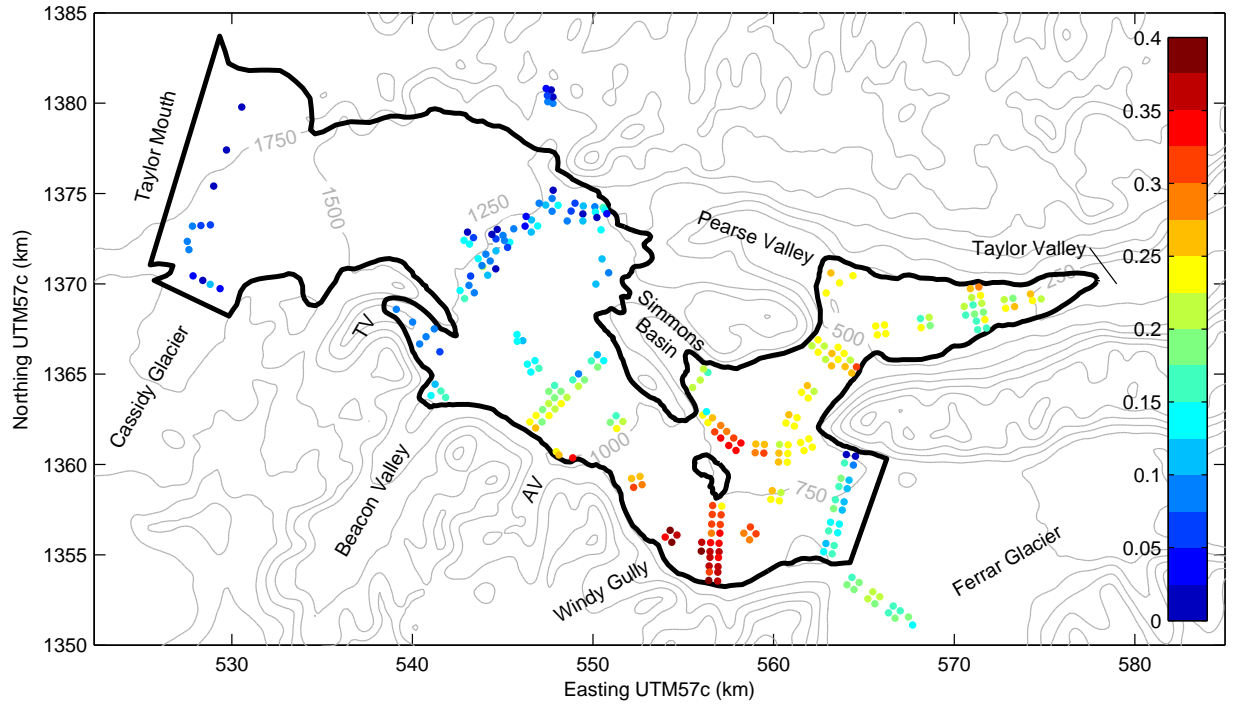


Figure 1.5. The measured ablation rates in the **3:4** interval were highest (about 0.4 m/yr) at the base of the steeply-sloping Windy Gully where the wind speeds, and hence the latent heat flux, were the highest. This plot also shows 250 m topographic contours generated from the RAMP digital elevation model *Liu et al.* [2001]. TV is Turnabout Valley and AV is Arena Valley.

sublimation or wind scour, the exposed ice surface was much smoother than the surrounding surfaces with ablation hollows.

### 1.3.3 Measured Ablation Rates

#### Large-Scale Spatial Variability of Ablation

For the **3:4** interval, ablation rates on most of the surface ranged from 5 to 30 cm/yr (figure 1.5). Above about 1150 m, however, much of the glacier (the northern 2/3 or so) was covered with patchy firn and, in some places, received net accumulation. Blue ice was exposed along the southern margin. Ablation did not vary monotonically with elevation. It tended to increase down the glacier to a local maximum (up to 40 cm/yr) at  $\sim 900$  m altitude near the foot of Windy Gully. Rates varied little between  $\sim 750$  m and 400 m altitude but then increased toward the terminus, where the highest values occurred (below our study area).

#### Temporal Variability of Ablation

In four separate campaigns, we obtained measurements at the same subset of sites: 67 poles arrayed on a 40 km-long flowline from an elevation of 1080 m to within 3 km of the terminus (figure 1.6). The four measurement periods were Nov 19th 2002 to Dec 12th 2002, Dec 13th 2003 to Jan 7th 2004, Jan 26th 2004, and Dec 27th 2006 to Jan 2nd 2007. The glacier ablated most rapidly during the Antarctic summer (e.g. **4:L**, December 2003 to late January 2004). The median ablation rate for that summer was 33.2 cm/yr (and standard deviation of 22.5 cm/yr). For the whole year from late 2002 to late 2003, **3:4**, the corresponding rates were  $23.7 \pm 5.59$  cm/yr (median $\pm$ std). But that year had higher ablation rates than the three-year interval from late 2003 to late 2006, **4:7** ( $17.9 \pm 5.11$  cm/yr).

## 1.4 Weather Data

### 1.4.1 Weather Station Setup

To constrain our analyses of sublimation we set up six weather stations, five on Taylor Glacier itself (stations 1-5 on the map in figure 1.3) and one on top of the Friis Hills (station 6). Data from the latter will not be considered here. The five glacier stations operated from November 2003 until December 2006. Each station measured wind speed and direction, temperature, and relative humidity. Stations 1, 2, and 4 measured incoming and outgoing long- and short-wave radiation. Station 5 measured net radiation. The instrumentation can be found in Table 3.1.

The sensors at all stations recorded data every 5 minutes. Twenty-minute averages were transmitted to the ARGOS satellite system, and locally-stored data were later retrieved from



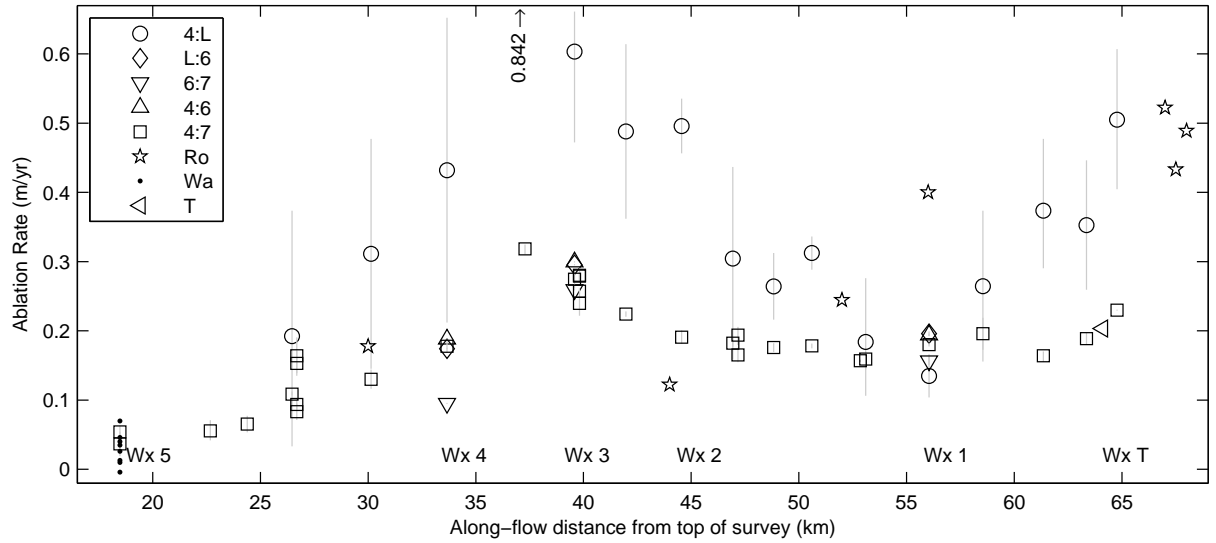


Figure 1.6. Measured ablation rates for intervals with weather station measurements. Summertime ablation rates were a factor of two faster than whole-year rates. For each set of 4 or 6 ablation poles (see map in figure 1.3), one symbol is plotted on the graph at the mean value of that group. The 25th and 75th percentile within the group is plotted as the bottom and top of the gray error bar associated with the mean symbol. Symbols without error bars represent single ablation poles, so statistics could not be calculated. The set of single dots near Wx 5 in the upper graph are long-term ablation rates from 1993-2003 (personal communication from E.D. Waddington, 2005). The stars are measurements done by *Robinson* [1984] from November 1976-November 1977. The left-pointing triangle is from *Hoffman et al.* [2008] for ablation from 1995-2006. The weather station locations are plotted as text (e.g. Wx 1).

Table 1.1. Summer averages of temperature, relative humidity, wind speed, vapor pressure of the air, vapor pressure difference between the air and surface, calculated sublimation rate (mm/20-min interval), and elevation for reference. Data from NDJ 2005/6. See section 3.2 for comparable data from other years.

	$T_{air}$	RH	$u_z$	$e_z$	$e_z - e_s$	$\dot{S}$	Elevation
Wx Bo <sup>a</sup>	-2.5	55.8	4.7	2.9	...	...	64
Wx T	-4.6	62.2	4.4	2.7	-1.5	0.0158	334
Wx 1	-5.9	60.2	5.4	2.5	-1.2	0.0169	490
Wx 2	-7.7	53.7	6.8	2	-1.5	0.0227	817
Wx 3	-8.3	45.7	7	1.6	-1.5	0.0222	857
Wx 4	-8	45.5	5.4	1.6	-1.5	0.019	1012
Wx 5	-11.4	54.2	4.6	1.5	-0.7	0.008	1302
Wx 6 <sup>a</sup>	-13.2	54.2	4.7	1.3	...	...	1581
Wx Be <sup>a</sup>	-9.1	45.7	4	1.4	...	...	1176

<sup>a</sup> Station located on rock, not ice. Surface temperature,  $e_s$ , and  $\dot{S}$  were not calculated for these stations.

Stations 1, 2, 4, and 5. We removed spurious numbers in the ARGOS transmissions with an outlier detection routine (see Appendix 1.10). Data gaps were short enough (median length less than 1 hour) to fill by linear interpolation. About 47% (23%) of the data at station 3 (station 6) were not received.

Additional data from three LTER weather stations [*Doran et al.*, 2002] supplemented our analyses; their station close to the terminus of Taylor Glacier provided wind speed and direction, temperature, relative humidity, incoming and outgoing shortwave, and a sonic distance sensor measuring ablation. LTER stations at Beacon Valley and Lake Bonney provided context. (See station locations T, Be, and Bo in figure 1.3).

## 1.4.2 Weather Station Data

Tables 1.1 and 1.2 summarize average weather conditions in one summer (November, December, January) and winter (June, July, August). Figures 1.7 and 1.8 show example timeseries for the whole study period from station 1. Superimposed on the pronounced seasonal cycle are large variations associated with storms and katabatic winds, both of which occur in all seasons. Interannual variability of average conditions does not reflect systematic differences but instead arises from random factors such as the number of storms.

## Winds

In all seasons, the fastest winds occur midway along the glacier (Wx 3), below the steep tributary valley Windy Gully. In summer, wind speeds on the glacier tend to be slower than in other seasons. The stations close to the ice-free portion of Taylor Valley (Wx 1 and T) often experience diurnal mountain/valley winds when solar heating warms the valley walls. Summertime katabatic winds generally descend from Windy Gully. Wintertime katabatic

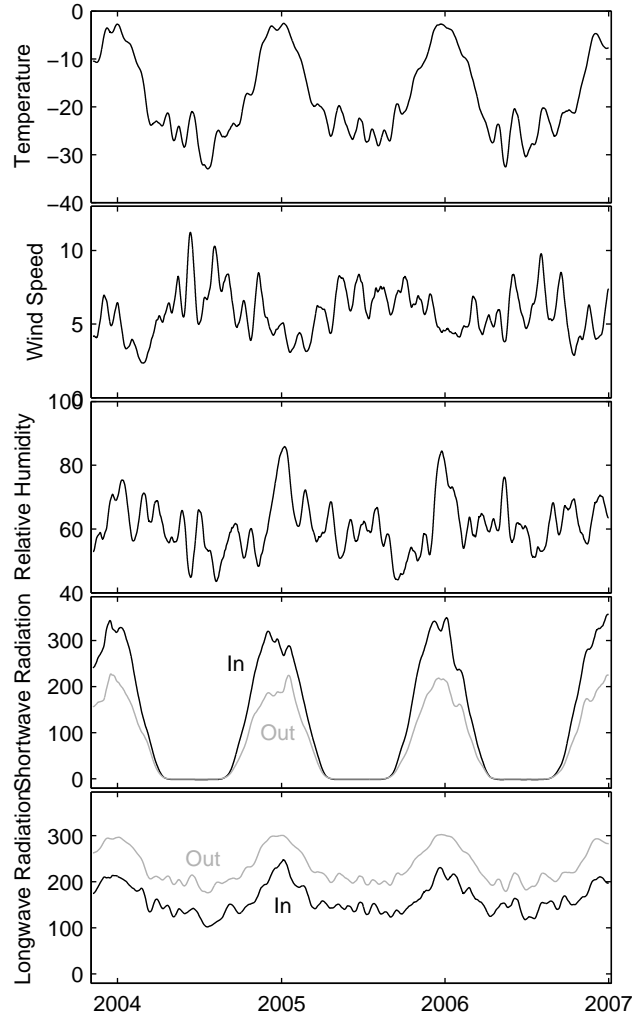


Figure 1.7. Measured weather variables from Wx 1: temperature ( $^{\circ}\text{C}$ ), wind speed ( $\text{m/s}$ ), relative humidity ( $\%$ ), shortwave radiation ( $\text{W/m}^2$ ), and longwave radiation ( $\text{W/m}^2$ ). Data were smoothed with a triangular filter that assigned the highest weight to the central point and the lowest weight to points 15 days prior to and 15 days after the central point. See section 3.2 for comparable data from other stations.

Table 1.2. Winter averages of weather variables. Data from MJJ 2006.

	$T_{air}$	RH	$u_z$	$e_z$	$e_z - e_s$	$\dot{S}$	Elevation
Wx Bo	-29.8	71	3	0.4	...	...	64
Wx T	-26.8	63	5.9	0.5	-0.1	0.0026	334
Wx 1	-27	48.1	6.1	0.4	-0.2	0.0037	490
Wx 2	-27	44.4	8.4	0.3	-0.2	0.0043	817
Wx 3	-26.2	39.2	9.9	0.3	-0.3	0.007	857
Wx 4	-29	41.7	5.6	0.3	-0.2	0.0036	1012
Wx 5	-30.9	50.7	8.3	0.3	-0.2	0.0029	1302
Wx 6	-29.7	45	4.2	0.3	...	...	1581
Wx Be	-31	61.8	4.6	0.3	...	...	1176

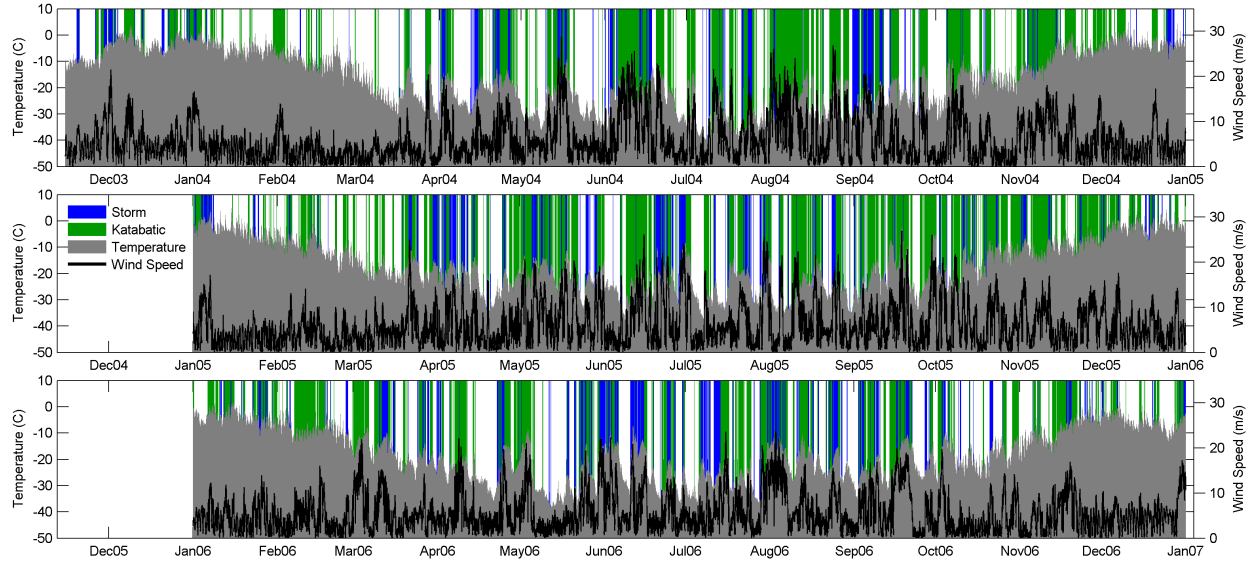


Figure 1.8. Unsmoothed 20-minute temperature and wind speed data for Wx 1, plotted with the glacier-wide timeseries of the katabatic and storm modes. Section 3.4 has comparable plots for other stations and a discussion of the modes.

winds descend alternately from Windy Gully or from the plateau, through Taylor Mouth. The 52.2 m/s maximum wind speed (30-second gust) was recorded at Wx 3 during a storm on May 15th, 2004.

## **Air Temperature**

Temperatures range from as low as  $-50^{\circ}\text{C}$ , during calm periods in the winter, up to  $5^{\circ}\text{C}$ , for a few days in summer at low elevations. Lapse rates tend to be strong ( $7.5^{\circ}\text{C}/\text{km}$ ) and well-organized in the summer and weaker ( $4^{\circ}\text{C}/\text{km}$ ) and less organized in the winter. A persistent winter-time inversion in the ice-free portion of Taylor Valley affects Wx Bo, sometimes affects Wx T, and rarely extends upglacier to Wx 1. Temperature increases at the onset of storms and katabatic wind events are often  $10^{\circ}\text{C}$  in a couple hours.

## **Relative Humidity**

Relative humidity tends to be higher in summer than winter. Summer storms can bring moist air from the ocean, but they can also bring strong downglacier winds which are dry due to adiabatic warming. When the wind speed is over 10 m/s, the relative humidity is rarely above 70%. At lower speeds, it spans the whole range.

## **Shortwave Radiation**

Daily mean incoming shortwave radiation values in the summer tend to be about  $300 \text{ W}/\text{m}^2$ . The mean albedos (when incoming shortwave is greater than  $100 \text{ W}/\text{m}^2$  to avoid spurious readings) for stations T, 1, 2, 4 are 0.58, 0.63, 0.60, and 0.61. They all have a subtle trend of increasing albedo over the course of the summer, generally from about 0.55 at the beginning of the summer to 0.65 at the end. Field observations suggest that this increase accompanies the formation of a hollow crust on the surface due to a small amount of subsurface melt along grain boundaries; the hollow space reflects white light.

## **Longwave Radiation**

Over the seasonal cycle, net longwave energy loss from the surface ranges from lows of  $\sim 50 \text{ W}/\text{m}^2$  in winter to highs approaching  $100 \text{ W}/\text{m}^2$  on clear days in summer. Outgoing longwave radiation is highly correlated with air temperature (as expected). Incoming longwave correlates with air temperature and cloudiness.

## **Snowfall**

Snowfall on the ablation zone was inferred by comparing sonic distance sensor data at station T, AVHRR imagery showing storms, measured ice albedo during summer, and direct field observations. Storms that brought snow to the ablation zone occurred a few times per

year. The snow was usually blown off the glacier within a few days, but sometimes remained for up to a month. A threshold wind speed of  $\sim 15\text{m/s}$  was required to blow the snow off the glacier, regardless of how long the snow had been there. When the snow blew away, the distance to the glacier surface was often greater than before the snowfall, indicating that the sublimation of ice continued even underneath the snowpack.

## Effects of Windy Gully

In the winter, Wx 3 is often warmer and dryer than even Wx T, which is 500 m lower in elevation. These conditions are a consequence of strong katabatic winds moving through Windy Gully and onto the main glacier. An air parcel that quickly descends through Windy Gully, with a vertical drop of 750 meters in just 10 horizontal kilometers, warms at a rate close to the adiabatic rate. On the other hand, an air parcel that descends the same vertical distance on Taylor Glacier must cover a horizontal distance of 30 km (generally with a lower wind speed too) and therefore the parcel has time to cool diabatically. Similarly, the air at the base of Windy Gully is very dry, because it has not had time to gain much moisture via sublimation from the ice surface.

### 1.4.3 Derived Parameters

Some of the calculations discussed below required values for parameters not directly measured, including surface temperatures, surface vapor pressures, and roughness lengths.

#### Surface Temperature

In our standard sublimation model, surface temperature values ( $T_s$ ) were adjusted to achieve a zero net energy budget (figure 1.9 and Appendix 1.11). The estimated surface temperatures were on average  $1.5^\circ\text{C}$  colder than the air temperature in summer and  $4.2^\circ\text{C}$  colder in winter at Wx 1. The persistently low temperatures of the glacier surface were maintained by the net loss of energy by longwave radiation. We also calculated a second estimate of  $T_s$  by developing a parameterization in terms of measured  $T_{air}$  and net radiation (Appendix 1.11).

#### Vapor Pressure

Vapor pressure at the surface was assumed to equal the saturation value at the estimated surface temperature (see *Box and Steffen* [2001] for a discussion of errors). Because vapor pressure depends strongly on temperature, the vapor pressure difference between the air and the surface peaks during the warm summer months with values around 1.5 mbar. Winter values were 5 to 10 times smaller.

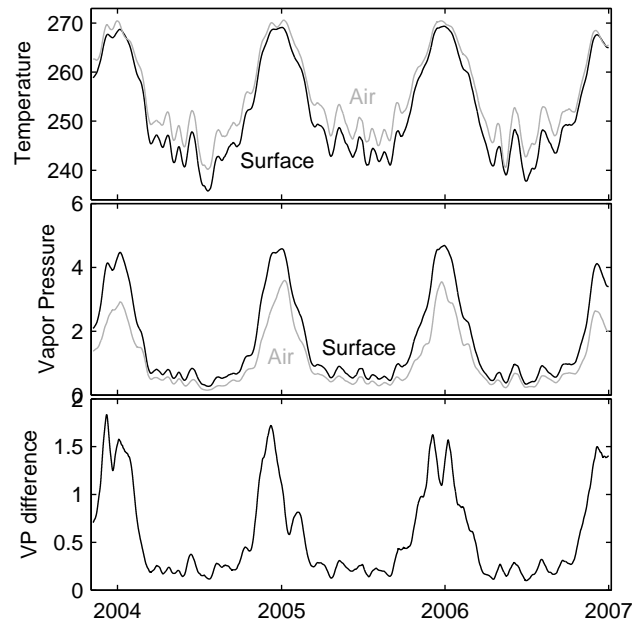


Figure 1.9. The measured air temperature (K) is usually higher than the modeled surface temperature (adjusted to make the energy budget go to zero). The measured vapor pressure (mbar) at screen height is usually lower than the surface vapor pressure calculated from the surface temperature assuming saturation. The vapor pressure difference (mbar) is much larger in summer than winter. All data from Wx 1. Data were smoothed with a 30-day triangular filter. See section 3.3 for comparable data from other stations.

## Roughness Lengths

Three of our stations included wind sensors at two heights, which allowed calculation of the surface roughness ( $Z_o$ ) from the Law of the Wall (see Appendix 1.12). Roughness can also be estimated from surface microtopography. The amplitude of surface undulations is of order 0.1 m, implying (according to standard parameterizations for turbulent flows) roughnesses of several millimeters. When needed, roughness lengths for humidity and temperature were calculated from surface roughness using an empirical relationship (see Appendix 1.12 for equations).

## 1.5 Sublimation Models

Although melting contributes to ablation near Taylor Glacier’s terminus [Johnston *et al.*, 2005; Fountain *et al.*, 2006], in most of the study region temperatures never rose to the melting point except locally around morainal debris. We therefore compared our ablation measurements to sublimation calculated from weather station data. We performed the calculation using several different formulae. In all cases the sublimation rate  $\dot{S}$  was derived from an estimated latent heat flux  $L$  according to

$$\dot{S} = L/(\lambda\rho_{ice}) \quad (1.1)$$

where the latent heat of sublimation  $\lambda = 2.8 \times 10^6$  J/kg and  $\rho_{ice}$  denotes ice density.

In order of increasing complexity, the primary formulae are:

1. A bulk aerodynamic flux equation with no stability correction [Cuffey and Paterson, 2010, equation 5.28].

$$L = \frac{\rho\omega\lambda k^2 u_z (e_z - e_s)/P}{\ln \frac{H_{wind}}{Z_o} \ln \frac{H_{RH}}{Z_{RH}}} \quad (1.2)$$

where  $\rho$  is air density,  $\omega$  the ratio of the molecular weight of water to air,  $\lambda$  the latent heat of sublimation,  $k$  von Kármán’s constant,  $u_z$  wind speed in m/s measured at height  $H_{wind}$ ,  $e_z$  vapor pressure at the measurement height  $H_{RH}$ ,  $e_s$  vapor pressure at the surface,  $P$  air pressure, and  $Z_o$  and  $Z_{RH}$  the roughness lengths for momentum and humidity, respectively. The calculation of  $e_s$  assumed the air at the surface was saturated at the parameterized surface temperature introduced in appendix 1.11. Unfortunately, the net energy budgets calculated using this model varied widely on 20-minute, daily, and seasonal timescales. The net energy budget was rarely zero; such a mismatch arose both from measurement uncertainties and from assumptions in formulae.

2. The energy budget mismatch from the first model led us to try another model in which we reduced the mismatch. Because we did not measure surface temperature ( $T_s$ ) directly, it was one of the most uncertain variables in the analysis. Thus, as an alternative to the previous model, we used the same formulation (Equation 1.2)



but adjusted  $T_s$  to balance the energy budget. Since the energy budget affects and depends on  $T_s$ , an iterative scheme was necessary to find a solution. The adjustment was made on a smoothed (time-averaged) version of the data series rather than on the 20-minute timescale. This strategy was adopted because the calculated net energy for some individual 20-minute intervals deviated widely from zero; fixing the problem by adjusting an unsmoothed  $T_s$  would require unrealistic temperatures. The rest of this paper considers results from this model.

3. Including a correction for atmospheric stability makes the equation more complex. Following *Brock and Arnold* [2000]

$$L = \frac{\rho\omega\lambda k^2 u_z (e_z - e_s)/P}{(\ln \frac{H_{wind}}{Z_o} + \alpha_m \frac{H_{RH}}{\Lambda}) (\ln \frac{H_{RH}}{Z_{RH}} + \alpha_e \frac{H_{RH}}{\Lambda})} \quad (1.3)$$

where the stability length scale  $\Lambda$  ranges from 0 to 230 m (10 and 90th percentile). The length scale is ill-defined for neutral conditions (when the air temperature is roughly equal to the surface temperature). We assumed the latent heat flux was zero under those conditions (18% of the data).  $\alpha_m$  and  $\alpha_e$  are stability correction constants equal to 5 [*Brock and Arnold*, 2000]. We found that sublimation calculated with this model did not match measurements as well as did calculations using model 2. Thus, although commonly applied to glaciers, equation 1.3 will not be considered further here.

### 1.5.1 Predicted Sublimation

Figure 1.10 plots, for different time periods, the covariation of ablation measurements with the sublimation rates calculated from Equations 1.1 and 1.2. For seasonal to annual averages, the modeled sublimation is linearly related to the measurements, with a least-squares regression slope of 0.85. The model over-predicts ablation at low rates. Overall, however, the match is very good. We therefore believe that the model can provide useful interpretations of shorter-period variations in sublimation, which were not directly measured. Rates range from about 0 mm/day during calm intervals in winter to 2.5 mm/day during warm and dry summer days. Although mean summer rates are more than twice as large as winter ones, the contribution of slow winter sublimation to the yearly total cannot be neglected (see section on magnitude and frequency below).

### 1.5.2 Sensitivity of Predictions to Input Values

To evaluate the sensitivity of modeled sublimation values to uncertainties of the input data, we performed a Monte Carlo analysis. Input variable timeseries were uniformly perturbed by a normally distributed random variable with zero mean and a standard deviation given as follows. For temperature, wind speed, and relative humidity, the standard deviation equaled the manufacturer's stated instrument accuracy (0.4°C, 0.3 m/s, 2%). For surface temperature, we chose an uncertainty of 0.6°C to be comparable to the adjustments of surface temperature required for energy balancing. We set the  $Z_o$  uncertainty to 0.001 m based

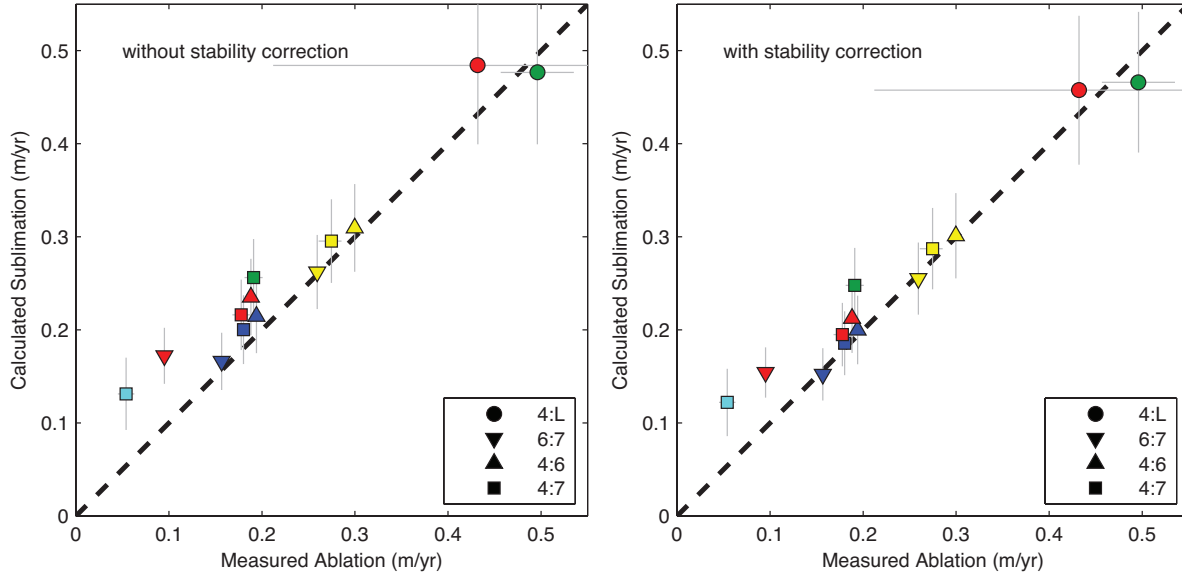


Figure 1.10. Modeled sublimation rates are linearly related to the ablation rates measured at ablation stakes close to the weather stations. The symbol shapes are the same as in figure 1.6. The width of the horizontal error bar depends on the measured variability in ablation, as in figure 1.6. The height of the vertical error bar is  $\pm$  one standard deviation away from the mean of the Monte Carlo simulation explained in the text.

on the common range of  $Z_o$  values used in the literature. We chose to uniformly perturb the input timeseries rather than perturb individual values because short-term random variations average out when considering seasonal or annual sublimation. In other words, instrument precision is less important than accuracy.

Sensitivities are illustrated by the resulting distributions of calculated sublimation rate summed over the whole period of record (Figure 1.11). The most important source of uncertainty is the surface temperature. Overall, the estimated uncertainty of model sublimation values is rather large. The standard deviation of the Monte Carlo results divided by the mean was between 14 and 18% for the different weather stations.

In addition to the uncertainties arising from input data, the calculated sublimation obviously depends on the assumption that the equations represent the complex process of turbulent moisture transfer in nature. The only indication of total uncertainty is the mismatch between measured and modeled sublimation rates depicted in figure 1.10.

## 1.6 Energy Budget

We define the net energy flux,  $E$ , using the budget equation

$$E = SW + LW + L + H + G \approx 0. \quad (1.4)$$

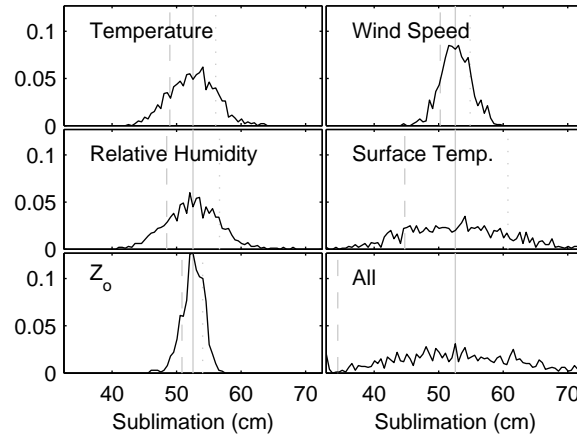


Figure 1.11. Histograms of modeled sublimation after perturbations to one or more input variables from a Monte Carlo simulation. The x-axis shows the total sublimation for the period of record at station 1 in cm. The text discusses the method of perturbation. The solid vertical line in each plot is the sublimation predicted by the unperturbed model. The dotted line is the model result using the (+) uncertainty and the dashed line is using the (-) uncertainty. The total number of points in each simulation was 1000 and each of the 81 histogram bins is 0.5 cm wide. The sublimation model is more sensitive to the uncertainties in surface temperature and roughness than to the instrument uncertainties associated with the measurements of temperature, relative humidity, and wind speed. See section 4.2 for comparable data from other stations.

As mentioned above, we measured incoming and outgoing shortwave  $SW$  and longwave  $LW$  radiation. Latent heat fluxes  $L$  were obtained from equation 1.2. An analogous equation gave sensible heat fluxes  $H$ . Heat flux into the subsurface  $G$  was calculated using finite-difference solutions to the diffusion equation for time- and depth-varying temperatures within the ice.  $G$  sums two terms: the change of energy stored as heat within the top numerical layer (0.04 m thick), and the Fourier heat flux through the layer. Points in the finite-difference grid were spaced closer together near the surface (18 in the first meter) than at depth (2-m spacing at 50 m depth). The surface boundary condition was the surface temperature appropriate for the sublimation model being considered, as described previously. The basal boundary condition was set according to the temperature profile from a force-balance model of the glacier [Kavanaugh and Cuffey, 2009].

The heat flux due to melt and subsequent runoff was assumed to be zero at our sites, which are far from the margins and the terminus. This assumption was based on field observations and the temperature record from the weather stations ( $\sim 2$  days per year with temperatures above  $0^\circ\text{C}$ ). Runoff does occur within 1 km of the terminus and within 100 m of the margin of the glacier elsewhere. The heat flux due to rain was also neglected, again because of field observations and the temperature record.

In the absence of measurement uncertainties, the net energy flux as defined here should equal zero.

### 1.6.1 Energy Budget Data

Figure 1.12 shows timeseries of the terms in the energy budget for Wx 1. Tables 1.3 and 1.4 show seasonal averages for all stations. Net shortwave radiation was the largest term in the energy budget in summer. Longwave radiation also peaked in summer, but it was more constant throughout the year. The calculated sensible heat flux warming the ice was largest in the winter, approximately balancing the heat lost by longwave radiation. In summer, the ice temperature was closer to the air temperature so the sensible heat flux was smaller but still positive. The calculated latent heat flux was almost always negative (very little condensation or hoar deposition) and was strongest in summer. Heat flowed into the subsurface during the spring and summer and flowed out during the winter, with a maximum magnitude smaller than the latent and sensible terms. The residual of the other terms is plotted as the net energy balance, as in equation 1.4.

## 1.7 Relation of Sublimation to Weather Modes

By systematically examining our station data and making comparisons to satellite imagery, we found that weather variability at Taylor Glacier reflects four distinct patterns or modes: (1) stormy weather related to cyclonic systems, (2) dominance of strong katabatic winds, (3) dominance of diurnal fluctuations in wind speed and direction, and (4) calm conditions. We discriminated these modes in our timeseries on the basis of measured wind speeds and cloud amounts (inferred from the longwave radiation) at our weather stations.

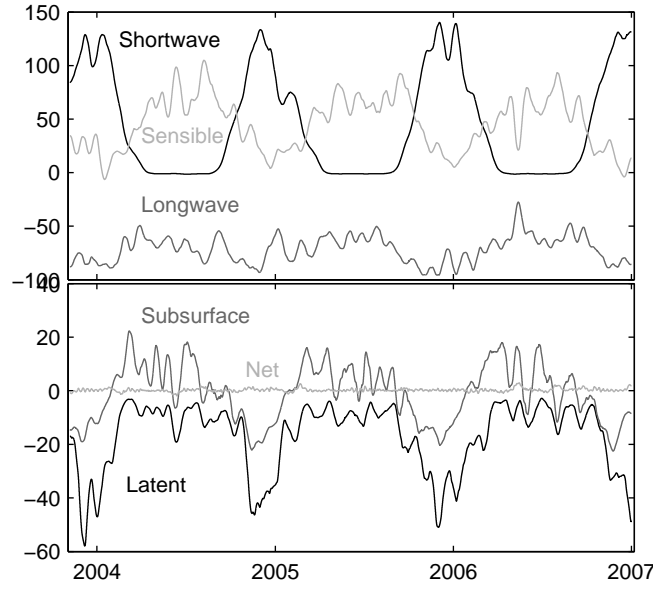


Figure 1.12. Relative magnitudes of the terms in the energy budget for station 1 (all units:  $\text{W}/\text{m}^2$ ). Data were smoothed with a 30-day triangular filter. Fluxes that added energy to the glacier surface were defined to be positive and fluxes that removed energy from the surface were negative. The modeled sublimation rates for all 5 stations exhibit maxima in the summer months. In summer, the warmer temperatures allow for higher vapor pressure differences so despite calmer winds and higher relative humidity, the sublimation rates are higher than in winter. Winter sublimation is quite variable because of storms. Similar plots for other stations are in section 5.1.

Table 1.3. Summertime components of the energy budget for NDJ 2005/6. Abbreviations defined in equation 1.4, and  $R$  stands for net radiation. See section 5.1 for comparable data from other years.

	SW	LW	R	H	L	G	E
Wx Bo	219	-88	131	...	...	...	...
Wx T	125	-85 <sup>a</sup>	40	7	-34	-13	0
Wx 1	116	-85	31	18	-36	-12	0
Wx 2	143	-89	54	8	-49	-12	1
Wx 3	120 <sup>b</sup>	-85 <sup>b</sup>	35 <sup>b</sup>	24	-48	-11	1
Wx 4	120	-85	35	18	-41	-12	0
Wx 5	...	...	0	27	-17	-11	-0
Wx 6	...	...	124	...	...	...	...
Wx Be	250	-88 <sup>c</sup>	162	...	...	...	...

<sup>a</sup> Assumed similar to Wx 1.

<sup>b</sup> Assumed similar to Wx 4.

<sup>c</sup> Assumed similar to Wx Bo.

Table 1.4. Wintertime components of the energy budget for MJJ 2006. Abbreviations defined in equation 1.4, and  $R$  stands for net radiation.

	SW	LW	R	H	L	G	E
Wx Bo	-0	-35	-35	...	...	...	...
Wx T	-0	-56 <sup>a</sup>	-56	56	-6	6	-0
Wx 1	-1	-56	-58	61	-8	5	0
Wx 2	-1	-67	-69	72	-9	5	-0
Wx 3	-1 <sup>b</sup>	-57 <sup>b</sup>	-58	68	-15	4	-1
Wx 4	-1	-57	-58	61	-8	5	0
Wx 5	...	...	-37	38	-6	5	-1
Wx 6	...	...	-46	...	...	...	...
Wx Be	0	-35 <sup>c</sup>	-35	...	...	...	...

<sup>a</sup> Assumed similar to Wx 1.

<sup>b</sup> Assumed similar to Wx 4.

<sup>c</sup> Assumed similar to Wx Bo.

Although sublimation occurred in all types of conditions, it occurred most rapidly during stormy weather and strong katabatic winds.

### 1.7.1 Example Time Period

A strong katabatic wind event raged for more than 5 days in early March, 2006; this event not only appears in our station data (Wx 1 shown in figure 1.13) but also can be seen clearly in AVHRR imagery from March 4th as dark streaks of warm air descending off the Antarctic plateau. The event began with marked increases of wind speeds (to about 10 m/s) at each station on March 1st. On March 1st and 2nd temperatures gradually rose from -20 to -12°C. Relative humidity fell from 60% to 20%, causing the vapor pressure difference between the air and the surface to rise from below 0.5 up to 1.5 mbar. Over three days, wind speeds also increased to about 20 m/s. The fast winds combined with the enhanced vapor pressure difference produced some of the highest sublimation rates of the fall.

The strong katabatic flow was followed by a calm period wherein wind speeds dropped to less than 2 m/s, the temperature abruptly dropped 8°C in 4 hours, and the relative and absolute humidities jumped up as well. The air mass came from Taylor Valley, as evidenced by easterly wind directions (not shown). Sublimation during this period was close to zero. The calm period lasted 2 days before the effects of a storm (also identified via AVHRR images) approaching from the Ross Sea began to be felt.

The storm brought faster winds and clouds to all stations. On the third day of the storm (March 12th), Wx 1 experienced rapidly oscillating conditions. Periods of fast downglacier wind, warm temperature, low relative humidity, and rapid sublimation alternated with the opposite. The system would stay in one state for as little as 1 hour during these fluctuations. The stations above Wx 1 experienced downglacier winds the whole time. Meanwhile, LTER

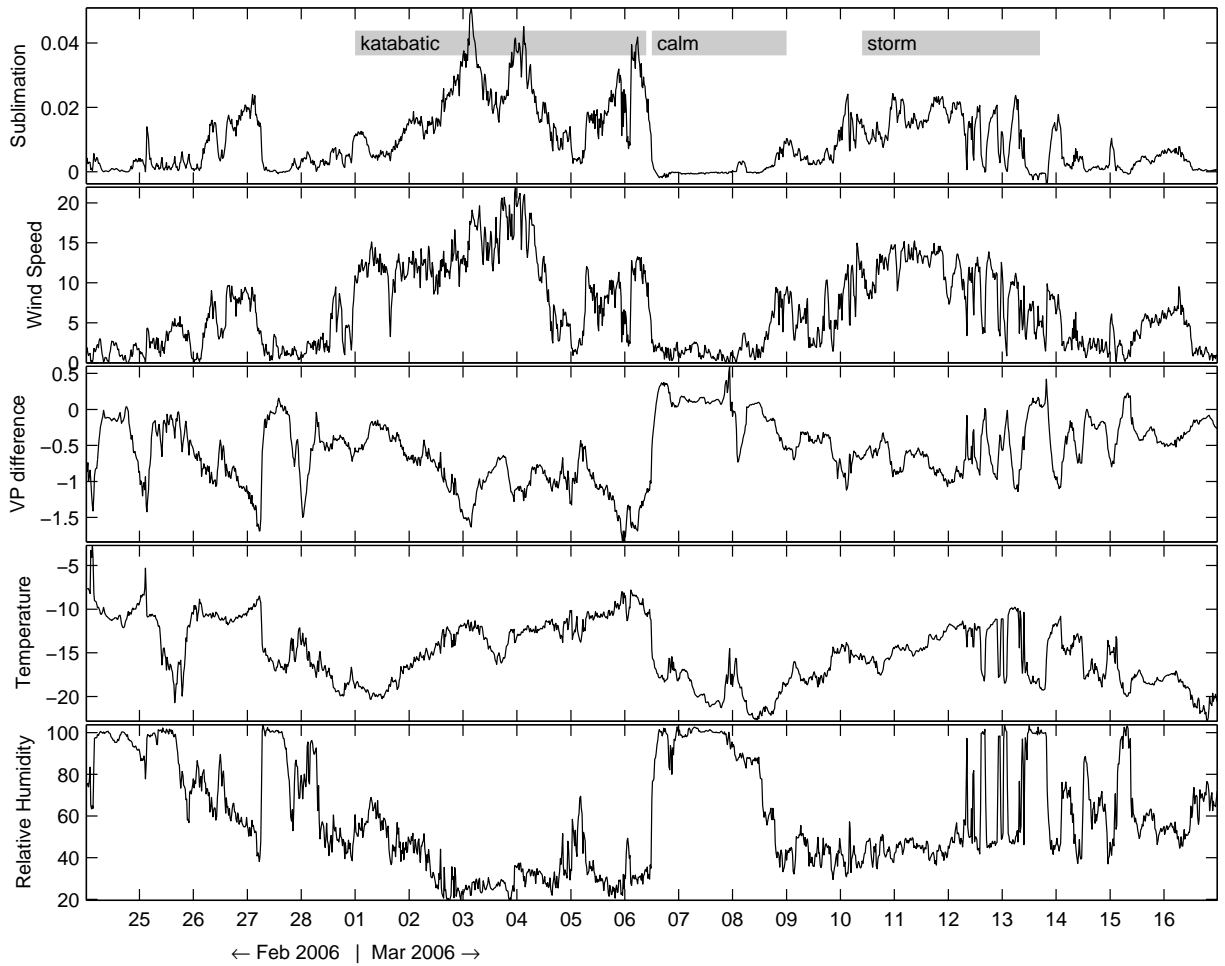


Figure 1.13. Weather patterns at Wx 1 are distinctly different during katabatic, calm, and stormy periods. Panels show sublimation (mm per 20-minute interval), wind speed (m/s), vapor pressure difference between the measurement height and the surface (mbar), temperature ( $^{\circ}\text{C}$ ), and relative humidity (%) for late February and early March 2006. When the vapor pressure difference and wind speed are large, the ablation is high. When the vapor pressure difference or the wind speeds are low, so is ablation. See 6.2 for comparable data from other stations.

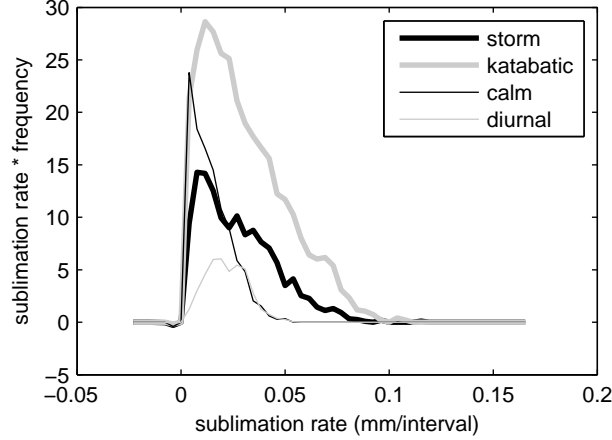


Figure 1.14. The relationship between the frequency and magnitude of sublimation at Wx 1 indicates that frequent, small events ( $<0.025$  mm/interval) contribute more to the total sublimation than infrequent, large events ( $>0.05$  mm/interval). Storms and katabatic wind periods have the largest sublimation rates while the high frequency of calm periods mean they are important too. See section 6.1 for comparable data from other stations.

stations below our station 1 experienced consistent, weak upglacier winds, low temperatures, and high humidities.

### 1.7.2 Magnitude versus frequency of sublimation

The importance of rapid but brief sublimation events compared to slow and persistent conditions can be assessed by transforming a timeseries of sublimation rate into a frequency distribution of the occurrence of sublimation as a function of rate [following *Wolman and Miller*, 1960; *Pickup and Rieger*, 1979]. Specifically, total sublimation in a time interval  $\tau$  is  $\int_{\tau} f(\dot{S}) \dot{S} d\dot{S}$  where  $f$  denotes the frequency of occurrence of sublimation of rate  $\dot{S}$ . Figure 1.14 plots the integrand of this formula for the four different weather modes, at one station. The fastest sublimation occurred during storms and periods with strong katabatic winds. However, these events (with sublimation  $>0.05$  mm per 20 minute interval) occurred infrequently (1-2% of the time) and contributed 10-15% of the total sublimation. Slow sublimation ( $<0.025$  mm/interval) happened during all four modes, was frequent (80-90% of the record) and accounted for 50-60% of the total sublimation. This result bodes well for our ability to understand sublimation in past and future climates, to the extent that forecasts of seasonal conditions are generally more accurate than forecasts of extreme events.



## 1.8 Discussion

### 1.8.1 Measured Ablation Rates

On typical land-based glaciers, ablation rates are highest at the terminus, where temperatures are warm and the climate is conducive to melt or fast sublimation. Ablation monotonically decreases with increasing elevation as temperatures decline. On Taylor Glacier, while temperature does generally decrease with elevation, ablation rates peak in the middle of the ablation zone’s elevation range, at 900 m. Our model results show that this odd ablation pattern can be explained by rapid sublimation caused by dry air moving quickly over the glacier. The source of the fast dry air is katabatic flow from Windy Gully, a steep tributary of Taylor Glacier.

In the early 1970s, ablation rates close to the terminus [*Robinson*, 1984] were twice as high as rates measured since 2000 by our surveys. The 11-year mean ablation rate reported by *Hoffman et al.* [2008] for a site next to Wx T falls on the trend of our data (figure 1.6), while the 7-year mean rates reported by *Fountain et al.* [2006] were generally a few cm/yr lower than our 4-year data. (The different time periods and locations used in these three studies preclude a direct comparison.) We speculate that the 1970’s ablation rates were higher because the local climate was warmer then [*Doran et al.*, 2002], which enhanced both sublimation and melt.

Our results showing a clear maximum of ablation near Windy Gully indicate that the spatial coverage of *Robinson*’s study was not sufficient to characterize the relation between ablation and elevation on this glacier, or to assess the glacier’s surface mass balance accurately. Robinson assumed a linear relationship between ablation and elevation, which proves to be a poor assumption given the effects of the complex topography on wind fields. Using Robinson’s relationship would underestimate ablation rates by a factor of two at 900 m altitude. His estimate of the overall mass balance of Taylor Glacier was a gain of  $9.5 \pm 23.3 \times 10^6$  tonnes/year, whereas our estimate (based on improved measurements of ice flux and surface balance) indicates that most of the glacier is nearly in mass equilibrium, even with the lower recent ablation rates [*Kavanaugh et al.*, 2009a]. (One sector, however – that which flows into Pearse Valley from the west – appears to be shrinking.)

Another contrast concerns the location of the equilibrium line. *Robinson* [1984] estimated it to be at an elevation just over 2000 m.a.s.l., based on air photos from between 1957 and 1973. Our ablation measurements indicate the equilibrium line is closer to 1400 m, although it is not a “line” but a broad and heterogeneous zone. Robinson may have based his estimate on the elevation of the highest exposed blue ice, but large patches of persistent snow (figure 1.3) at lower elevations maintain a positive surface mass balance. It should also be noted that over most of the glacier Robinson’s elevation figures are about 300 meters higher than those indicated by our GPS surveys.

Although we do not have meteorological measurements at the Taylor-Ferrar confluence, observations suggest that the low sublimation rates measured there (figure 1.5) reflect gen-

erally low local wind speeds. The downglacier winds are steered north by the western prow of the mountain ridge that separates Taylor Valley from Ferrar Valley.

Ablation on Taylor Glacier, especially close to Windy Gully, is rapid compared to that in other Antarctic “blue ice” areas. In *Bintanja’s* [1999] classification of blue ice areas, Taylor Glacier is a Type II (“located on a valley glacier”), and Taylor Glacier shares many characteristics with the more extensively-studied Type I blue ice zones (in the lee of a mountain). Our measurements reveal maximum rates (40 cm/yr for the **3:4** interval) much higher than those reported in *Bintanja’s* compilation at the elevation of Windy Gully (900 m), or in fact at any elevation [see figure 6 of *Bintanja*, 1999].

## 1.8.2 Weather Data

The mean annual temperature at the station closest to the terminus (Wx T) was  $-17.4^{\circ}\text{C}$ , almost identical to the  $-17^{\circ}\text{C}$  estimated by *Robinson* [1984] from crevasse temperatures. *Robinson* [1984] found a lapse rate of  $4^{\circ}\text{C}/\text{km}$  by measuring temperature in shallow boreholes. *Johnston et al.* [2005] used temperature sensors to find a summertime lapse rate along the lower Taylor of about  $8^{\circ}\text{C}/\text{km}$ . We found that the lapse rate across the entire ablation zone had a median value of  $6.4^{\circ}\text{C}/\text{km}$  for the period of record but varied significantly with the season, from about  $4^{\circ}\text{C}/\text{km}$  in winter to  $7.5^{\circ}\text{C}/\text{km}$  in summer. In winter, small lapse rates prevailed when wind speeds were less than about 7 m/s. With faster winds, adiabatic warming of air descending the glacier increased the lapse rate into the range  $5\text{--}10^{\circ}\text{C}/\text{km}$ .

## 1.8.3 Modeled Ablation Rates

In the relationship between our modeled and measured sublimation rates (figure 1.10), the departure from a slope of unity might arise from multiple factors. Model over-prediction at low ablation rates might arise from temporary accumulation; we occasionally observed snow patches in the vicinity of Wx 5. Accumulation is not included in our model because we did not obtain continuous measurements of surface height (e.g. taken with sonic distance sensors).

For sites in Queen Maud Land, Antarctica, *Bintanja and Reijmer* [2001] found that 70% of the annual sublimation happened in summer (NDJF). On Taylor Glacier, 54 to 68% happened in summer (stations 5 and T, respectively). We attribute the greater importance of winter ablation at Taylor Glacier to strong winter winds that favor sublimation.

## 1.8.4 Energy Budget

Not surprisingly, the energy budget of Taylor Glacier’s surface has the same general features as other Antarctic sites: gain of radiative energy in summer and loss in winter; year-round loss of latent heat by sublimation (condensation and hoar deposition being common but quantitatively negligible processes); small gains and losses of heat to the subsurface in

winter and summer, respectively. Sensible heating of the surface is unusually large at Taylor Glacier because of strong down-slope katabatic winds and frequent cyclonic disturbances.

On the ablation zone of Canada Glacier, approximately 15 km east of Taylor Glacier, *Lewis et al.* [1998] determined an energy budget for 21 December - 21 January 1994/5 that was very similar to the budget at our lowest station, Wx 1, for the same calendar days but in 2005/6. The similarity extended to our respective calculations of sublimation: 3.65 cm w.e. for Canada Glacier and 3.2 cm w.e. for Taylor Glacier. One difference was that the Taylor Glacier sensible heat flux was positive. Moreover, in 1995/6 on Canada Glacier, *Lewis et al.* [1998] found a significantly higher net radiation that produced a large quantity of melt. We did not observe melt at our weather station sites on Taylor Glacier.

Sublimation from Lake Hoare (an ice-covered lake 10 km east of Taylor Glacier terminus) in 1986 was estimated from meteorological data to be  $35.0 \pm 6.3$  cm [*Clow et al.*, 1988] which is in line with the values we found on Taylor Glacier.

Compared to the blue-ice sites in Queen Maud Land (QML) studied by *Bintanja* [2000], summertime latent heat losses at Taylor Glacier were large. Yet the net shortwave and longwave values were nearly identical. Thus, it was the large sensible heat fluxes that sustained surface conditions conducive to rapid sublimation at Taylor Glacier. The larger sensible fluxes at Taylor, in turn, appear to reflect warmer air more than strong winds. At Scharffenbergbotnen (in QML), for example, the reported summer wind speeds were similar to those near the terminus of Taylor (Wx T), but air temperature at Wx T was higher, sensible heat flux was  $+7$  W/m<sup>2</sup> instead of  $-7$  W/m<sup>2</sup>, and latent flux was  $-34$  W/m<sup>2</sup> instead of  $-29$  W/m<sup>2</sup>.

## 1.9 Conclusion

Field evidence and model results confirm that sublimation accounts for most of the mass lost from Taylor Glacier. Sublimation rates vary in a complex spatial pattern, largely because the mountainous topography interacts with regional air flow regimes (katabatic, cyclonic, and diurnal) to generate non-uniform winds on the glacier. Superimposed on the general decrease of sublimation rate with altitude is a pronounced maximum mid-way along the glacier, related to strong winds emanating from a tributary valley, Windy Gully, and their propagation downglacier.

We found that a simple model for sublimation – one without corrections for atmospheric stability – explains much of the variability in ablation, temporally and spatially. The model sublimation rates compare well with observed ablation. Wind speed, vapor pressure difference between the surface and screen height, and temperature (through its effect on vapor pressure) were the dominant variables affecting the sublimation rates, as one would expect from standard boundary-layer theory.

Brief “events” of fast sublimation occurred during storms and strong katabatic winds. However, these extreme events accounted for a minor portion of the total annual sublimation. More important were the common, medium-sized storm and katabatic events during which

wind speeds and temperatures were elevated and the air drier than average – all conditions that favor sublimation. Slow but persistent sublimation is important for the annual total.

Sublimation varies strongly over the annual cycle. Summer rates exceed winter ones by a multiple of 1.9 on average.

## 1.10 Appendix: Outliers and Gap Filling

We eliminated outliers in a multistep process. The first step was to divide a given timeseries into sections of 20 datapoints. For each section, we then calculated the 10th, 50th, and 90th percentile of the data variable ( $V_i$  is the  $i^{th}$  percentile). Then we defined

$$D = \max(V_{50} - V_{10}, V_{90} - V_{50}) \quad (1.5)$$

A point  $v$  was an outlier if

$$v - V_{50} > r * D \quad (1.6)$$

where the ratio factor  $r$  was 1.8.

Outliers were removed from the data. The ratio factor (1.8) and the number of datapoints in a section (20) were chosen by inspection to minimize the number of outliers left in the data and minimize the removal of true values.

Gaps in the data, due to missing ARGOS transmissions or removed outliers, were filled by interpolating across the gap. We tested linear, nearest neighbor, cubic, and spline methods of interpolation. For stations 1, 2, 4, and 5 where we had ARGOS and locally-stored data, we were able to compare the interpolated points to the real data that was not transmitted. The linear and cubic methods best matched the locally-stored data; since the linear method was slightly simpler, we used it.

## 1.11 Appendix: Surface Temperature

### 1.11.1 Parameterized

At the three stations where longwave radiation was measured directly, the radiative ice surface temperature  $T_{rad}$  was calculated from the upwelling longwave radiation  $LW$  using the Stefan-Boltzman equation assuming an emissivity  $\epsilon$  of 1.

$$T_{rad} = (LW/(\epsilon\sigma))^{1/4} \quad (1.7)$$

To estimate surface temperature  $T_s$  at other stations, we developed a parameterization with a lagged version of air temperature  $T_{air}$  and measured net radiation  $R$ .

$$T_s = a < T_{air} > + b R + c (< T_{air} > - R) + d \quad (1.8)$$

$\langle x \rangle$  denotes a lagged version of  $x$ . The parameters  $a$ ,  $b$ ,  $c$ , and  $d$  were chosen via regression to minimize  $\Sigma|T_{rad} - T_s|$  for stations 1, 2, and 4. The lagged air temperature record was created by applying a triangular filter to the air temperature data. The filter weighted the most recent data most heavily and past data was weighted less and less with age. The filter width (4 hours) was chosen to maximize the correlation between the radiative surface temperature and the parameterized surface temperature. After computing  $T_s$  in this way, we noticed that the result had a bias depending on the temperature. So, to adjust the fit we added an offset variable that calculated the mean residual in 1°C bins and then subtracting the residual from the model. This whole parameterization was used at stations 3, 5, and T, where we did not have direct measurements of upwelling longwave radiation.

We did a few ad hoc tests of different parameterizations for surface temperature, ultimately choosing the one that best fit the radiative temperature (described above) and made sense physically for the sublimation. Parameterizations we tried were: radiative temperature from other stations; radiative temperature with an offset of a few degrees; air temperature with an offset; *Peck* [1996]; lagged air temperature; lagged air temperature and shortwave radiation; and a parametric fit with lagged air temperature and net radiation. The other parameterizations gave results similar to the one we chose, but with slightly different slopes and intercepts for figure 1.10.

### 1.11.2 Adjusted for Energy Balance

For the “standard” model, we adjusted the surface temperature until the net energy flux to the glacier surface was zero. The energy budget terms affected by this adjustment were the latent, sensible, and subsurface heat fluxes. For example, if the initial net energy budget was positive, we increased the surface temperature. This led to a reduced sensible heat flux to the glacier, an increased latent heat loss from the glacier, and either an increased loss of heat to the subsurface or a reduced gain of heat from the subsurface. The subsurface term was usually the smallest of these terms and had the smallest change upon correction.

## 1.12 Appendix: Roughness Length

The Law of The Wall predicts how velocity of a fluid will vary in a boundary layer near a surface. Given a ground surface roughness and a wind speed at some height above the ground, the theory gives an estimate of the wind speed at other heights. Alternatively, if wind speed is known at two heights, the roughness can be calculated.

$$Z_o = \exp((u_1 \ln(H_2) - u_2 \ln(H_1))/(u_1 - u_2)) \quad (1.9)$$

where  $u_x$  is the wind velocity at height  $H_x$ . We have done this calculation for the three stations where we have wind sensors at two heights.

The roughness lengths for temperature and moisture can be related to that for momentum

by

$$\ln \left( \frac{Z_T}{Z_o} \right) = 0.317 - 0.565 R_* - 0.183 R_*^2 \quad (1.10)$$

$$\ln \left( \frac{Z_q}{Z_o} \right) = 0.396 - 0.512 R_* - 0.180 R_*^2 \quad (1.11)$$

$$R_* = \frac{u_* z_0}{\nu} \quad (1.12)$$

where  $R_*$  is the Reynolds number and  $\nu$  is the kinematic viscosity of air ( $1.461 \times 10^{-5} \text{ m}^2/\text{s}$ ) [*Brock and Arnold*, 2000].

See *Smeets and van den Broeke* [2008] for a discussion of roughness lengths in the ablation zone of the Greenland Ice Sheet.

# Chapter 2

## Ablation Data

### 2.1 Field Site

Figures 2.1 and 2.2 map the main features of the study region. Taylor Glacier’s source on Taylor Dome (2365 m.a.s.l.) is located about 30 km west of the boundary of the figures. Ice flowing from the dome converges into Taylor Glacier proper at Taylor Mouth (1700 m.a.s.l.). Between Taylor Mouth and about 1100 m.a.s.l., the glacier surface consists of patchy areas of blue ice and firn. It is heavily crevassed because of flow over bedrock steps and bumps. Our study focused on the main part of the ablation zone (i.e., from which most mass loss occurs), which begins in a broad and gently-sloping area north of Beacon Valley (about 1300 m.a.s.l.) and extends to the main terminus in Taylor Valley (50 m.a.s.l., see figure 2.3). The glacier has a number of tributaries and distributary lobes. Significant tributaries include Cassidy Glacier and Windy Gully. Significant distributaries flow into Beacon Valley (and Turnabout Valley), Arena Valley, and the upper and lower ends of Pearse Valley and Simmons Basin. Taylor Glacier also has a wide confluence with Ferrar Glacier but does not receive much mass from it [Kavanaugh *et al.*, 2009a]. The mountains around the glacier rise up to 1500 meters above the glacier; these features strongly affect the pattern of winds.

### 2.2 Fieldwork Anecdotes

To get to our field site, we took commercial airlines to Christchurch, New Zealand. While there, we were outfitted with a variety of cold-weather gear to supplement what we brought of our own. From Christchurch, we flew in an Air Force or Air National Guard plane 8 hours south to McMurdo Station, the main United States base in Antarctica. We typically spent at least a week in McMurdo getting survival training, collecting camping equipment, selecting food for the season, and preparing our science gear for the trip out to the glacier. McMurdo had a very industrial feel to it, but fortunately we did not have to walk very far to get a nice view (figure 2.4).

From McMurdo, we took an hour-long helicopter ride to the glacier. Once there, we set

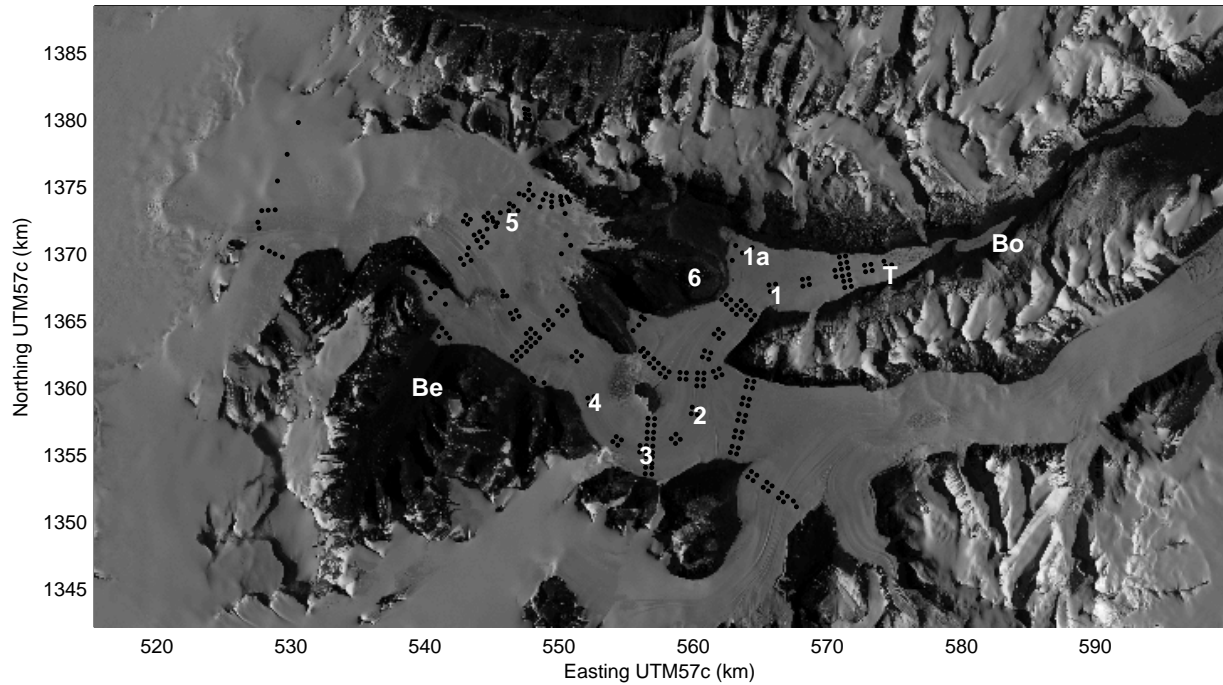


Figure 2.1. A SPOT image of Taylor Glacier, Antarctica showing this study's weather station locations (numbered by elevation), and LTER weather stations at Lake Bonney (Bo), Taylor Glacier (T), and Beacon Valley (Be). Station 1 started at 1a and moved less than 2 months later to 1. Black dots represent ablation poles. The patchy snow line is near Wx 5; the glacier surface to the east is blue ice. Image credit: SPIRIT Program ©CNES 2009 and Spot Image 2008 all rights reserved.



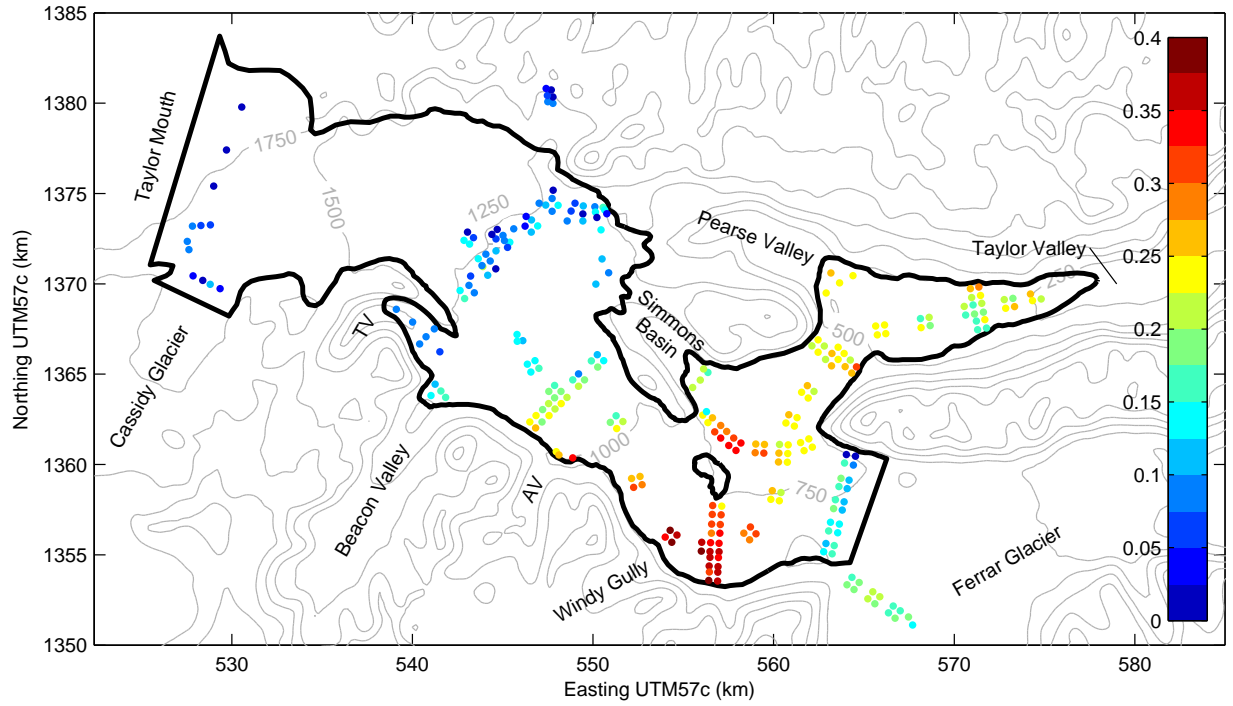


Figure 2.2. The measured ablation rates in the **3:4** interval were highest (about 0.4 m/yr) at the base of the steeply-sloping Windy Gully where the wind speeds, and hence the latent heat flux, were the highest. This plot also shows 250 m topographic contours generated from the RAMP digital elevation model *Liu et al.* [2001]. TV is Turnabout Valley and AV is Arena Valley.



Figure 2.3. The terminus of Taylor Glacier, looking up-glacier to the west. Picture taken from a helicopter by Andy Bliss.



Figure 2.4. Mount Erebus and Castle Rock from the southern tip of Ross Island near McMurdo station. Sir James Clark Ross named Mount Erebus after one of his ships on an early expedition to Antarctica. It is the southernmost active volcano in the world and has an active lava lake in its summit crater. The mountain is 3794 m tall, though it does not look that tall from sea level. Photo by Andy Bliss.



Figure 2.5. Camp 1 with Johnny, Sarah, and Jeff. The multicolored tent was our kitchen tent. The yellow tents were double-walled canvas tents, state-of-the-art technology in 1912 when Sir Robert Falcon Scott died in one returning from South Pole. A quote, from just after he reached the pole and found that Roald Amundsen had beaten him to it, “Great god! This is an awful place.” Photo by Andy Bliss.

up the first of three camps with a tent for each person, a kitchen tent, and a gear tent (figure 2.5). We had 3 to 5 people in the field at a time. To power our computers, radios, GPSes, and other field gadgets, we had solar panels. For sleeping, we had warm sleeping bags and 3 or 4 sleeping pads for insulation from the ice. For drinking water, we melted ice. For food, we ate simply, and savored any freshies the helicopter crews managed to provide. There were a lot of surprisingly delicious frozen steaks. To Kurt’s dismay, there were no lobster tails. We cleaned our dishes with a splash of water and paper towels. Since the whole area was designated as an environmentally-protected area, we did our best to pack out all of our waste and leave no trace. There was an unfortunate event at our second camp though, when a large gust of wind blew our kitchen tent over and scattered the entire contents across the nunatak we were camped on. Lesson: anchor the tent with at least 1 ton of rocks (I’m not kidding). Lesson 2: be wary of camping downwind of “Windy Gully.” I still remember the futile chase after a can of Pringles and then a camp chair that were bouncing across the rocky landscape. Some glaciologist 1000 years from now will probably find them and wonder “What the...”

We got around the glacier via snowmobiles that were outfitted by the McMurdo mechanics





Figure 2.6. Northwest Mountain. Photo by Andy Bliss.

with extra cleats on the treads for traction on the ice. One of the snowmobiles was named Dr. Frankenvinny because it had been cobbled together from spare parts by a mechanic named Vinny (see figure 2.7). The snowmobiles pulled Nansen sleds to carry extra gear. Usually one person would drive the snowmobile and a second person would ride on the sled. We wore instep crampons or STABILicers on our giant FDX boots to be able to walk easily on the ice. I found the STABILicers to be significantly more comfortable. Occasionally, while we were waiting for the GPSes to collect their data, Kurt would take a nap on the sled. I would usually take pictures of the landscape. Is it not a beautiful landscape (figure 2.6)?

## 2.3 Ablation Measurement Technique

We assessed ablation rates at a network of survey sites (Figure 2.1), using the standard technique of repeated pole-height measurements. Three-meter aluminum conduit poles were initially placed 2 m into the ice or firn. Exposed heights were determined as the average of measurements on the north and south sides of each pole (figure 2.7). Each measurement was from the top of the pole to the “average” height of the glacier surface, as determined by the person in the field. The goal was to get the best estimate of actual ablation, allowing for changes in the depth of ablation hollows. We used retractable tape measures, which blew



Figure 2.7. A typical ablation pole installation. Here Jeff and Kurt were measuring the pole's position with GPS, and making notes about the character of the glacier surface. Picture by Andy Bliss.

around in the wind. Next time we will try a 2-m measuring stick. For poles which tilted over due to ablation, we measured the along-pole distance from the top of the pole to the surface and the vertical distance to the surface. We did not include data from tilted poles below. We also estimated depths of undulations on the surface; ice surfaces undulate at horizontal and vertical scales of order 10 cm and 1-10 cm, respectively.

The configuration of the survey grid was primarily determined by the requirements of an ice dynamics study. Consequently, the density and spatial coverage are unusually large for a mass balance program. The entire network was used in the first year of the study. Because of logistical constraints, subsequent measurements were obtained only at subsets of locations.

Measurements span a 4 year period, from November 2002 to January 2007. The timeline of our fieldwork is shown in figure 2.8. In the 2002-3 summer field season (abbreviated as **3**), we installed 273 poles and measured initial heights. We revisited the entire network of poles in the 2003-2004 season (**4**) and also visited 73 poles along a flowline at season's end on January 26th, 2004 (**L** for late-season). Four poles near three of the weather stations were visited on February 1st, 2006 (**6**), by H. Basagic of Portland State University. Finally, 163 poles were measured again within one week of January 1st, 2007 (**7**), again by H. Basagic.

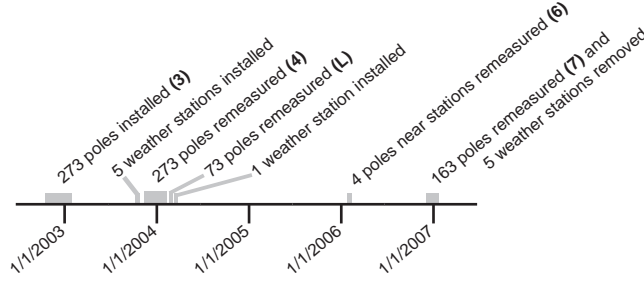


Figure 2.8. The timeline shows when ablation pole and weather station measurements were made. The numbers in parentheses refer to different intervals of time in subsequent figures and in the text.

## 2.4 Uncertainties in Ablation Measurements

For each pole height measurement, surface undulations introduce an uncertainty of one to a few centimeters (estimated as 25% of the undulation depth). Some indication of this uncertainty comes from the difference between the measurement of the north and south sides of the poles (figure 2.9). For the first measurement (**3**), the mean difference for all poles was 0.009 cm. The standard deviation was 0.72 cm which led to the 25% figure, as most of the undulations were in the range of 3-10 cm deep. A simple t-test showed that for **3** the mean difference was not significantly different from zero. Interestingly, for **4** the mean height difference was 0.31 cm, and was significantly different from zero (std = 1.01 cm). Likewise, for **L**:  $0.37 \pm 0.97$  cm and for **7**:  $0.16 \pm 1.57$  cm. We speculate that there may have been faster sublimation on the north sides of the poles because of reflected solar radiation or enhanced longwave radiation from the pole. However, this usually did not manifest in an obvious ablation well or moat around the base of the poles.

More significant for our analyses is that local spatial variability – differences between nearby poles – showed that a single pole might do a poor job of representing the mean ablation of the local region. Fortunately, the local spatial variability tended to average itself out when considering longer time periods. For the **4:L** interval (one to two months), the average pole height change was 3.2 cm and the average standard deviation of measurements among clustered poles was 36.0% of the ablation. For **3:4**, the numbers were 19.2 cm and 15.6%. For **3:7**, they were 67.7 cm and 8.0%. Sources of local variability included both measurement errors and sublimation variations, the latter related to microtopography, temporary coverage by snow dunes, and perhaps micrometeorological effects. The sublimation from the ice surface was greatly reduced when covered by a snow dune. After a snow dune was removed via sublimation or wind scour, the exposed ice surface was much smoother than the surrounding surfaces with ablation hollows.

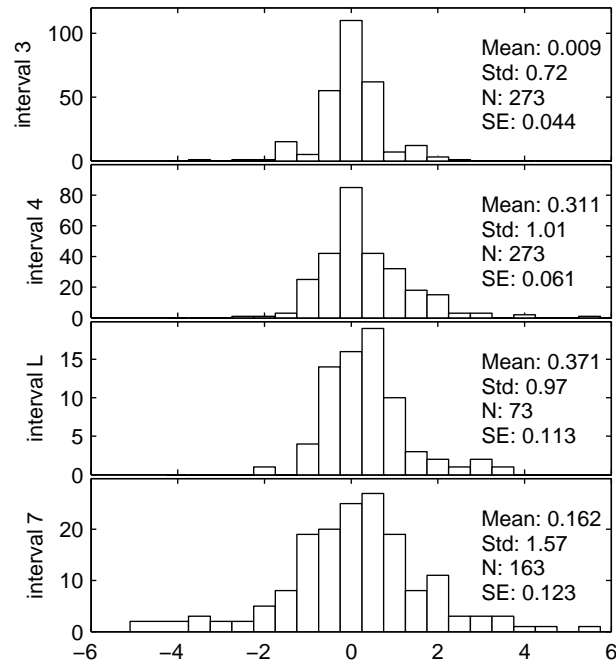


Figure 2.9. Histogram of the difference between north- and south-side pole heights. When installed there was no difference; after a year, the north sides had ablated more and this persisted to the three year mark. Also noted: mean, standard deviation, number of points, and standard error of the mean.



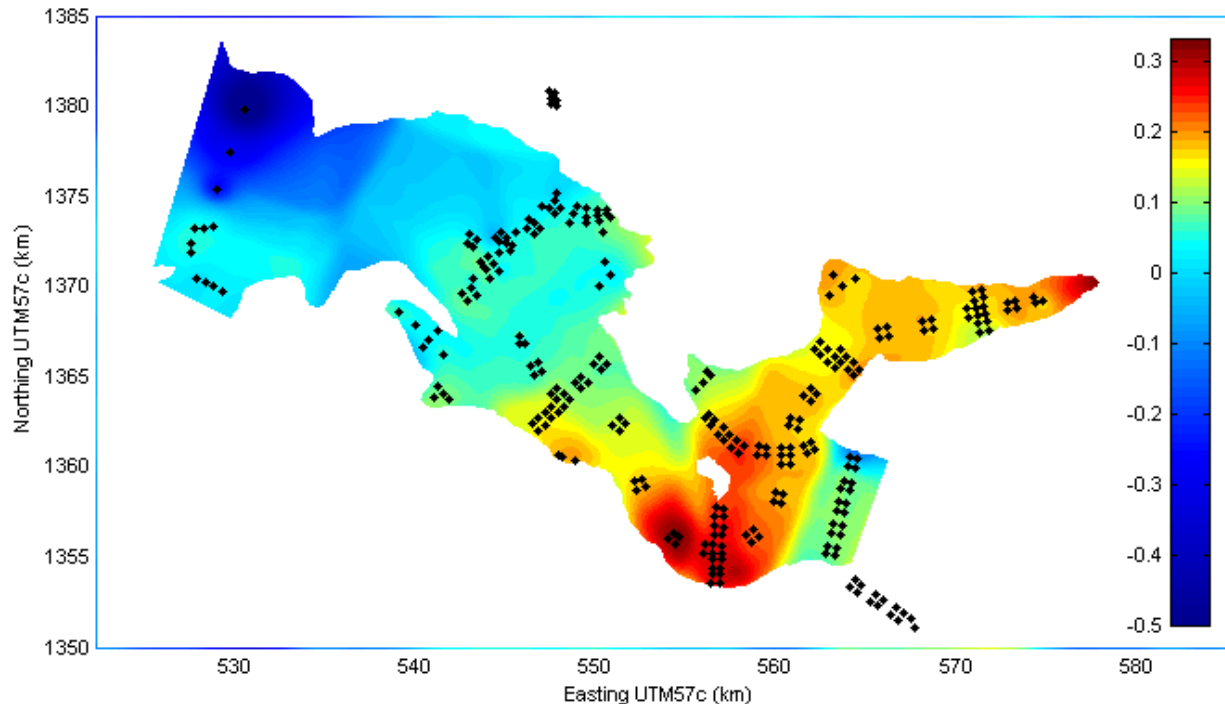


Figure 2.10. Interpolated ablation field for the **3:7** interval, in m/yr.

## 2.5 Measured Ablation Rates

### 2.5.1 Large-Scale Spatial Variability of Ablation

For the **3:4** interval, ablation rates on most of the surface ranged from 5 to 30 cm/yr (figure 2.2). Above about 1150 m, however, much of the glacier (the northern 2/3 or so) was covered with patchy firn and, in some places, received net accumulation. Blue ice was exposed along the southern margin. Ablation did not vary monotonically with elevation. It tended to increase down the glacier to a local maximum (up to 40 cm/yr) at  $\sim 900$  m altitude near the foot of Windy Gully. Rates varied little between  $\sim 750$  m and 400 m altitude but then increased toward the terminus, where the highest values occurred (below our study area).

### 2.5.2 Spatial Extrapolation of Ablation

Using the method developed by *Kavanaugh et al.* [2009b] for spatial extrapolation between sparse datapoints, we created a map of ablation rates for the whole glacier for the **3:7** interval (figure 2.10). This map made it easy to visualize the pattern of ablation rates and would allow a calculation of total ablation from the glacier. For a similar calculation, see *Kavanaugh et al.* [2009a].

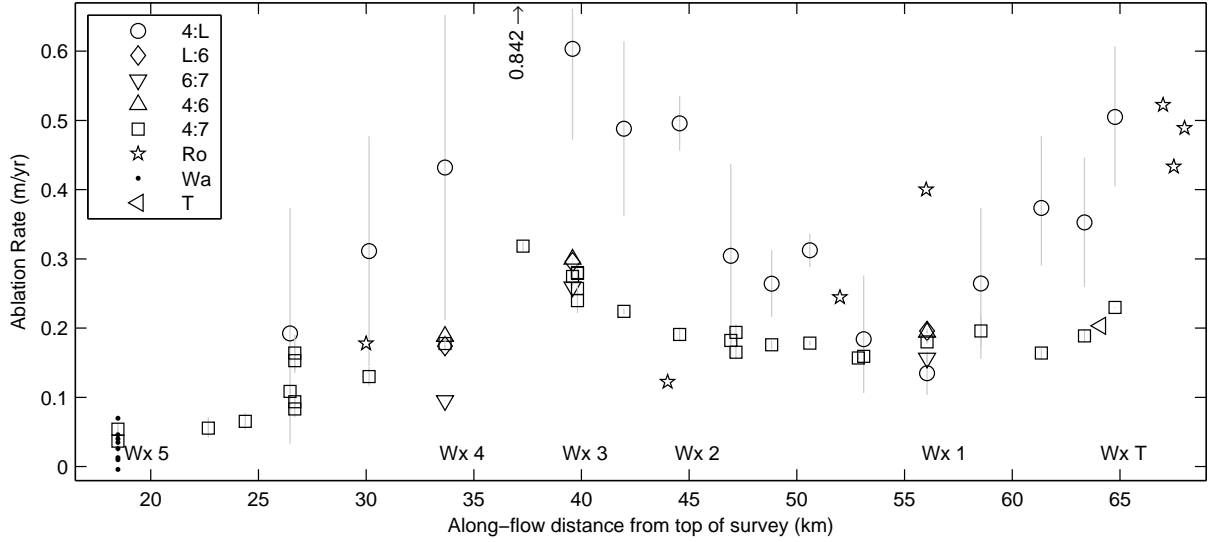


Figure 2.11. Measured ablation rates for intervals with weather station measurements. Summertime ablation rates were a factor of two faster than whole-year rates. For each set of 4 or 6 ablation poles (see map in figure 2.1), one symbol is plotted on the graph at the mean value of that group. The 25th and 75th percentile within the group is plotted as the bottom and top of the gray error bar associated with the mean symbol. Symbols without error bars represent single ablation poles, so statistics could not be calculated. The set of single dots near Wx 5 in the upper graph are long-term ablation rates from 1993-2003 (personal communication from E.D. Waddington, 2005). The stars are measurements done by *Robinson* [1984] from November 1976-November 1977. The left-pointing triangle is from *Hoffman et al.* [2008] for ablation from 1995-2006. Along-flow distance was measured down the centerline of the glacier from the western side of the study area. The weather station locations are plotted as text (e.g. Wx 1).

### 2.5.3 Temporal Variability of Ablation

In four separate campaigns, we obtained measurements at the same subset of sites: 67 poles arrayed on a 40 km-long flowline from an elevation of 1080 m to within 3 km of the terminus (figure 2.11). The four measurement periods were Nov 19th 2002 to Dec 12th 2002, Dec 13th 2003 to Jan 7th 2004, Jan 26th 2004, and Dec 27th 2006 to Jan 2nd 2007. The glacier ablated most rapidly during the Antarctic summer (e.g. **4:L**, December 2003 to late January 2004). The median ablation rate for that summer was 33.2 cm/yr (and standard deviation of 22.5 cm/yr). For the whole year from late 2002 to late 2003, **3:4**, the corresponding rates were  $23.7 \pm 5.59$  cm/yr (median  $\pm$  std). But that year had higher ablation rates than the three-year interval from late 2003 to late 2006, **4:7** ( $17.9 \pm 5.11$  cm/yr).

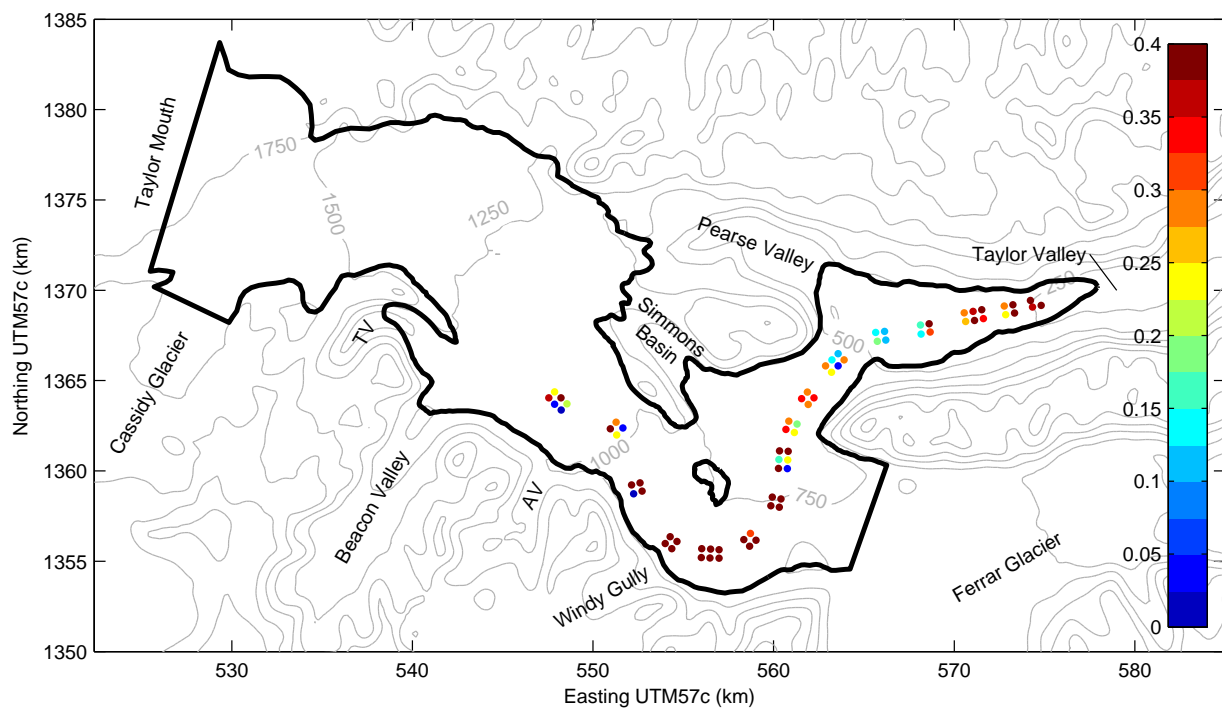


Figure 2.12. Ablation Rates for the  $3:L$  interval.

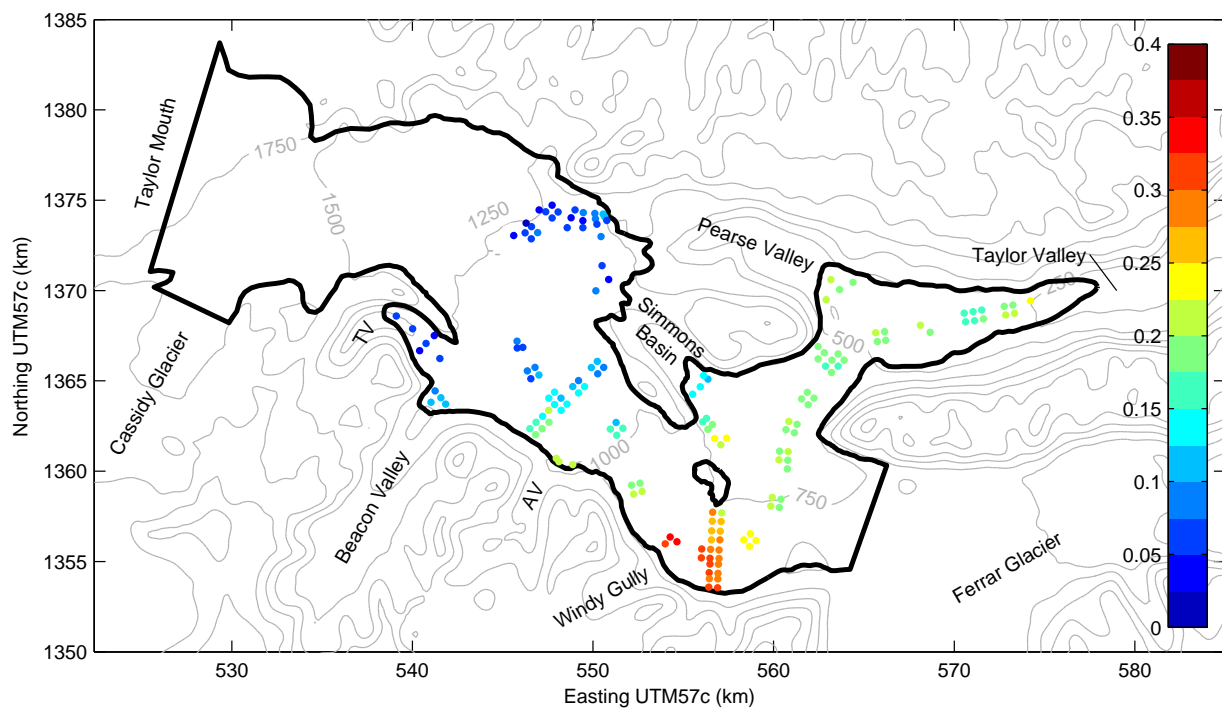


Figure 2.13. Ablation Rates for the  $2:7$  interval.

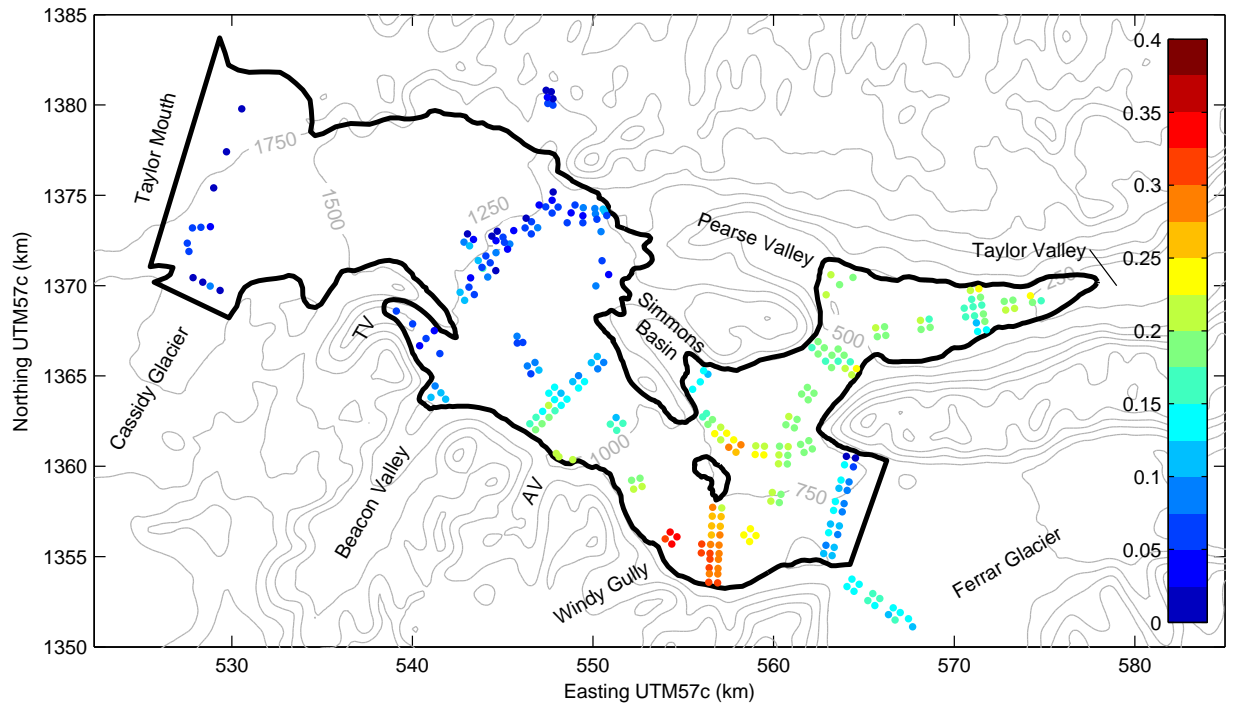


Figure 2.14. Ablation Rates for the 2:7 interval, extrapolated from the measured points (figure 2.13) to all ablation poles.

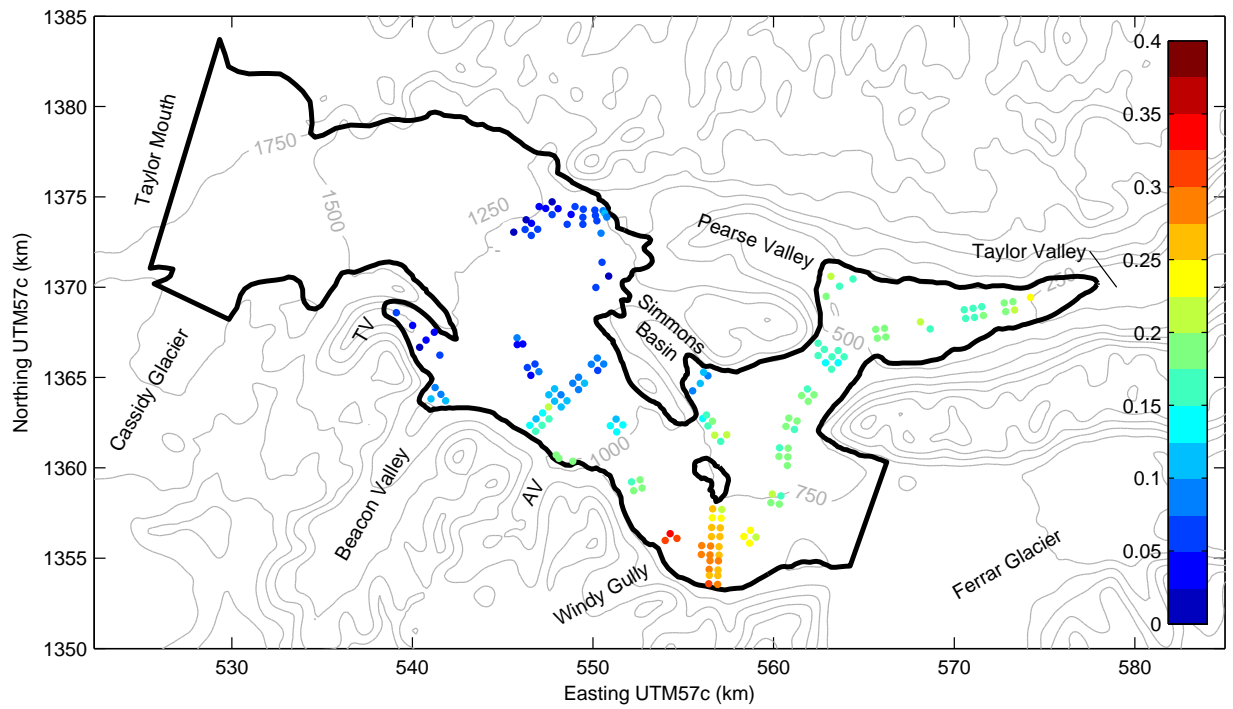


Figure 2.15. Ablation Rates for the 3:7 interval.

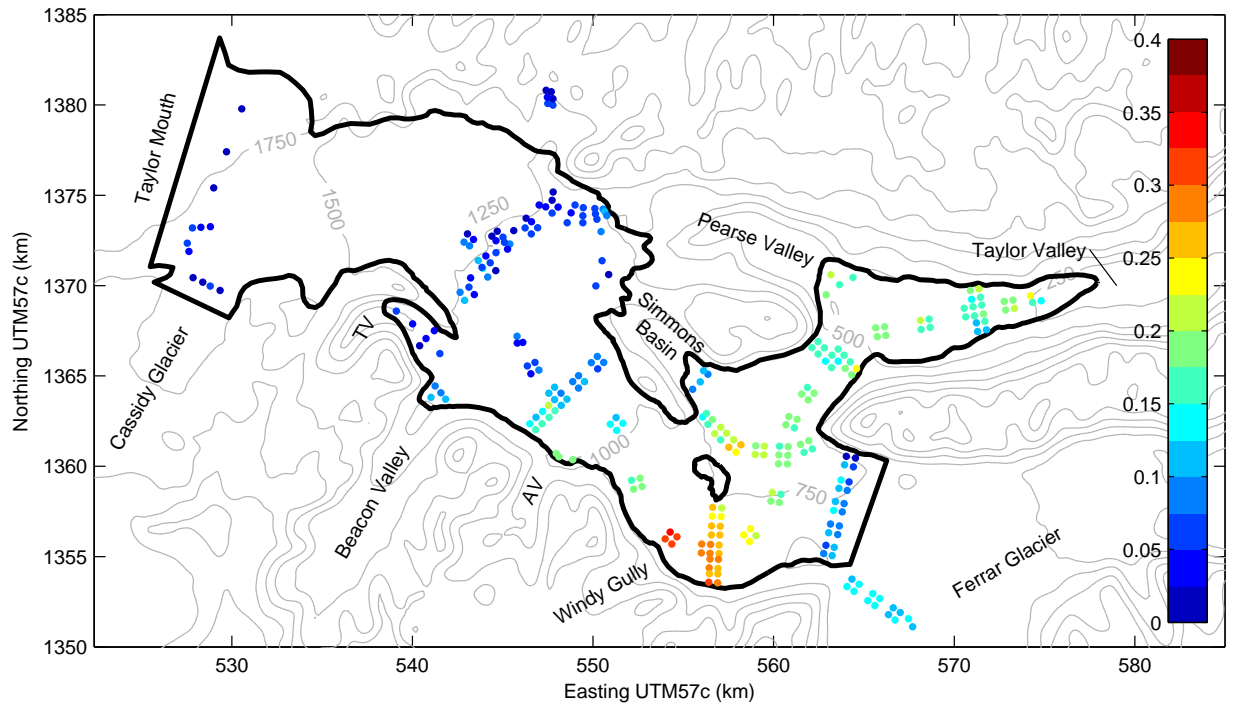


Figure 2.16. Ablation Rates for the **3:7** interval, extrapolated from the measured points (figure 2.15) to all ablation poles.

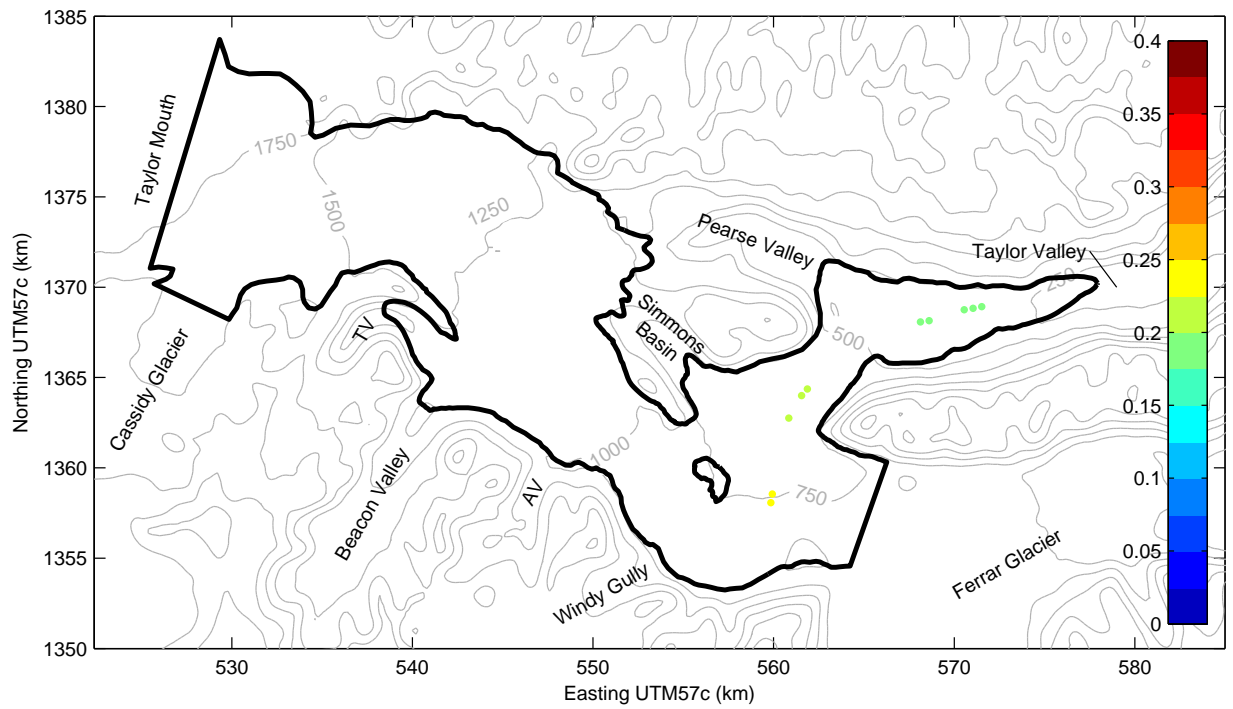


Figure 2.17. Ablation Rates for the **2:10** interval.

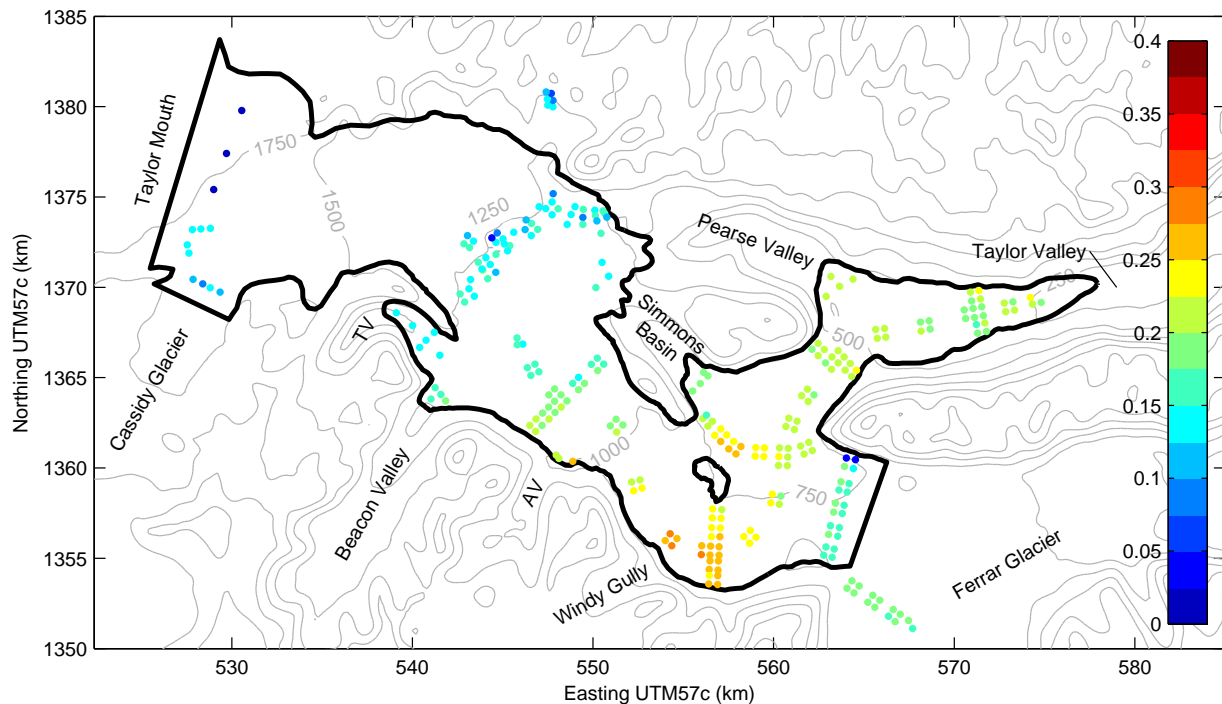


Figure 2.18. Ablation Rates for the **2:10** interval, extrapolated from the measured points (figure 2.17) to all ablation poles.

## 2.6 Discussion

### 2.6.1 Measured Ablation Rates

On typical land-based glaciers, ablation rates are highest at the terminus, where temperatures are warm and the climate is conducive to melt or fast sublimation. Ablation monotonically decreases with increasing elevation as temperatures decline. On Taylor Glacier, while temperature does generally decrease with elevation, ablation rates peak in the middle of the ablation zone's elevation range, at 900 m. Our model results show that this odd ablation pattern can be explained by rapid sublimation caused by dry air moving quickly over the glacier. The source of the fast dry air is katabatic flow from Windy Gully, a steep tributary of Taylor Glacier.

In the early 1970s, ablation rates close to the terminus [Robinson, 1984] were twice as high as rates measured since 2000 by our surveys. The 11-year mean ablation rate reported by Hoffman *et al.* [2008] for a site next to Wx T falls on the trend of our data (figure 2.11), while the 7-year mean rates reported by Fountain *et al.* [2006] were generally a few cm/yr lower than our 4-year data. (The different time periods and locations used in these three studies preclude a direct comparison.) We speculate that the 1970's ablation rates were higher because the local climate was warmer then [Doran *et al.*, 2002], which enhanced both sublimation and melt.

Our results showing a clear maximum of ablation near Windy Gully indicate that the

spatial coverage of *Robinson*’s study was not sufficient to characterize the relation between ablation and elevation on this glacier, or to assess the glacier’s surface mass balance accurately. Robinson assumed a linear relationship between ablation and elevation, which proves to be a poor assumption given the effects of the complex topography on wind fields. Using Robinson’s relationship would underestimate ablation rates by a factor of two at 900 m altitude. His estimate of the overall mass balance of Taylor Glacier was a gain of  $9.5 \pm 23.3 \times 10^6$  tonnes/year, whereas our estimate (based on improved measurements of ice flux and surface balance) indicates that most of the glacier is nearly in mass equilibrium, even with the lower recent ablation rates [*Kavanaugh et al.*, 2009a]. (One sector, however – that which flows into Pearse Valley from the west – appears to be shrinking.)

Another contrast concerns the location of the equilibrium line. *Robinson* [1984] estimated it to be at an elevation just over 2000 m.a.s.l., based on air photos from between 1957 and 1973. Our ablation measurements indicate the equilibrium line is closer to 1400 m, although it is not a “line” but a broad and heterogeneous zone. Robinson may have based his estimate on the elevation of the highest exposed blue ice, but large patches of persistent snow (figure 2.1) at lower elevations maintain a positive surface mass balance. It should also be noted that over most of the glacier Robinson’s elevation figures are about 300 meters higher than those indicated by our GPS surveys.

Although we do not have meteorological measurements at the Taylor-Ferrar confluence, observations suggest that the low sublimation rates measured there (figure 2.2) reflect generally low local wind speeds. The downglacier winds are steered north by the western prow of the mountain ridge that separates Taylor Valley from Ferrar Valley.

Ablation on Taylor Glacier, especially close to Windy Gully, is rapid compared to that in other Antarctic “blue ice” areas. In *Bintanja*’s [1999] classification of blue ice areas, Taylor Glacier is a Type II (“located on a valley glacier”), and Taylor Glacier shares many characteristics with the more extensively-studied Type I blue ice zones (in the lee of a mountain). Our measurements reveal maximum rates (40 cm/yr for the **3:4** interval) much higher than those reported in *Bintanja*’s compilation at the elevation of Windy Gully (900 m), or in fact at any elevation [see figure 6 of *Bintanja*, 1999].

# Chapter 3

## Weather Data

### 3.1 Weather Station Setup

To constrain our analyses of sublimation we set up six weather stations, five on Taylor Glacier itself (stations 1-5 on the map in figure 2.1) and one on top of the Friis Hills (station 6). The five glacier stations operated from November 2003 until December 2006; station 6 continued into 2007.

#### 3.1.1 Setup Anecdotes

At the start of our second field season, we set up a network of weather stations. In McMurdo we had difficulty programming the stations to take the measurements at the proper interval and send the data to the ARGOS satellite system. The programming language that the stations used was quite arcane and had complicated dependencies among the different components of the system. In the end, with the help of the manufacturer and Jonathan Thom from the University of Wisconsin, I was able to figure it out. Lesson: test your field equipment before leaving home. Corollary: buy the field equipment far enough in advance to test it before leaving home.

We took a few days to set up the network of 5 weather stations (a sixth, Wx 3, was added late in the season). A typical setup day started with a helicopter ride to the weather station site on the glacier, where we were dropped off with a load of gear. For the weather stations on ice, we then drilled 3 holes into the glacier with a motorized drill and put a 4x4 in each hole. On top of the 4x4's we installed a steel tripod to hold the weather instruments. The setup design is shown in figure 3.1. The "tripod on 4x4's" design comes from the Long Term Ecological Research group which has weather stations in other parts of the Dry Valleys. They found it to work well for ice stations in this region with 0-40 cm ablation per year and very fast winds that would topple many other designs commonly used on temperate glaciers with weaker winds and faster ablation. For the station installed on rock (Wx 6) we secured the tripod to bedrock using anchor bolts. We then set about adding instruments (as listed below) to the tower and wiring them to the data logger. On stations 1, 2, and





Figure 3.1. Wx 4 was located upglacier from Windy Gully (white sloping ice directly behind the weather station). Photo by Andy Bliss.

4 the radiation sensors were located on a separate mast with its own footings 4-5 meters from the main station. The separation was designed to reduce the error associated with shadows from other parts of the station and longwave radiation emitted from or blocked by the station. Some shading by the mast was unavoidable, but minimal (see figures 3.17, 3.18, and 3.19). We also installed an antenna on each station so it could relay data back to us via the ARGOS satellite system – a network of polar-orbiting satellites designed to collect data from oceanographic buoys. The ARGOS system had fairly good coverage, but very low data capacity: 16 four-digit hex values per transmission.

### 3.1.2 Instrumentation

Each station measured wind speed and direction, temperature, and relative humidity. Stations 1, 2, and 4 additionally measured barometric pressure, wind close to the glacier surface, and incoming and outgoing long- and short-wave radiation. Stations 5 and 6 measured net radiation. The variables measured at different stations are listed in Table 3.1. To give a sense of a typical installation, figure 3.1 shows Wx 4 as it was being set up.

Three gel-cell batteries (about 80 Ah each) powered each station. A 20-Watt solar panel recharged the battery bank in the summer, when the sun was up. The power requirements of

Table 3.1. Weather Station Instrumentation. The table shows the height at instrument installation. Ablation of the ice surface increased the distance between the sensors and the surface over time. Instrument accuracies were taken from the manufacturer’s literature. The Monte Carlo column shows the range of values used in the simulation described in section 4.2.

Parameter	Instrument	Height	Instrument Accuracy	Monte Carlo	Stations
Wind Speed and Direction	RM Young 05103	3 m	$\pm 0.3 \text{ m s}^{-1}$ , $\pm 3^\circ$	$\pm 0.3 \text{ m s}^{-1}$	1, 2, 3, 4 <sup>a</sup> , 5, 6
Wind Speed and Direction	RM Young 05103	1 m	$\pm 0.3 \text{ m s}^{-1}$ , $\pm 3^\circ$	$\pm 0.3 \text{ m s}^{-1}$	1, 2, 4
Temperature	HMP45C	2.5 m	$\pm 0.3\text{-}0.5^\circ\text{C}$	$\pm 0.4^\circ\text{C}$	1, 2, 3, 4, 5, 6
Relative Humidity	HMP45C	2.5 m	$\pm 1\text{-}3\%$ <sup>b</sup>	$\pm 2\%$	1, 2, 3, 4, 5, 6
Shortwave Radiation	Zipp & Zonen CM21	1.5 m	Directional: $\pm 10 \text{ W m}^{-2}$ <sup>c</sup>	...	1, 2, 4
Longwave Radiation	Zipp & Zonen CG1	1.5 m	Window Heating: $15 \text{ W m}^{-2}$ <sup>d</sup>	...	1, 2, 4
Net Radiation	Zipp & Zonen NR-LITE	2 m	Directional: $< 30 \text{ W m}^{-2}$ <sup>e</sup>	...	5, 6
Barometric Pressure	CS105	1.5 m	$\pm 2.0 \text{ mb}$ <sup>f</sup>	...	1, 2, 4

<sup>a</sup> This sensor stopped working July 30th, 2005.

<sup>b</sup> At  $20^\circ\text{C}$ , against factory reference:  $\pm 1\%$ , field calibrated against references:  $\pm 2\%$  (0-90% RH) and  $\pm 3\%$  (90-100% RH)

<sup>c</sup> Temperature dependence:  $< \pm 1\%$ , Spectral Selectivity:  $\pm 2\%$

<sup>d</sup> Temperature dependence:  $< \pm 2\%$ , Thermal gradient:  $< 1 \text{ W m}^{-2}$

<sup>e</sup> Asymmetry Error:  $\pm 5\%$

<sup>f</sup> Over the range  $-20$  to  $+45^\circ\text{C}$ ,  $\pm 3.0 \text{ mb}$  over  $-40$  to  $+60^\circ\text{C}$

Table 3.2. Weather station name lookup table. ‘Wx’ names are used throughout the text. Our stations (numbered) are organized by elevation. ‘Met’ names were used in my computer code, and may inadvertently appear in figures.

Wx:	Bo	T	1	2	3	4	5	6	Be
Met:	8	7	1	3	6	2	4	5	9

the ARGOS transmitter were significant compared to the weather station by itself. Station 3 lost its solar panel in early October 2005, likely due to an accumulation of strain on the mount and 40 m/s wind gusts at the time of failure; the batteries were able to carry through the rest of that summer and the following winter. Figure 3.2 shows the timeseries of battery voltage measured by the data loggers.

Additional data from three LTER weather stations [Doran *et al.*, 2002] supplemented our analyses; their station close to the terminus of Taylor Glacier provided wind speed and direction, temperature, relative humidity, incoming and outgoing shortwave, and a sonic distance sensor. LTER stations at Beacon Valley and Lake Bonney provided context. The LTER abbreviations for these stations were TARM, BENM, and BOYM, respectively. Our abbreviations were Wx T, Wx Be, and Wx Bo. Station locations are shown in figure 2.1). The sonic distance sensor on station T recorded the distance between the sensor and the ice. This was effectively a measurement of ice ablation, which we use in section 4.1 to compare to our model of sublimation.

### 3.1.3 Data Properties

The sensors at all of our stations recorded data every 5 minutes. Twenty-minute averages were transmitted to the ARGOS satellite system, and locally-stored data were later retrieved from Stations 1, 2, 4, and 5. Local storage provided a clean, continuous data series whereas the ARGOS transmissions provided near real-time data that allowed us to realize, for example, that the radiation sensors on station 1 were not set up correctly after it was moved in early 2004. For stations 3 and 6, we removed spurious numbers in the ARGOS transmissions with an outlier detection routine. Data gaps were short enough (median length less than 1 hour) to fill by linear interpolation. About 47% (23%) of the data at station 3 (station 6) were not received.

### Outlier Removal

We eliminated outliers in a multistep process. The first step was to divide a given timeseries into sections of 20 datapoints. For each section, we then calculated the 10th, 50th, and 90th percentile of the data variable ( $V_i$  is the  $i^{th}$  percentile). Then we defined

$$D = \max(V_{50} - V_{10}, V_{90} - V_{50}) \quad (3.1)$$

A point  $v$  was an outlier if

$$v - V_{50} > r * D \quad (3.2)$$

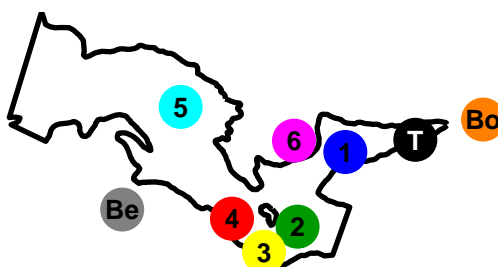
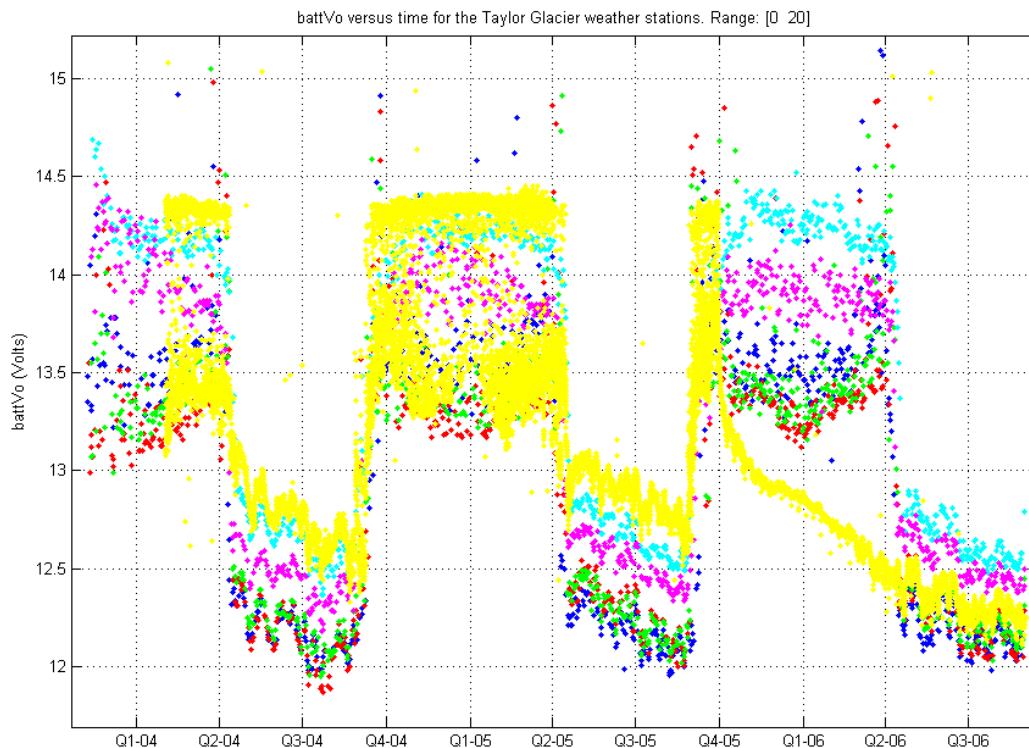


Figure 3.2. Battery voltage was above 13 V when the batteries were being charged by the solar panels. In the winter it remained above 12 V because we had plenty of batteries. Station 3's solar panel failed in early October 2005.

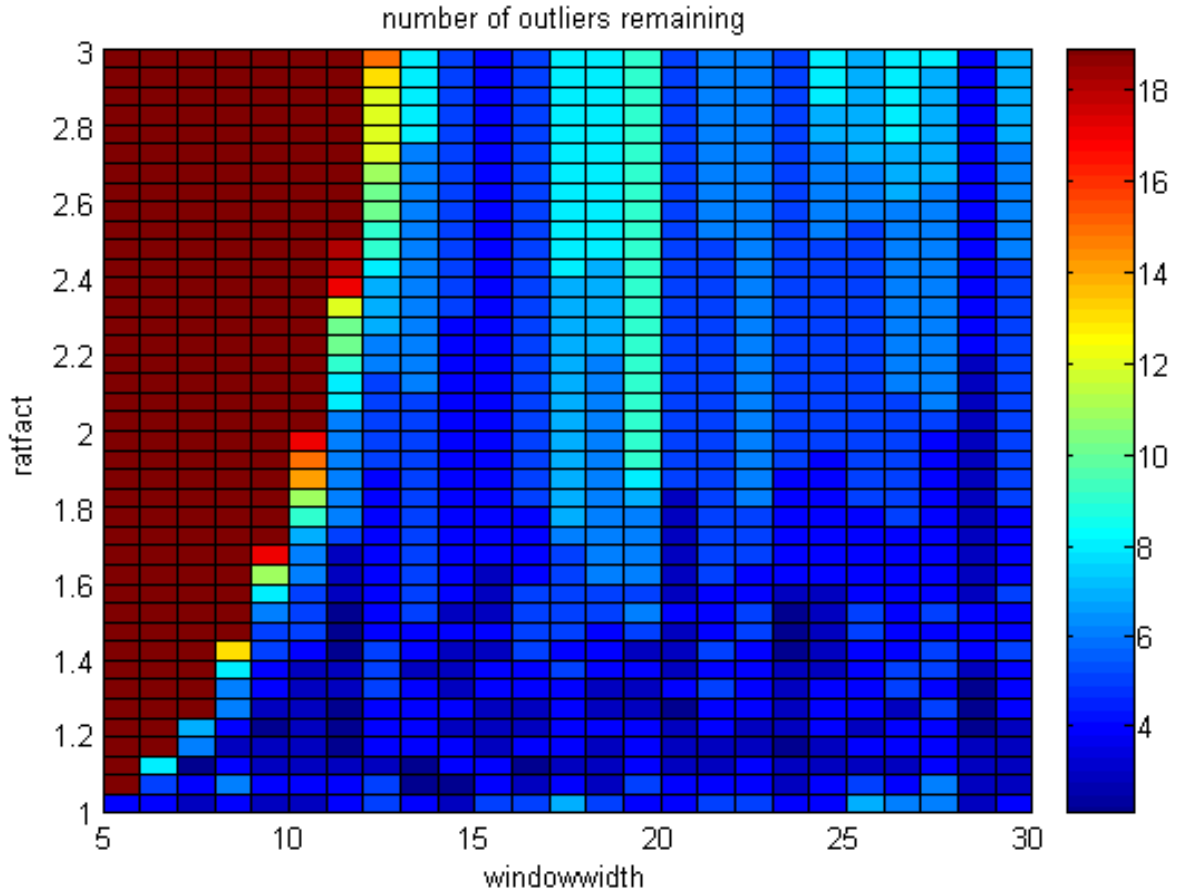


Figure 3.3. Outlier points remaining in the dataset after running the outlier detection routine with different window widths and ratio factors. The dataset shown is temperature from Wx 4, mid-November 2003 to the end of January 2004.

where the ratio factor  $r$  was 1.8.

Outliers were removed from the data. The ratio factor (1.8) and the number of datapoints in a section (20) were chosen by inspection to minimize the number of outliers left in the data and minimize the removal of true values. True outliers were identified by comparing the ARGOS transmitted data with the data collected from the Storage Modules at stations 1, 4, and 5. For the purpose of selecting the ratio factor and number of points (window width) to include in the outlier routine, we considered data for the period from mid-November 2003 till the end of January 2004. Figure 3.3 is an example plot that shows the number of true outliers left in the dataset after running the outlier detection program with the parameters (window width and ratio factor) given on the x- and y-axes. The total number of points that the outlier routine deleted generally was in the range of 1-5%. We also looked at the absolute magnitude of the difference between the ARGOS-transmitted and storage module data to get a sense for how bad the remaining outliers were. In general, the outlier routine got rid of the worst ones and the remaining ones were relatively small.

## Gap Filling

Gaps in the data, due to missing ARGOS transmissions or removed outliers, were filled by interpolating across the gap. Gaps in the ARGOS transmissions arose because there was not always a satellite overhead when the station was transmitting and sometimes the data got garbled in transmission. This primarily affected stations 3 and 6 where we did not collect locally-stored data. At the other stations, less than 10 points per station per variable out of the whole record (over 80,000 points) were obvious sensor malfunctions that were removed by hand. We tested linear, nearest neighbor, cubic, and spline methods of interpolation. For stations 1, 2, 4, and 5 where we had ARGOS and locally-stored data, we were able to compare the interpolated points to the real data that was not transmitted. The linear and cubic methods best matched the locally-stored data; since the linear method was slightly simpler, we used it.

## LTER Weather Data

The LTER stations recorded data on a 15-minute interval. To facilitate comparison with our data, we interpolated the LTER data onto our 20-minute timescale. The error associated with this was small, but probably not insignificant. For reference, the temperature change from one time interval to the next in our data averaged  $0.4^{\circ}\text{C}$ , relative humidity changed by 2%, wind speed by 0.8 m/s and incoming solar radiation by  $11.8 \text{ W/m}^2$ . If these variables changed at constant rates, then the linear interpolation would be 100% accurate. However, we know that they do not change at constant rates, and the error associated with the interpolation will rise with the degree of non-linearity.

## 3.2 Weather Station Data

Tables 3.3 through 3.15 summarize average weather conditions for a variety of different time intervals, which may be useful for comparison to other studies. Figures 3.4 through 3.12 show example timeseries for the whole study period from different stations. Superimposed on the pronounced seasonal cycle are large variations associated with storms and katabatic winds, both of which occur in all seasons. Interannual variability of average conditions does not reflect systematic differences but instead arises from random factors such as the number of storms.

Table 3.3. Summer averages of temperature ( $^{\circ}\text{C}$ ), relative humidity (%), wind speed ( $\text{m s}^{-1}$ ), vapor pressure of the air (mbar), vapor pressure difference between the air and surface (mbar), calculated sublimation rate (mm per 20-min interval), and elevation (m.a.s.l.) for reference. Data from NDJ 2005/6.

	$T_{air}$	RH	$u_z$	$e_z$	$e_z - e_s$	$\dot{S}$	Elevation
Wx Bo <sup>a</sup>	-2.5	55.8	4.7	2.9	...	...	64
Wx T	-4.6	62.2	4.4	2.7	-1.5	0.0158	334
Wx 1	-5.9	60.2	5.4	2.5	-1.2	0.0169	490
Wx 2	-7.7	53.7	6.8	2	-1.5	0.0227	817
Wx 3	-8.3	45.7	7	1.6	-1.5	0.0222	857
Wx 4	-8	45.5	5.4	1.6	-1.5	0.019	1012
Wx 5	-11.4	54.2	4.6	1.5	-0.7	0.008	1302
Wx 6 <sup>a</sup>	-13.2	54.2	4.7	1.3	...	...	1581
Wx Be <sup>a</sup>	-9.1	45.7	4	1.4	...	...	1176

<sup>a</sup> Station located on rock, not ice. Surface temperature,  $e_s$ , and  $\dot{S}$  were not calculated for these stations.

Table 3.4. Weather Variables Table – MJJ 2006.

	$T_{air}$	RH	$u_z$	$e_z$	$e_z - e_s$	$\dot{S}$	Elevation
Wx Bo	-29.8	71	3	0.4	...	...	64
Wx T	-26.8	63	5.9	0.5	-0.1	0.0026	334
Wx 1	-27	48.1	6.1	0.4	-0.2	0.0037	490
Wx 2	-27	44.4	8.4	0.3	-0.2	0.0043	817
Wx 3	-26.2	39.2	9.9	0.3	-0.3	0.007	857
Wx 4	-29	41.7	5.6	0.3	-0.2	0.0036	1012
Wx 5	-30.9	50.7	8.3	0.3	-0.2	0.0029	1302
Wx 6	-29.7	45	4.2	0.3	...	...	1581
Wx Be	-31	61.8	4.6	0.3	...	...	1176

Table 3.5. Weather Variables Table – Winter 2004

Winter4	$T_{air}$	RH	$u_z$	$e_z$	$e_z - e_s$	$\dot{S}$	Elevation
Wx Bo <sup>a</sup>	-29.8	65.7	4	0.4	...	...	64
Wx T	-27.5	59.3	6.4	0.4	-0.1	0.0032	334
Wx 1	-27.8	45	7.1	0.3	-0.2	0.004	490
Wx 2	-27.9	41.2	9.6	0.3	-0.2	0.005	817
Wx 3	-27.1	36.2	10.9	0.3	-0.3	0.0073	857
Wx 4	-29.6	37.1	5.4	0.2	-0.2	0.0033	1012
Wx 5	-31.3	42.9	8.8	0.2	-0.2	0.0037	1302
Wx 6 <sup>a</sup>	-30.2	38.4	4.5	0.2	...	...	1581
Wx Be <sup>a</sup>	-31.6	53.5	5	0.3	...	...	1176

<sup>a</sup> Station located on rock, not ice. Surface temperature,  $e_s$ , and  $\dot{S}$  were not calculated for these stations.

Table 3.6. Weather Variables Table – Summer 2004/5

Summer5	$T_{air}$	RH	$u_z$	$e_z$	$e_z - e_s$	$\dot{S}$	Elevation
Wx Bo <sup>a</sup>	-1.9	55.5	4.6	3	...	...	64
Wx T	-4.1	60.8	4.5	2.8	-1.5	0.0155	334
Wx 1	-5.5	59.8	5.2	2.5	-1.2	0.0155	490
Wx 2	-7.7	57.2	6.2	2.1	-1.4	0.0198	817
Wx 3	-8.4	50	6.9	1.7	-1.5	0.0226	857
Wx 4	-8	49.2	5.3	1.7	-1.6	0.0197	1012
Wx 5	-11.2	56.7	5.1	1.6	-0.9	0.0109	1302
Wx 6 <sup>a</sup>	-13.1	58.8	4.4	1.4	...	...	1581
Wx Be <sup>a</sup>	-9.1	47.9	4.3	1.5	...	...	1176

<sup>a</sup> Station located on rock, not ice. Surface temperature,  $e_s$ , and  $\dot{S}$  were not calculated for these stations.

Table 3.7. Weather Variables Table – Winter 2005

Winter5	$T_{air}$	RH	$u_z$	$e_z$	$e_z - e_s$	$\dot{S}$	Elevation
Wx Bo <sup>a</sup>	-26.4	70.8	3.7	0.5	...	...	64
Wx T	-23.6	62	6.5	0.6	-0.2	0.0033	334
Wx 1	-24	48.4	7.3	0.5	-0.2	0.0046	490
Wx 2	-24.6	45.6	9.8	0.4	-0.2	0.0054	817
Wx 3	-24	40.5	10.6	0.4	-0.3	0.0078	857
Wx 4	-25.7	41.4	6.8	0.3	-0.2	0.0051	1012
Wx 5	-28.7	50.2	7.7	0.3	-0.2	0.0032	1302
Wx 6 <sup>a</sup>	-27.6	47.4	4.9	0.3	...	...	1581
Wx Be <sup>a</sup>	-27.9	60.3	5.1	0.4	...	...	1176

<sup>a</sup> Station located on rock, not ice. Surface temperature,  $e_s$ , and  $\dot{S}$  were not calculated for these stations.

Table 3.8. Weather Variables Table – NDJF

NDJF	$T_{air}$	RH	$u_z$	$e_z$	$e_z - e_s$	$\dot{S}$	Elevation
Wx Bo <sup>a</sup>	-3.9	58	4.3	2.7	...	...	64
Wx T	-5.9	63.2	4.1	2.5	-1.3	0.0132	334
Wx 1	-7	59.5	4.9	2.2	-1.1	0.014	492
Wx 2	-8.8	55.2	5.9	1.8	-1.3	0.0181	817
Wx 3	-10.1	47.9	6.7	1.5	-1.3	0.0192	857
Wx 4	-9.3	49.3	4.6	1.5	-1.4	0.0158	1012
Wx 5	-12.5	56.1	5	1.4	-0.8	0.0086	1302
Wx 6 <sup>a</sup>	-13.9	55.5	4	1.2	...	...	1581
Wx Be <sup>a</sup>	-10.4	50	3.7	1.4	...	...	1176

<sup>a</sup> Station located on rock, not ice. Surface temperature,  $e_s$ , and  $\dot{S}$  were not calculated for these stations.



Table 3.9. Weather Variables Table – MAMJJASO

MAMJJASO	$T_{air}$	RH	$u_z$	$e_z$	$e_z - e_s$	$\dot{S}$	Elevation
Wx Bo <sup>a</sup>	-25.4	70.3	3.3	0.6	...	...	64
Wx T	-23.4	62.9	5.6	0.6	-0.2	0.0031	334
Wx 1	-23.7	48.8	6.3	0.5	-0.3	0.0045	490
Wx 2	-24.2	44.9	8.6	0.4	-0.3	0.0057	817
Wx 3	-23.8	40	9.8	0.4	-0.4	0.0083	857
Wx 4	-25.7	42.5	5.7	0.4	-0.3	0.0047	1012
Wx 5	-28.2	48.6	7.6	0.3	-0.2	0.0036	1302
Wx 6 <sup>a</sup>	-27.3	45.8	4.3	0.3	...	...	1581
Wx Be <sup>a</sup>	-27.3	57.7	4.4	0.4	...	...	1176

<sup>a</sup> Station located on rock, not ice. Surface temperature,  $e_s$ , and  $\dot{S}$  were not calculated for these stations.

Table 3.10. Weather Variables Table – December 21, 2003 - January 21, 2004 for comparison to *Lewis et al.* [1998].

Lewis4	$T_{air}$	RH	$u_z$	$e_z$	$e_z - e_s$	$\dot{S}$	Elevation
Wx Bo <sup>a</sup>	-1.4	62.7	4.7	3.4	...	...	64
Wx T	-3.4	70.3	4	3.3	-1.5	0.015	334
Wx 1	-4.2	62.8	5.2	2.7	-1.5	0.0178	499
Wx 2	-5.8	58.8	5.4	2.3	-1.5	0.0204	817
Wx 3	NaN	NaN	NaN	NaN	NaN	NaN	857
Wx 4	-6.2	48.1	4.9	1.8	-1.6	0.019	1012
Wx 5	-9.1	56.8	4.1	1.7	-0.9	0.0093	1302
Wx 6 <sup>a</sup>	-11.2	56.4	4.3	1.5	...	...	1581
Wx Be <sup>a</sup>	-7.4	49.8	4	1.7	...	...	1176

<sup>a</sup> Station located on rock, not ice. Surface temperature,  $e_s$ , and  $\dot{S}$  were not calculated for these stations.

Table 3.11. Weather Variables Table – December 21, 2004 - January 21, 2005.

Lewis5	$T_{air}$	RH	$u_z$	$e_z$	$e_z - e_s$	$\dot{S}$	Elevation
Wx Bo <sup>a</sup>	-0.1	66	4.4	4	...	...	64
Wx T	-2.1	72.1	4.1	3.7	-1.4	0.0136	334
Wx 1	-3.3	72.6	4.2	3.4	-0.9	0.0123	490
Wx 2	-5	68.4	4.8	2.9	-1.4	0.0175	817
Wx 3	-5.4	59	5.9	2.4	-1.5	0.0221	857
Wx 4	-5.5	57.1	5.9	2.3	-1.5	0.0224	1012
Wx 5	-8	63.8	4.5	2.1	-0.9	0.0113	1302
Wx 6 <sup>a</sup>	-10.3	66.4	4.6	1.9	...	...	1581
Wx Be <sup>a</sup>	-6.3	54.2	4.5	2	...	...	1176

<sup>a</sup> Station located on rock, not ice. Surface temperature,  $e_s$ , and  $\dot{S}$  were not calculated for these stations.

Table 3.12. Weather Variables Table – December 21, 2005 - January 21, 2006.

Lewis6	$T_{air}$	RH	$u_z$	$e_z$	$e_z - e_s$	$\dot{S}$	Elevation
Wx Bo <sup>a</sup>	-0.1	59.4	4.5	3.6	...	...	64
Wx T	-2.1	67.7	4	3.5	-1.5	0.0142	334
Wx 1	-3.3	67.7	4.3	3.2	-1.3	0.0155	490
Wx 2	-4.6	59	5.3	2.6	-1.8	0.0239	817
Wx 3	-5.2	50.3	5.6	2.1	-1.5	0.0207	857
Wx 4	-4.7	49	3.8	2.1	-1.6	0.0162	1012
Wx 5	-8.1	58.3	3.7	1.9	-0.8	0.0077	1302
Wx 6 <sup>a</sup>	-9.9	54.8	3.7	1.6	...	...	1581
Wx Be <sup>a</sup>	-5.9	47.8	3.6	1.8	...	...	1176

<sup>a</sup> Station located on rock, not ice. Surface temperature,  $e_s$ , and  $\dot{S}$  were not calculated for these stations.

Table 3.13. Weather Variables Table – Summer, All Years.

Summer	$T_{air}$	RH	$u_z$	$e_z$	$e_z - e_s$	$\dot{S}$	Elevation
Wx Bo <sup>a</sup>	-2.9	53.1	4.6	2.7	...	...	64
Wx T	-4.5	60.5	3.9	2.7	-1.9	0.0149	334
Wx 1	-6.2	59.4	5.2	2.4	-1.2	0.0159	495
Wx 2	-8.1	56.4	6	2	-1.4	0.0197	817
Wx 3	-8.9	48.3	6.6	1.6	-1.4	0.021	857
Wx 4	-8.6	48.6	4.9	1.6	-1.5	0.0175	1012
Wx 5	-11.7	56.1	4.6	1.5	-0.8	0.0086	1302
Wx 6 <sup>a</sup>	-13.5	57.2	4.3	1.3	...	...	1581
Wx Be <sup>a</sup>	-9.7	49.4	4	1.5	...	...	1176

<sup>a</sup> Station located on rock, not ice. Surface temperature,  $e_s$ , and  $\dot{S}$  were not calculated for these stations.

Table 3.14. Weather Variables Table – Winter, All Years.

Winter	$T_{air}$	RH	$u_z$	$e_z$	$e_z - e_s$	$\dot{S}$	Elevation
Wx Bo <sup>a</sup>	-28.7	69.2	3.6	0.5	...	...	64
Wx T	-25.9	61.4	6.3	0.5	-0.1	0.003	334
Wx 1	-26.2	47.1	6.8	0.4	-0.2	0.0041	490
Wx 2	-26.5	43.7	9.3	0.3	-0.2	0.0049	817
Wx 3	-25.8	38.7	10.5	0.3	-0.3	0.0074	857
Wx 4	-28.1	40.1	6	0.3	-0.2	0.004	1012
Wx 5	-30.3	48	8.3	0.3	-0.2	0.0033	1302
Wx 6 <sup>a</sup>	-29.1	43.6	4.5	0.3	...	...	1581
Wx Be <sup>a</sup>	-30.2	58.5	4.9	0.3	...	...	1176

<sup>a</sup> Station located on rock, not ice. Surface temperature,  $e_s$ , and  $\dot{S}$  were not calculated for these stations.

Table 3.15. Weather Variables Table – Three Whole Years, December 2003 – November 2006.

whole	$T_{air}$	RH	$u_z$	$e_z$	$e_z - e_s$	$\dot{S}$	Elevation
W <sub>X</sub> Bo <sup>a</sup>	-18.3	66.2	3.6	1.3	...	...	64
W <sub>X</sub> T	-17.6	63	5.2	1.3	-0.5	0.0065	334
W <sub>X</sub> 1	-18.2	52.3	5.8	1.1	-0.5	0.0076	491
W <sub>X</sub> 2	-19.1	48.3	7.7	0.9	-0.6	0.0098	817
W <sub>X</sub> 3	-19.8	42.3	8.9	0.7	-0.6	0.0114	857
W <sub>X</sub> 4	-20.3	44.8	5.3	0.7	-0.6	0.0083	1012
W <sub>X</sub> 5	-23.1	51.1	6.7	0.7	-0.4	0.0052	1302
W <sub>X</sub> 6 <sup>a</sup>	-22.9	49	4.2	0.6	...	...	1581
W <sub>X</sub> Be <sup>a</sup>	-21.7	55.1	4.2	0.7	...	...	1176

<sup>a</sup> Station located on rock, not ice. Surface temperature,  $e_s$ , and  $\dot{S}$  were not calculated for these stations.

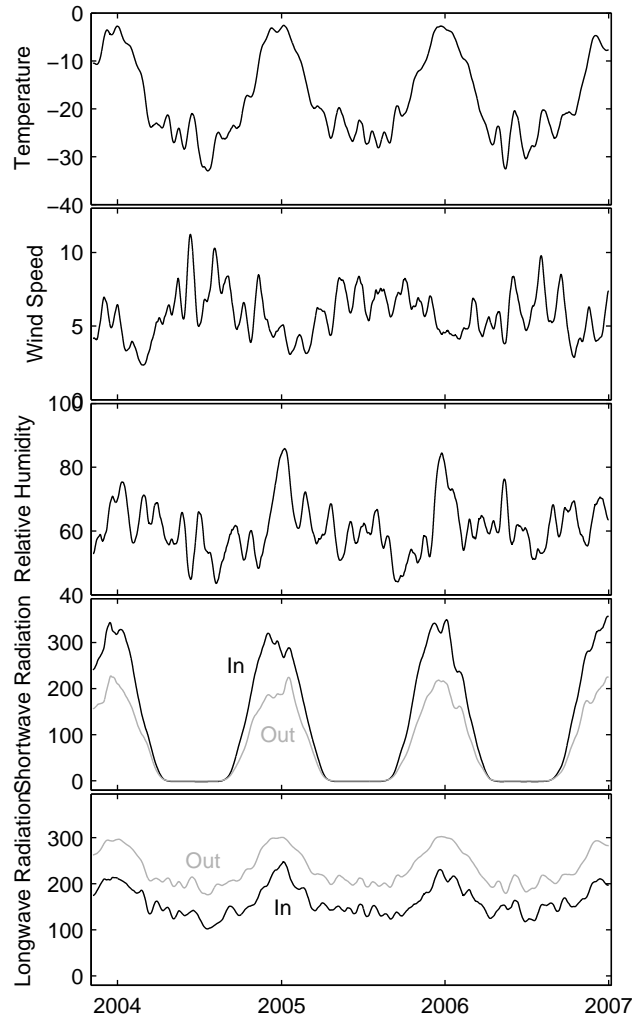


Figure 3.4. Weather variables timeseries, measured by Wx 1: temperature ( $^{\circ}\text{C}$ ), wind speed ( $\text{m/s}$ ), relative humidity (%), shortwave radiation ( $\text{W/m}^2$ ), and longwave radiation ( $\text{W/m}^2$ ). Data were smoothed with a triangular filter that assigned the highest weight to the central point and the lowest weight to points 15 days prior to and 15 days after the central point.

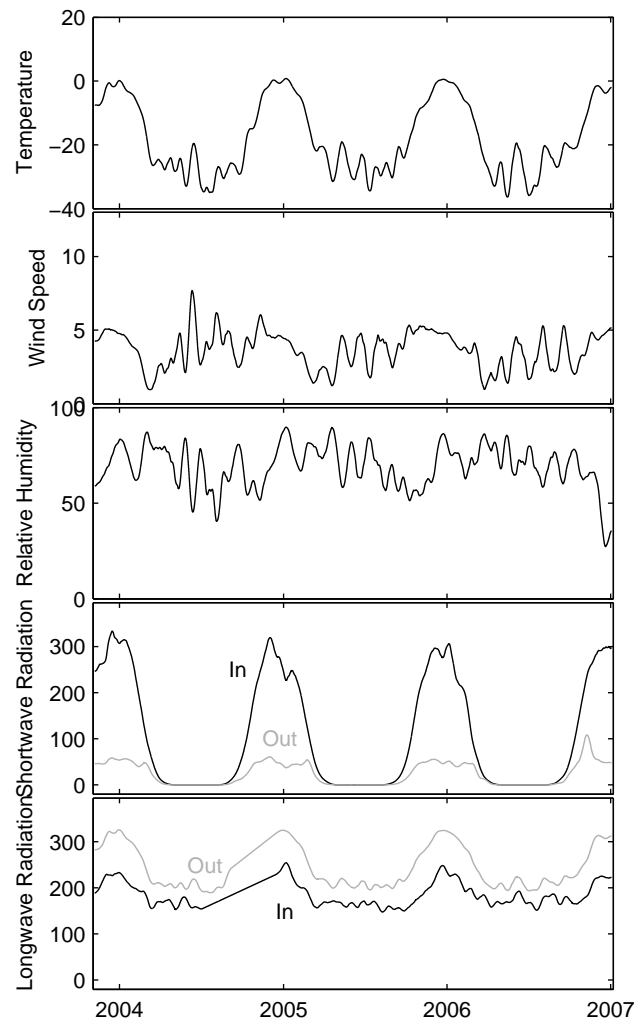


Figure 3.5. Weather variables timeseries – Wx Bo.

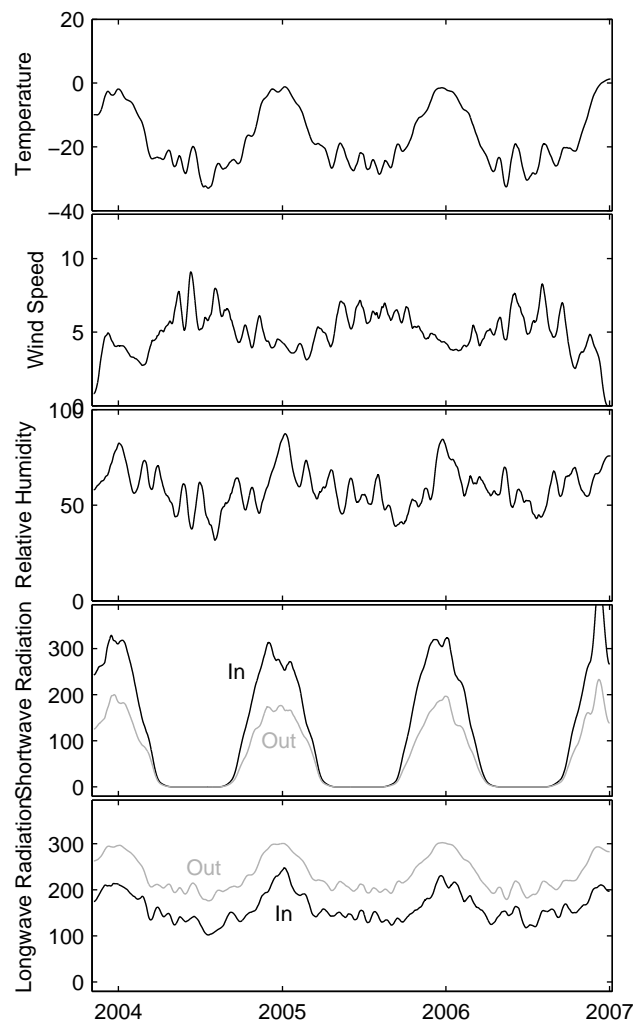


Figure 3.6. Weather variables timeseries – Wx T.

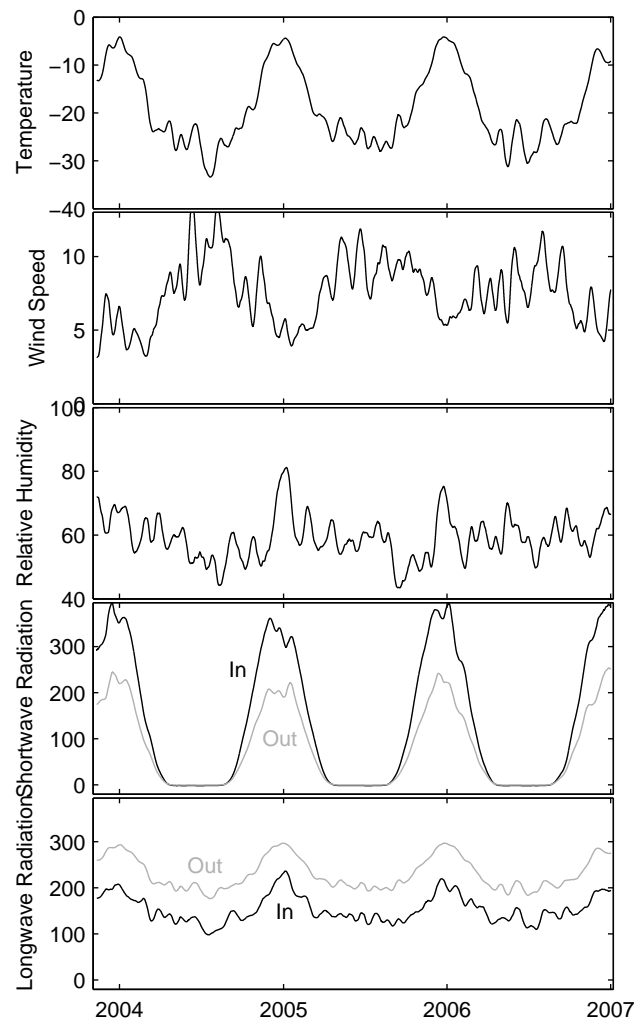


Figure 3.7. Weather variables timeseries – Wx 2.

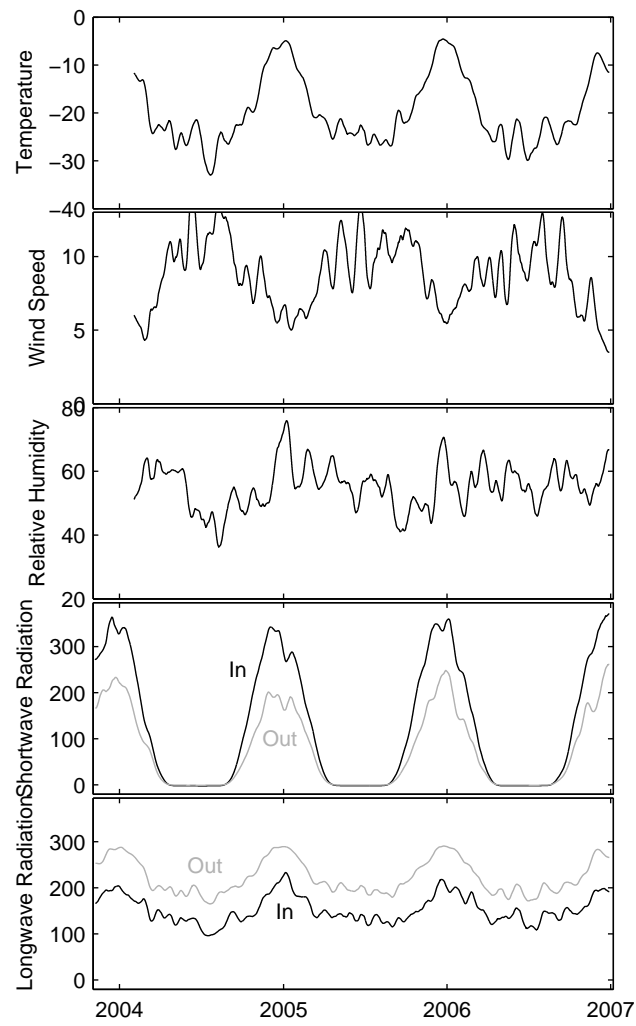


Figure 3.8. Weather variables timeseries – Wx 3.



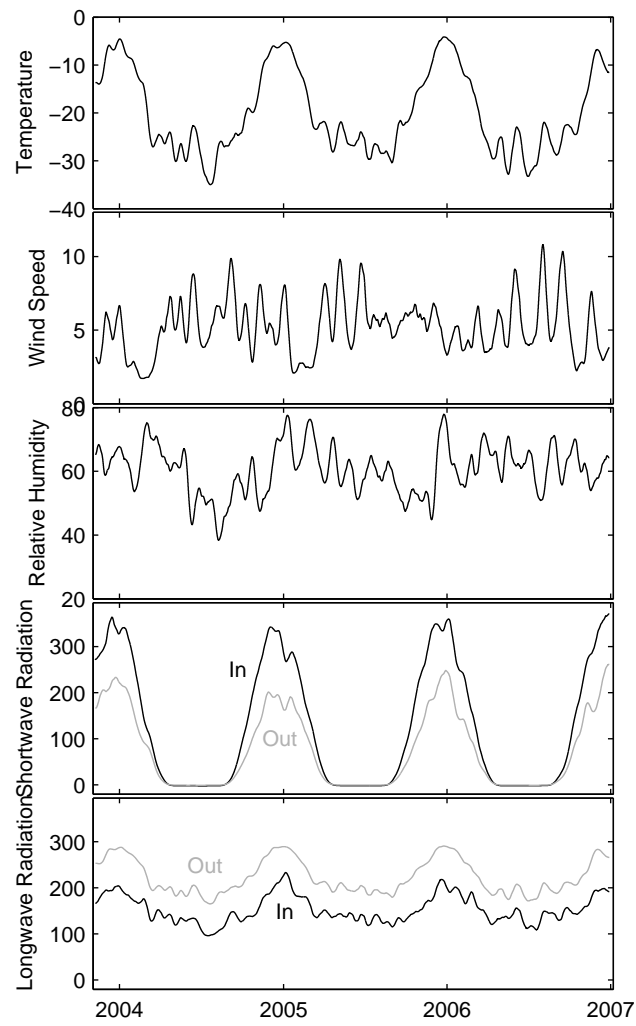


Figure 3.9. Weather variables timeseries – Wx 4.

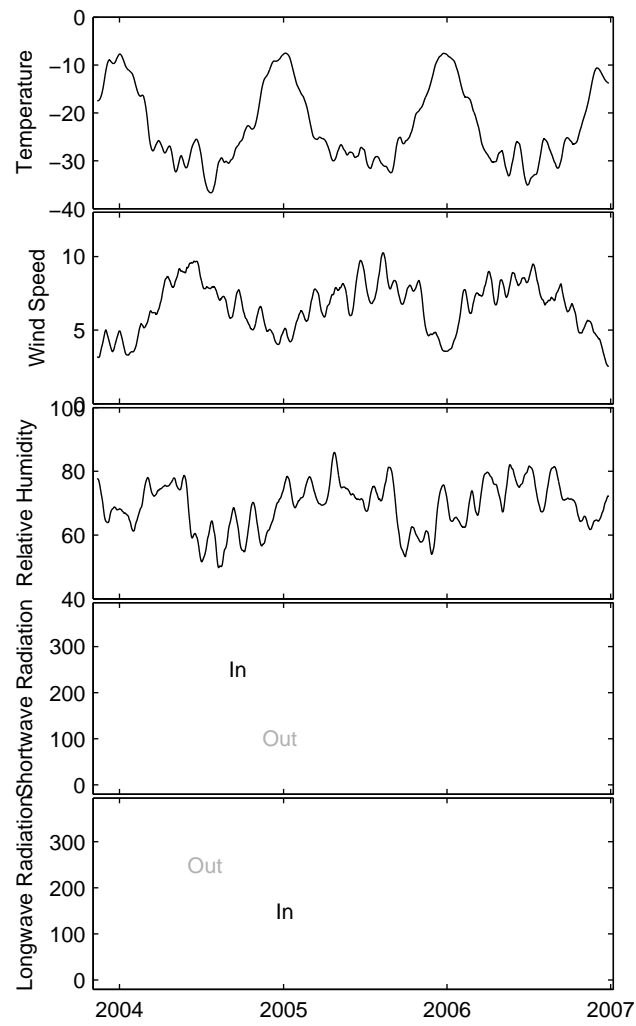


Figure 3.10. Weather variables timeseries – Wx 5.

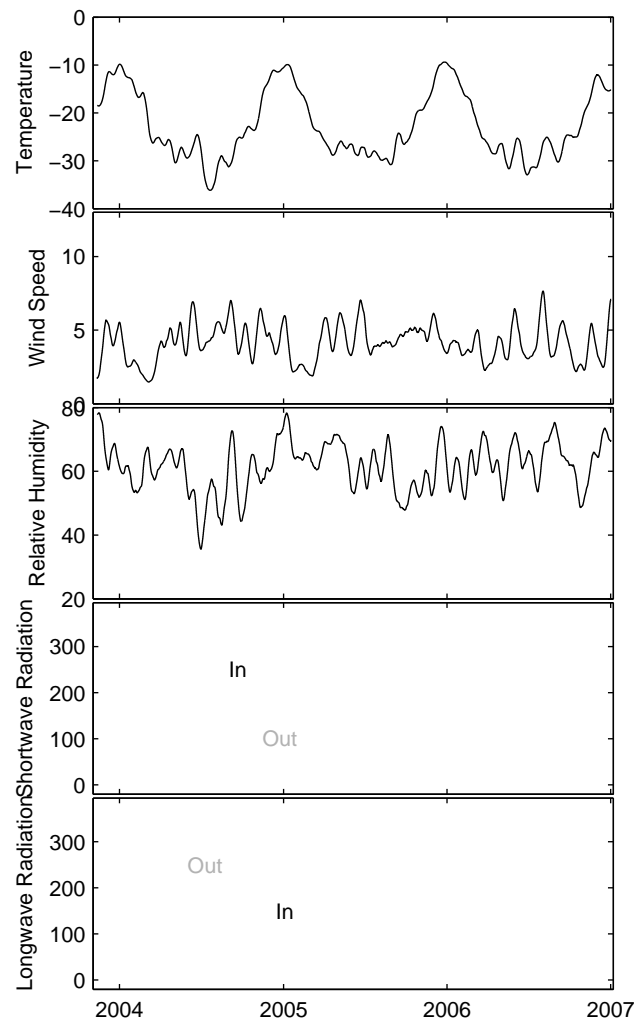


Figure 3.11. Weather variables timeseries – Wx 6.

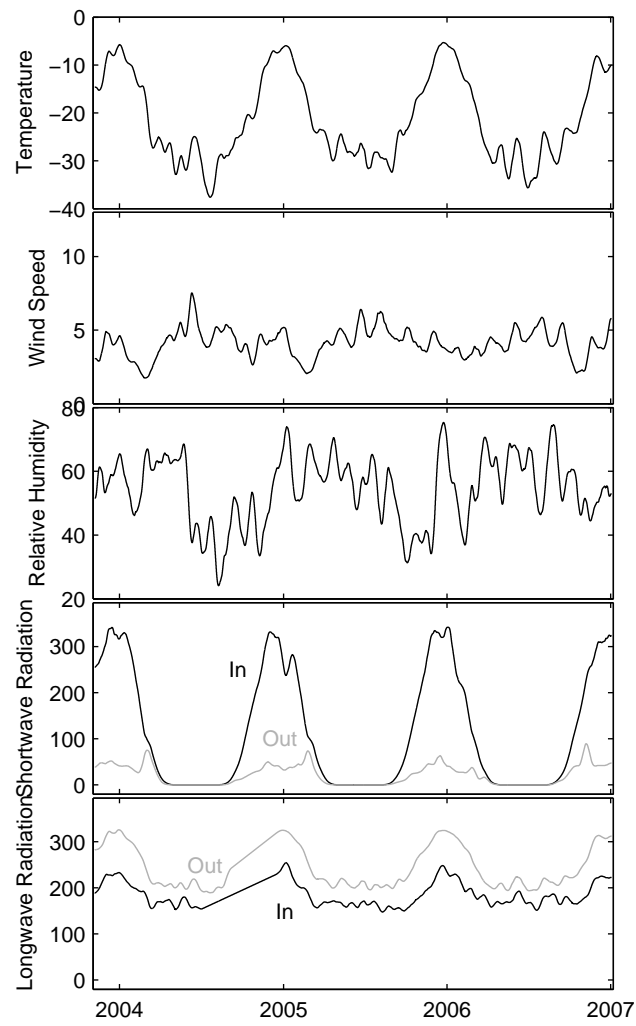


Figure 3.12. Weather variables timeseries – Wx Be.

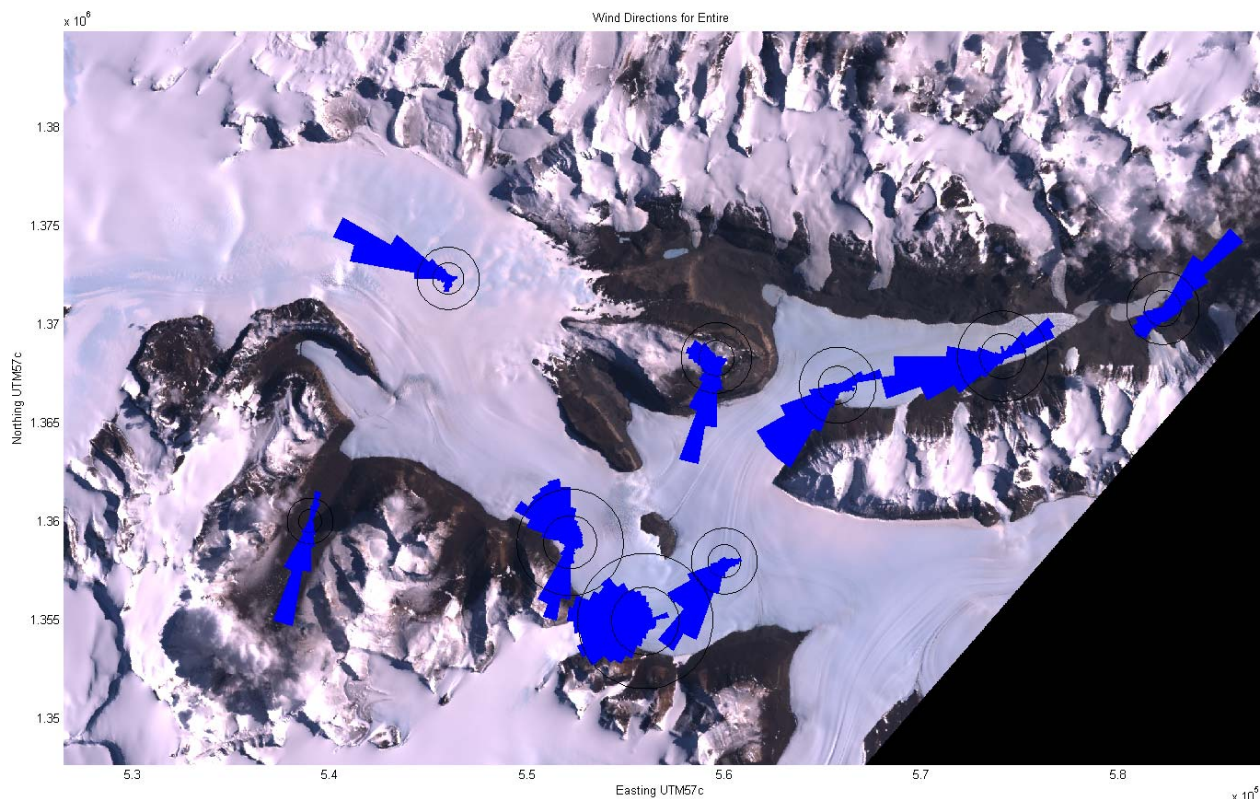


Figure 3.13. Wind Directions for the entire record. The background image is from Landsat.

### 3.2.1 Winds

In all seasons, the fastest winds occur midway along the glacier (Wx 3), below the steep tributary valley Windy Gully. In summer, wind speeds on the glacier tend to be slower than in other seasons. The stations close to the ice-free portion of Taylor Valley (Wx 1 and T) often experience diurnal mountain/valley winds when solar heating warms the valley walls. Summertime katabatic winds generally descend from Windy Gully. Wintertime katabatic winds descend alternately from Windy Gully or from the plateau, through Taylor Mouth. The 52.2 m/s maximum wind speed (30-second gust) was recorded at Wx 3 during a storm on May 15th, 2004.

Wind directions on the glacier were strongly controlled by the topography. There were interesting patterns that developed as air masses from different areas interacted. The three primary source locations of the air masses were: Taylor Valley, Windy Gully, and Taylor Mouth (at the west end of our study area). Figures 3.13, 3.14, and 3.15 show histograms of wind direction, plotted on a compass rose to illustrate the patterns of wind direction. *Nylen et al.* [2004] made similar plots for the LTER stations in Taylor Valley.

The directional constancy of the wind is defined as the vector mean of the wind velocity divided by the scalar mean wind speed. If the wind steadily comes from one direction, it has a value close to 1. If the wind direction is random, it has a value of 0. While many areas of Antarctica are known to have high directional constancies [*Parish and Cassano, 2001*],



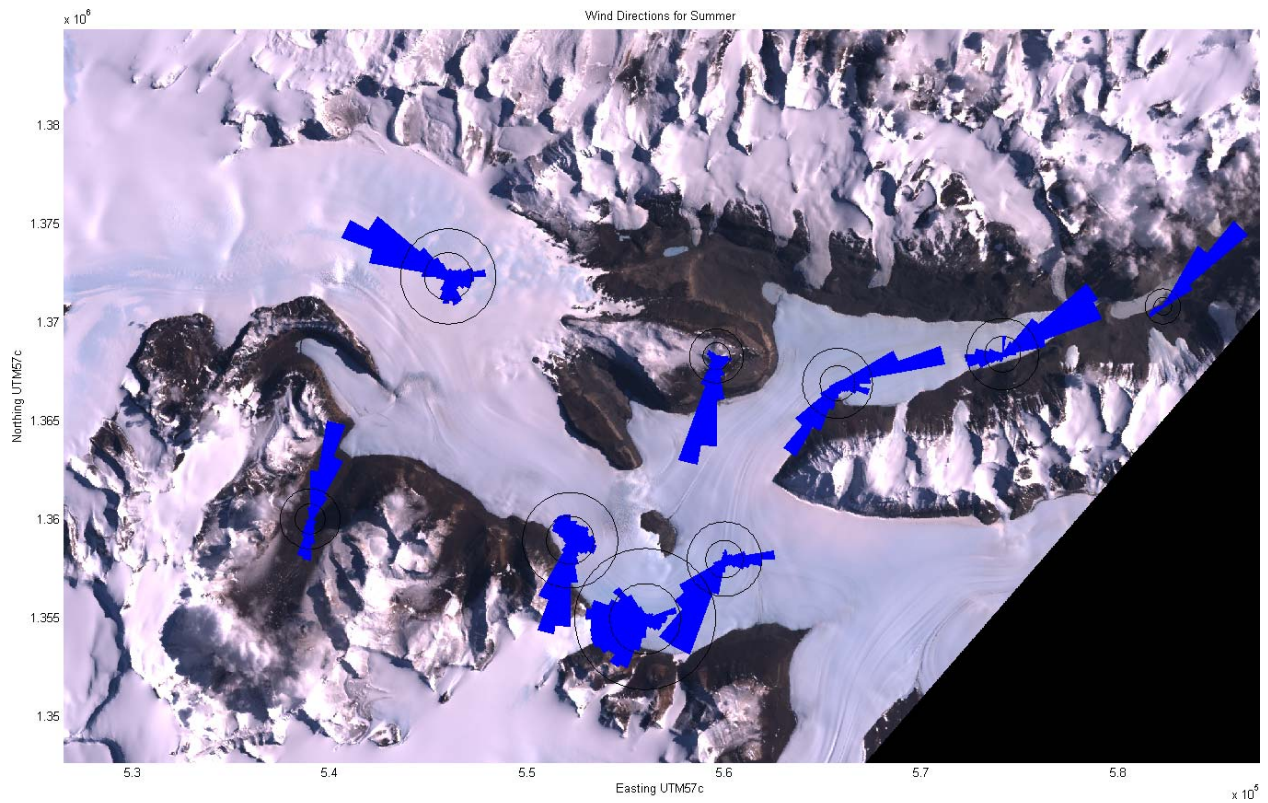


Figure 3.14. Wind Directions for Summer.

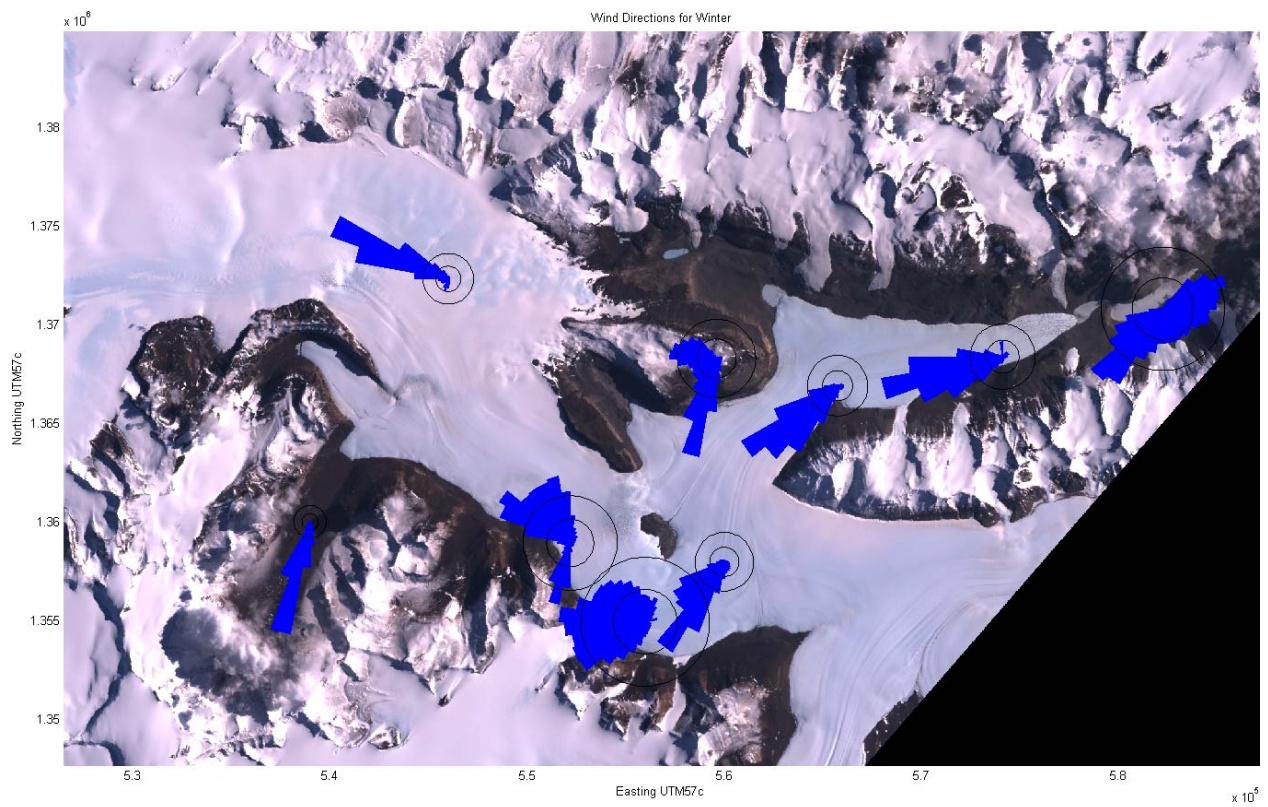


Figure 3.15. Wind Directions for Winter.

Table 3.16. Directional constancy of the wind at each station.

	Entire Year	Summer	Winter
Bo	0.03	0.57	0.61
T	0.54	0.27	0.84
1	0.74	0.48	0.90
2	0.87	0.75	0.92
3	0.67	0.67	0.65
4	0.47	0.65	0.44
5	0.71	0.34	0.81
6	0.77	0.87	0.75
Be	0.59	0.11	0.95

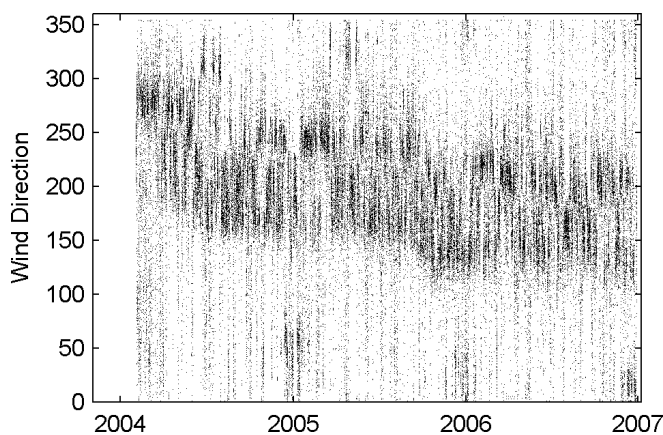


Figure 3.16. Wx 3 wind direction, showing the sensor rotation over time.

Taylor Glacier’s complex topography and competing wind regimes cause the constancies to be low at some stations. For comparison, *Bintanja* [1999] found directional constancies of 0.65 for a blue ice site and 0.91 for a snow site in Scharffenbergbotnen, Queen Maud Land.

The wind sensor on station 3 rotated over the course of the deployment, as shown in figure 3.16. This error was not corrected due to a lack of an easy method. The wind sensor was also programmed differently from the rest of the station network, resulting in a shorter measurement interval which also contributed to the scatter in the wind direction data.

The top wind sensor on station 4 failed during a strong wind on July 30th, 2005. The last measurement it recorded for the maximum 30-second wind speed within a 20-minute interval was 41 m/s. Upon revisiting the station, we discovered that the sensor had been decapitated. To maintain a consistent timeseries, we inserted an adjusted version of the lower wind sensor’s data in place of the top sensor’s data for subsequent wind speed measurements. The adjustment was based on a linear least-squares fit for the time before the sensor failed. The equation was  $u_{top} = 1.22u_{bottom} + 0.024$ . Wind direction was simply substituted: the bottom sensor’s direction was assigned to the top.

### 3.2.2 Air Temperature

Temperatures range from as low as  $-50^{\circ}\text{C}$ , during calm periods in the winter, up to  $5^{\circ}\text{C}$ , for a few days in summer at low elevations. The mean annual temperature at the station closest to the terminus (Wx T) was  $-17.4^{\circ}\text{C}$ , almost identical to the  $-17^{\circ}\text{C}$  estimated by *Robinson* [1984] from crevasse temperatures. Lapse rates tend to be strong ( $7.5^{\circ}\text{C}/\text{km}$ ) and well-organized in the summer and weaker ( $4^{\circ}\text{C}/\text{km}$ ) and less organized in the winter. A persistent winter-time inversion in the ice-free portion of Taylor Valley affects Wx Bo, sometimes affects Wx T, and rarely extends upglacier to Wx 1. Temperature increases at the onset of storms and katabatic wind events are often  $10^{\circ}\text{C}$  in a couple hours. Lapse rates and inversions are discussed further in sections 3.3.5 and 3.3.6.

### 3.2.3 Relative Humidity

Relative humidity tends to be higher in summer than winter. Summer storms can bring moist air from the ocean, but they can also bring strong downglacier winds which are dry due to adiabatic warming. When the wind speed is over 10 m/s, the relative humidity is rarely above 70%. At lower speeds, it spans the whole range.

### 3.2.4 Shortwave Radiation

Daily mean incoming shortwave radiation values in the summer tend to be about  $300\text{ W}/\text{m}^2$  (e.g. figure 3.4). Common noontime values in the summer were  $650\text{ W}/\text{m}^2$  (01:00 UTC) (e.g. figure 3.17). Less solar radiation reached the surface on overcast days, as one would expect. On partly cloudy days, radiation would often spike above the expected value due to reflections off of the clouds (see section 3.3.7 for more). The different seasonal patterns of solar radiation seen at the different stations (figures 3.17, 3.18, and 3.19) arose from shading of the stations by nearby mountains. On cloudy nights in summer the diffuse radiation kept the solar radiation higher than it was on clear nights (the sun was still above the horizon, just blocked by mountains). To help understand the solar variability across the glacier, we calculated the skyview factors for each grid cell of the RAMP DEM [*Liu et al.*, 2001]. The skyview factor was a measure of the fraction of sky visible from a certain point on the Earth's surface. As expected (see figure 3.21), areas close to cliffs did not have line of sight to a large portion of the sky, and as such, would not receive as much solar radiation as another site farther from the cliff.

The mean albedos (when incoming shortwave is greater than  $100\text{ W}/\text{m}^2$  to avoid spurious readings) for stations T, 1, 2, 4 were 0.58, 0.63, 0.60, and 0.61. Snowfall on the glacier temporarily increased the albedo to  $>0.7$  (figure 3.22). Ignoring the snow, all stations had a subtle trend of increasing ice albedo over the course of the summer (especially 2004/5), generally from about 0.55 at the beginning of the summer to 0.65 at the end. Field observations suggest that this increase accompanies the formation of a hollow crust on the surface due to a small amount of subsurface melt along grain boundaries; the hollow space reflects white light (figure 3.23).



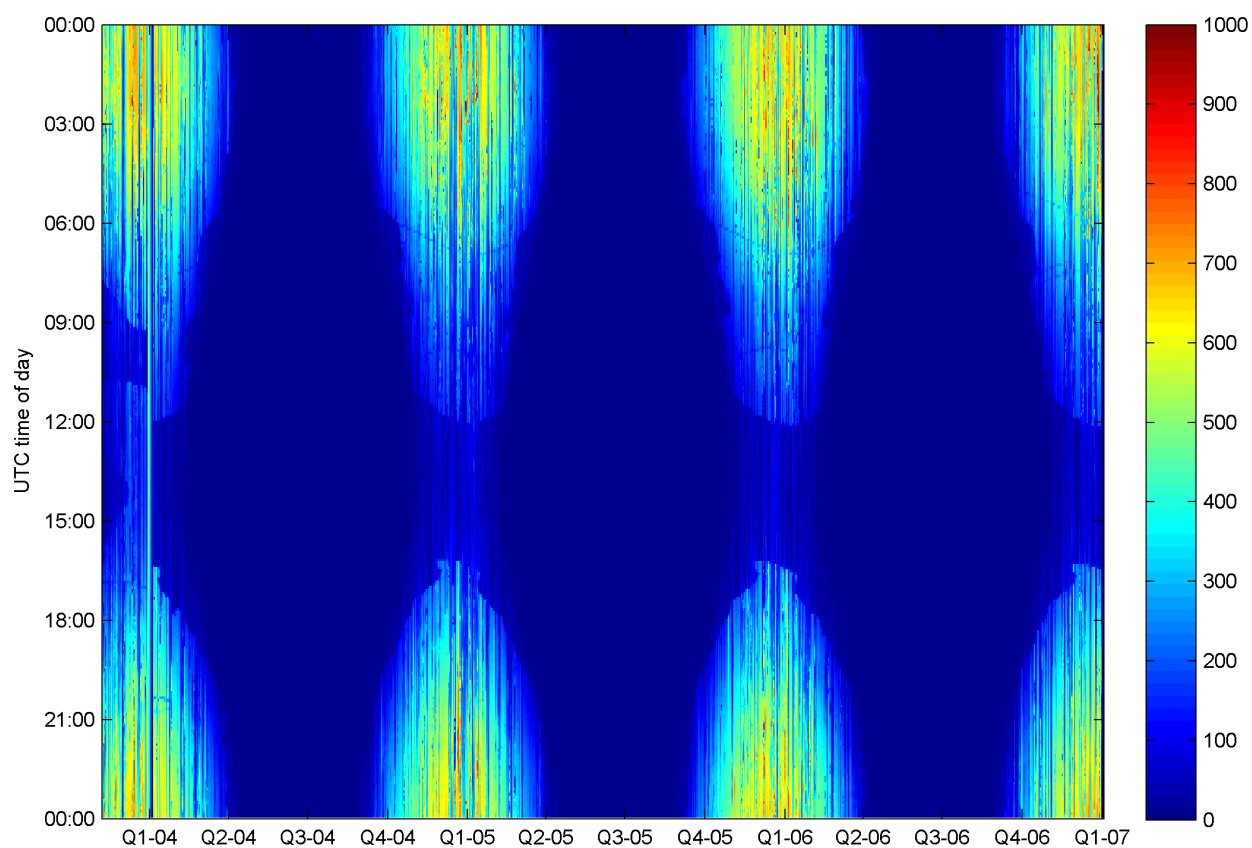


Figure 3.17. Incoming shortwave radiation at Wx 1. Day of the year was plotted along the x-axis and time of day along the y-axis, with the incoming shortwave as the colors ( $\text{W/m}^2$ ). Local noon was 01:00 UTC. These were 5-minute data instead of the usual 20-minute data. Faint dark lines (e.g. close to 06:00) were caused by shading of the sensor by parts of the station. Again, note that the station moved in early January 2004.

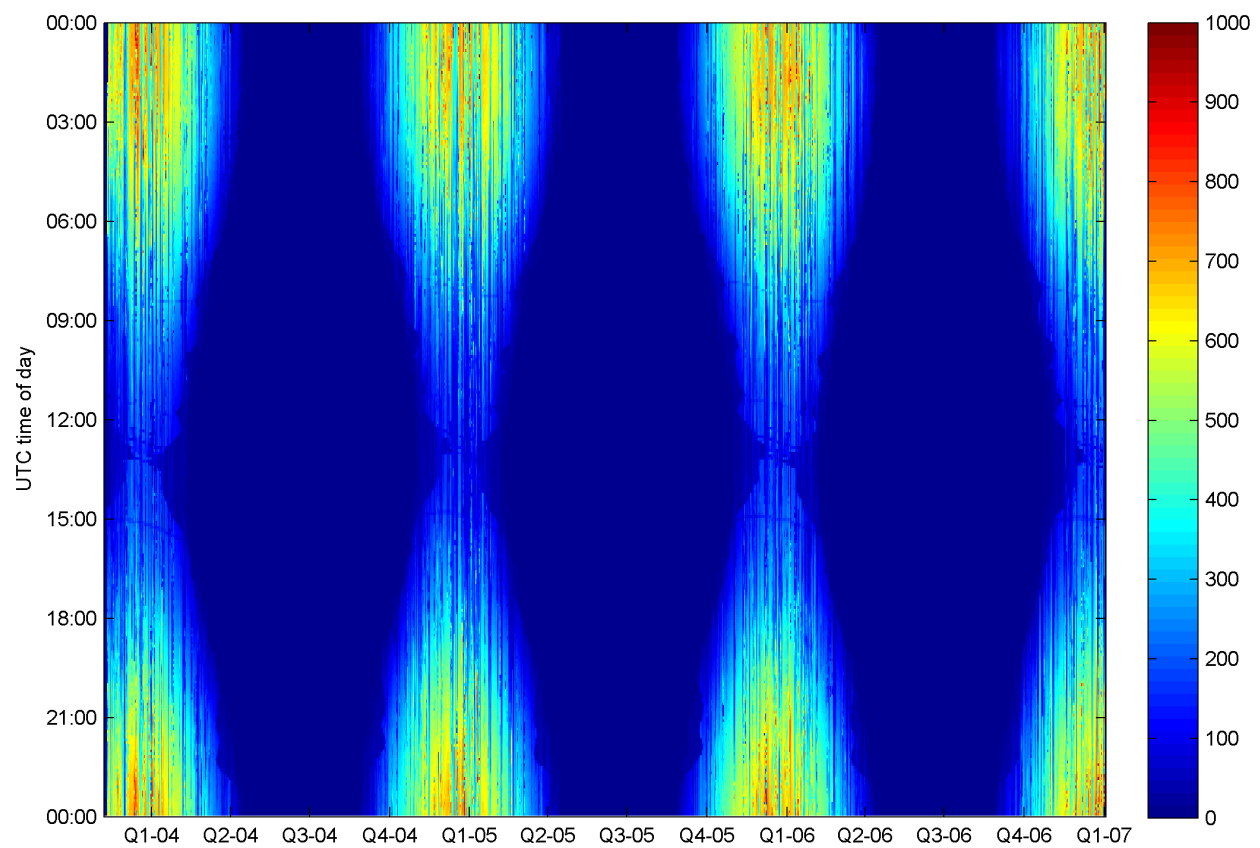


Figure 3.18. Incoming shortwave radiation at Wx 2. Axes as in figure 3.17.

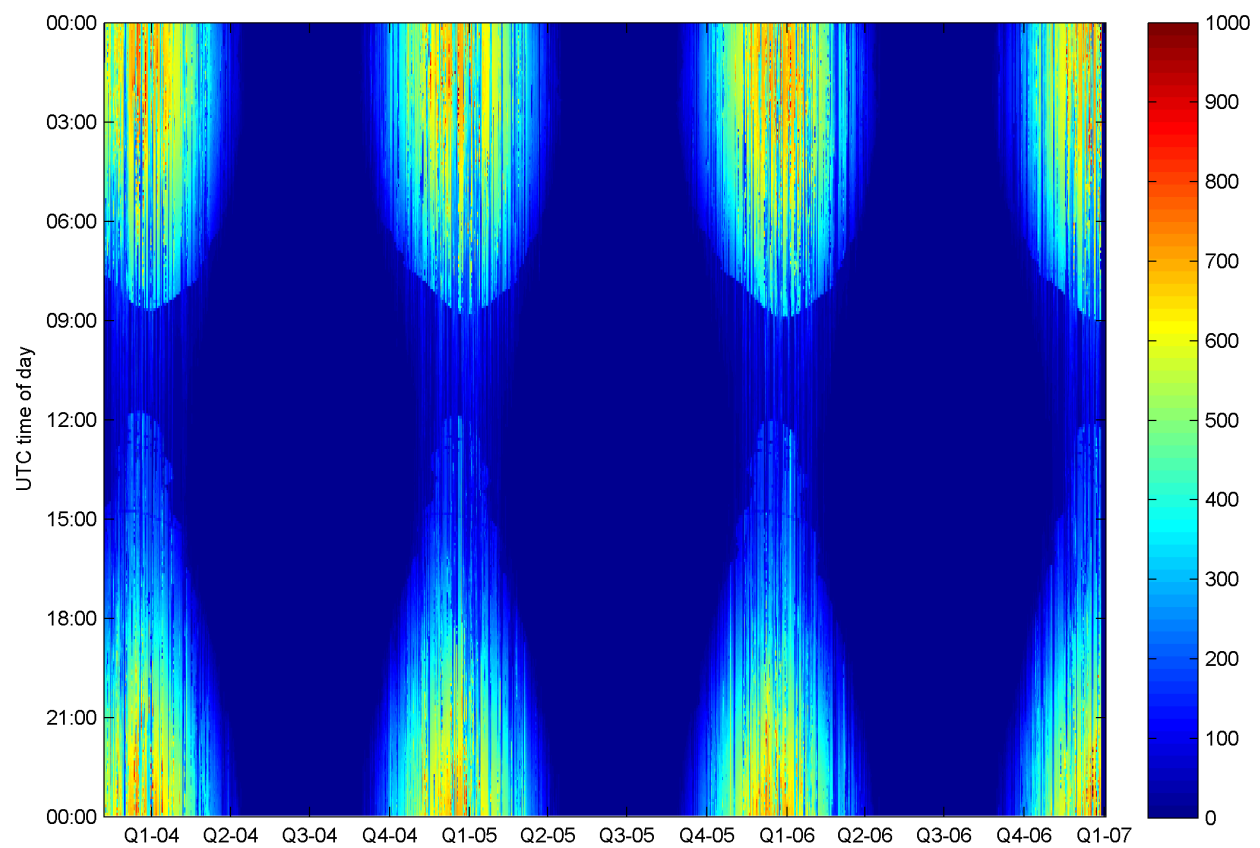


Figure 3.19. Incoming shortwave radiation at Wx 4. Axes as in figure 3.17.

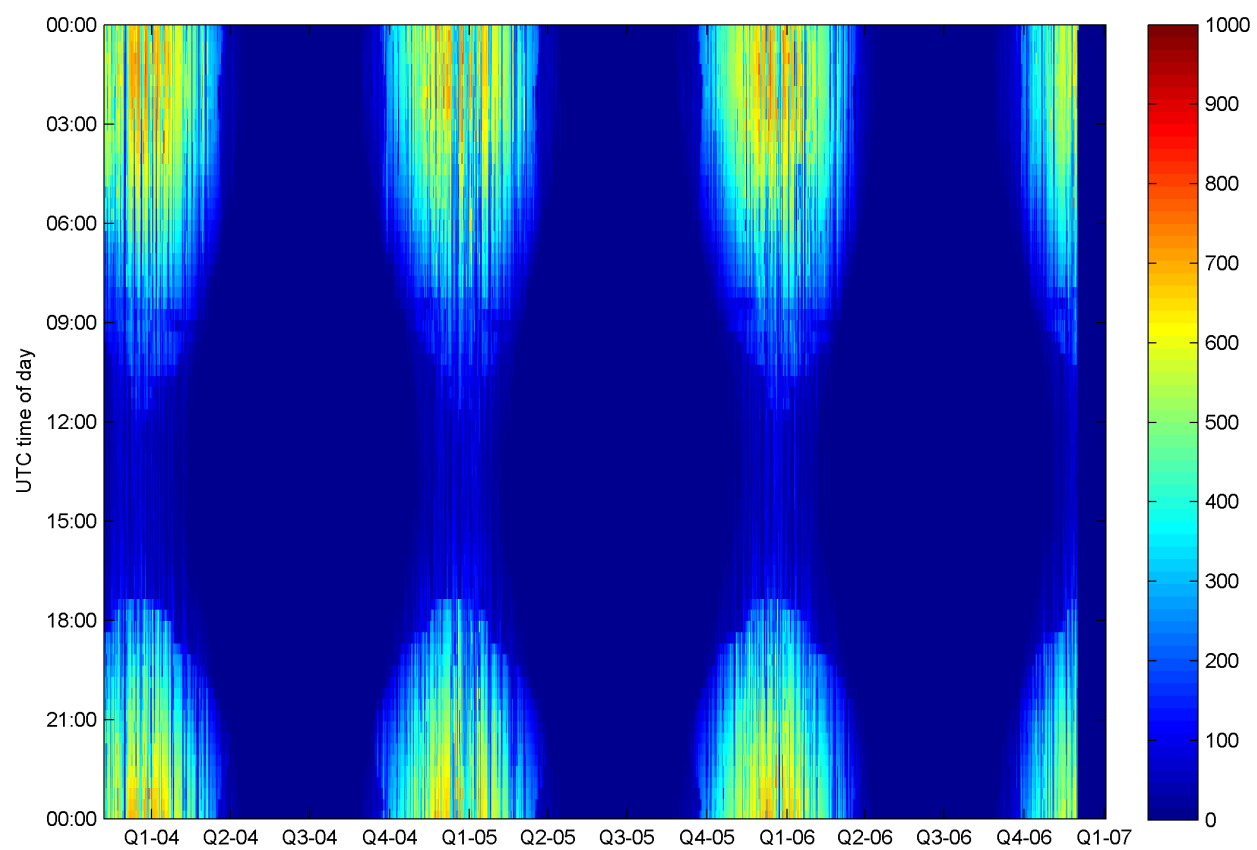


Figure 3.20. Incoming shortwave radiation at Wx T. Axes as in figure 3.17. These were 20-minute data.

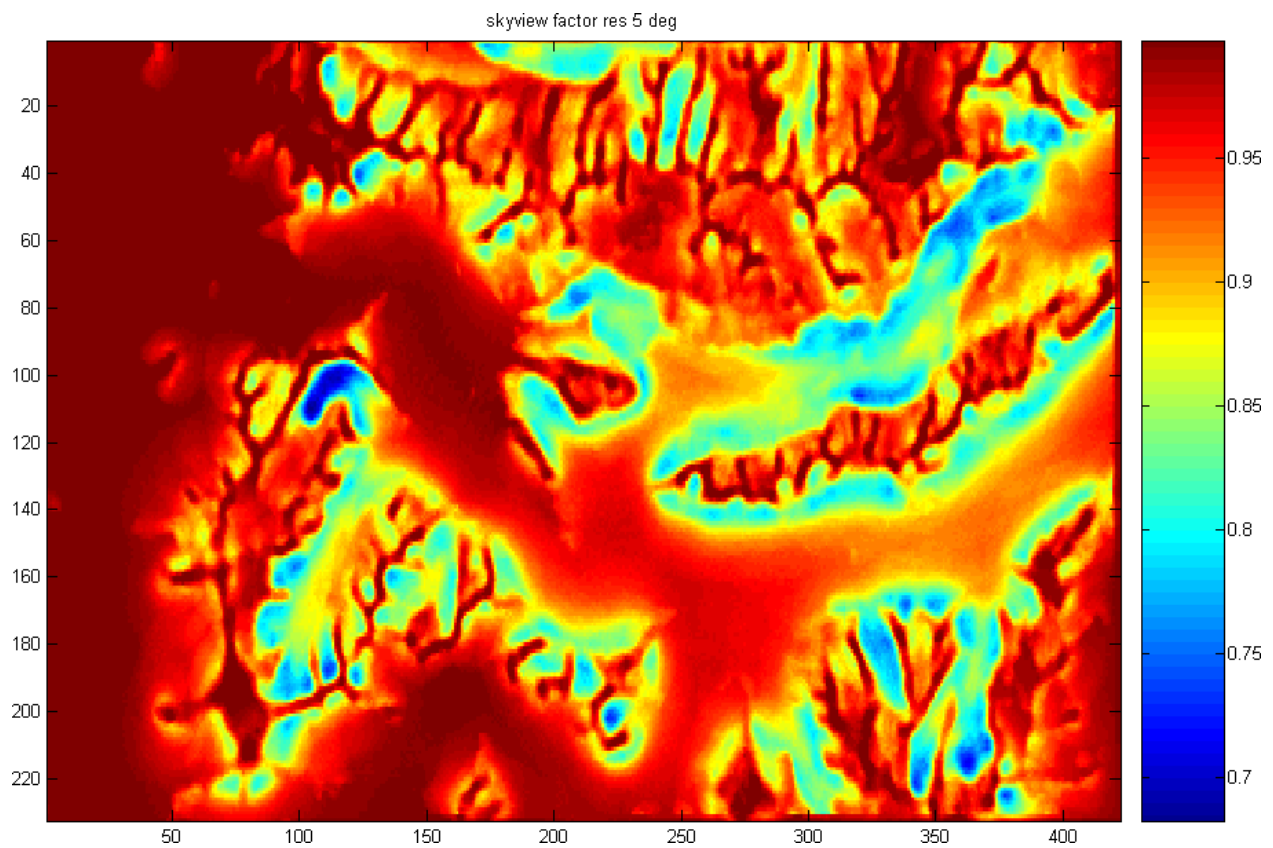


Figure 3.21. The skyview factor plotted here measures the percentage of the sky visible from a grid cell of a DEM. A flat plain would have a skyview factor of 1 and a slot canyon would have a skyview factor close to 0.

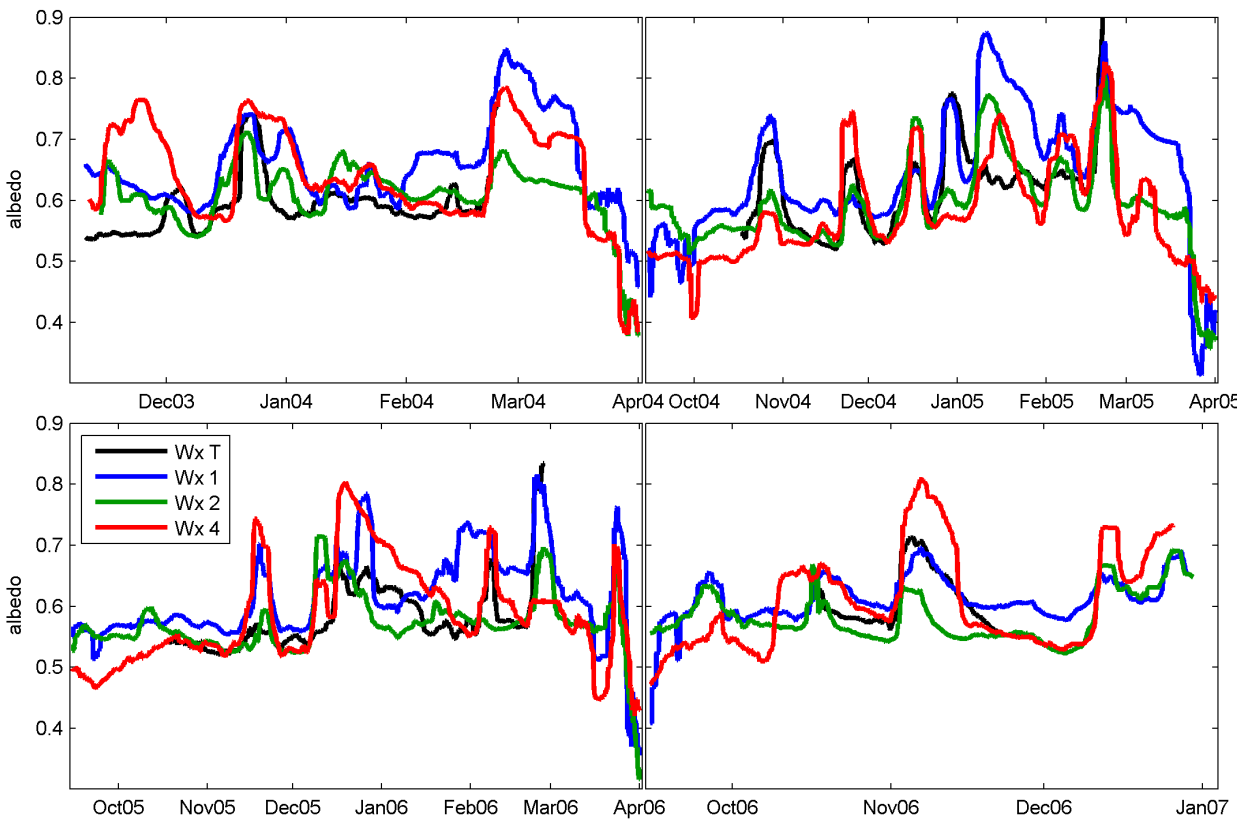


Figure 3.22. Timeseries of albedo showed snowfall events (albedo increased rapidly to  $>0.7$ ) as well as a subtle trend of the baseline (non-snow) albedo over each summer. Data were smoothed with a running median filter with a window width of 3 days.

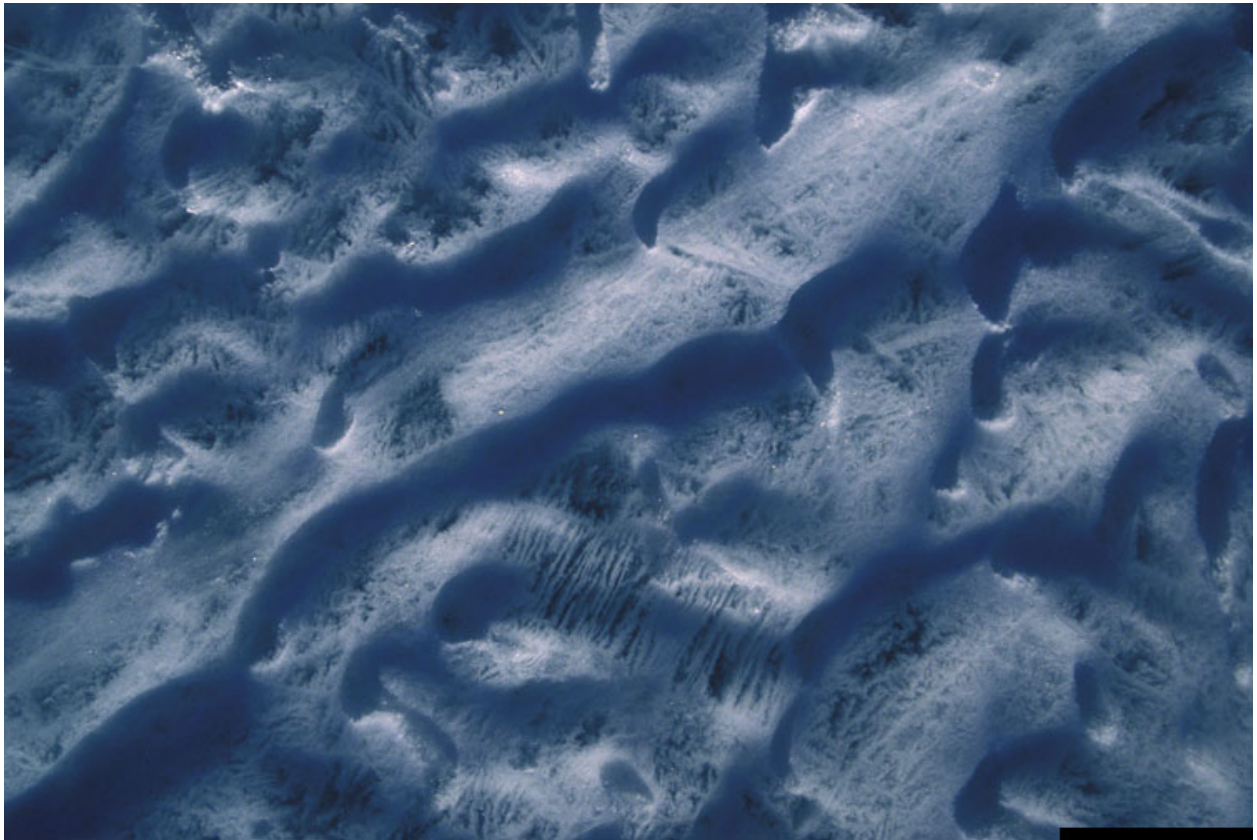


Figure 3.23. A hollow crust, such as the one pictured, can form near the surface of the ice, causing higher albedo. The black scale bar in the lower right represents 10 cm. Photo by Andy Bliss.

Station 3 did not measure shortwave radiation. To perform the energy budget calculations described below, we assumed 3's radiation was equal to Wx 4.

### 3.2.5 Longwave Radiation

Over the seasonal cycle, net longwave energy loss from the surface ranges from lows of  $\sim 50 \text{ W/m}^2$  in winter to highs approaching  $100 \text{ W/m}^2$  on clear days in summer. Outgoing longwave radiation is highly correlated with air temperature (as expected). Incoming longwave correlates with air temperature and cloudiness. Our stations were far from the margins of the glacier where the enhanced longwave radiation from the rock surfaces can significantly affect the ablation of ice [Lewis *et al.*, 1998].

Stations T, 3, and Be did not measure longwave radiation. To perform the energy budget calculations described below, we assumed Wx 3's radiation would be equal to Wx 4 because of their proximity. Similarly, Wx T was assigned Wx 1's data because they were close together. Wx Be did not have a neighbor with similar properties (e.g. in a valley, on a rock surface) so it was assigned the data from Wx Bo.

### 3.2.6 Air Pressure

We measured air pressure at stations 1, 2, and 4. The sensor at station 1 suffered from a drift relative to the other two sensors (figure 3.24). While there did not seem to be a strong correlation between times of low pressure (or falling pressure) and stormy periods, there were small-scale pressure effects. The pressure difference between Wx 2 and 4 explains much of the variance of wind speed at Wx 4, especially at wind speeds greater than  $10 \text{ m/s}$  (figure 3.25). The correlation is not as strong for Wx 2's wind speeds.

### 3.2.7 Snowfall

Snowfall on the ablation zone was inferred by comparing sonic distance sensor data at station T, AVHRR imagery showing storms, measured ice albedo during summer, and direct field observations. Storms that brought snow to the ablation zone occurred a few times per year. For the years 2003 to 2006 Fountain *et al.* [2009] found snow accumulation at station T of 6, 6, 13, and 14 cm. The snow was usually blown off the glacier within a few days, but sometimes remained for up to a month. A threshold wind speed of  $\sim 15 \text{ m/s}$  was required to blow the snow off the glacier, regardless of how long the snow had been there. When the snow blew away, the distance to the glacier surface was often greater than before the snowfall, indicating that the sublimation of ice continued even underneath the snowpack. Morse *et al.* [1999] found snow accumulation rates that varied from 1 to  $10 \text{ cm/yr}$  in the accumulation zone of Taylor Glacier, above our study area.



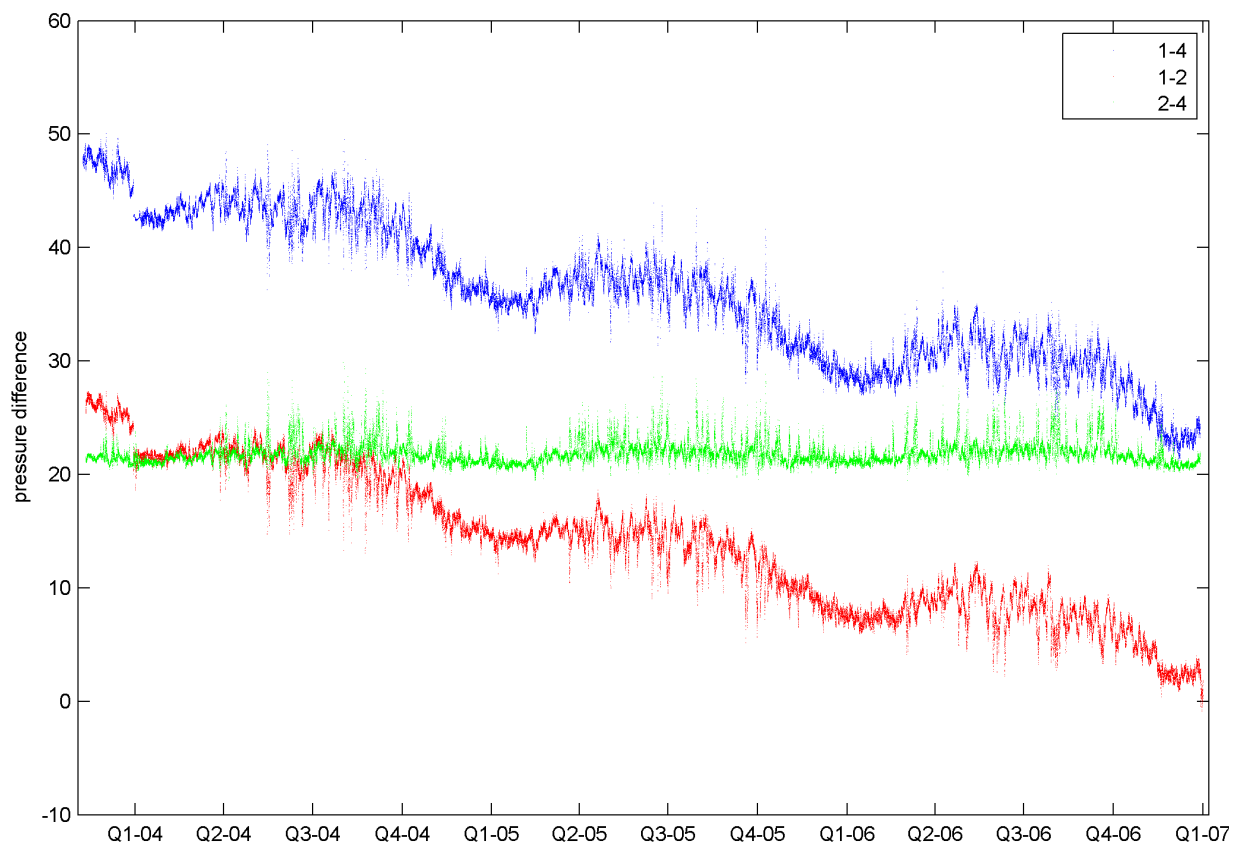


Figure 3.24. Pressure differences between stations. Station 1's pressure sensor drifted about 6.5 mbar/year compared to the other two stations. The jump in January 2004 was from station 1's move to a new location. Blue: Wx 1 - 4, red: Wx 1 - 2, green: Wx 2 - 4.

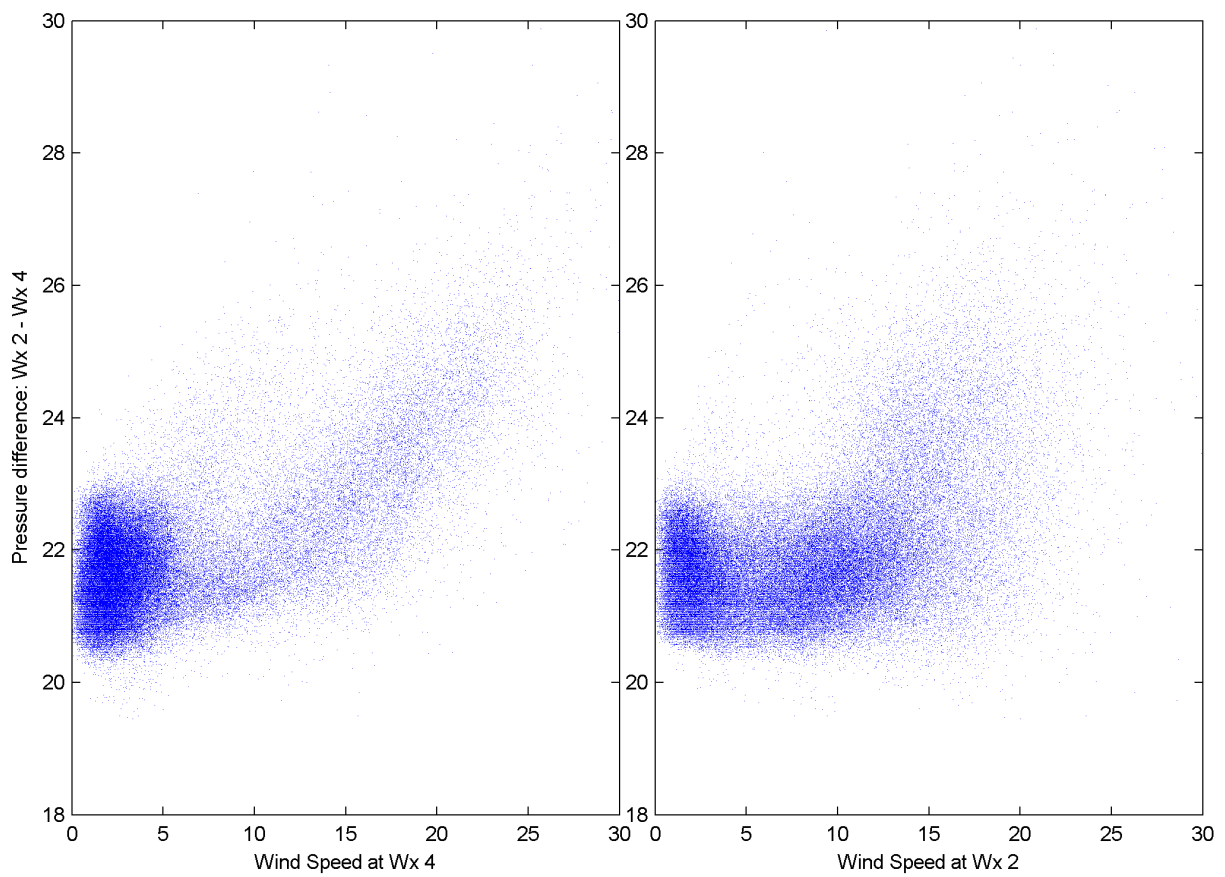


Figure 3.25. The air pressure difference between Wx 2 and 4 (mbar) affects the wind speed (m/s) at both stations.

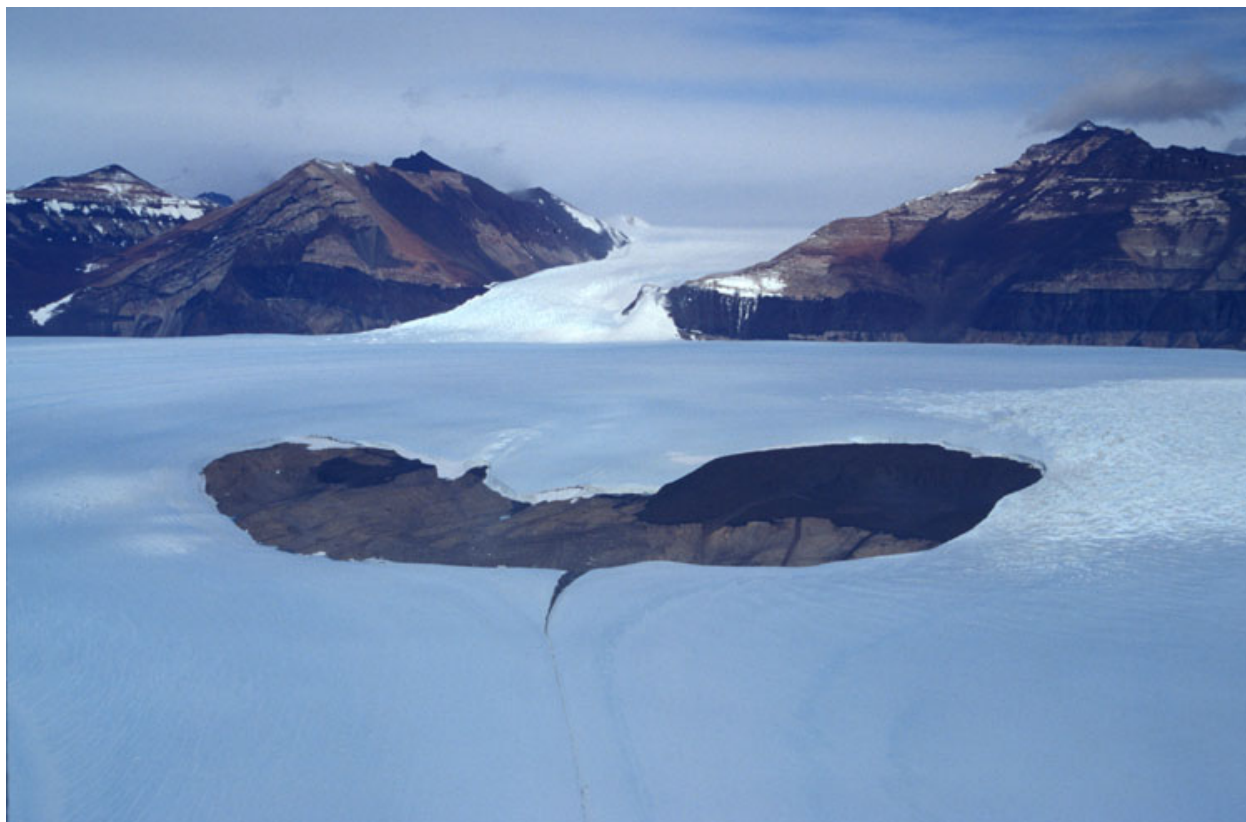


Figure 3.26. Windy Gully (upper center) is a steep tributary of Taylor Glacier. Cavendish Rocks is a nunatak in the middle of Taylor Glacier. Photo taken from a helicopter by Andy Bliss.

### 3.2.8 Effects of Windy Gully

In the winter, Wx 3 is often warmer and dryer than even Wx T, which is 500 m lower in elevation. These conditions are a consequence of strong katabatic winds moving through Windy Gully and onto the main glacier. An air parcel that quickly descends through Windy Gully, with a vertical drop of 750 meters in just 10 horizontal kilometers, warms at a rate close to the adiabatic rate. On the other hand, an air parcel that descends the same vertical distance on Taylor Glacier must cover a horizontal distance of 30 km (generally with a lower wind speed too) and therefore the parcel has time to cool diabatically. Similarly, the air at the base of Windy Gully is very dry, because it has not had time to gain much moisture via sublimation from the ice surface. Figure 3.26 illustrates the relative steepness of Windy Gully compared to Taylor Glacier.

### 3.2.9 Correlations between stations and Autocorrelations

Tables 3.17, 3.18, and 3.19 show correlations among stations for wind speed, temperature, and relative humidity. For all three variables, stations that were close together tended to be highly correlated. Wind speed correlations varied widely: from zero to 0.75. Wx 5 was often

Table 3.17. Wind Speed correlations between stations.

	Bo	T	1	2	3	4	5	6	Be
Bo	1	0.67	0.59	0.47	0.39	0.41	-0.03	0.44	0.43
T	...	1	0.65	0.51	0.43	0.4	0.14	0.38	0.48
1	...	...	1	0.75	0.6	0.62	0.12	0.64	0.54
2	...	...	...	1	0.74	0.57	0.23	0.59	0.45
3	...	...	...	...	1	0.53	0.28	0.52	0.43
4	...	...	...	...	...	1	0.05	0.82	0.55
5	...	...	...	...	...	...	1	0.07	0.16
6	...	...	...	...	...	...	...	1	0.5
Be	...	...	...	...	...	...	...	...	1

Table 3.18. Temperature correlations between stations.

	Bo	T	1	2	3	4	5	6	Be
Bo	1	0.96	0.93	0.9	0.87	0.91	0.89	0.86	0.91
T	...	1	0.96	0.94	0.91	0.93	0.92	0.9	0.94
1	...	...	1	0.97	0.95	0.96	0.94	0.93	0.94
2	...	...	...	1	0.98	0.96	0.96	0.96	0.95
3	...	...	...	...	1	0.96	0.96	0.94	0.94
4	...	...	...	...	...	1	0.96	0.93	0.96
5	...	...	...	...	...	...	1	0.96	0.96
6	...	...	...	...	...	...	...	1	0.93
Be	...	...	...	...	...	...	...	...	1

in a world by itself, but was most highly correlated with Wx 3 at the base of Windy Gully – they both responded strongly to some katabatic/foehn events. Stations 3, 2, and 1 were relatively highly correlated, which made sense because they were roughly downwind from one another. Temperature correlations were usually above 0.9 regardless of which stations were being compared, but the correlations did get stronger as distance between stations decreased. Relative humidity correlations also varied widely: from zero to 0.81. Stations on the glacier tended to be better correlated with each other than with stations on rock (Bo, 6, Be).

The autocorrelation of wind speed, temperature and relative humidity proved interesting (figure 3.27). The temperature autocorrelation for the entire year was stronger than for summer or winter because the temperature variance over the whole year was larger than the variance within a season. The variance of wind speed and relative humidity was relatively constant regardless of interval, so this effect was not seen in that data. The autocorrelation plot of air temperature shows that about 90% of the variability of the present temperature can be explained by the previous day's temperature. The stations' autocorrelation depended on the daily range of temperature. For instance, the mean daily range of temperature during summer at Wx 5 was 7.3°C, yielding a pronounced trough in the autocorrelation plot at a

Table 3.19. Relative Humidity correlations between stations.

	Bo	T	1	2	3	4	5	6	Be
Bo	1	0.69	0.36	0.17	0.22	0.32	0.17	0.02	0.47
T	...	1	0.67	0.42	0.37	0.44	0.31	0.22	0.42
1	...	...	1	0.71	0.6	0.6	0.48	0.46	0.37
2	...	...	...	1	0.81	0.67	0.58	0.65	0.43
3	...	...	...	...	1	0.75	0.64	0.63	0.55
4	...	...	...	...	...	1	0.71	0.56	0.66
5	...	...	...	...	...	...	1	0.67	0.59
6	...	...	...	...	...	...	...	1	0.47
Be	...	...	...	...	...	...	...	...	1

lag of half a day before a peak at a lag of one day. Station 6's mean summer daily range was only 3.6°C and it lacked a trough in autocorrelation.

The autocorrelation of wind speed also shows interesting differences among stations. Wx 5 has a consistently lower autocorrelation than the other stations. Possible reasons for this include: (1) broader, flatter topography led to less topographic channeling of winds, (2) different wind regimes affect Wx 5: Windy Gully/Beacon Valley katabatic/storms, Taylor katabatic, valley wind coming out of Pearse Valley. Wx 1's autocorrelation plot for summer has a plateau at lags of 45-70 at a correlation of about 0.4. Wx 3's speed data has a significantly poorer short term memory than the stations in its geographical area because its measurement interval was slightly different.

### 3.3 Derived Parameters

Some of the calculations discussed below required values for parameters not directly measured, including surface temperatures, surface vapor pressures, and roughness lengths. The following sections describe how we derived these parameters.

#### 3.3.1 Surface Temperature

In our standard sublimation model, surface temperature values ( $T_s$ ) were adjusted to achieve a zero net energy budget (figure 3.28). The estimated surface temperatures were on average 1.5°C colder than the air temperature in summer and 4.2°C colder in winter at Wx 1. The persistently low temperatures of the glacier surface were maintained by the net loss of energy by longwave radiation. We also calculated another estimate of  $T_s$  by developing a parameterization in terms of measured  $T_{air}$  and net radiation.

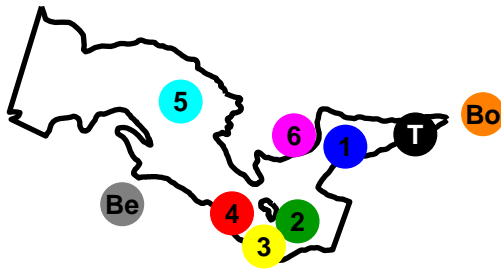
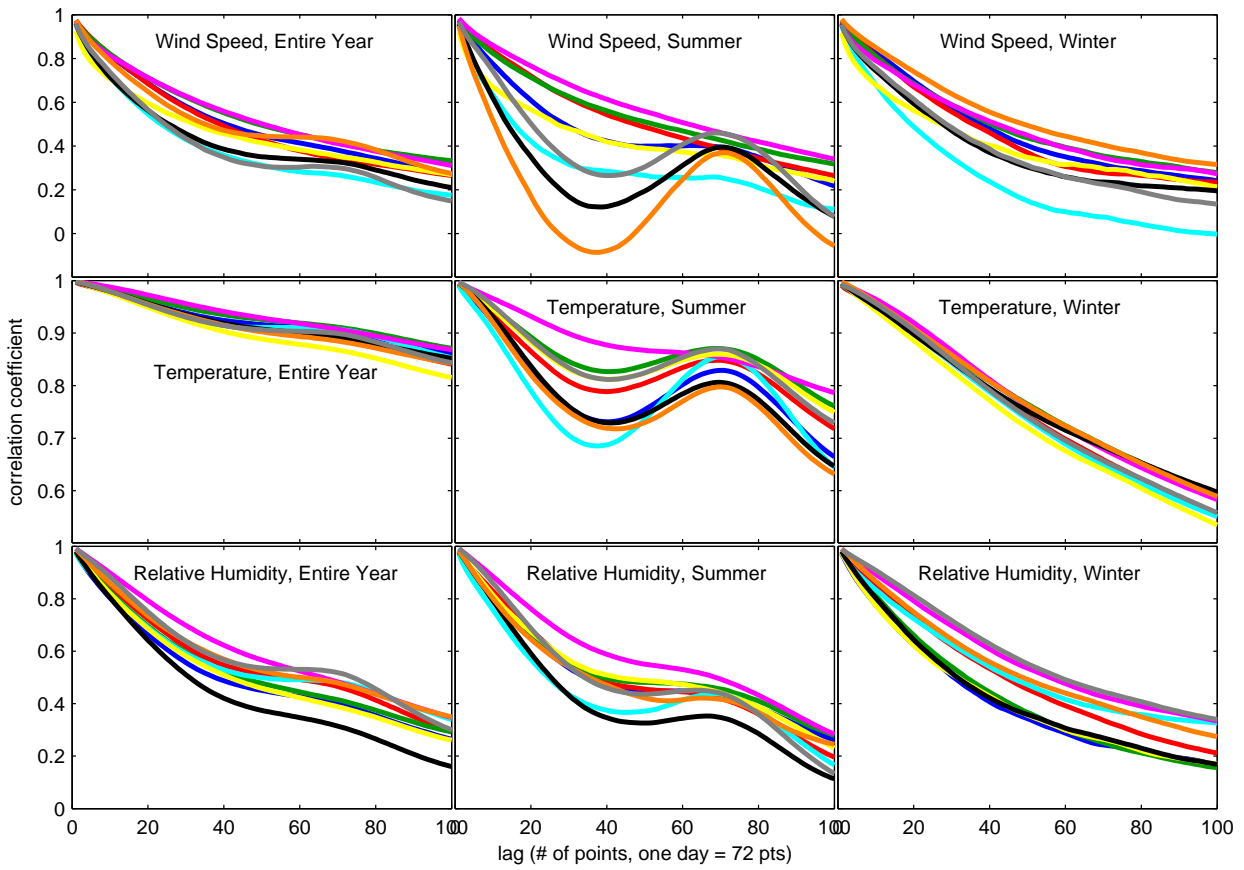


Figure 3.27. Autocorrelations of wind speed, temperature, and relative humidity for the whole year, summer, and winter.

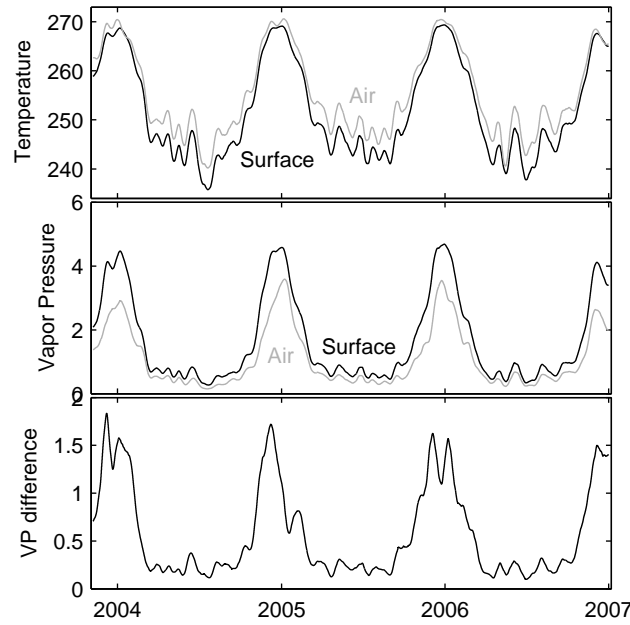


Figure 3.28. The measured air temperature (K) is usually higher than the modeled surface temperature (adjusted to make the energy budget go to zero). The measured vapor pressure (mbar) at screen height is usually lower than the surface vapor pressure calculated from the surface temperature assuming saturation. The vapor pressure difference (mbar) is much larger in summer than winter. All data from Wx 1. Data were smoothed with a 30-day triangular filter.

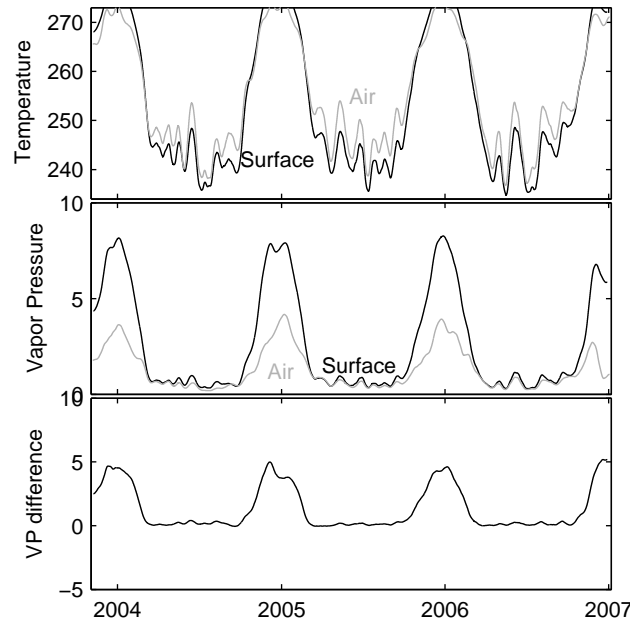


Figure 3.29. Derived variables timeseries – Wx Bo.

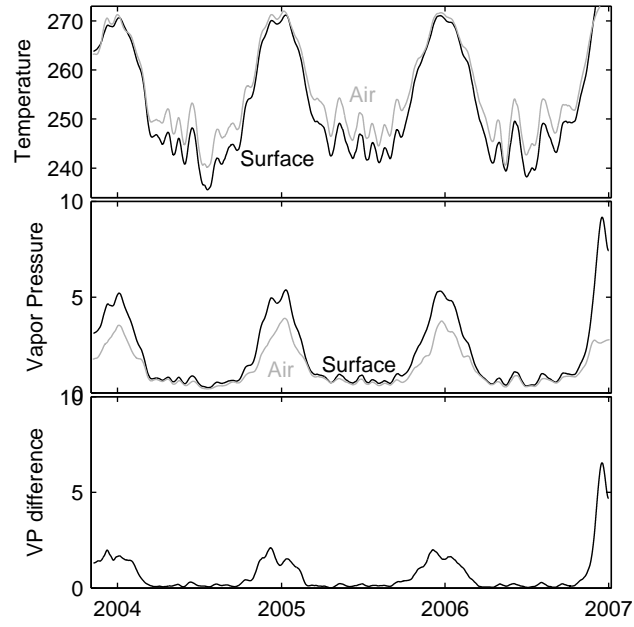


Figure 3.30. Derived variables timeseries – Wx T.

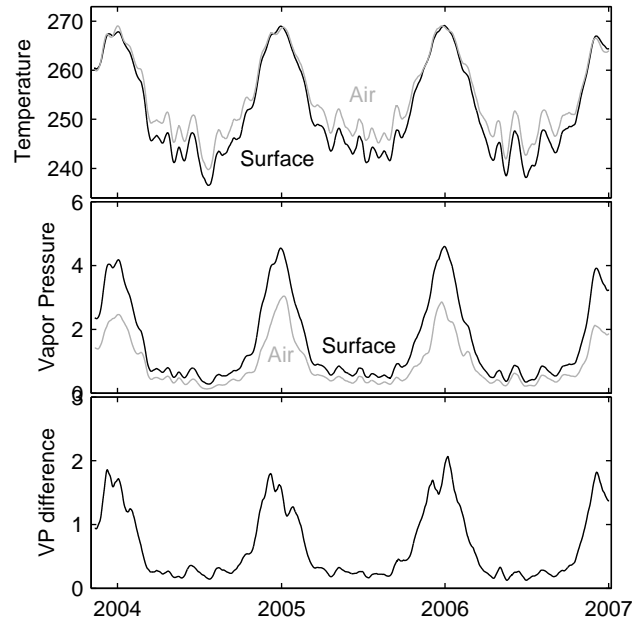


Figure 3.31. Derived variables timeseries – Wx 2.



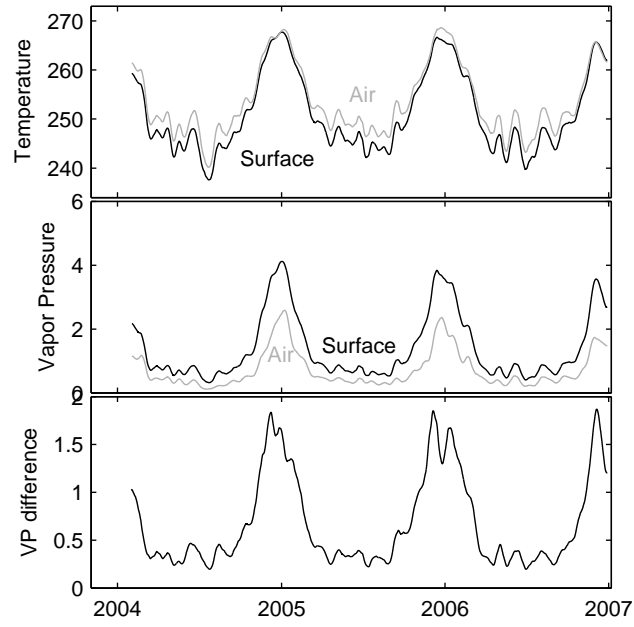


Figure 3.32. Derived variables timeseries – Wx 3.

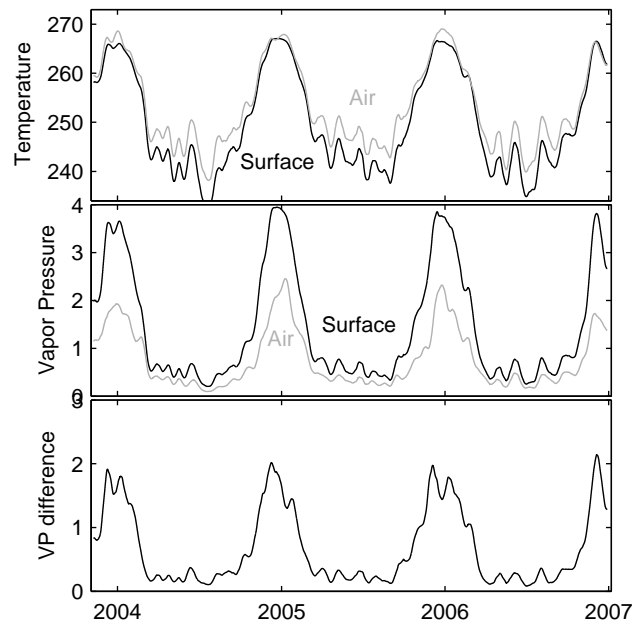


Figure 3.33. Derived variables timeseries – Wx 4.

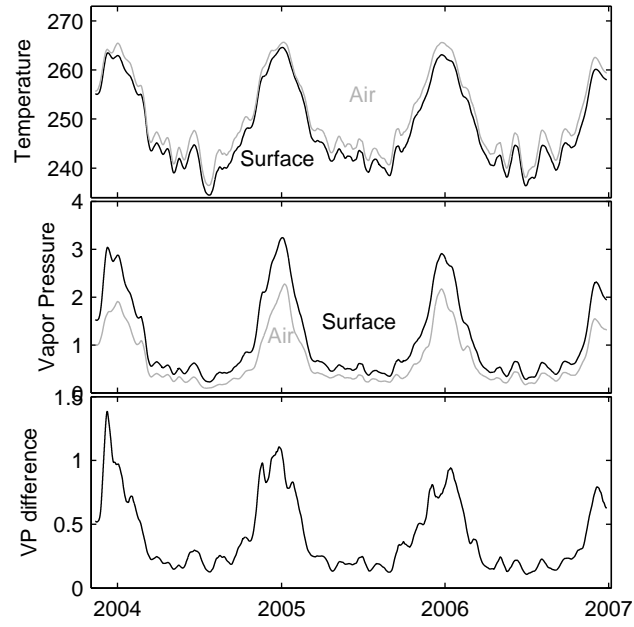


Figure 3.34. Derived variables timeseries – Wx 5.

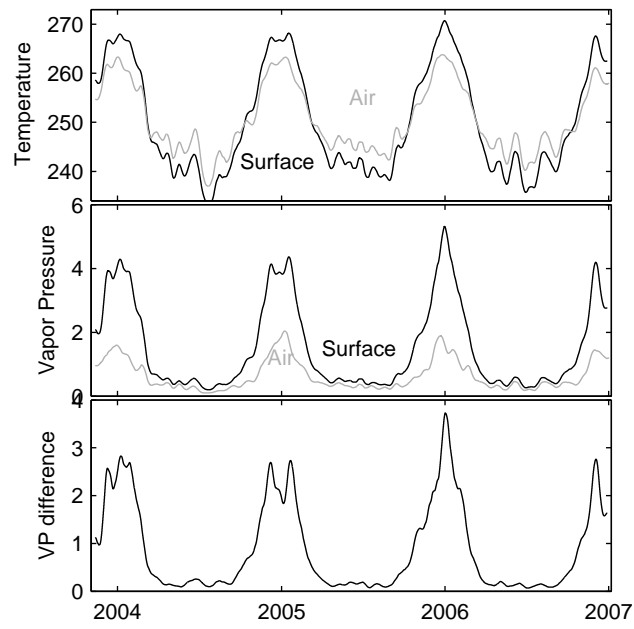


Figure 3.35. Derived variables timeseries – Wx 6.

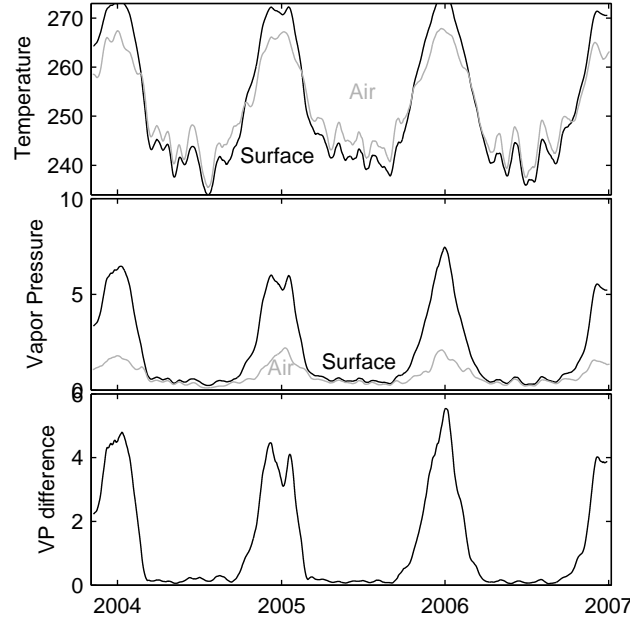


Figure 3.36. Derived variables timeseries – Wx Be.

### $T_s$ Parameterized with $T_{air}$ and $R$

At the three stations where longwave radiation was measured directly, the radiative ice surface temperature  $T_{rad}$  was calculated from the upwelling longwave radiation  $LW$  using the Stefan-Boltzman equation assuming an emissivity  $\epsilon$  of 1.

$$T_{rad} = (LW/(\epsilon\sigma))^{1/4} \quad (3.3)$$

To estimate surface temperature  $T_s$  at other stations, we developed a parameterization with a lagged version of air temperature  $T_{air}$  and measured net radiation  $R$ .

$$T_s = a < T_{air} > + bR + c(< T_{air} > - R) + d \quad (3.4)$$

$< x >$  denotes a lagged version of  $x$ . The parameters  $a$ ,  $b$ ,  $c$ , and  $d$  were chosen via regression to minimize  $\Sigma|T_{rad} - T_s|$  for stations 1, 2, and 4. The lagged air temperature record was created by applying a triangular filter to the air temperature data. The filter weighted the most recent data most heavily and past data was weighted less and less with age. The filter width (4 hours) was chosen to maximize the correlation between the radiative surface temperature and the parameterized surface temperature. After computing  $T_s$  in this way, we noticed that the result had a bias depending on the temperature. So, to adjust the fit we added an offset variable that calculated the mean residual in  $1^\circ\text{C}$  bins and then subtracted the residual from the model.

We did a few ad hoc tests of different parameterizations for surface temperature, ultimately choosing the one that best fit the radiative temperature (described above) and made sense physically for the sublimation. Parameterizations we tried were: radiative temperature

from other stations; radiative temperature with an offset of a few degrees; air temperature with an offset; *Peck* [1996]; lagged air temperature; lagged air temperature and shortwave radiation; and a parametric fit with lagged air temperature and net radiation. The other parameterizations gave results similar to the one we chose, but with slightly different slopes and intercepts for a regression of measured versus modeled ablation rates (e.g. figure 4.1).

### **$T_s$ Adjusted for Energy Balance**

For the “standard” sublimation model, we adjusted the surface temperature until the net energy flux to the glacier surface was zero. The energy budget terms affected by this adjustment were the latent, sensible, and subsurface heat fluxes. For example, if the initial net energy budget was positive, we increased the surface temperature. This led to a reduced sensible heat flux to the glacier, an increased latent heat loss from the glacier, and either an increased loss of heat to the subsurface or a reduced gain of heat from the subsurface. The subsurface term was usually the smallest of these terms and had the smallest change upon correction.

The adjustment procedure involved a number of steps:

1. Initialize the runs with a surface temperature parameterized from the air temperature and net radiation (described in the previous section). Also, use a rough estimate of ablation rates to adjust the instrument heights over the period of interest.
2. Run the code once through, calculating the sensible and latent heat fluxes based on the approximate surface temperature and assumed instrument heights. Also calculate the net energy budget  $E$ , as described in equation 5.1.
3. Calculate a new surface temperature  $T_s$  that reduces the net energy budget. First, create a smoothed version of the net energy budget  $\langle E \rangle$ , as calculated from the previous iteration. If we did not smooth  $E$ , the equation would give unrealistic surface temperatures. Second, use the Stefan-Boltzman equation to calculate the longwave radiation that would be expected from ice (with an emissivity of 1) with the “old” surface temperature  $T_{sOld}$ . Third, add the net energy budget number to the longwave number. Fourth, run that sum through equation 3.4 to get a new surface temperature  $T_{sEB}$ . In compact form:

$$T_{sEB} = \left( \frac{\langle E \rangle + \sigma T_{sOld}^4}{\sigma} \right)^{1/4}. \quad (3.5)$$

4.  $T_{sEB}$  also yielded some unrealistic values, so we chose to allow the surface temperature to converge slowly to the final value, as follows.

$$T_s = (1 - c) T_{sOld} + c T_{sEB} \quad (3.6)$$

where  $c$  is a constant equal to 0.2.

5. Recalculate the sensible and latent heat fluxes with the new surface temperature and use the previous iteration's ablation to make a surface height adjustment.
6. Repeat until the last three items until the solution has converged.

Three iterations was enough to allow all the terms to adjust to the new surface temperature. The difference between the second and third iterations averaged only 1.8% of the total calculated sublimation. Since the computer time for each iteration was significant, we ran just one experiment to the 6th iteration, to make sure it was reasonable to stop after the 3rd. The difference between the 3rd and 6th was 1.06%, and the difference between the 5th and 6th was just 0.3%. Future work may investigate different procedures for making this surface temperature correction.

### 3.3.2 Vapor Pressure

Vapor pressure at the surface was assumed to equal the saturation value at the estimated surface temperature (see *Box and Steffen* [2001] for a discussion of errors). Because vapor pressure depends strongly on temperature, the vapor pressure difference between the air and the surface peaks during the warm summer months with values around 1.5 mbar. Winter values were 5 to 10 times smaller.

### 3.3.3 Subsurface Temperature

The temperature structure of the subsurface was calculated with a finite-difference model of temperature diffusion. Points in the finite-difference grid were spaced closer together near the surface (18 in the first meter) than at depth (2-m spacing at 50 m depth). The surface boundary condition was the surface temperature appropriate for the sublimation model being considered, as described previously. The model also included ablation from the surface, appropriate for the station location. The basal boundary condition was set according to the temperature profile from a force-balance model of the glacier [*Kavanaugh and Cuffey*, 2009]. The heat flux and storage terms close to the ice surface were not sensitive to the basal boundary condition because the magnitude of the basal heat flux was small compared to the surface fluxes. Initial model temperatures were also from *Kavanaugh and Cuffey* [2009]. Before starting the main run, we ran the first day of the model once through so the surface heat fluxes could adjust, and then initialized the main run with the result of the first day.

The calculated temperature structure within the ice is shown in figure 3.37. The amplitude of the seasonal cycle of temperature decreases with increasing depth. The phase lag behind the surface temperature also increases with depth. Selected temperature profiles are shown in figure 3.38. The initialization left a signature on the first few weeks of data, so those temperatures should be discounted.

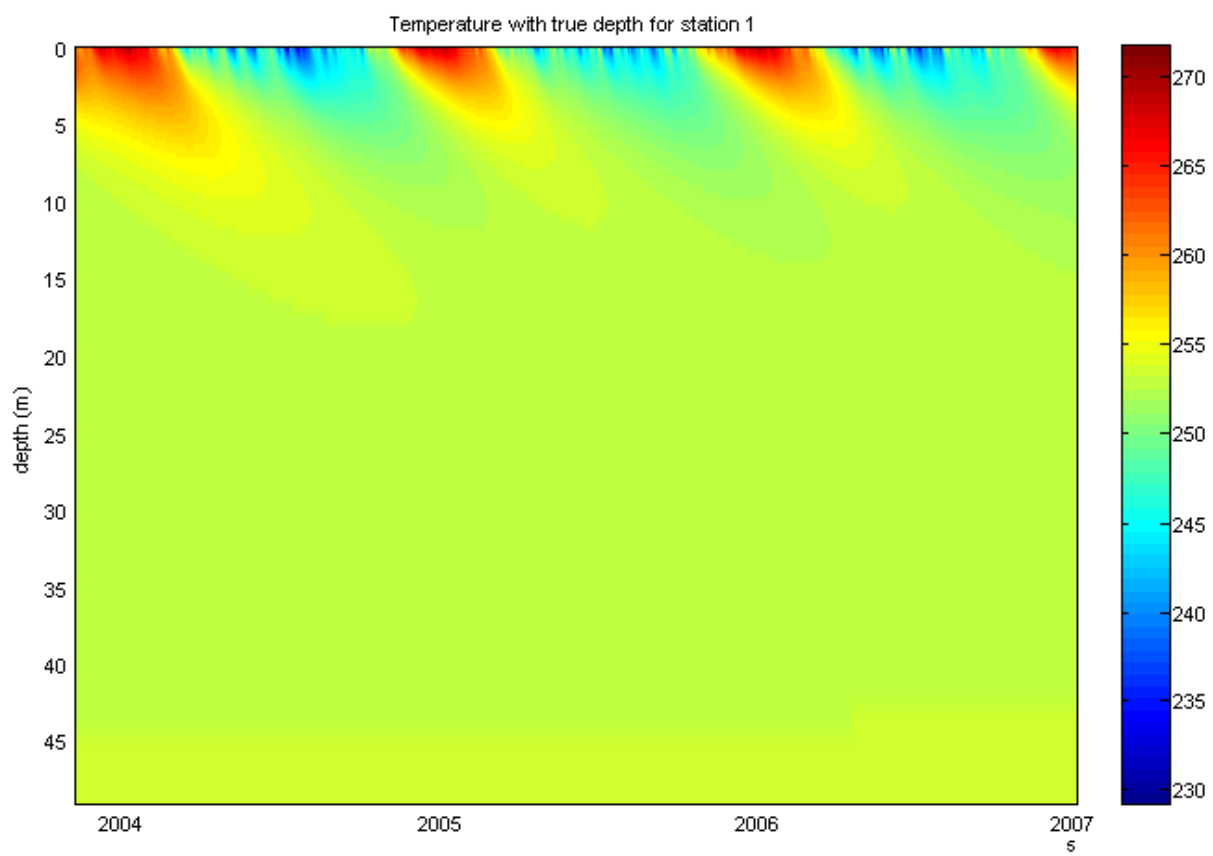


Figure 3.37. Temperature with depth for Wx 1. Scale: Kelvin.

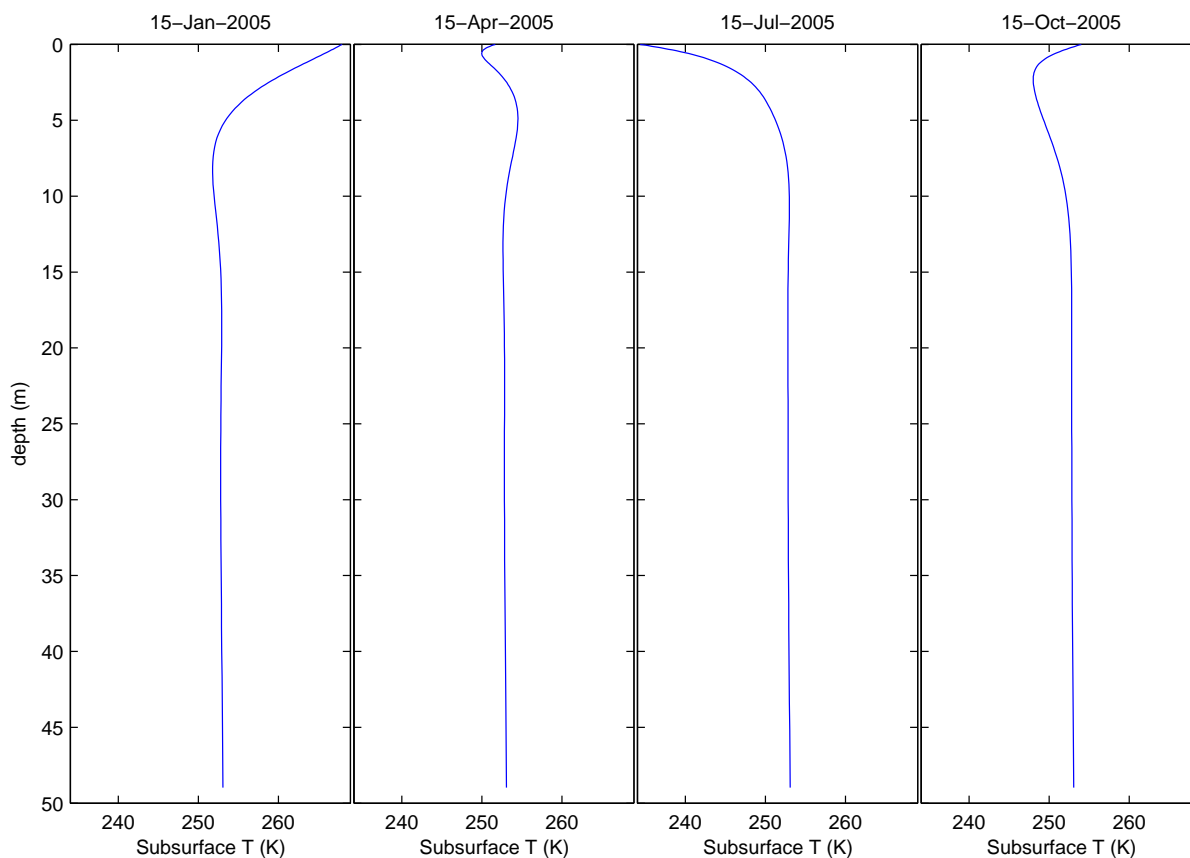


Figure 3.38. Subsurface temperature profiles for Wx 1. In summer (far left panel) the surface temperature was warmer than the rest of the ice. By fall (left), the surface temperature was close to the mean annual surface temperature (colder than the mean annual air temperature). A warm layer of ice, a vestige of the previous summer's heat remained in the subsurface with a temperature peak at about 5 m depth. In winter (right panel), the surface temperature was about 15 K colder than the temperature at depth, and the previous summer's warmth had been wiped out. When spring rolled around (far right), the surface temperature had increased back to the mean and a layer of cold ice remained below.

### 3.3.4 Roughness Lengths

Three of our stations included wind sensors at two heights, which allowed calculation of the surface roughness ( $Z_o$ ) from the Law of the Wall. Roughness can also be estimated from the surface microtopography. In the end, we used a constant value for  $Z_o$  in our sublimation model. The discussion here helps to justify our choice of 0.005 meter.

#### Law of the Wall

The Law of The Wall predicts how velocity of a fluid will vary in a boundary layer near a surface. Given a ground surface roughness and a wind speed at some height above the ground, the theory gives an estimate of the wind speed at other heights. Alternatively, if wind speed is known at two heights, the roughness can be calculated.

$$Z_o = \exp \left( \frac{u_1 \ln(H_2) - u_2 \ln(H_1)}{u_1 - u_2} \right) \quad (3.7)$$

where  $u_x$  is the wind velocity at height  $H_x$ . We have done this calculation for the three stations where we have wind sensors at two heights ( $H_1$  and  $H_2$ ). Since the ice surface was continually ablating, the instrument heights increased over time. We adjusted the instrument height timeseries according to the modeled sublimation (as described in chapter 4). The roughness calculation was quite sensitive to the measurement height. We did not get good height measurements for Wx 1 after Jeff Kavanaugh moved it, and that is evident in figure 3.39. Gaps in the data were filled with the median value over the period of record. The results are shown in table 3.20 and figures 3.39, 3.40, and 3.41). The calculation produced values with a range larger than expected, so we also plotted  $Z_o$  for times when the top wind speed was faster than 10 m/s. This resulted in a more reasonable range of  $Z_o$ , as shown in figure 3.42.

The calculated roughness was lower (smoother surface) in the summer. This goes against the intuition that the surface should be smoother in winter when ablation rates are slower and there is no solar radiation to aid the formation of ablation hollows. Whether the summer-time smoothness was a robust result is an open question. Our estimation of the instrument heights could bias the result if modeled summertime ablation rates were wrong. However, similarities in the peaks and valleys of the smoothed data at stations 2 and 4 would indicate that the signal is far from random. Again, whether these peaks and valleys represented true variability in surface roughness, or if they were a function of atmospheric stability is an open question.

#### Microtopography

Roughness can also be estimated from surface microtopography. We made two types of topographic measurements: ablation cup depths and surface sinuosity. Ablation cup depths are straightforward: the difference in height between the tops and bottoms of the cups. As an exercise, consider that air flowing over a rough ice surface could be similar to water flowing



Table 3.20. Mean and median roughness calculated from the Law of the Wall. The  $\%>0.03$  column refers to the figures below, where I cut off a portion of the data to show the result more effectively.

Station	Mean (m)	Median (m)	$\%>0.03$
Wx 1	0.00342	0.00074	9.3
Wx 2	0.00939	0.00381	14.6
Wx 4	0.00763	0.00500	9.6

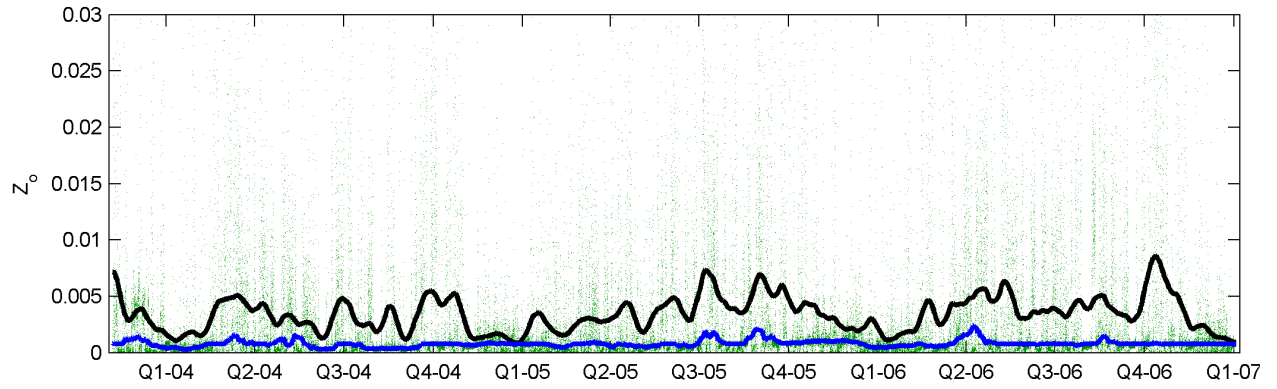


Figure 3.39.  $Z_o$  timeseries for Wx 1. The green dots plot unsmoothed data. The black line shows data smoothed with a triangular filter with a width of 30 days. The blue line shows a running median, again with 30 days of data.

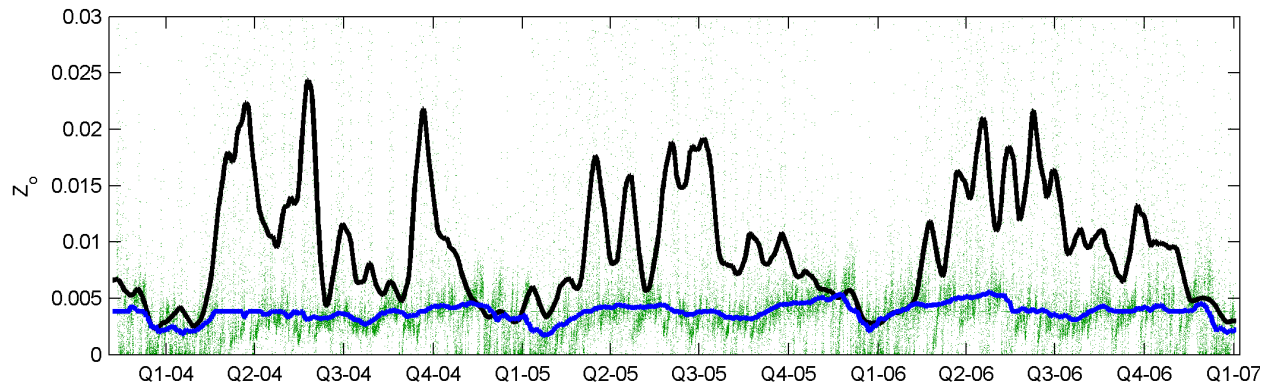


Figure 3.40.  $Z_o$  timeseries for Wx 2.

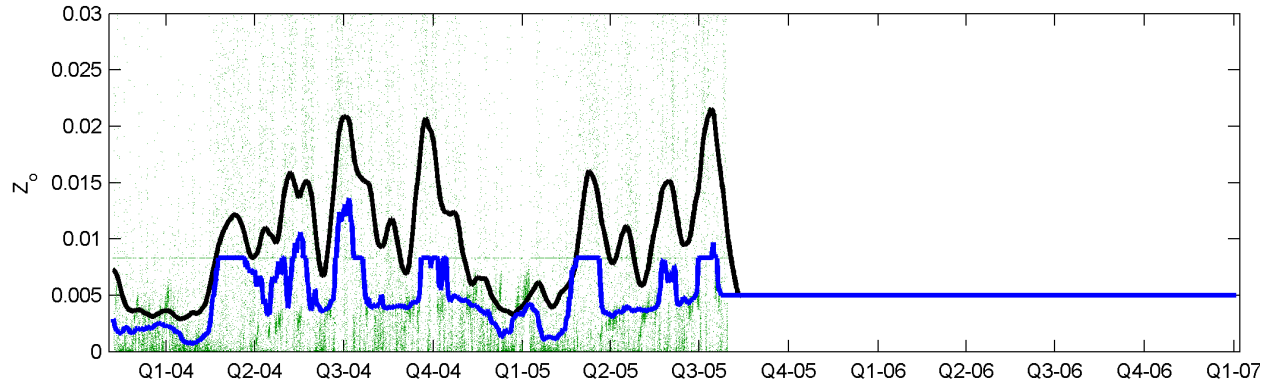


Figure 3.41.  $Z_o$  timeseries for Wx 4.

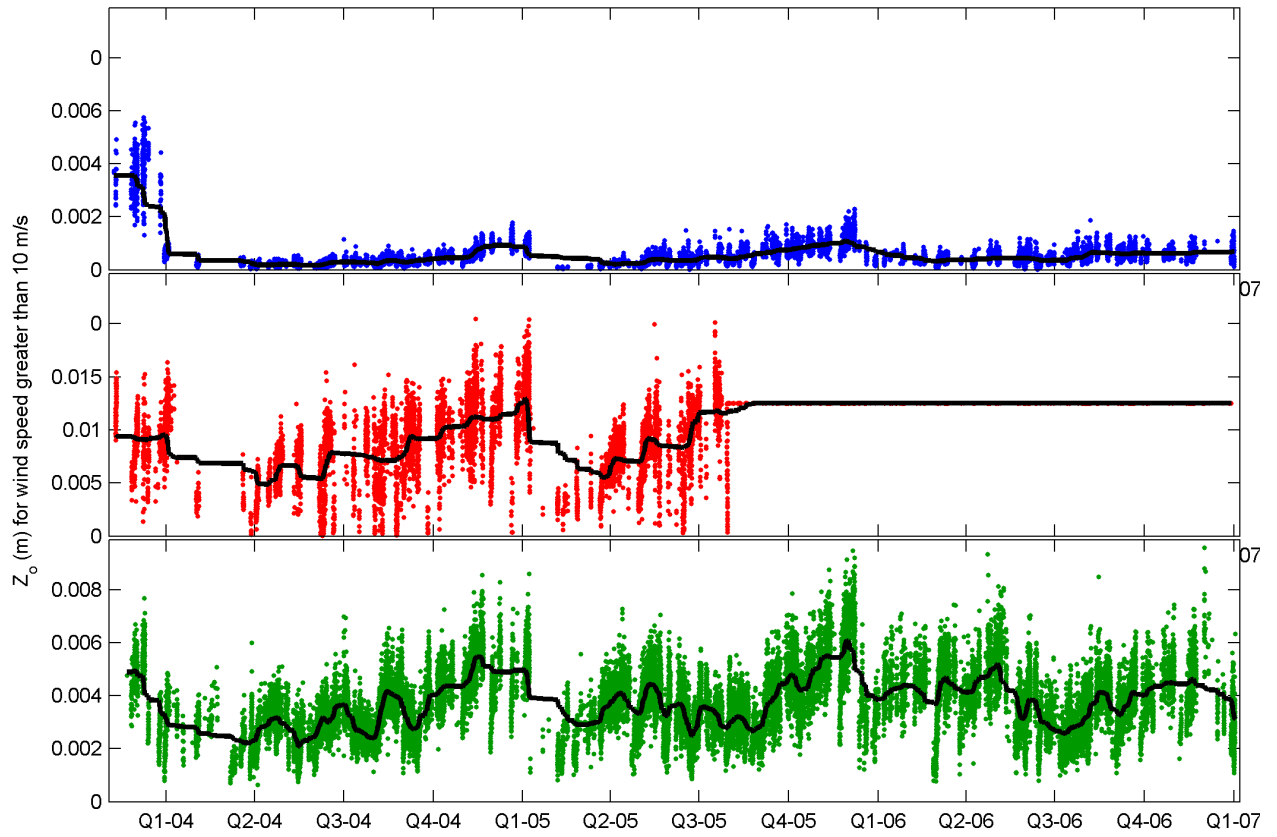


Figure 3.42.  $Z_o$  timeseries for times with the upper wind speed  $>10$  m/s. The  $Z_o$  calculation was better behaved when considering fast wind speeds. The black lines are the same data smoothed with a 5-day triangular filter (with gaps removed). Blue: Wx 1, red: Wx 4, green: Wx 2.

over a rough stream bed (both are turbulent flows). The fluvial geomorphology literature calculates a roughness length for the flow of water over the bed:  $Z_o = D_{84}/10$  where  $D_{84}$  is the 84th percentile of pebble sizes in the stream bed. Field observations indicate that the ablation cups' size and depth are very regular over spatial scales up to kilometers (i.e. "pebble" sizes are fairly homogeneous and the median ablation cup size would also be very similar to the 84th percentile. Hence, an ablation cup depth of 5 cm (common on Taylor Glacier) would translate into a roughness length of 5 mm, in line with roughness estimates for ablating ice surfaces [Cuffey and Paterson, 2010, p. 155].

Another measure of microtopography we made was surface sinuosity. This measurement was made at the end of the summer in 2004 (interval **L**). Surface sinuosity between point A on the ice surface and point B was defined as the distance hugging the rough surface divided by the straight-line distance between A and B. The distance hugging the surface was measured by laying a piece of string across the bumps in the ice next to or below a meter stick. Rough surfaces have high sinuosity and flat surfaces have a sinuosity of 1. We found that the sinuosity followed a pattern similar to the ablation rates: from the upper end of our survey, it increased to a maximum at the base of Windy Gully and then gently declined towards the terminus.

Since there was such an interesting correlation between sinuosity and ablation rates, we created a model ice surface from a repeating parabolic form (figure 3.44) to perform further calculations. The "parabolic egg carton" surface had realistic characteristics: a horizontal length scale of 20 cm and a variable vertical height (in the example shown the peak-to-trough height was 4 cm). Vertical cross sections through the surface (figure 3.45) illustrate the roughness, and allow calculation of sinuosity. By generating surfaces with a variety of amplitudes, and then taking 100 random profiles from each surface, we found a relation between surface amplitude and sinuosity (figure 3.46) that indicates the lowest sinuosities found in the ablation zone of Taylor Glacier (1.02) correspond to surface irregularity heights of 2.8 cm; the high sinuosities (1.08) found near Windy Gully and the ablation maximum correspond to heights of 5.4 cm. Because of the high regularity of the model surface (and the real ice surface), these heights would approximate the  $D_{84}$  and translate into  $Z_o$  of 2.8 mm or 5.4 mm, well within the range found by the other methods described above.

## Humidity and Temperature Roughness Lengths

When needed, roughness lengths for humidity  $Z_q$  and temperature  $Z_T$  were calculated from surface roughness using an empirical relationship [following e.g. Brock and Arnold, 2000].

$$\ln \left( \frac{Z_T}{Z_o} \right) = 0.317 - 0.565 R_* - 0.183 R_*^2 \quad (3.8)$$

$$\ln \left( \frac{Z_q}{Z_o} \right) = 0.396 - 0.512 R_* - 0.180 R_*^2 \quad (3.9)$$

$$R_* = \frac{u_* Z_o}{\nu} \quad (3.10)$$

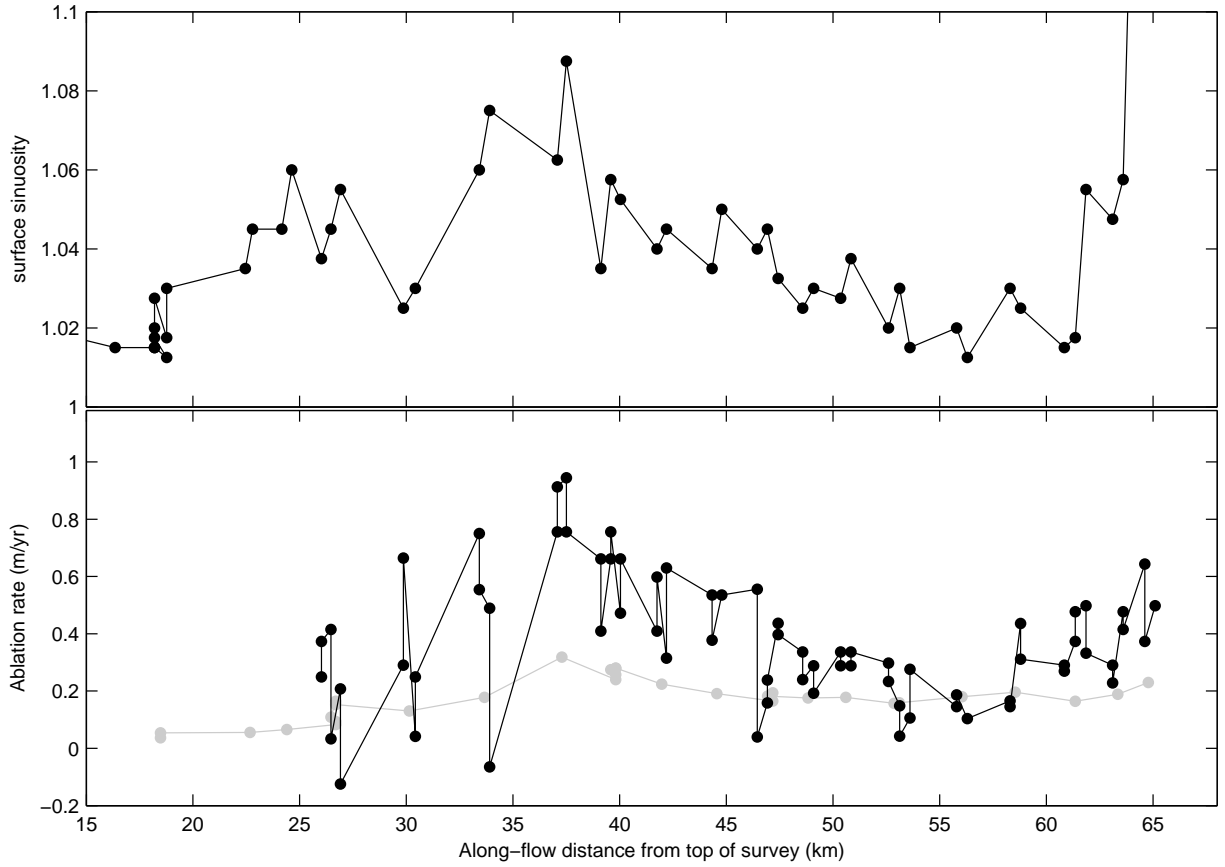


Figure 3.43. Surface sinuosity (top) and ablation rates (bottom with **4:L** in black and **4:7** in gray). The sinuosity measurement closest to the terminus (distance of 64 km) was 1.26. Sinuosity generally increases and decreases in a manner similar to ablation rates.

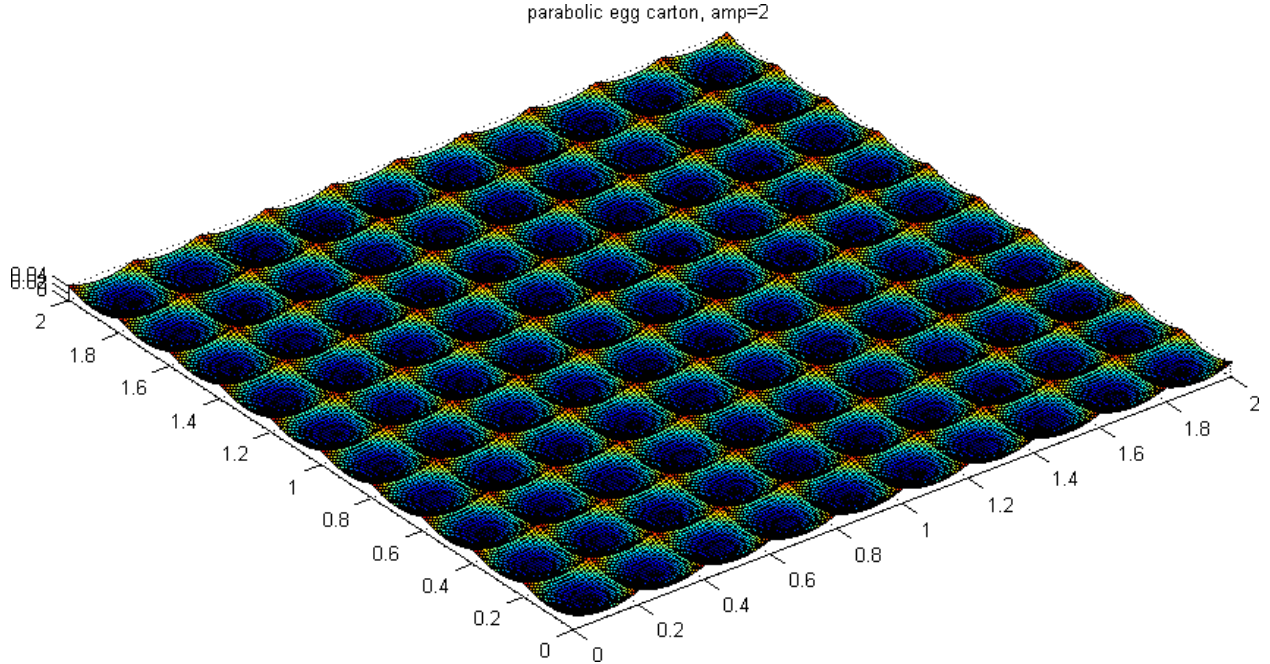


Figure 3.44. A perspective view of the 4 cm parabolic egg carton. No vertical exaggeration, units are meters, colors are height.

where  $R_*$  is the Reynolds number,  $\nu$  is the kinematic viscosity of air ( $1.461 \times 10^{-5} \text{ m}^2/\text{s}$ ), and  $u_*$  is the friction velocity.

See *Smeets and van den Broeke* [2008] for a discussion of roughness lengths in the ablation zone of the Greenland Ice Sheet.

### 3.3.5 Lapse Rates

We calculated lapse rates across the entire ablation zone by making a linear fit to the temperatures from our stations at different elevations. This is not a true “Environmental Lapse Rate” – the temperature in the atmosphere above a point on the surface – but it is nevertheless interesting. We are essentially assuming that the isotherms within the atmosphere are horizontal. The median lapse rate was  $6.4^\circ\text{C}/\text{km}$  for the period of record but varied significantly with the season, from about  $4^\circ\text{C}/\text{km}$  in winter to  $7.5^\circ\text{C}/\text{km}$  in summer (figures 3.47 and 3.48). In winter, small lapse rates prevailed when wind speeds were less than about 7 m/s (figure 3.49), often corresponding to times with an inversion at the low-elevation stations close to Taylor Valley (see section 3.3.6). With faster winds, adiabatic warming of air descending the glacier increased the lapse rate into the range  $5\text{--}10^\circ\text{C}/\text{km}$ .

Our values for lapse rate compare well to previous work, even though their methods were different. *Robinson* [1984] estimated a lapse rate of  $4^\circ\text{C}/\text{km}$  by measuring temperature in shallow boreholes at different elevations. This made use of the fact that temperature beneath the surface does not change as fast as it does in the air. Thus, he could measure temperature at one location, travel to another location and make a second measurement that would reflect the actual difference in temperature between the two locations, rather than the

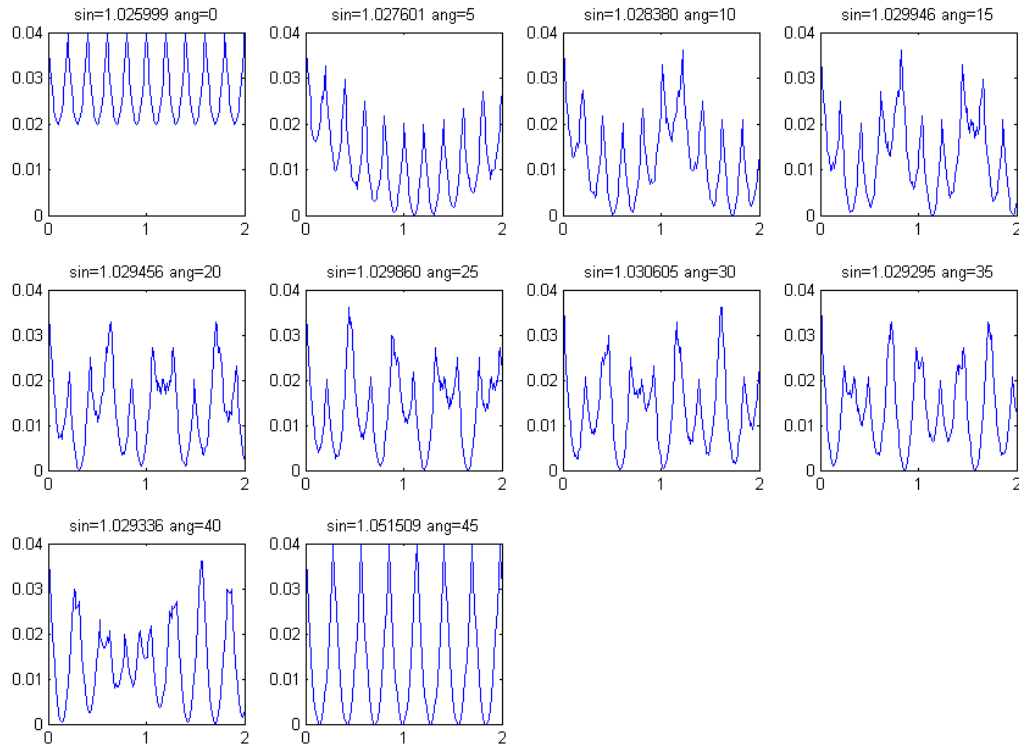


Figure 3.45. Profiles from the 4 cm parabolic egg carton have sinuosities close to 1.03. Exaggerated vertical scale, units are meters. Subplot titles indicate the sinuosity for that profile, as well as the angle from which the profile was taken (0 was an edge of the domain).

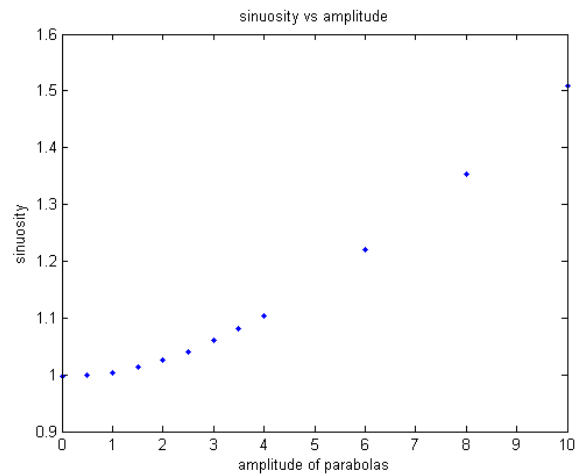


Figure 3.46. Sinuosity versus surface height amplitude. By varying the vertical scale of the parabolic egg carton, and then taking 100 random profiles, and averaging their sinuosities, we arrive at a relationship between sinuosity and amplitude.

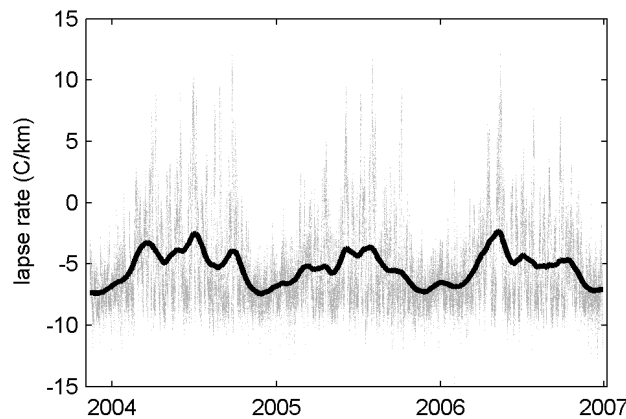


Figure 3.47. Lapse rate with time. The gray dots are all the data, calculated from our 6 stations. The black line is the same data smoothed with a triangular filter with a width of 60 days.

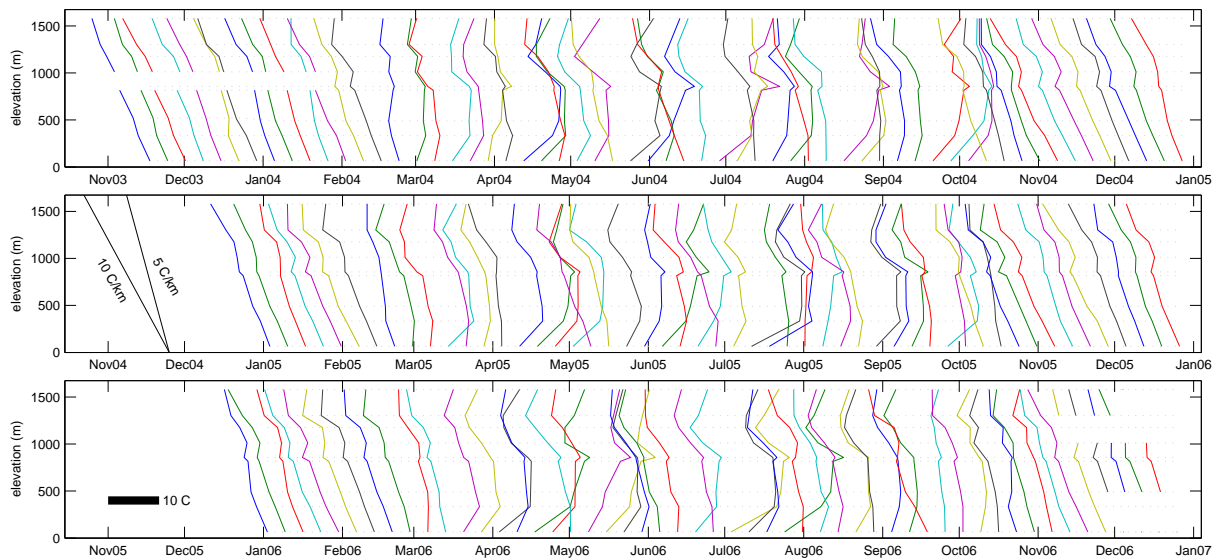


Figure 3.48. Weekly-mean temperatures at each station, plotted against station elevation (y-axis) and time (x-axis). For each week, the temperature of the lowest-elevation station (Wx Bo) was plotted on the x-axis based on the date. Higher-elevation stations tended to be colder and thus plot above and left of the lowest station. During inversions, the higher-elevation stations were warmer and thus plotted above and right from Wx Bo. The legend on the left side of the middle panel shows the dry and saturated adiabatic lapse rates, for scale. The temperature drop with elevation was usually close to linear in summer. Inversions were common in the winter months, March-September, especially at Wx Bo in Taylor Valley where the surface slope is flat and the cold air was able to pool.

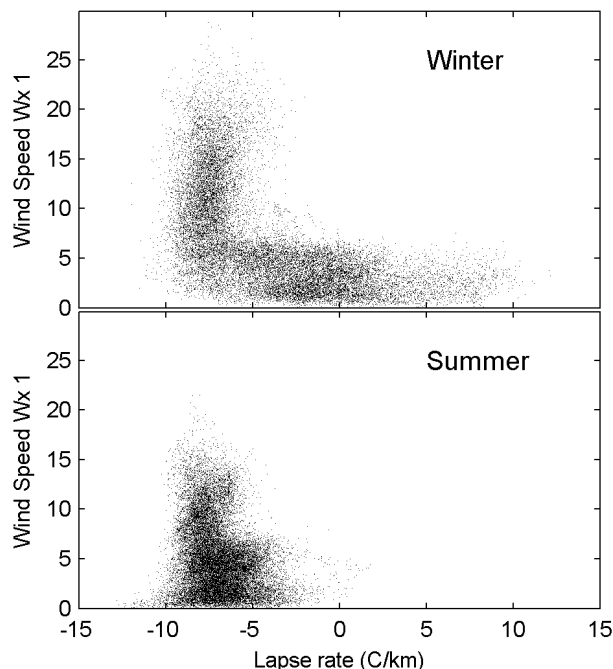


Figure 3.49. Lapse rate and wind speed. Fast winds on the glacier meant the lapse rate was close to adiabatic. Slow winds allowed a wider range of lapse rates, which were sometimes affected by inversions, as can be seen in figure 3.48.

temperature change over time. The depth of the boreholes was not noted, but it is possible that they reached down to the previous winter's cold layer, which would explain why his lapse rate was similar to our winter rate. *Johnston et al.* [2005] used 5 temperature sensors to find a summertime lapse rate along the lower 9.2 km of Taylor Glacier. The average for the 1999/2000 field season was 8°C/km, with a range from 7-10°C/km.

Since we also had humidity sensors at a range of elevations, we calculated both relative humidity lapse rates and vapor pressure lapse rates. While it was difficult to compare relative humidity from place to place, because the relative humidity depends on temperature, the relative humidity lapse rates plot (figure 3.50) shows dry air in the vicinity of Windy Gully, at an elevation of 860 m. Vapor pressure lapse rates, like temperature, exhibited a strong seasonal cycle. When temperature lapse rates were strong in summer, vapor pressure lapse rates were also strong, exceeding 1 mbar/km. To put that in context: with the cold temperatures at Taylor Glacier, the 90th percentile of vapor pressure at all stations was 2.2 mbar. Winter-time vapor pressure lapse rates were more modest, again because of the cold temperatures. For most of the period of record, the air on Taylor Glacier was flowing downhill and gaining moisture via sublimation from the glacier.

### 3.3.6 Inversions

As noted above, the lapse rate on Taylor Glacier sometimes was controlled by an inversion in Taylor Valley. We identified periods with an inversion by looking for times when the



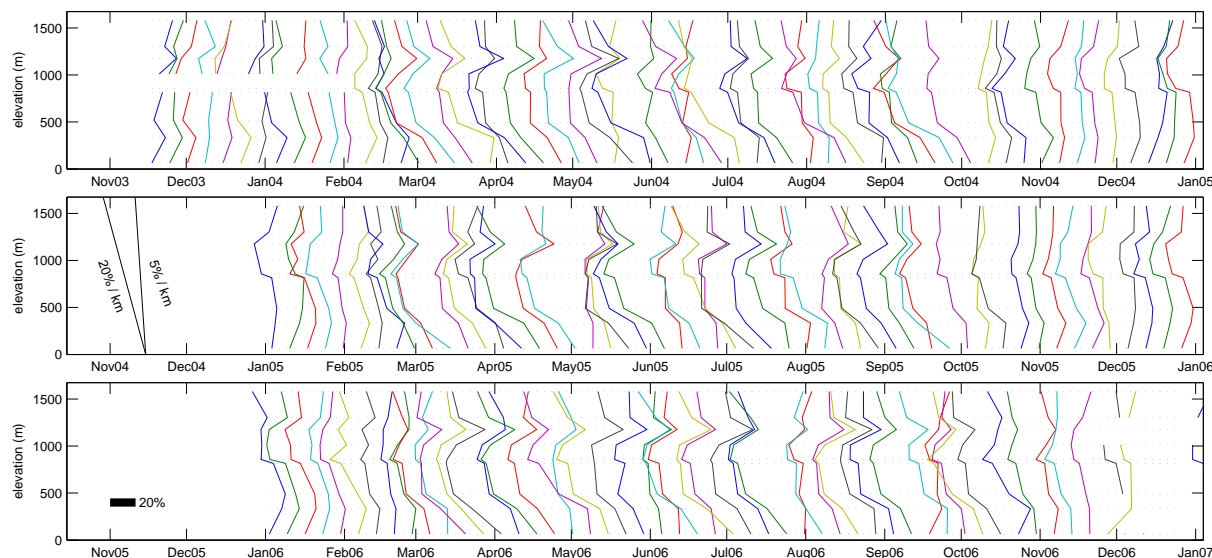


Figure 3.50. Weekly-mean relative humidity at each station, plotted against station elevation (y-axis) and time (x-axis). For each week, the relative humidity of the lowest-elevation station (Wx Bo) was plotted on the x-axis based on the date. Higher-elevation stations which had lower (higher) relative humidity plot above and left (right) of the lowest station. Since relative humidity depends on temperature, it is difficult to interpret this plot, but it clearly shows the dry air emanating from Windy Gully at 860 m.

Table 3.21. Percent time a station had the warmest temperature in the network. The second row shows station elevations in meters.

Wx Bo	Wx T	Wx 1	Wx 2	Wx 3	Wx 4	Wx 5	Wx 6	Wx Be
53.2	12.6	8.7	6.1	11.9	2.7	0.4	3.5	0.7
64	334	491	817	857	1012	1302	1581	1176

lowest elevation station (Wx Bo) did not have the highest temperature amongst our network of stations. The percentage of time that each station had the highest temperature is listed in table 3.21. Fifty three percent of the time Wx Bo was warmer than all the other stations, indicating there was not an inversion in Taylor Valley. Forty seven percent of the time another station had the warmest temperature, meaning there was an inversion at least a few hundred meters thick. Generally, the percentages fell off rapidly with elevation. Two anomalies stick out though: Wx 3 with its adiabatically-warmed air at the base of Windy Gully, and Wx 6 which is high above the glacier surface on the Friis Hills and as such occasionally had air that was disconnected, so to speak, from the air at the glacier surface.

Inversions were strongest and lasted longest in the winter (table 3.22), as expected from the radiation conditions. In spring and fall inversions were still quite common, occurring almost 60% of the time. When the sun was down, the net surface radiation budget was almost always negative, which allowed the surface to cool. On the glacier slopes, this cold

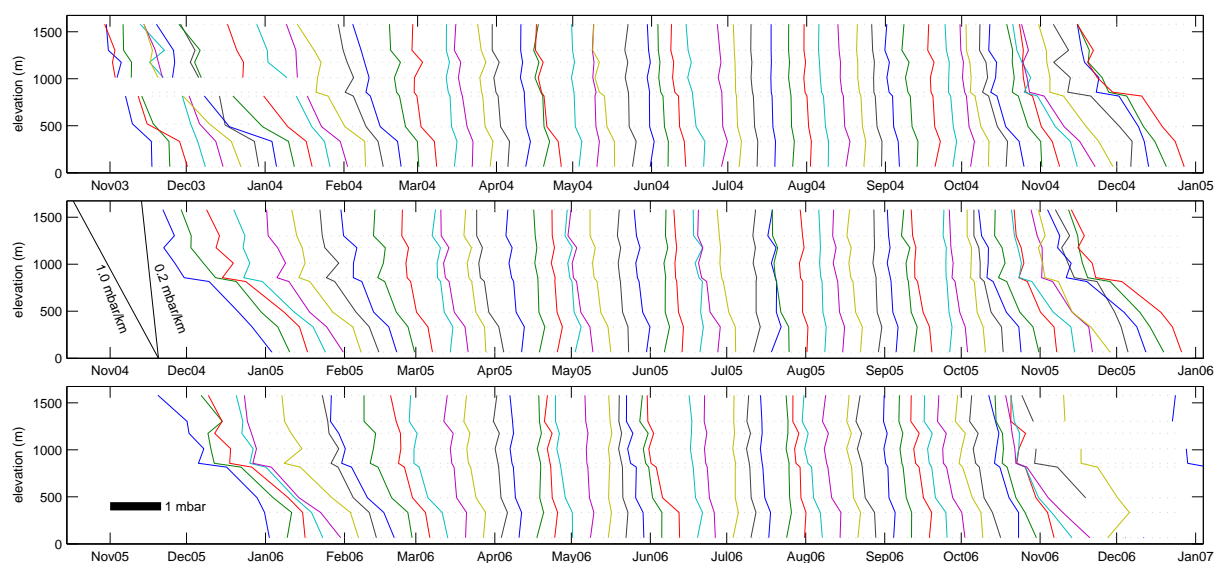


Figure 3.51. Weekly-mean vapor pressure at each station, plotted against station elevation (y-axis) and time (x-axis). For each week, the vapor pressure of the lowest-elevation station (Wx Bo) was plotted on the x-axis based on the date. Higher-elevation stations which had lower vapor pressure plot above and left of the lowest station. Vapor pressure lapse rates were strongest in summer, when the air temperatures were warmer and hence the saturation vapor pressure was higher. Air from Windy Gully (860 m) tends to be dry relative to the air nearby because it descends rapidly down the Gully before reaching the weather station and the air does not have time to gather much moisture from the glacier surface.

Table 3.22. Inversions: frequency of occurrence (in percent) for different seasons and modes. See section 3.4 for a description of the modes.

	Entire Year	Spring	Summer	Fall	Winter
All Modes	46.8	57.8	6.2	59.8	67.3
Storm	34.7	37.7	5.7	64.6	36.2
Katabatic	34.9	44.8	7.9	44.7	44.6
Calm	58.0	72.5	6.4	65.0	88.8
Diurnal	12.1	63.4	1.4	17.6	87.6

surface air descended the slope due to its negative buoyancy. The cold air was often able to pool in Taylor Valley, where the slope was close to zero. Storm winds and katabatic winds were able to erode the inversion layer and warm Wx Bo until it regained its status as the warmest station we considered. Summertime solar radiation heated the rock surface of Taylor Valley and the air at Wx Bo faster than longwave radiation could cool it. Surface heating generally led to unstable air, vertical mixing of the air, and infrequent inversions in that season.

### 3.3.7 Cloudiness

We devised two measures of cloudiness: one from incoming shortwave radiation  $SW_{in}$  and one from incoming longwave radiation  $LW_{in}$ . The shortwave parameterization followed *Brock and Arnold* [2000] and compared the measured  $SW_{in}$  to the potential shortwave radiation  $SW_{pot}$  calculated from the sun's position in the sky.

$$SW_{pot} = I_0 \psi^{P/P_0} \cos \theta \quad (3.11)$$

where  $I_0$  is the solar constant (1368 W/m<sup>2</sup>);  $\psi$  the clear-sky transmissivity (0.83, tuned to match the measurements on clear days);  $P$  and  $P_0$  the atmospheric and sea level pressures, respectively; and  $\theta$  the solar zenith angle (calculated using *Iqbal* [1983]). Figures 3.52 and 3.53 show two examples of the shortwave measurements and the result of equation 3.11. When the ratio  $r_{sw} = SW_{in}/SW_{pot}$  was less than 0.2, it was assumed that the sky was completely cloudy (cloud fraction  $n = 1$ ). A ratio of 1 indicated clear skies ( $n = 0$ ). For intermediate values of  $r_{sw}$ ,  $n$  varied linearly (see figure 3.54).

$$n = \begin{cases} 1 & \text{if } r_{sw} < 0.2 \\ 1.25 - 1.25r_{sw} & \text{if } 0.2 \leq r_{sw} \leq 1 \\ 0 & \text{if } r_{sw} > 1 \end{cases} \quad (3.12)$$

Occasionally,  $SW_{in}$  was larger than  $SW_{pot}$  due to multiple reflections off of clouds, for example. This method only worked in summer when the sun was up and it did not account for shading by mountains, so we also used a parameterization that considered longwave radiation.

For a given air temperature close to the surface, the incoming longwave radiation  $LW_{in}$  was higher during cloudy periods than during clear skies because clouds effectively radiate

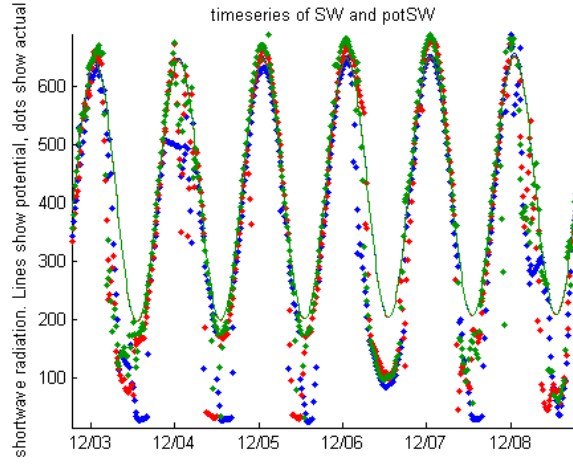


Figure 3.52. Example timeseries of  $SW_{in}$  (dots: blue= $W_x$  1, green= $W_x$  2, red= $W_x$  4) and  $SW_{pot}$  (lines, same colors) for December 2004. The match was good on clear days (e.g. 12/5), cloudy days stand out (e.g. 12/8), and the model often overpredicted the measured at night when the sun went behind mountains. Time plotted in UTC, local time is UTC+13.

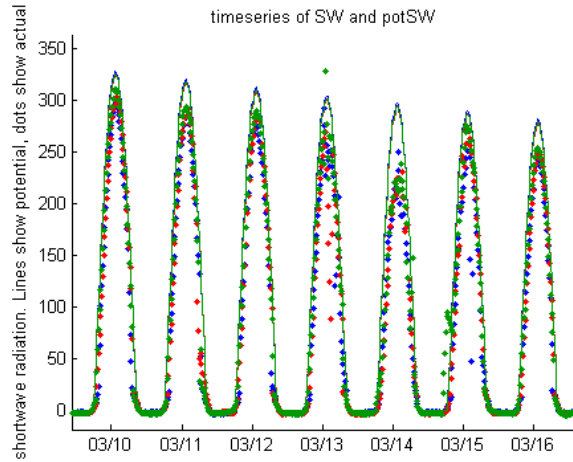


Figure 3.53.  $SW_{in}$  and  $SW_{pot}$  for March 2005. At the daily maximum value, the potential was higher than the actual by a significant margin (about 25 W/m<sup>2</sup>). This was partly due to the fact that the simple model did not include attenuation in the atmosphere, which would be most important when the sun was close to the horizon, like it was in March. Note the scale is different from figure 3.52.

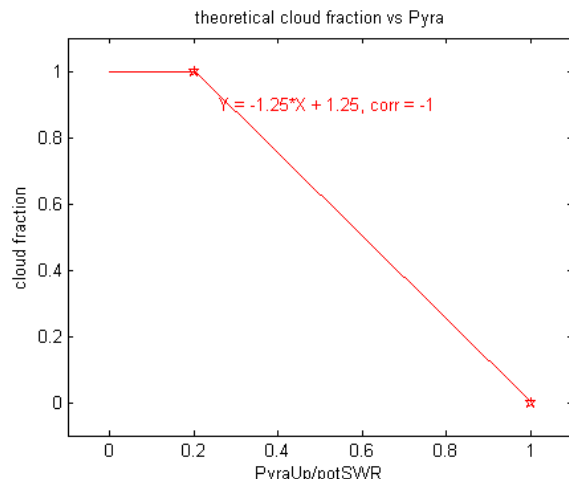


Figure 3.54. Cloud fraction (percentage of the sky covered with clouds) decreases as the measured incoming shortwave radiation approaches the potential shortwave radiation.

from a lower altitude than the clear sky. Incoming longwave radiation was measured by a pyrgeometer and calculated as  $LW_{in} = \sigma T^4 + R_{tov}$  where  $T$  was the temperature measured at the cold junction of the thermopile (K), and  $R_{tov}$  the thermopile output voltage converted to a radiation ( $\text{W}/\text{m}^2$ ) using a calibration factor. Since  $T$  varied significantly depending on the season, it was easier to distinguish cloudy periods by just considering  $R_{tov}$ . We created a cloudiness index by comparing  $R_{tov}$  to an expected clear-sky value (see figure 3.55).

These shortwave and longwave methods, when smoothed with a 1-day triangular filter, captured many of the cloudy periods observed with AVHRR imagery. They also agreed with each other reasonably well when smoothed. Since the longwave parameterization of cloudiness was continuous throughout the year, we chose it to help distinguish between katabatic/foehn and storm weather patterns.

## 3.4 Modes of Weather Variability

We derived timeseries for different modes of weather variability. Based on data from six weather stations, we have identified four different weather patterns that influence Taylor Glacier. (1) Storms occur throughout the year but are less frequent and less intense during the summer. Their signature in the local weather is: high winds from the south, cloudy skies, and low relative humidity. Storms are distinguished from katabatic/foehn events based on whether the pyranometer and pyrgeometer data show clouds. (2) Under clear skies, katabatic/foehn events can also have high winds. From our station data it is hard (or impossible) to distinguish between katabatic and foehn winds, so I use the terms loosely and interchangeably. Mesoscale modeling can illuminate the regional context of station data [Speirs *et al.*, 2010], but I have not pursued it. There are two distinct katabatic wind patterns on the glacier. The first occurs primarily during the summer and involves air flowing down a steep valley (Windy Gully) from the Ferrar Glacier to the south. The second katabatic

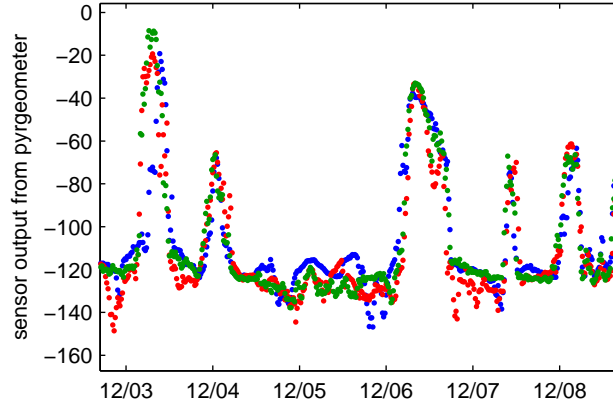


Figure 3.55. Cloudy periods showed up clearly in the longwave radiation data for December 2004. The plot shows  $R_{tov}$ , defined in the text. For this example, when the values were in the range -100 to -150  $\text{W}/\text{m}^2$ , the sky was clear. From 0 to -100  $\text{W}/\text{m}^2$ , the sky was cloudy. Compare to shortwave radiation depicted in figure 3.52.

pattern occurs during the winter (usually) when the wind blows directly from the East Antarctic Plateau. Because of the geometry of the glacier’s valley, katabatic winds and storm winds follow similar trajectories over the glacier. (3) Summer is often characterized by diurnal fluctuations in wind speed and direction, especially at lower elevations where the glacier is confined within a deep valley. Each afternoon the mountain wind brings faster wind speeds and higher relative humidity to the eastern parts of the glacier from Taylor Valley and the ocean. (4) Calm intervals make up the rest of the record.

We discriminated these modes in our timeseries on the basis of measured wind directions, wind speeds, and cloud amounts (inferred from the longwave radiation) at our weather stations. For each mode we developed an expected value of each variable at each weather station (see figure 3.56 for an example). If a variable at a station matched the expected value for a mode, that mode received a weight of 1. Within a plausible range around the expected value, the mode received less weight. Then we averaged the weights from all stations for each mode. The dominant mode for a given time was the mode which received the highest weight. Because we averaged over all stations, the dominant mode applied to the entire glacier. In chapter 6, we will use these modes to discuss the conditions favorable to sublimation on Taylor Glacier.

While the expectation and weighting functions were numerically subjective and based solely on our weather station data, the characteristics described below were observable through satellite imagery and NCEP reanalysis data as well. For the case studies described in section 6.2, our mode parameterization matched the observed conditions well. Section 6.1 considers how these different modes affect sublimation rates on Taylor Glacier.

### 3.4.1 Characteristics of the Storm Mode

- wind direction from the south at all stations

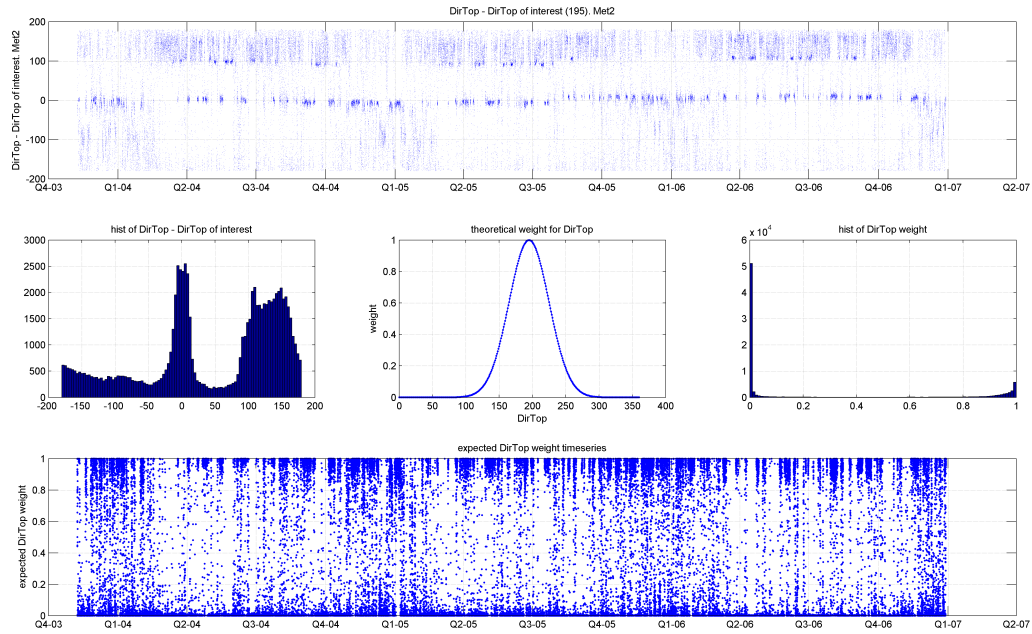


Figure 3.56. Example of the expectation and weighting process. In this case, the expected wind direction for the katabatic/foehn mode at Wx 4 was  $195^\circ$ . The top panel shows the wind direction timeseries (data minus expectation). The middle-left panel shows a histogram of the top panel. The katabatic/foehn wind direction shows up as a clear peak. The middle-center panel shows the weighting function, with 195 weighted 1. The middle-right panel shows a histogram of the bottom panel. The bottom panel shows the timeseries of the weights. When this and other stations highly weight the katabatic mode, it becomes the dominant one.

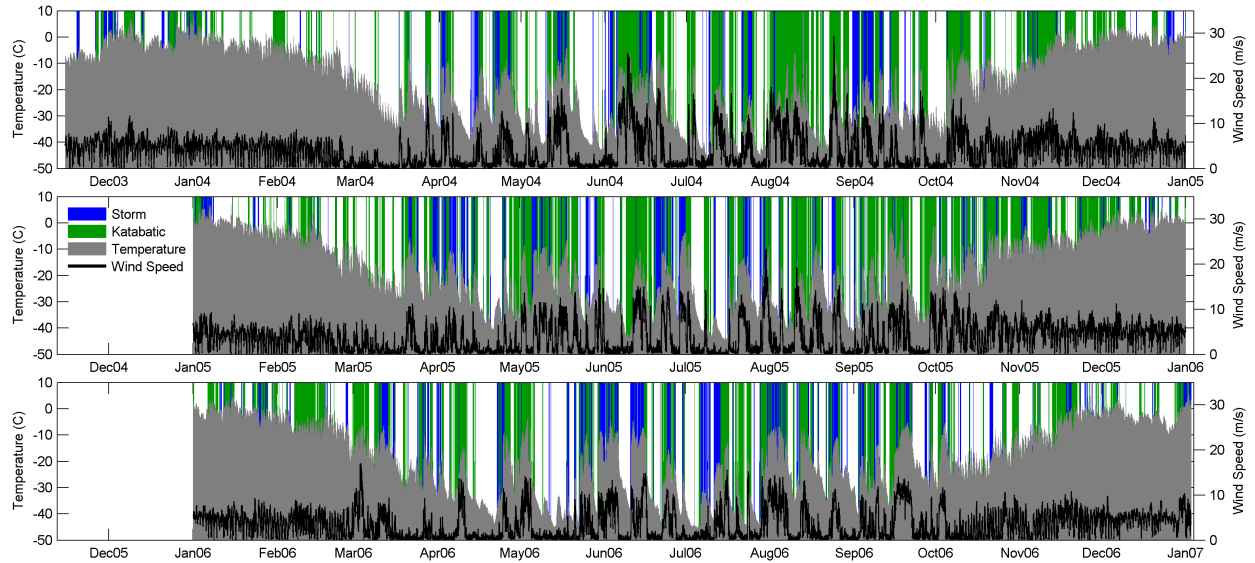


Figure 3.57. Temperature and wind speed for Wx Bo, plotted with the glacier-wide timeseries of the katabatic and storm modes. These are 20-minute data.

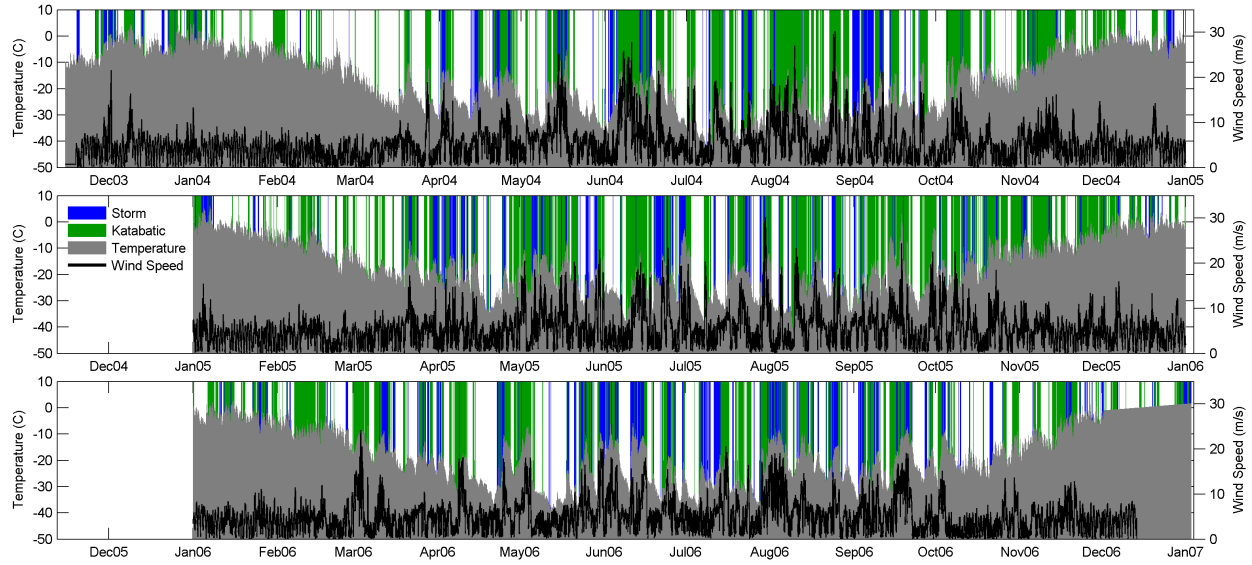


Figure 3.58. Temperature and wind speed for Wx T, plotted with the glacier-wide timeseries of the katabatic and storm modes. These are 20-minute data.

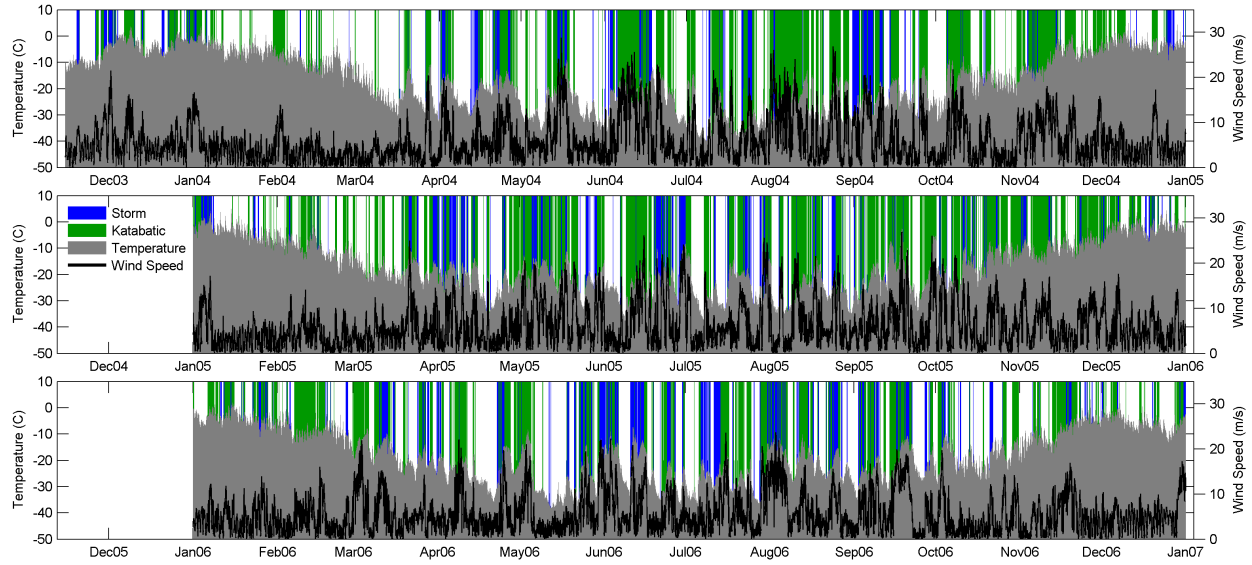


Figure 3.59. Temperature and wind speed for Wx 1, plotted with the glacier-wide timeseries of the katabatic and storm modes. These are 20-minute data.



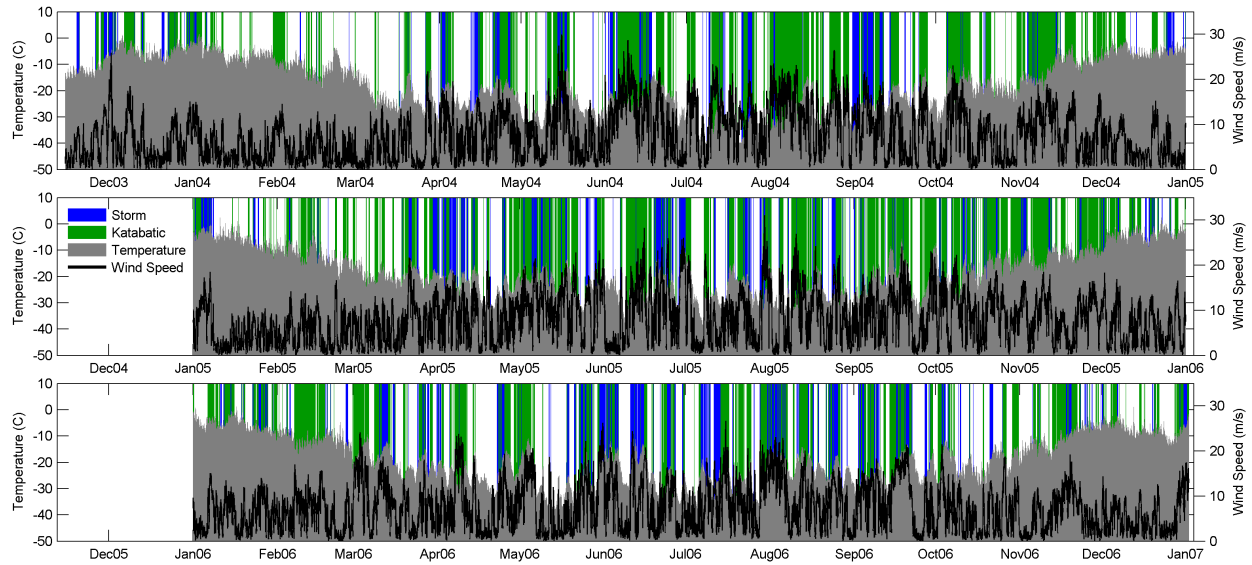


Figure 3.60. Temperature and wind speed for Wx 2, plotted with the glacier-wide timeseries of the katabatic and storm modes. These are 20-minute data.

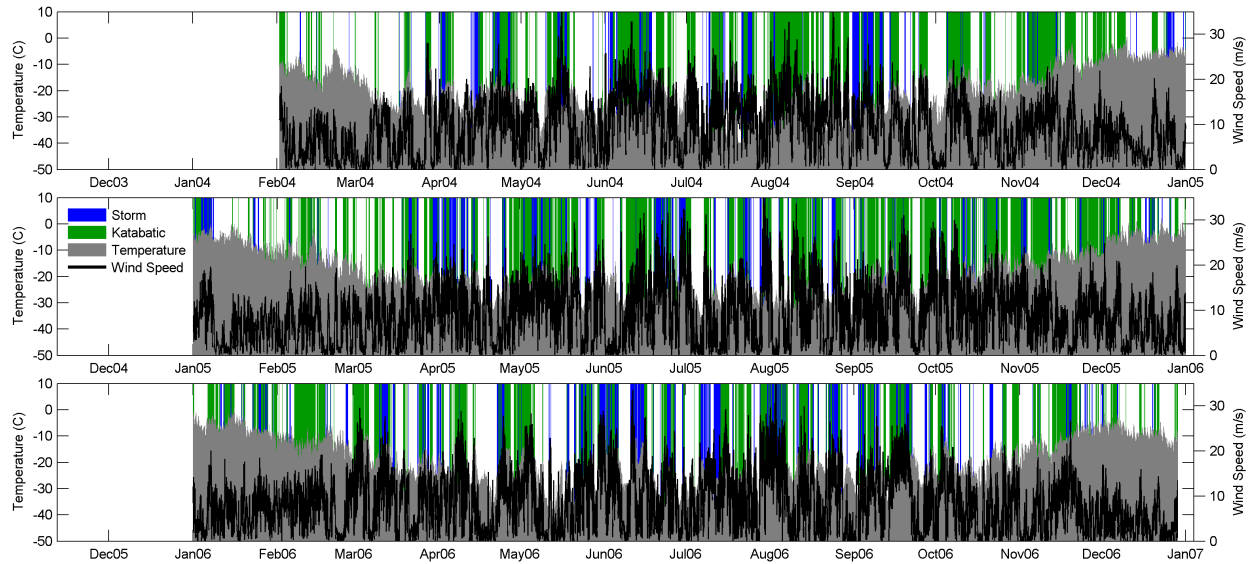


Figure 3.61. Temperature and wind speed for Wx 3, plotted with the glacier-wide timeseries of the katabatic and storm modes. These are 20-minute data.

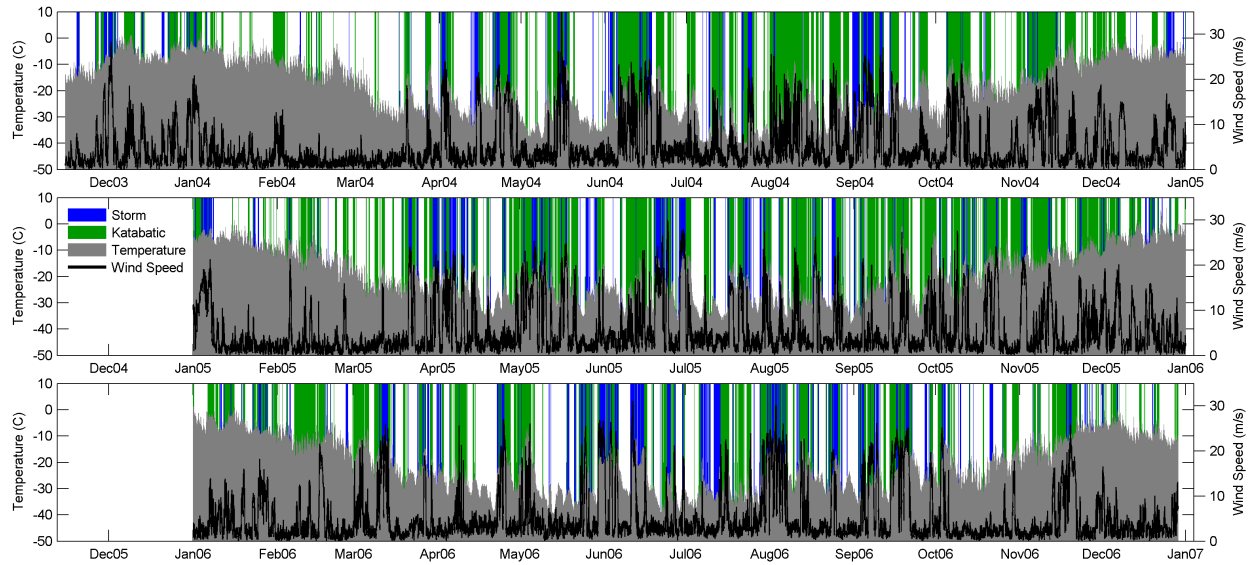


Figure 3.62. Temperature and wind speed for Wx 4, plotted with the glacier-wide timeseries of the katabatic and storm modes. These are 20-minute data.

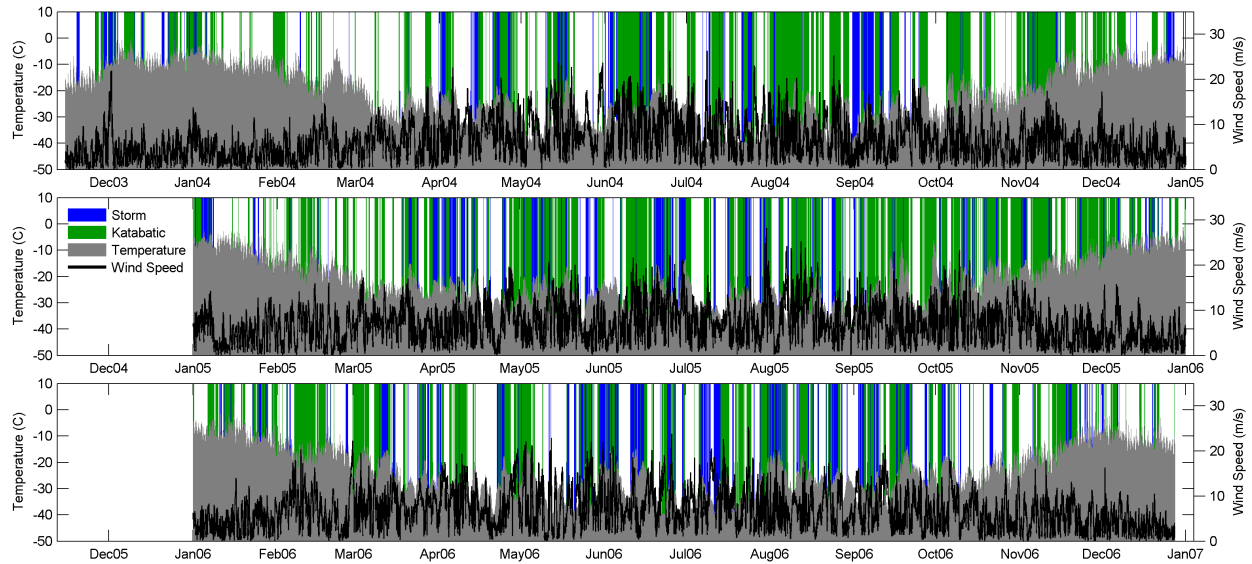


Figure 3.63. Temperature and wind speed for Wx 5, plotted with the glacier-wide timeseries of the katabatic and storm modes. These are 20-minute data.

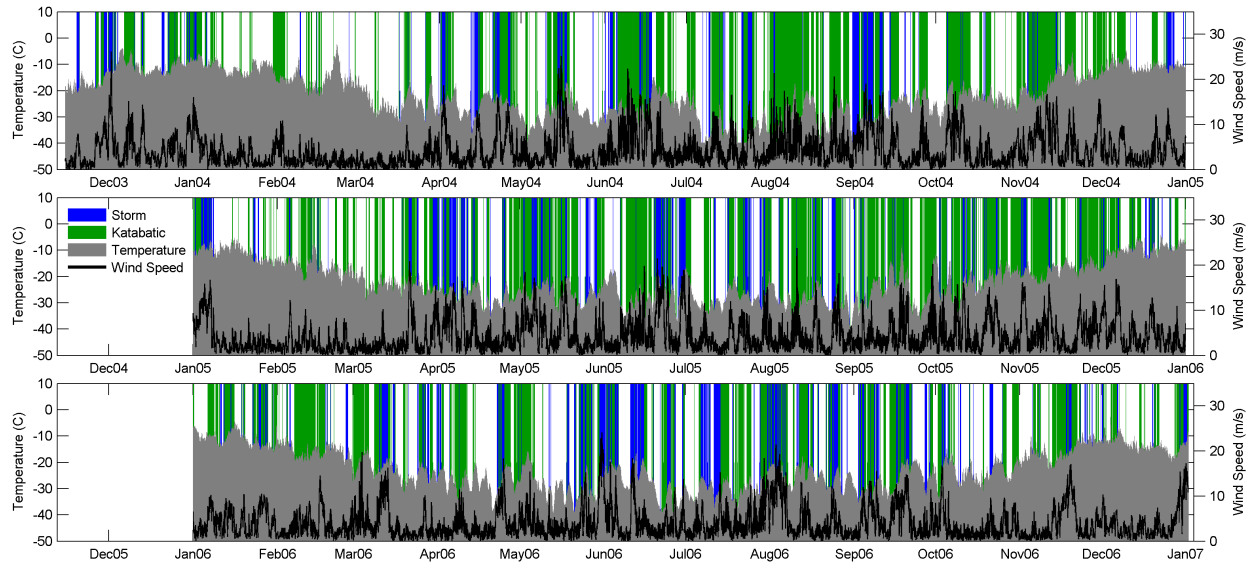


Figure 3.64. Temperature and wind speed for Wx 6, plotted with the glacier-wide timeseries of the katabatic and storm modes. These are 20-minute data.

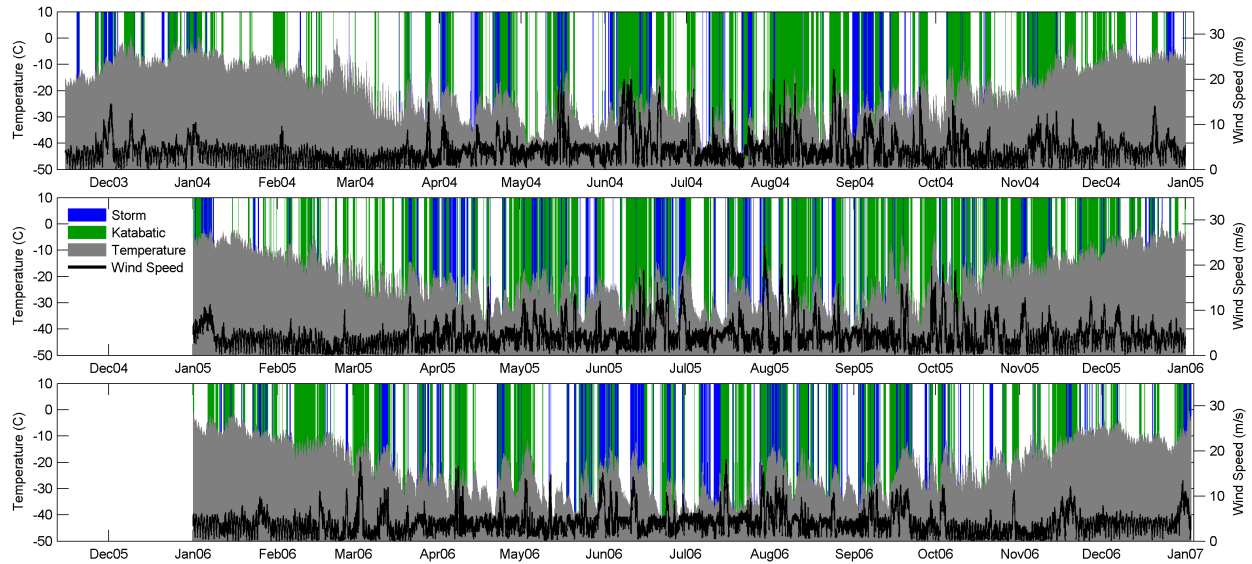


Figure 3.65. Temperature and wind speed for Wx Be, plotted with the glacier-wide timeseries of the katabatic and storm modes. These are 20-minute data.

- consistently high wind speeds
- cloudy skies: lower or more variable incoming shortwave flux, high incoming longwave flux
- relative humidity tends to be low

### 3.4.2 Characteristics of the Katabatic/Foehn Mode

Katabatic/foehn – from Windy Gully

- winds blowing from Windy Gully at all stations except Wx 5
- consistently high wind speeds
- clear skies: high incoming shortwave flux, low incoming longwave flux
- relative humidity tends to be low
- tends to occur in summer

Katabatic – from the East Antarctic Plateau

- wind directions are steady from the plateau at most stations while some stations may receive wind from Windy Gully
- consistently high wind speeds
- clear skies: low incoming longwave flux
- stations Bo, T, and 1 sometimes fall into an inversion layer where the wind speeds drop, direction changes to be from downglacier, and relative humidity goes up
- relative humidity tends to be low
- tends to occur in winter

### 3.4.3 Characteristics of the Diurnal Mode

mountain-valley wind or land-sea breeze

- diurnal cycle in wind direction, wind speed, and temperature especially at stations 1 and T, sometimes extending to other stations
- wind speeds, relative humidity, and temperature are high each afternoon on the eastern parts of the glacier when the wind blows from Taylor Valley and the ocean
- slower winds and lower relative humidity each morning when the wind blows off the glacier
- the temperature pattern isn't necessarily distinguishable from the regular summer diurnal temperature pattern

### 3.4.4 Characteristics of the Calm Mode

- the absence of the other conditions
- weak winds with highly-variable wind directions

Table 3.23. Modes: frequency of occurrence (in percent) for different seasons.

	Entire Year	Spring	Summer	Fall	Winter
Storm	13.9	14.4	12.0	10.9	18.4
Katabatic	27.6	34.7	26.7	22.1	26.7
Calm	54.8	50.0	50.9	65.6	54.0
Diurnal	3.8	0.8	10.4	1.5	0.9

### 3.4.5 Frequency of Modes

The calm mode was the most common mode in all seasons, as noted in table 3.23. Fall tended to have calmer weather than other seasons. The katabatic mode occurred twice as often as the storm mode, except in winter when storms occurred 18.4% of the time and katabatics 26.7%. The larger number of storms in the winter was consistent with the general pattern of storminess globally in the mid-high latitudes, that observed around Antarctica, and that observed in the southwestern Ross Sea [Monaghan *et al.*, 2005]. The diurnal mode was strongest in summer (10.4%) when the sun’s radiation was intense enough to generate a mountain and valley wind.

# Chapter 4

## Sublimation Models

Although melting contributes to ablation near Taylor Glacier’s terminus [Johnston *et al.*, 2005; Fountain *et al.*, 2006], in most of the study region temperatures never rose to the melting point except locally around morainal debris. We therefore compared our ablation measurements to sublimation calculated from weather station data. We performed the calculation using several different formulae. In all cases the sublimation rate  $\dot{S}$  was derived from an estimated latent heat flux  $L$  according to

$$\dot{S} = L/(\lambda\rho_{ice}) \quad (4.1)$$

where the latent heat of sublimation  $\lambda = 2.8 \times 10^6$  J/kg and  $\rho_{ice} = 910$  kg/m<sup>3</sup> denotes ice density.

In order of increasing complexity, the primary formulae are:

1. A bulk aerodynamic flux equation with no stability correction [Cuffey and Paterson, 2010, equation 5.28].

$$L = \frac{\rho\omega\lambda k^2 u_z (e_z - e_s)/P}{\ln \frac{H_{wind}}{Z_o} \ln \frac{H_{RH}}{Z_{RH}}} \quad (4.2)$$

where  $\rho$  is air density,  $\omega$  the ratio of the molecular weight of water to air,  $\lambda$  the latent heat of sublimation,  $k$  von Kármán’s constant,  $u_z$  wind speed in m/s measured at height  $H_{wind}$ ,  $e_z$  vapor pressure at the measurement height  $H_{RH}$ ,  $e_s$  vapor pressure at the surface,  $P$  air pressure, and  $Z_o$  and  $Z_{RH}$  the roughness lengths for momentum and humidity, respectively. The calculation of  $e_s$  assumed the air at the surface was saturated at the parameterized surface temperature introduced in appendix 3.3.1. Unfortunately, the net energy budgets calculated using this model varied widely on 20-minute, daily, and seasonal timescales. The net energy budget was rarely zero; such a mismatch arose both from measurement uncertainties and from assumptions in formulae.

2. The energy budget mismatch from the first model led us to try another model in which we reduced the mismatch. Because we did not measure surface temperature ( $T_s$ ) directly, it was one of the most uncertain variables in the analysis. Thus, as

an alternative to the previous model, we used the same formulation (Equation 4.2) but adjusted  $T_s$  to balance the energy budget. Since the energy budget affects and depends on  $T_s$ , an iterative scheme was necessary to find a solution. The adjustment was made on a smoothed (time-averaged) version of the data series rather than on the 20-minute timescale. This strategy was adopted because the calculated net energy for some individual 20-minute intervals deviated widely from zero; fixing the problem by adjusting an unsmoothed  $T_s$  would require unrealistic temperatures. The rest of this paper considers results from this model.

3. Including a correction for atmospheric stability makes the equation more complex. Following *Brock and Arnold* [2000]

$$L = \frac{\rho\omega\lambda k^2 u_z (e_z - e_s)/P}{(\ln \frac{H_{wind}}{Z_o} + \alpha_m \frac{H_{RH}}{\Lambda}) (\ln \frac{H_{RH}}{Z_{RH}} + \alpha_e \frac{H_{RH}}{\Lambda})} \quad (4.3)$$

where the stability length scale  $\Lambda$  ranges from 0 to 230 m (10 and 90th percentile). The length scale is ill-defined for neutral conditions (when the air temperature is roughly equal to the surface temperature). We assumed the latent heat flux was zero under those conditions (18% of the data).  $\alpha_m$  and  $\alpha_e$  are stability correction constants equal to 5 [*Brock and Arnold*, 2000]. We found that sublimation calculated with this model did not match measurements as well as did calculations using model 2. Thus, although commonly applied to glaciers, equation 4.3 will not be considered further here.

## 4.1 Predicted Sublimation

Figure 4.1 plots, for different time periods, the covariation of ablation measurements with the sublimation rates calculated from Equations 4.1 and 4.2. For seasonal to annual averages, the modeled sublimation is linearly related to the measurements, with a least-squares regression slope of 0.85. The model over-predicts ablation at low rates. Overall, however, the match is very good. We therefore believe that the model can provide useful interpretations of shorter-period variations in sublimation, which were not directly measured. Rates range from about 0 mm/day during calm intervals in winter to 2.5 mm/day during warm and dry summer days. Although mean summer rates are more than twice as large as winter ones, the contribution of slow winter sublimation to the yearly total cannot be neglected (see section 6.1 on magnitude and frequency below).

At station T we have continuous measurements of ice ablation from a sonic distance sensor. This allowed us to compare our model with measurements on a finer timescale than our own measurements of ablation close to our weather stations would allow (figures 4.2 and 4.3). Again, the model compares favorably with the measurements but the model prediction for summertime is not quite as large as the measured ablation.

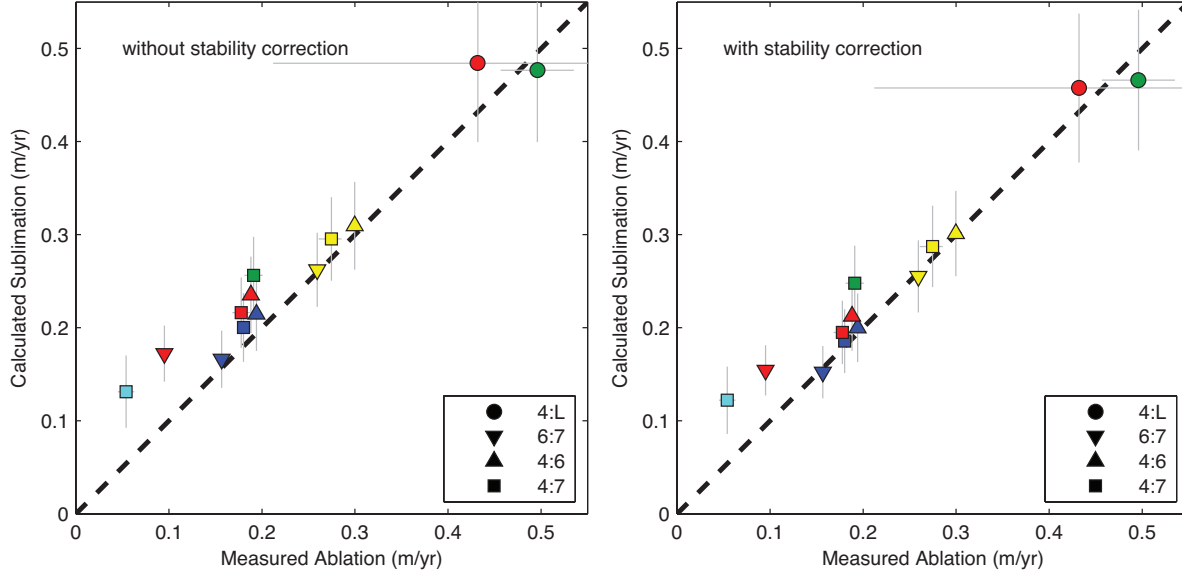


Figure 4.1. Modeled sublimation rates are linearly related to the ablation rates measured at ablation stakes close to the weather stations. The modeled sublimation in the left (right) panel does not (does) include a stability correction; the correction is small. The symbol shapes are the same as in figure 2.11 and colors correspond to stations: Wx 1 blue, Wx 2 green, Wx 3 yellow, Wx 4 red, Wx 5 cyan. Note that ablation is not directly comparable to sublimation. The two points with the lowest measured ablation rates probably had significant snowfall which decreased the measured ablation, leading to a mismatch. The rest of the glacier received little snowfall. The width of the horizontal error bar depends on the measured variability in ablation, as in figure 2.11. The height of the vertical error bar is  $\pm$  one standard deviation away from the mean of the Monte Carlo simulation explained in the text.

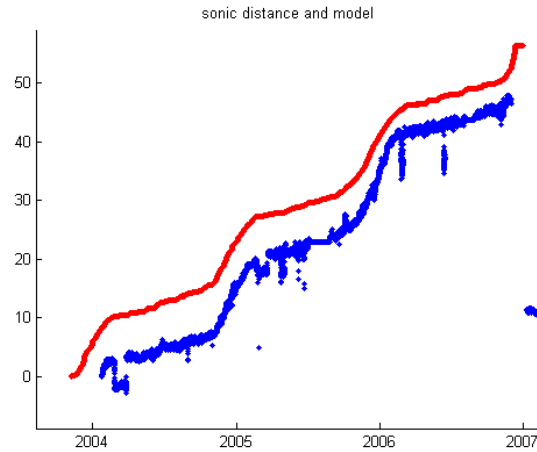


Figure 4.2. The upper line (red) shows modeled sublimation at Wx T (in cm). The lower line (blue) shows measured ablation at the same location. The measurements were noisy due to the sensor used. The occasional spikes and dips were due to snowfall of a few centimeters. The instrument was reset at the beginning of 2007.



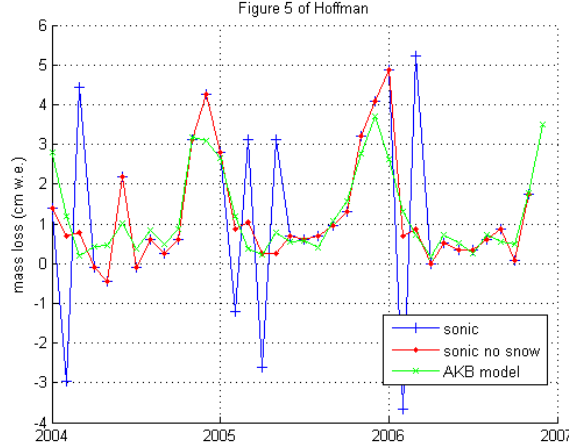


Figure 4.3. Monthly measurements of surface height change (blue includes snow; red without snow) and modeled sublimation for 2004-6. The correspondence was good, except in summer when the model prediction was low. Compare to figure 5 of *Hoffman et al.* [2008].

## 4.2 Sensitivity of Predictions to Input Values

To evaluate the sensitivity of modeled sublimation values to uncertainties of the input data, we performed a Monte Carlo analysis. Input variable timeseries were uniformly perturbed by a normally distributed random variable with zero mean and a standard deviation given as follows. For temperature, wind speed, and relative humidity, the standard deviation equaled the manufacturer's stated instrument accuracy (0.4°C, 0.3 m/s, 2%). For surface temperature, we chose an uncertainty of 0.6°C to be comparable to the adjustments of surface temperature required for energy balancing. We set the  $Z_o$  uncertainty to 0.001 m based on the common range of  $Z_o$  values used in the literature. We chose to uniformly perturb the input timeseries rather than perturb individual values because short-term random variations average out when considering seasonal or annual sublimation. In other words, instrument precision is less important than accuracy.

Sensitivities are illustrated by the resulting distributions of calculated sublimation rate summed over the whole period of record (Figure 4.4). The most important source of uncertainty is the surface temperature. Overall, the estimated uncertainty of model sublimation values is rather large. The standard deviation of the Monte Carlo results divided by the mean was between 14 and 18% for the different weather stations.

In addition to the uncertainties arising from input data, the calculated sublimation obviously depends on the assumption that the equations represent the complex process of turbulent moisture transfer in nature. The only indication of total uncertainty is the mismatch between measured and modeled sublimation rates depicted in figure 4.1.

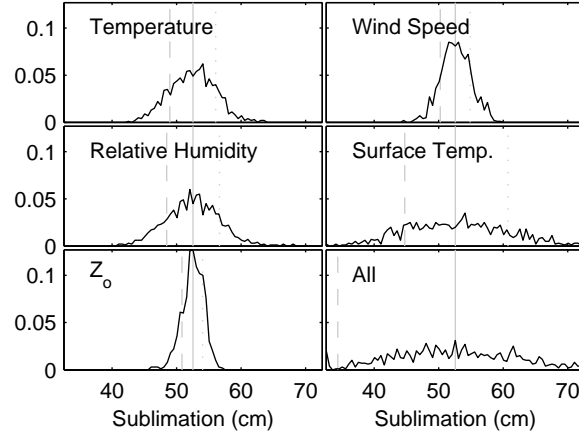


Figure 4.4. Histograms of modeled sublimation after perturbations to one or more input variables from a Monte Carlo simulation. The x-axis shows the total sublimation for the period of record at station 1 in cm. The text discusses the method of perturbation. The solid vertical line in each plot is the sublimation predicted by the unperturbed model. The dotted line is the model result using the (+) uncertainty and the dashed line is using the (-) uncertainty. The total number of points in each simulation was 1000 and each of the 81 histogram bins is 0.5 cm wide. The sublimation model is more sensitive to the uncertainties in surface temperature and roughness than to the instrument uncertainties associated with the measurements of temperature, relative humidity, and wind speed.

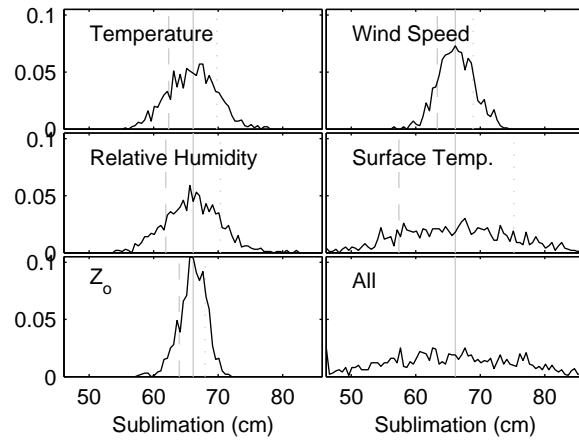


Figure 4.5. Constant Offset Uncertainty Test – Wx 2.

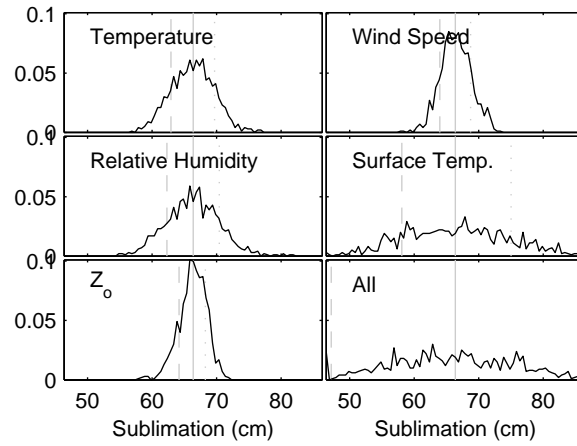


Figure 4.6. Constant Offset Uncertainty Test – Wx 3.

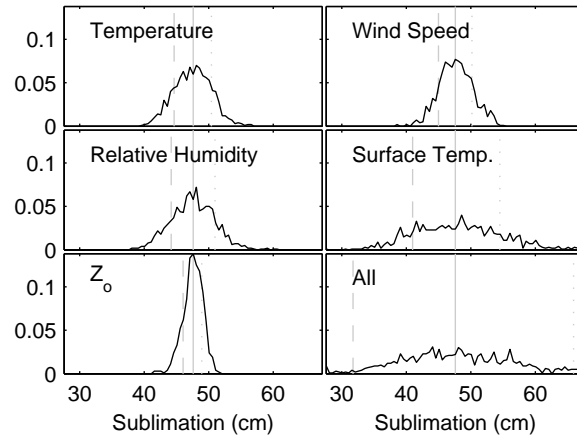


Figure 4.7. Constant Offset Uncertainty Test – Wx 4.

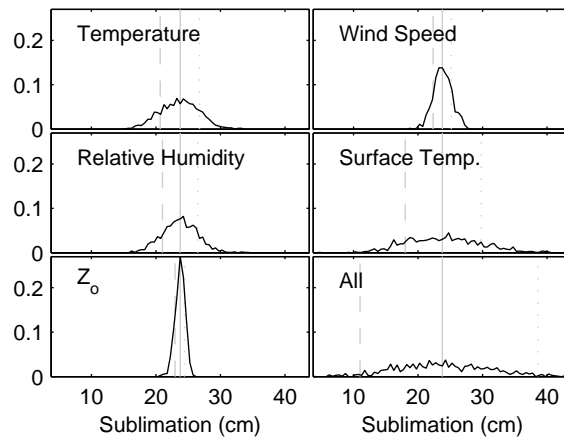


Figure 4.8. Constant Offset Uncertainty Test – Wx 5.

### 4.3 Discussion of Modeled Ablation Rates

In the relationship between our modeled and measured sublimation rates (figure 4.1), the departure from a slope of unity might arise from multiple factors. Model over-prediction at low ablation rates might arise from temporary accumulation; we occasionally observed snow patches in the vicinity of Wx 5. Accumulation is not included in our model because we did not obtain continuous measurements of surface height (e.g. taken with sonic distance sensors).

When comparing, on a monthly basis, our model of sublimation to surface height measurements at Wx T (figure 4.3), our numbers were low during summer. This could be due to deficiencies in the model or input parameters, or more likely, there could have been melt at the station. Unlike the stations higher on the glacier, temperatures at that station do exceed 0°C for multiple days each summer. Since the latent heat of melt is small compared to the latent heat of sublimation, there could be enough melt to explain the discrepancy without affecting the energy budget significantly. Melt channels are observed in the vicinity of the station. Melt is difficult to predict accurately though, as demonstrated by *Hoffman et al.* [2008]. They tuned their model separately for summer and winter ablation rates, something we did not do.

For sites in Queen Maud Land, Antarctica, *Bintanja and Reijmer* [2001] found that 70% of the annual sublimation happened in summer (NDJF). On Taylor Glacier, 54 to 68% happened in summer (stations 5 and T, respectively). We attribute the greater importance of winter ablation at Taylor Glacier to strong winter winds that favor sublimation.

# Chapter 5

## Energy Budget

We define the net energy flux,  $E$ , using the budget equation

$$E = SW + LW + L + H + G \approx 0. \quad (5.1)$$

As mentioned above, we measured incoming and outgoing shortwave  $SW$  and longwave  $LW$  radiation. Latent heat fluxes  $L$  were obtained from equation 4.2. An analogous equation gave sensible heat fluxes  $H$ . Heat flux into the subsurface  $G$  was calculated using finite-difference solutions to the diffusion equation for time- and depth-varying temperatures within the ice.  $G$  sums two terms: the change of energy stored as heat within the top numerical layer (0.04 m thick), and the Fourier heat flux through the layer. Points in the finite-difference grid were spaced closer together near the surface (18 in the first meter) than at depth (2-m spacing at 50 m depth). The surface boundary condition was the surface temperature appropriate for the sublimation model being considered, as described previously. The basal boundary condition was set according to the temperature profile from a force-balance model of the glacier [Kavanaugh and Cuffey, 2009].

The heat flux due to melt and subsequent runoff was assumed to be zero at our sites, which are far from the margins and the terminus. This assumption was based on field observations and the temperature record from the weather stations ( $\sim 2$  days per year with temperatures above  $0^\circ\text{C}$ ). Runoff does occur within 1 km of the terminus and within 100 m of the margin of the glacier elsewhere. The heat flux due to rain was also neglected, again because of field observations and the temperature record.

In the absence of measurement uncertainties, the net energy flux as defined here should equal zero.

### 5.1 Energy Budget Data

Figures 5.1 to 5.6 show timeseries of the terms in the energy budget for different stations. Tables 5.1 to 5.13 show seasonal averages for all stations. Net shortwave radiation was the largest term in the energy budget in summer. Longwave radiation also peaked in summer,

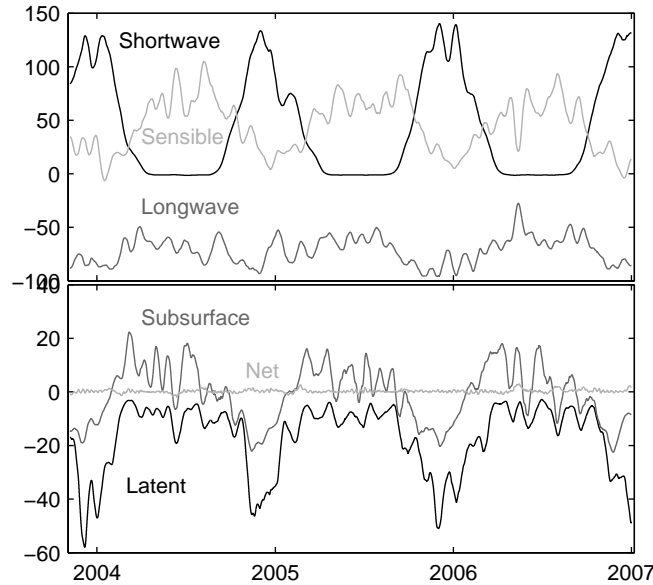


Figure 5.1. Relative magnitudes of the terms in the energy budget for station 1 (all units:  $\text{W}/\text{m}^2$ ). Data were smoothed with a 30-day triangular filter. Fluxes that added energy to the glacier surface were defined to be positive and fluxes that removed energy from the surface were negative. The modeled sublimation rates for all 5 stations exhibit maxima in the summer months. In summer, the warmer temperatures allow for higher vapor pressure differences so despite calmer winds and higher relative humidity, the sublimation rates are higher than in winter. Winter sublimation is quite variable because of storms.

but it was more constant throughout the year. The calculated sensible heat flux warming the ice was largest in the winter, approximately balancing the heat lost by longwave radiation. In summer, the ice temperature was closer to the air temperature so the sensible heat flux was smaller but still positive. The calculated latent heat flux was almost always negative (very little condensation or hoar deposition) and was strongest in summer. Heat flowed into the subsurface during the spring and summer and flowed out during the winter, with a maximum magnitude smaller than the latent and sensible terms. The residual of the other terms is plotted as the net energy balance, as in equation 5.1.

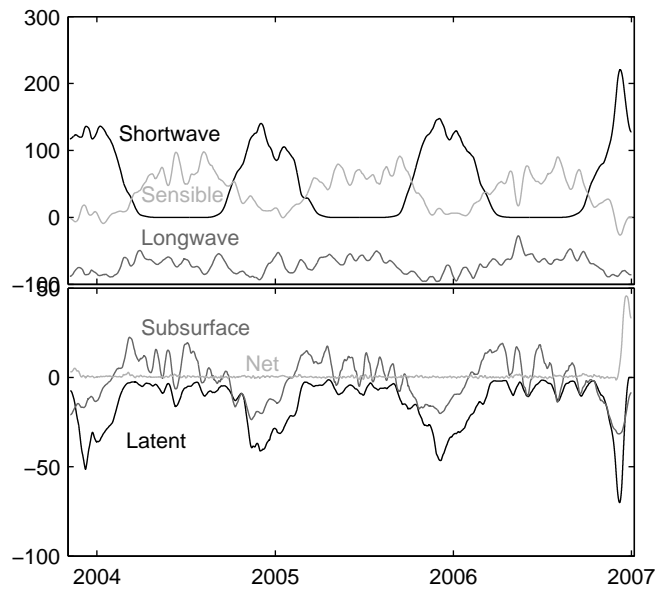


Figure 5.2. Energy budget timeseries –  $W \times T$ .

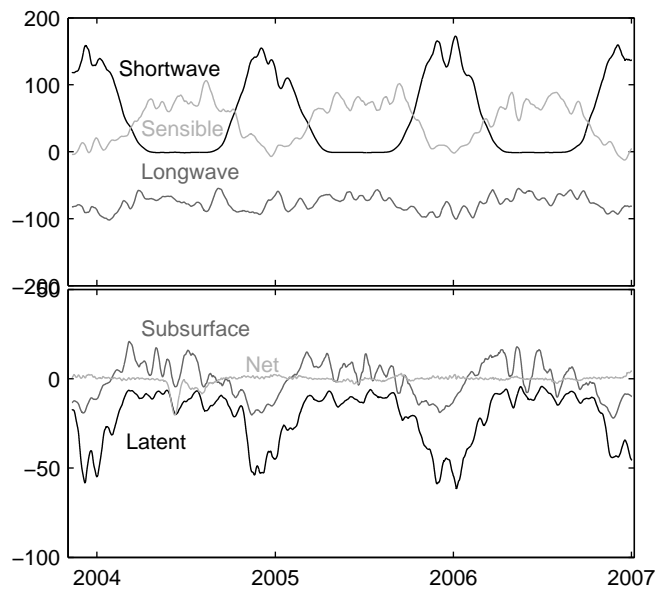


Figure 5.3. Energy budget timeseries –  $W \times 2$ .

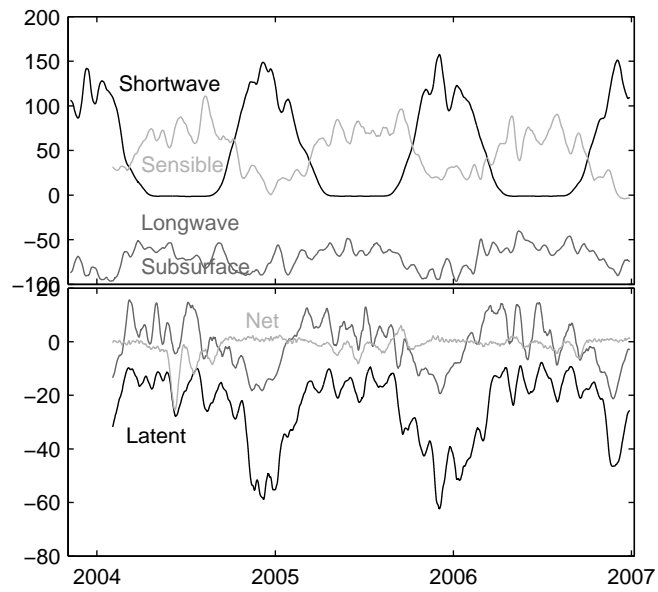


Figure 5.4. Energy budget timeseries – Wx 3.

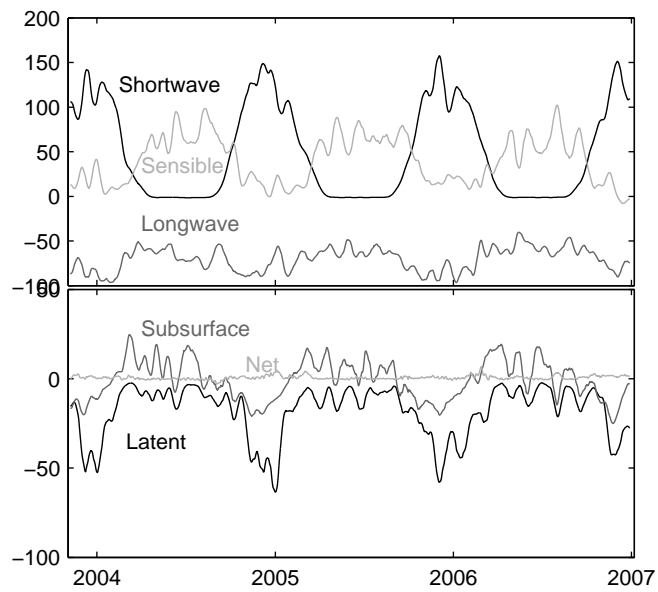


Figure 5.5. Energy budget timeseries – Wx 4.



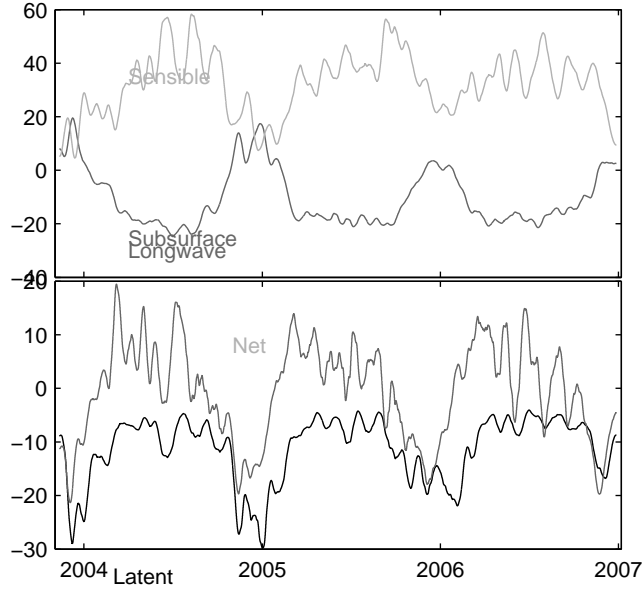


Figure 5.6. Energy budget timeseries – Wx 5.

Table 5.1. Summertime components of the energy budget for NDJ 2005/6. Abbreviations defined in equation 1.4, and  $R$  stands for net radiation.

	SW	LW	R	H	L	G	E
Wx Bo	219	-88	131	...	...	...	...
Wx T	125	-85 <sup>a</sup>	40	7	-34	-13	0
Wx 1	116	-85	31	18	-36	-12	0
Wx 2	143	-89	54	8	-49	-12	1
Wx 3	120 <sup>b</sup>	-85 <sup>b</sup>	35 <sup>b</sup>	24	-48	-11	1
Wx 4	120	-85	35	18	-41	-12	0
Wx 5	...	...	0	27	-17	-11	-0
Wx 6	...	...	124	...	...	...	...
Wx Be	250	-88 <sup>c</sup>	162	...	...	...	...

<sup>a</sup> Assumed similar to Wx 1.

<sup>b</sup> Assumed similar to Wx 4.

<sup>c</sup> Assumed similar to Wx Bo.

Table 5.2. Wintertime components of the energy budget for MJJ 2006. Abbreviations defined in equation 1.4, and  $R$  stands for net radiation.

	SW	LW	R	H	L	G	E
Wx Bo	-0	-35	-35	...	...	...	...
Wx T	-0	-56 <sup>a</sup>	-56	56	-6	6	-0
Wx 1	-1	-56	-58	61	-8	5	0
Wx 2	-1	-67	-69	72	-9	5	-0
Wx 3	-1 <sup>b</sup>	-57 <sup>b</sup>	-58 <sup>b</sup>	68	-15	4	-1
Wx 4	-1	-57	-58	61	-8	5	0
Wx 5	...	...	-37	38	-6	5	-1
Wx 6	...	...	-46	...	...	...	...
Wx Be	0	-35 <sup>c</sup>	-35	...	...	...	...

<sup>a</sup> Assumed similar to Wx 1.

<sup>b</sup> Assumed similar to Wx 4.

<sup>c</sup> Assumed similar to Wx Bo.

Table 5.3. Energy Balance Table – Winter 2004

Winter4	SW	LW	R	H	L	G	E
Wx Bo	-0	-39	-39	...	...	...	...
Wx T	-0	-68 <sup>a</sup>	-68	66	-7	9	0
Wx 1	-1	-68	-69	68	-9	9	-0
Wx 2	-1	-73	-74	71	-11	8	-6
Wx 3	-1 <sup>b</sup>	-65 <sup>b</sup>	-67 <sup>b</sup>	67	-16	6	-9
Wx 4	-1	-65	-67	64	-7	10	-0
Wx 5	...	...	-42	42	-8	7	-1
Wx 6	...	...	-49	...	...	...	...
Wx Be	0	-39 <sup>c</sup>	-39	...	...	...	...

<sup>a</sup> Assumed similar to Wx 1.

<sup>b</sup> Assumed similar to Wx 4.

<sup>c</sup> Assumed similar to Wx Bo.

Table 5.4. Energy Balance Table – Summer 2004/5

Summer5	SW	LW	R	H	L	G	E
W <sub>x</sub> Bo	216	-83	133	...	...	...	...
W <sub>x</sub> T	111	-77 <sup>a</sup>	34	14	-33	-15	0
W <sub>x</sub> 1	101	-77	24	23	-33	-13	0
W <sub>x</sub> 2	128	-82	46	10	-42	-13	1
W <sub>x</sub> 3	124 <sup>b</sup>	-80 <sup>b</sup>	44 <sup>b</sup>	18	-49	-12	1
W <sub>x</sub> 4	124	-80	44	14	-42	-14	1
W <sub>x</sub> 5	...	...	19	17	-23	-12	0
W <sub>x</sub> 6	...	...	115	...	...	...	...
W <sub>x</sub> Be	244	-83 <sup>c</sup>	161	...	...	...	...

<sup>a</sup> Assumed similar to W<sub>x</sub> 1.<sup>b</sup> Assumed similar to W<sub>x</sub> 4.<sup>c</sup> Assumed similar to W<sub>x</sub> Bo.

Table 5.5. Energy Balance Table – Winter 2005

Winter5	SW	LW	R	H	L	G	E
W <sub>x</sub> Bo	-0	-43	-43	...	...	...	...
W <sub>x</sub> T	-0	-61 <sup>a</sup>	-61	65	-7	3	-0
W <sub>x</sub> 1	-1	-61	-62	69	-10	3	0
W <sub>x</sub> 2	-1	-67	-69	75	-12	4	-1
W <sub>x</sub> 3	-1 <sup>b</sup>	-62 <sup>b</sup>	-63 <sup>b</sup>	74	-17	3	-3
W <sub>x</sub> 4	-1	-62	-63	70	-11	4	0
W <sub>x</sub> 5	...	...	-37	40	-7	3	-0
W <sub>x</sub> 6	...	...	-45	...	...	...	...
W <sub>x</sub> Be	0	-43 <sup>c</sup>	-43	...	...	...	...

<sup>a</sup> Assumed similar to W<sub>x</sub> 1.<sup>b</sup> Assumed similar to W<sub>x</sub> 4.<sup>c</sup> Assumed similar to W<sub>x</sub> Bo.

Table 5.6. Energy Balance Table – NDJF for comparison to other authors’ work.

NDJF	SW	LW	R	H	L	G	E
Wx Bo	197	-85	112	...	...	...	...
Wx T	107	-81 <sup>a</sup>	27	11	-28	-9	0
Wx 1	99	-81	19	21	-30	-9	0
Wx 2	122	-86	37	12	-39	-9	1
Wx 3	110 <sup>b</sup>	-81 <sup>b</sup>	30 <sup>b</sup>	22	-41	-9	1
Wx 4	110	-81	30	15	-34	-9	1
Wx 5	...	...	4	23	-18	-8	0
Wx 6	...	...	104	...	...	...	...
Wx Be	217	-85 <sup>c</sup>	132	...	...	...	...

<sup>a</sup> Assumed similar to Wx 1.

<sup>b</sup> Assumed similar to Wx 4.

<sup>c</sup> Assumed similar to Wx Bo.

Table 5.7. Energy Balance Table – MAMJJASO for comparison to other authors’ work.

MAMJJASO	SW	LW	R	H	L	G	E
Wx Bo	16	-46	-30	...	...	...	...
Wx T	13	-66 <sup>a</sup>	-53	56	-7	4	0
Wx 1	12	-66	-54	60	-10	4	0
Wx 2	14	-72	-58	66	-12	4	-1
Wx 3	15 <sup>b</sup>	-64 <sup>b</sup>	-50 <sup>b</sup>	62	-18	3	-2
Wx 4	15	-64	-50	56	-10	4	0
Wx 5	...	...	-35	38	-8	4	-0
Wx 6	...	...	-28	...	...	...	...
Wx Be	20	-46 <sup>c</sup>	-26	...	...	...	...

<sup>a</sup> Assumed similar to Wx 1.

<sup>b</sup> Assumed similar to Wx 4.

<sup>c</sup> Assumed similar to Wx Bo.

Table 5.8. Energy Balance Table – December 21, 2003 – January 21, 2004 for comparison to *Lewis et al.* [1998].

	Lewis4	SW	LW	R	H	L	G	E
W <sub>x</sub> Bo	257	-92	165	...	...	...	...	...
W <sub>x</sub> T	126	-85 <sup>a</sup>	42	-0	-32	-9	0	
W <sub>x</sub> 1	116	-85	32	16	-38	-9	0	
W <sub>x</sub> 2	131	-91	40	12	-44	-7	1	
W <sub>x</sub> 3	114 <sup>b</sup>	-88 <sup>b</sup>	26 <sup>b</sup>	...	...	...	...	
W <sub>x</sub> 4	114	-88	26	25	-41	-8	2	
W <sub>x</sub> 5	...	...	2	24	-20	-6	1	
W <sub>x</sub> 6	...	...	120	...	...	...	...	
W <sub>x</sub> Be	284	-92 <sup>c</sup>	192	...	...	...	...	

<sup>a</sup> Assumed similar to W<sub>x</sub> 1.

<sup>b</sup> Assumed similar to W<sub>x</sub> 4.

<sup>c</sup> Assumed similar to W<sub>x</sub> Bo.

Table 5.9. Energy Balance Table – December 21, 2004 – January 21, 2005 for comparison to *Lewis et al.* [1998].

	Lewis5	SW	LW	R	H	L	G	E
W <sub>x</sub> Bo	212	-80	132	...	...	...	...	...
W <sub>x</sub> T	101	-63 <sup>a</sup>	37	5	-29	-12	2	
W <sub>x</sub> 1	87	-63	23	14	-27	-9	2	
W <sub>x</sub> 2	118	-71	47	3	-38	-11	2	
W <sub>x</sub> 3	116 <sup>b</sup>	-69 <sup>b</sup>	47 <sup>b</sup>	13	-47	-10	2	
W <sub>x</sub> 4	116	-69	47	14	-48	-10	3	
W <sub>x</sub> 5	...	...	22	13	-24	-10	1	
W <sub>x</sub> 6	...	...	117	...	...	...	...	
W <sub>x</sub> Be	237	-80 <sup>c</sup>	157	...	...	...	...	

<sup>a</sup> Assumed similar to W<sub>x</sub> 1.

<sup>b</sup> Assumed similar to W<sub>x</sub> 4.

<sup>c</sup> Assumed similar to W<sub>x</sub> Bo.

Table 5.10. Energy Balance Table – December 21, 2005 – January 21, 2006 for comparison to *Lewis et al.* [1998].

Lewis6	SW	LW	R	H	L	G	E
Wx Bo	231	-85	146	...	...	...	...
Wx T	120	-84 <sup>a</sup>	36	6	-30	-10	1
Wx 1	120	-84	37	8	-33	-10	1
Wx 2	152	-90	62	2	-51	-11	2
Wx 3	111 <sup>b</sup>	-86 <sup>b</sup>	25 <sup>b</sup>	29	-44	-8	1
Wx 4	111	-86	25	21	-35	-10	1
Wx 5	...	...	3	23	-16	-9	0
Wx 6	...	...	147	...	...	...	...
Wx Be	276	-85 <sup>c</sup>	191	...	...	...	...

<sup>a</sup> Assumed similar to Wx 1.

<sup>b</sup> Assumed similar to Wx 4.

<sup>c</sup> Assumed similar to Wx Bo.

Table 5.11. Energy Balance Table – Summer, All Years

Summer	SW	LW	R	H	L	G	E
Wx Bo	222	-87	135	...	...	...	...
Wx T	125	-82 <sup>a</sup>	43	7	-32	-15	3
Wx 1	111	-82	29	18	-34	-13	0
Wx 2	135	-87	49	7	-42	-13	1
Wx 3	120 <sup>b</sup>	-83 <sup>b</sup>	37 <sup>b</sup>	18	-45	-12	1
Wx 4	120	-83	37	15	-38	-13	1
Wx 5	...	...	8	22	-19	-11	0
Wx 6	...	...	113	...	...	...	...
Wx Be	248	-87 <sup>c</sup>	162	...	...	...	...

<sup>a</sup> Assumed similar to Wx 1.

<sup>b</sup> Assumed similar to Wx 4.

<sup>c</sup> Assumed similar to Wx Bo.

Table 5.12. Energy Balance Table – Winter, All Years

Winter	SW	LW	R	H	L	G	E
Wx Bo	-0	-39	-39	...	...	...	...
Wx T	-0	-62 <sup>a</sup>	-62	62	-6	6	-0
Wx 1	-1	-62	-63	66	-9	6	0
Wx 2	-1	-69	-71	73	-11	6	-2
Wx 3	-1 <sup>b</sup>	-61 <sup>b</sup>	-62 <sup>b</sup>	70	-16	5	-4
Wx 4	-1	-61	-62	65	-9	6	0
Wx 5	...	...	-39	40	-7	5	-1
Wx 6	...	...	-47	...	...	...	...
Wx Be	0	-39 <sup>c</sup>	-39	...	...	...	...

<sup>a</sup> Assumed similar to Wx 1.<sup>b</sup> Assumed similar to Wx 4.<sup>c</sup> Assumed similar to Wx Bo.

Table 5.13. Energy Balance Table – Three Whole Years, December 2003 – November 2006.

whole	SW	LW	R	H	L	G	E
Wx Bo	76	-59	17	...	...	...	...
Wx T	44	-71 <sup>a</sup>	-27	41	-14	-0	0
Wx 1	41	-71	-30	47	-16	-0	0
Wx 2	50	-77	-27	48	-21	-0	-0
Wx 3	46 <sup>b</sup>	-70 <sup>b</sup>	-24 <sup>b</sup>	51	-25	-1	-1
Wx 4	46	-70	-24	43	-18	-0	1
Wx 5	...	...	-22	33	-11	-0	-0
Wx 6	...	...	15	...	...	...	...
Wx Be	85	-59 <sup>c</sup>	26	...	...	...	...

<sup>a</sup> Assumed similar to Wx 1.<sup>b</sup> Assumed similar to Wx 4.<sup>c</sup> Assumed similar to Wx Bo.

## 5.2 Discussion of the Energy Budget

Not surprisingly, the energy budget of Taylor Glacier's surface has the same general features as other Antarctic sites: gain of radiative energy in summer and loss in winter; year-round loss of latent heat by sublimation (condensation and hoar deposition being common but quantitatively negligible processes); small gains and losses of heat to the subsurface in winter and summer, respectively. Sensible heating of the surface is unusually large at Taylor Glacier because of strong down-slope katabatic winds and frequent cyclonic disturbances.

On the ablation zone of Canada Glacier, approximately 15 km east of Taylor Glacier, *Lewis et al.* [1998] determined an energy budget for 21 December - 21 January 1994/5 that was very similar to the budget at our lowest station, Wx 1, for the same calendar days but in 2005/6. The similarity extended to our respective calculations of sublimation: 3.65 cm w.e. for Canada Glacier and 3.2 cm w.e. for Taylor Glacier. One difference was that the Taylor Glacier sensible heat flux was positive. Moreover, in 1995/6 on Canada Glacier, *Lewis et al.* [1998] found a significantly higher net radiation that produced a large quantity of melt. We did not observe melt at our weather station sites on Taylor Glacier.

Sublimation from Lake Hoare (an ice-covered lake 10 km east of Taylor Glacier terminus) in 1986 was estimated from meteorological data to be  $35.0 \pm 6.3$  cm [*Clow et al.*, 1988] which is in line with the values we found on Taylor Glacier.

Compared to the blue-ice sites in Queen Maud Land (QML) studied by *Bintanja* [2000], summertime latent heat losses at Taylor Glacier were large. Yet the net shortwave and longwave values were nearly identical. Thus, it was the large sensible heat fluxes that sustained surface conditions conducive to rapid sublimation at Taylor Glacier. The larger sensible fluxes at Taylor, in turn, appear to reflect warmer air more than strong winds. At Scharffenbergbotnen (in QML), for example, the reported summer wind speeds were similar to those near the terminus of Taylor (Wx T), but air temperature at Wx T was higher, sensible heat flux was  $+7 \text{ W/m}^2$  instead of  $-7 \text{ W/m}^2$ , and latent flux was  $-34 \text{ W/m}^2$  instead of  $-29 \text{ W/m}^2$ .



# Chapter 6

## Sublimation Variability, Analyzed

By systematically examining our station data and making comparisons to satellite imagery, we found that weather variability at Taylor Glacier reflects four distinct patterns or modes: (1) stormy weather related to cyclonic systems, (2) dominance of strong katabatic winds, (3) dominance of diurnal fluctuations in wind speed and direction, and (4) calm conditions. Although sublimation occurred in all types of conditions, it occurred most rapidly during stormy weather and strong katabatic winds. Case studies illustrate this in more detail.

### 6.1 Magnitude versus frequency of sublimation

The importance of rapid but brief sublimation events compared to slow and persistent conditions can be assessed by transforming a timeseries of sublimation rate into a frequency distribution of the occurrence of sublimation as a function of rate [following *Wolman and Miller*, 1960; *Pickup and Rieger*, 1979]. Specifically, total sublimation in a time interval  $\tau$  is  $\int_{\tau} f(\dot{S}) \dot{S} d\dot{S}$  where  $f$  denotes the frequency of occurrence of sublimation of rate  $\dot{S}$ . Figure 6.1 plots the integrand of this formula for the four different weather modes, at one station. The fastest sublimation occurred during storms and periods with strong katabatic winds. However, these events (with sublimation  $>0.05$  mm per 20 minute interval) occurred infrequently (1-2% of the time) and contributed 10-15% of the total sublimation. Slow sublimation ( $<0.025$  mm/interval) happened during all four modes, was frequent (80-90% of the record) and accounted for 50-60% of the total sublimation. This result bodes well for our ability to understand sublimation in past and future climates, to the extent that forecasts of seasonal conditions are generally more accurate than forecasts of extreme events.

Cumulative timeseries of sublimation (figure 6.7) show that the katabatic/foehn mode produced the most sublimation at all stations except Wx 5. Because sublimation at Wx 5 was relatively steady, the higher frequency of the calm mode meant that it produced the most sublimation there. Station 5 rarely was swept up in the warm, fast, and dry katabatic/foehn winds from Windy Gully which were so effective at producing fast sublimation at the other stations.

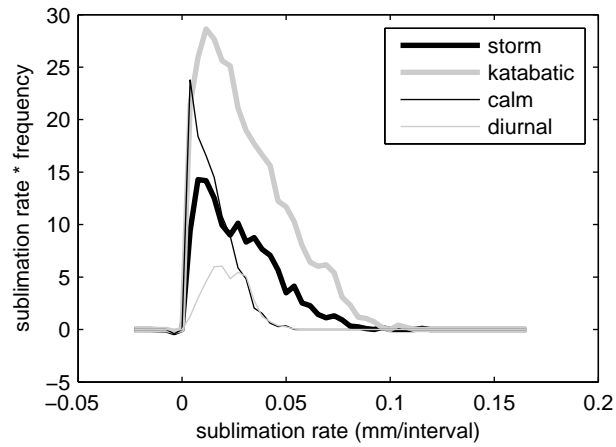


Figure 6.1. The relationship between the frequency and magnitude of sublimation at Wx 1 indicates that frequent, small events ( $<0.025$  mm/interval) contribute more to the total sublimation than infrequent, large events ( $>0.05$  mm/interval). Storms and katabatic wind periods have the largest sublimation rates while the high frequency of calm periods mean they are important too.

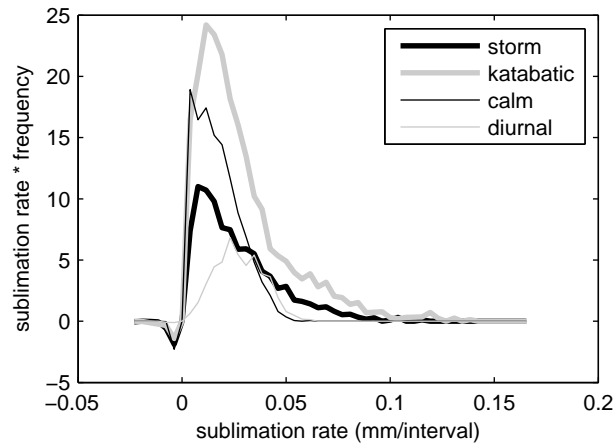


Figure 6.2. Magnitude-frequency of sublimation with modes – Wx T.

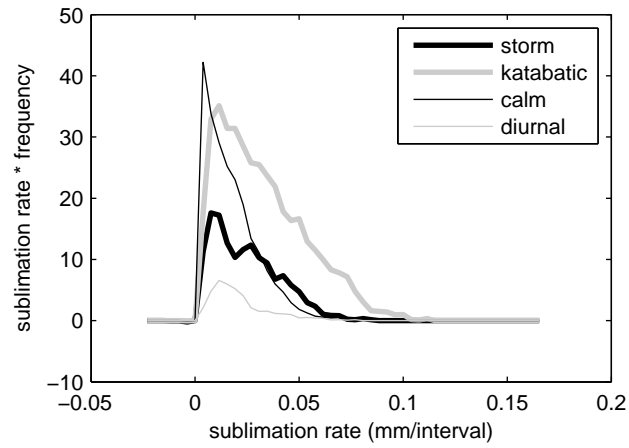


Figure 6.3. Magnitude-frequency of sublimation with modes – Wx 2.

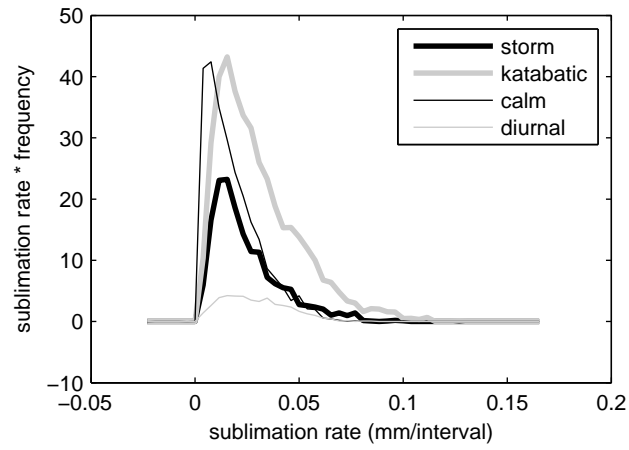


Figure 6.4. Magnitude-frequency of sublimation with modes – Wx 3.

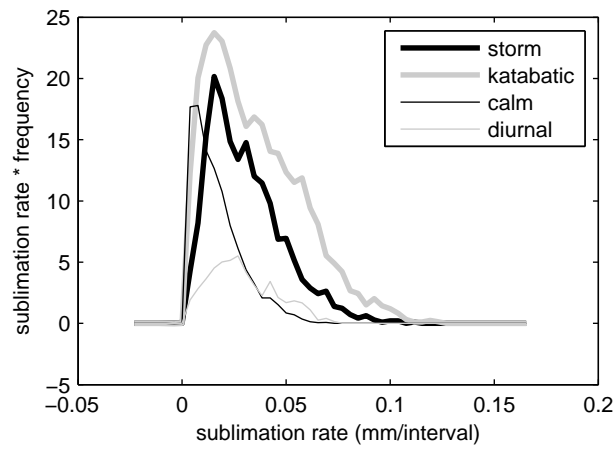


Figure 6.5. Magnitude-frequency of sublimation with modes – Wx 4.

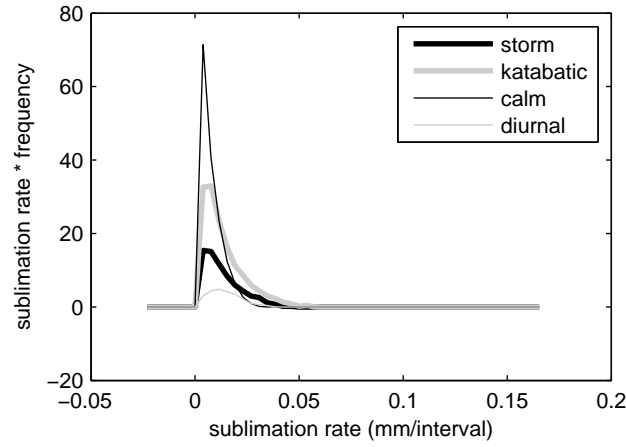


Figure 6.6. Magnitude-frequency of sublimation with modes – Wx 5.

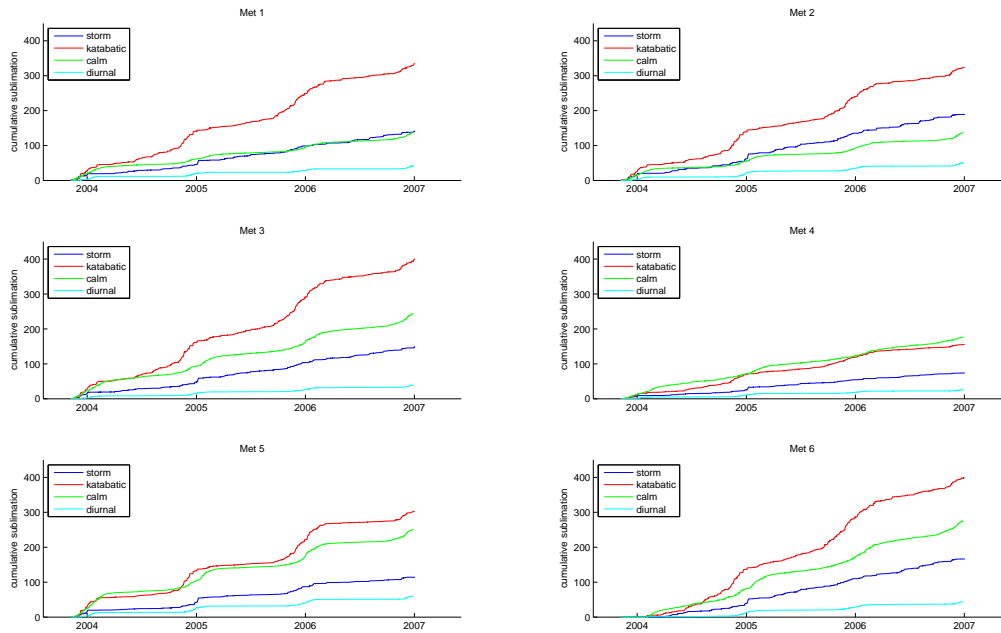


Figure 6.7. Cumulative sum of modeled sublimation for different modes of weather variability. Refer to table 3.2 to convert between the ‘Met’ and ‘Wx’ notation. Ignore Met 5: it was on rock, not ice.

## 6.2 Example Time Periods

### 6.2.1 March 2006: katabatic/foehn and then a storm

A strong katabatic/foehn wind event raged for more than 5 days in early March, 2006; this event not only appears in our station data (Wx 1 shown in figure 6.8, more stations in figures 6.13 through 6.18) but also can be seen clearly in AVHRR imagery from March 4th as dark streaks of warm air descending off the Antarctic plateau (figure 6.9). The event began with marked increases of wind speeds (to about 10 m/s) at each station on March 1st. On March 1st and 2nd temperatures gradually rose from -20 to -12°C. Relative humidity fell from 60% to 20%, causing the vapor pressure difference between the air and the surface to rise from below 0.5 up to 1.5 mbar. Over three days, wind speeds also increased to about 20 m/s. The fast winds combined with the enhanced vapor pressure difference produced some of the highest sublimation rates of the fall.

The strong katabatic flow was followed by a calm period wherein wind speeds dropped to less than 2 m/s, the temperature abruptly dropped 8°C in 4 hours, and the relative and absolute humidities jumped up as well. The air mass came from Taylor Valley, as evidenced by easterly wind directions (not shown). Sublimation during this period was close to zero. The calm period lasted 2 days before the effects of a storm approaching from the Ross Sea began to be felt.

The storm (also identified via AVHRR images, e.g. figure 6.10) brought faster winds and clouds to all stations. On the third day of the storm (March 12th), Wx 1 experienced rapidly oscillating conditions. Periods of fast downglacier wind, warm temperature, low relative humidity, and rapid sublimation alternated with the opposite. The system would stay in one state for as little as 1 hour during these fluctuations. The stations above Wx 1 experienced downglacier winds the whole time. Meanwhile, LTER stations below our station 1 experienced consistent, weak upglacier winds, low temperatures, and high humidities. The low stations were in an inversion, Wx 1 was on the border – in and out of the inversion, and higher stations were outside the inversion experiencing the effects of the storm.

The NOAA-NCEP reanalysis corresponding to the days when the AVHRR images were captured show that the synoptic conditions were remarkably similar between the two cases (figures 6.11 and 6.12). All four fields shown (Temperature, Wind Speed, Pressure Anomaly, and Sublimation Heat Flux) were from the surface layer of the model. In both cases the reanalysis is fairly consistent with our weather station data.

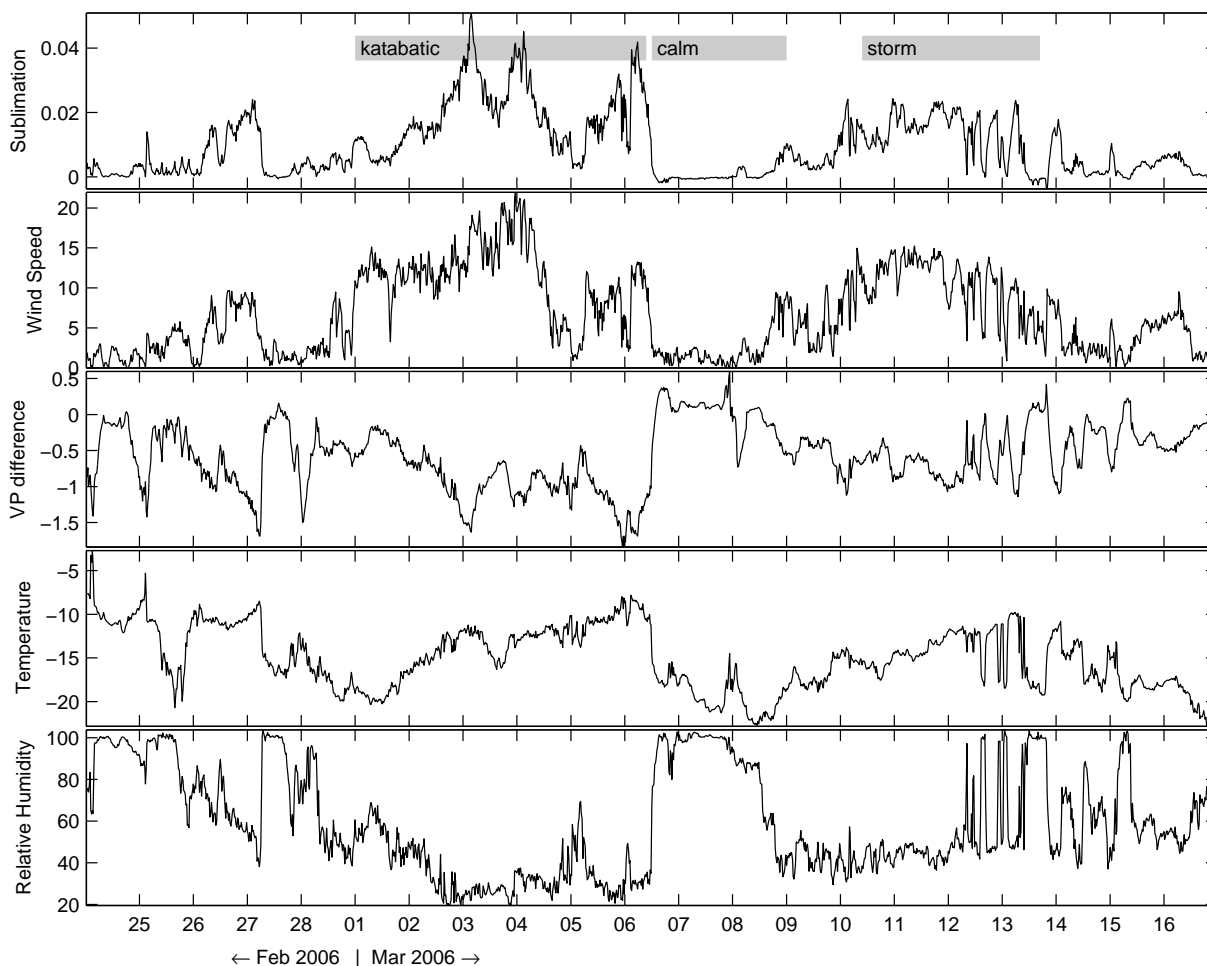


Figure 6.8. Weather patterns at Wx 1 are distinctly different during katabatic, calm, and stormy periods. Panels show sublimation (mm per 20-minute interval), wind speed (m/s), vapor pressure difference between the measurement height and the surface (mbar), temperature ( $^{\circ}\text{C}$ ), and relative humidity (%) for late February and early March 2006. When the vapor pressure difference and wind speed are large, the ablation is high. When the vapor pressure difference or the wind speeds are low, so is ablation.

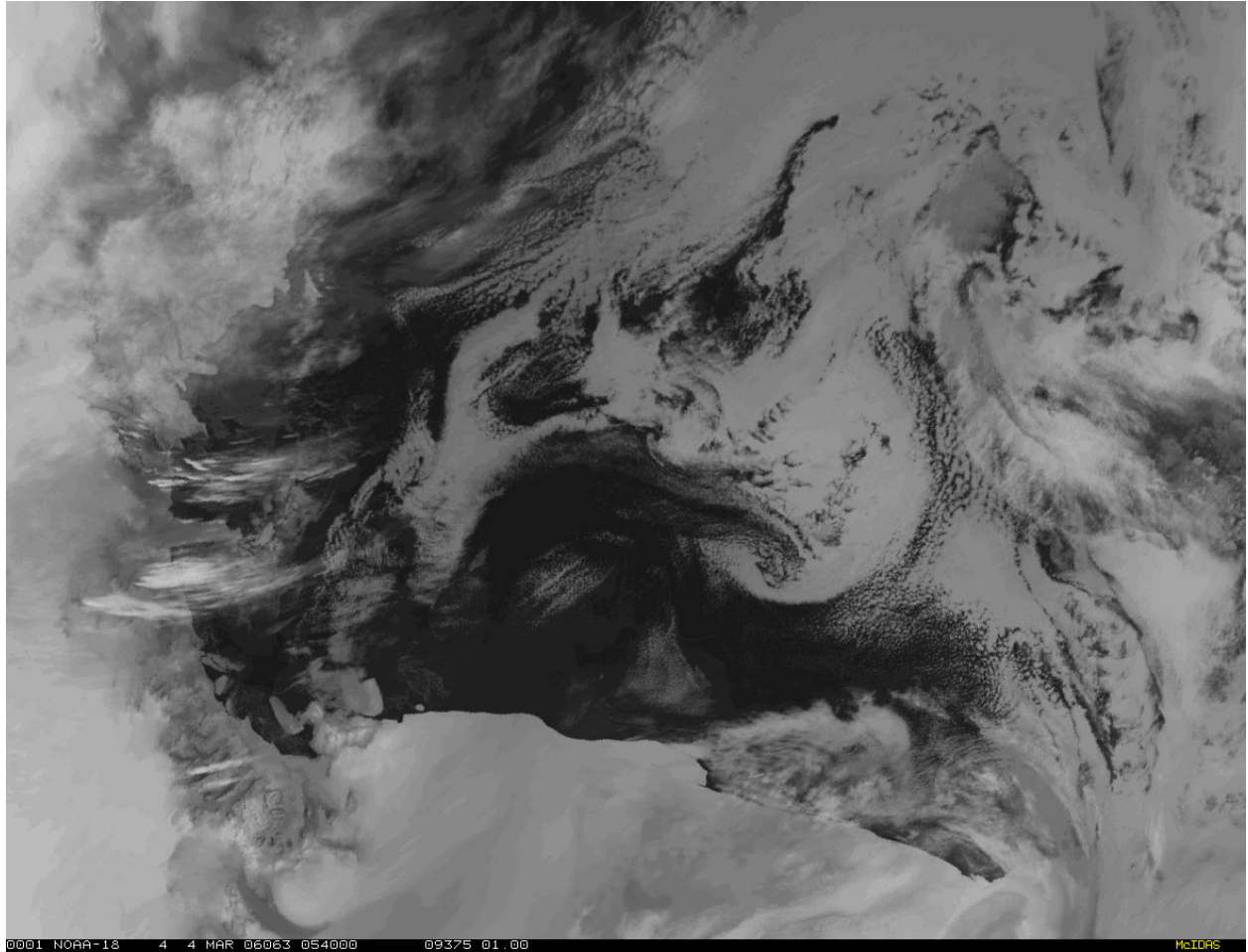


Figure 6.9. Advanced Very High Resolution Radiometer (AVHRR) image of the Taylor Glacier region on March 4th, 2006. The dark (warm) trace of the katabatic/foehn wind can be seen emanating from Skelton Glacier, just south of Taylor Glacier. White (cold) cloud streaks are also visible, indicating fast winds aloft. From <http://avhrr.acecrc.org.au/>

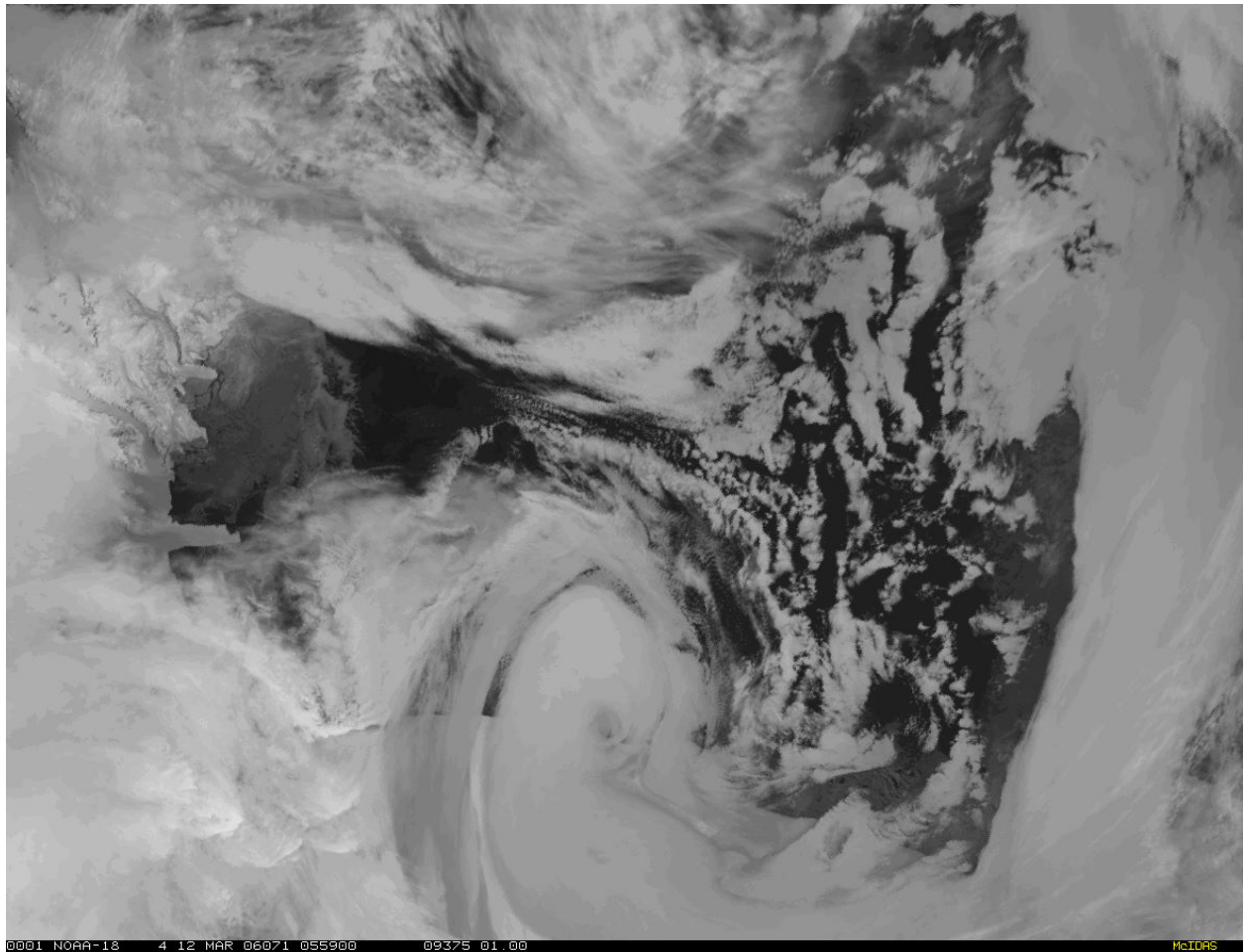


Figure 6.10. This AVHRR image was taken March 12th, 2006 when Taylor Glacier was in the midst of the storm. A comma cloud is clearly visible and Taylor Glacier is under thick clouds.



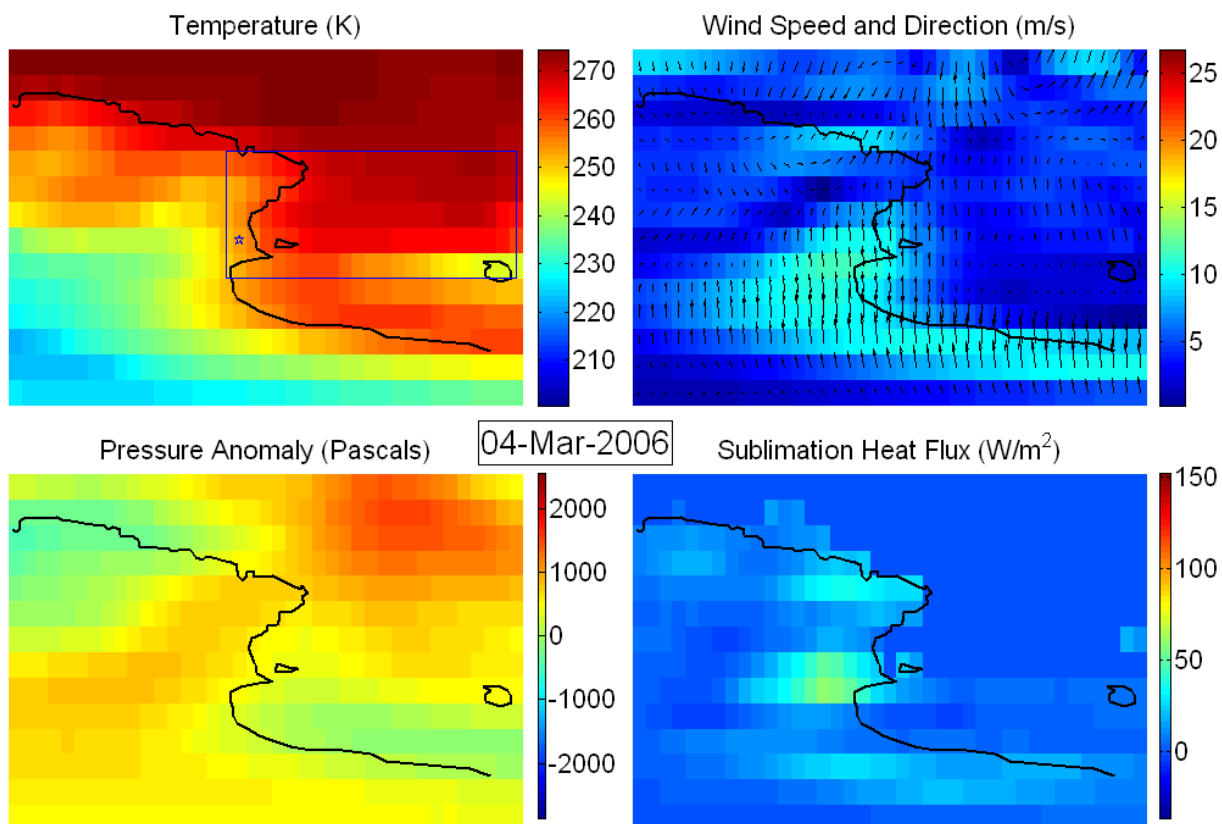


Figure 6.11. NOAA-NCEP reanalysis for March 4th, 2006 during a katabatic/foehn event. The blue star and box show the approximate locations of Taylor Glacier and the AVHRR images respectively. Data from <http://iridl.ldeo.columbia.edu/>

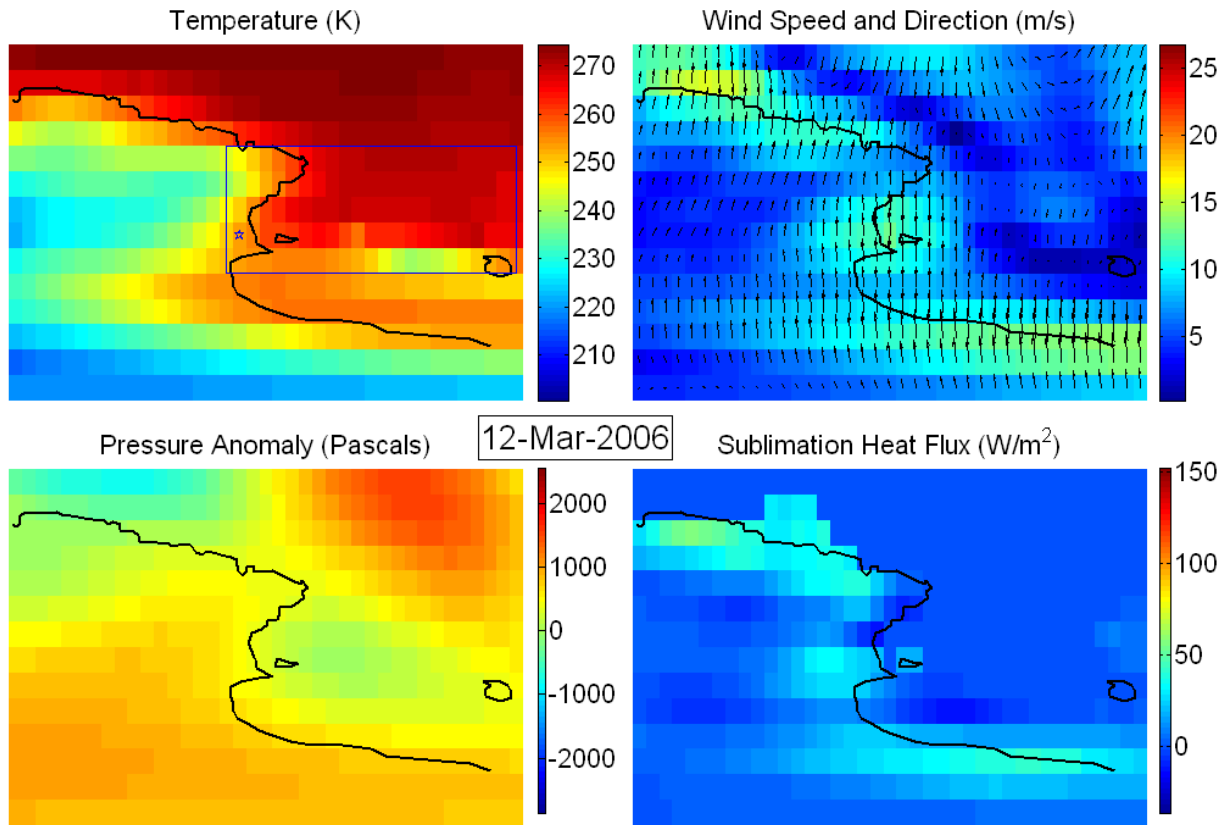


Figure 6.12. NOAA-NCEP reanalysis for March 12th, 2006 during a storm.

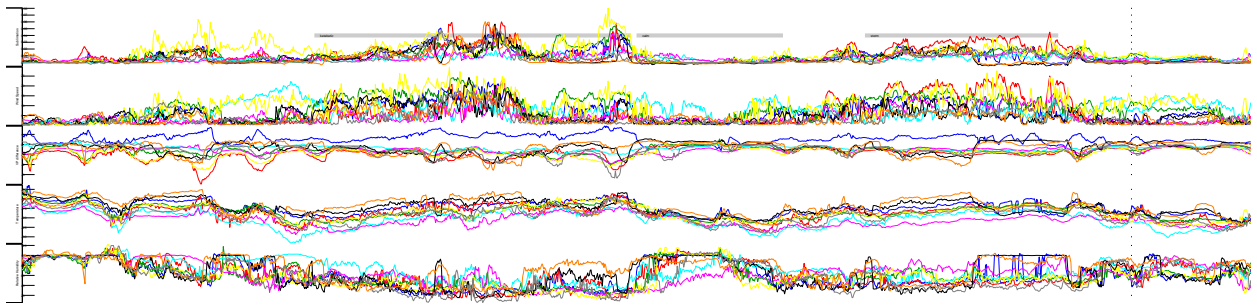


Figure 6.13. Ablation variables example for All Stations. Axes are the same as in figure 6.8. Refer to figure 6.19 for an index map with the station color coding.

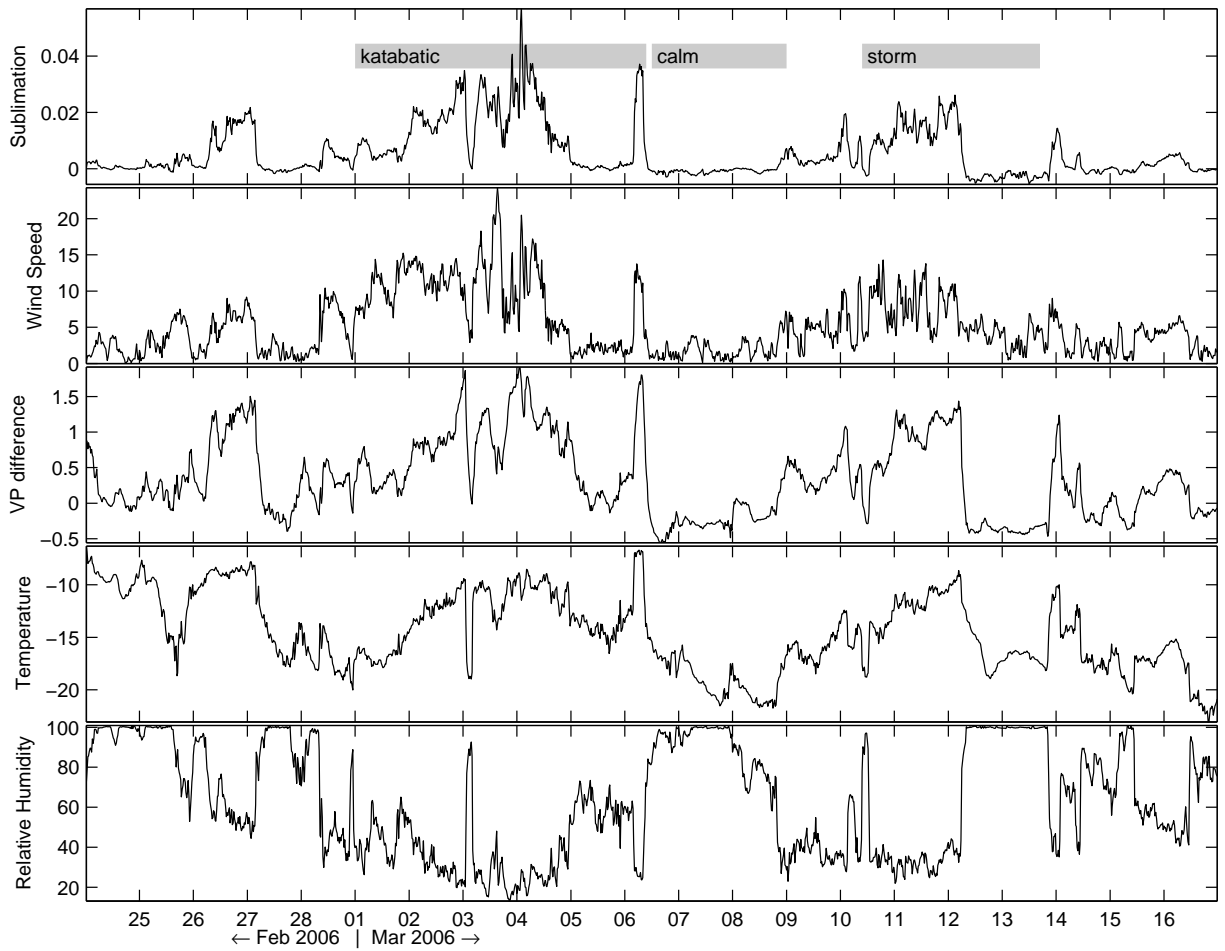


Figure 6.14. Ablation variables example – Wx T.

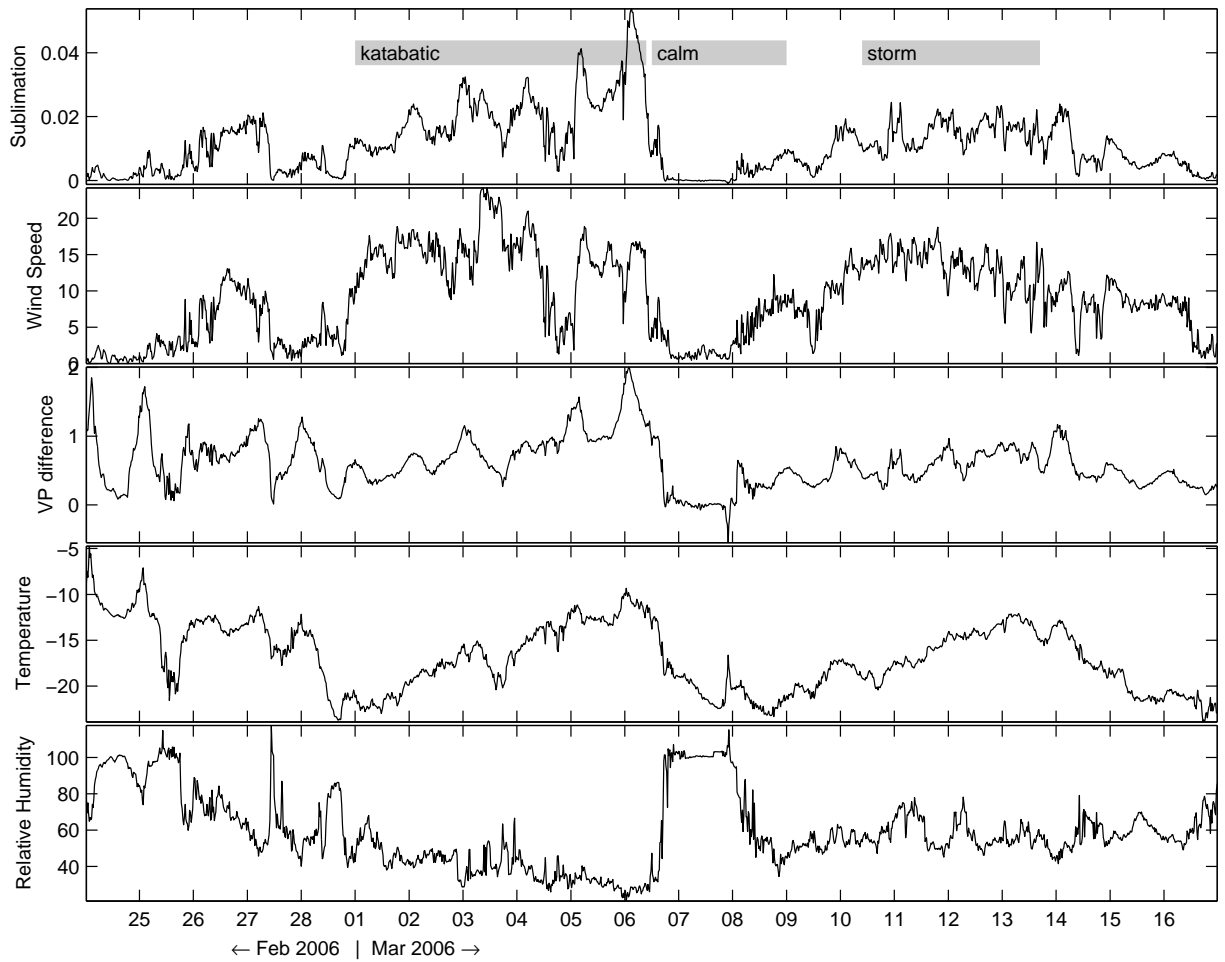


Figure 6.15. Ablation variables example – Wx 2.

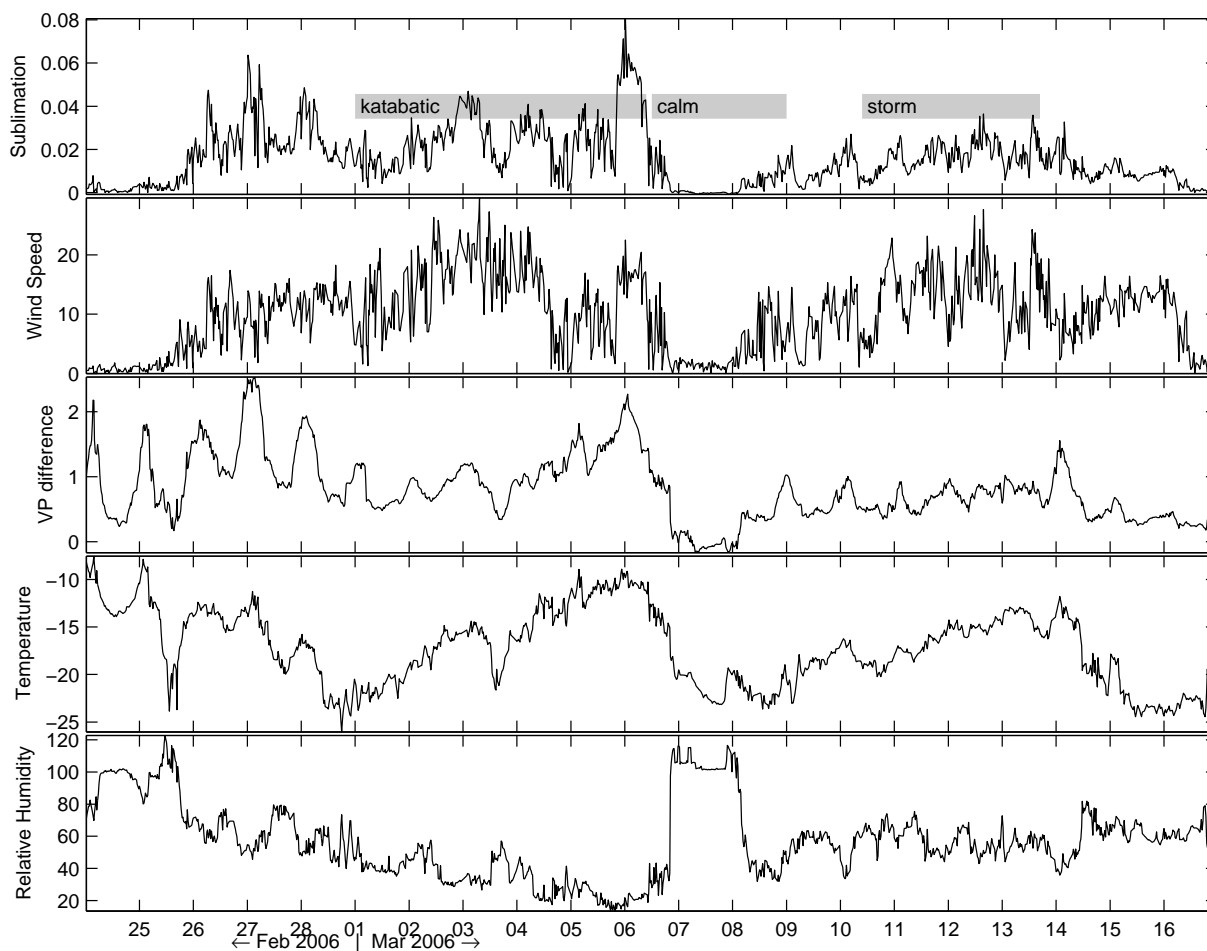


Figure 6.16. Ablation variables example – Wx 3.

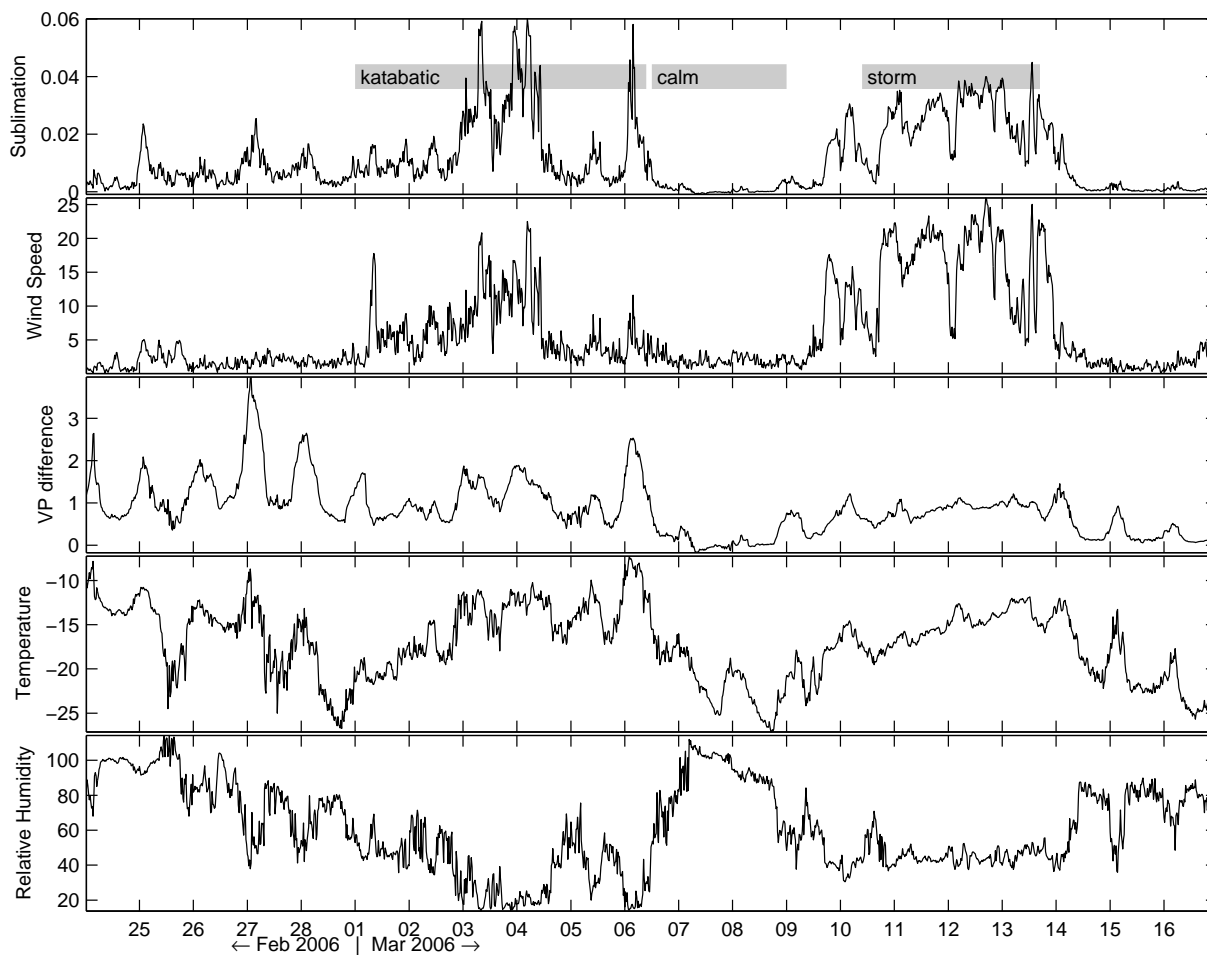


Figure 6.17. Ablation variables example – Wx 4.

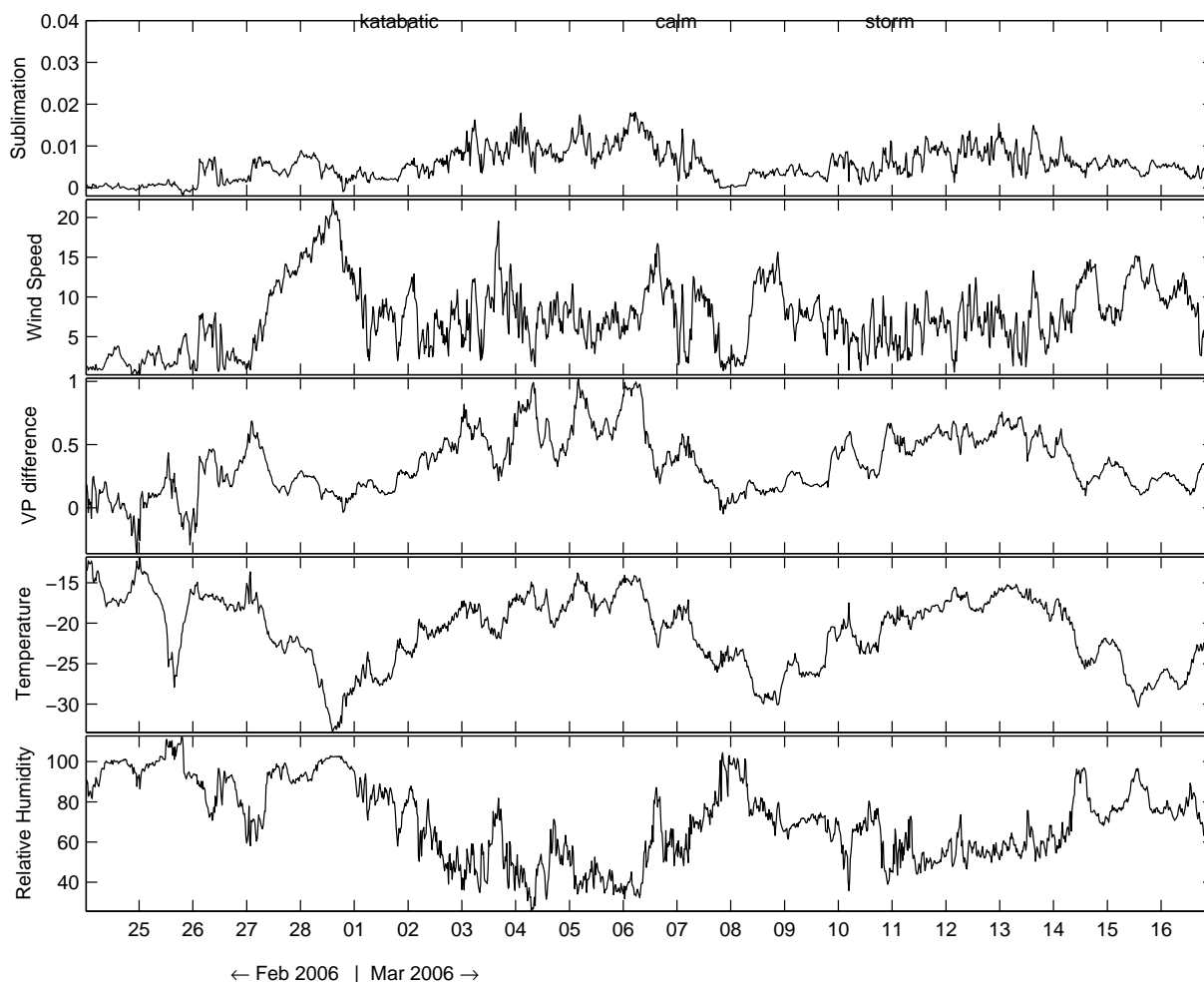


Figure 6.18. Ablation variables example – Wx 5.

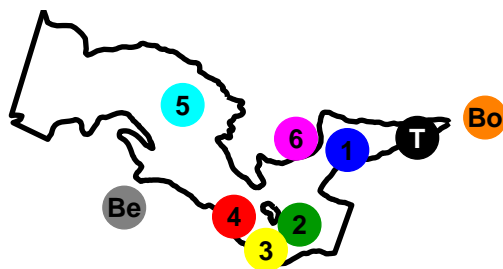
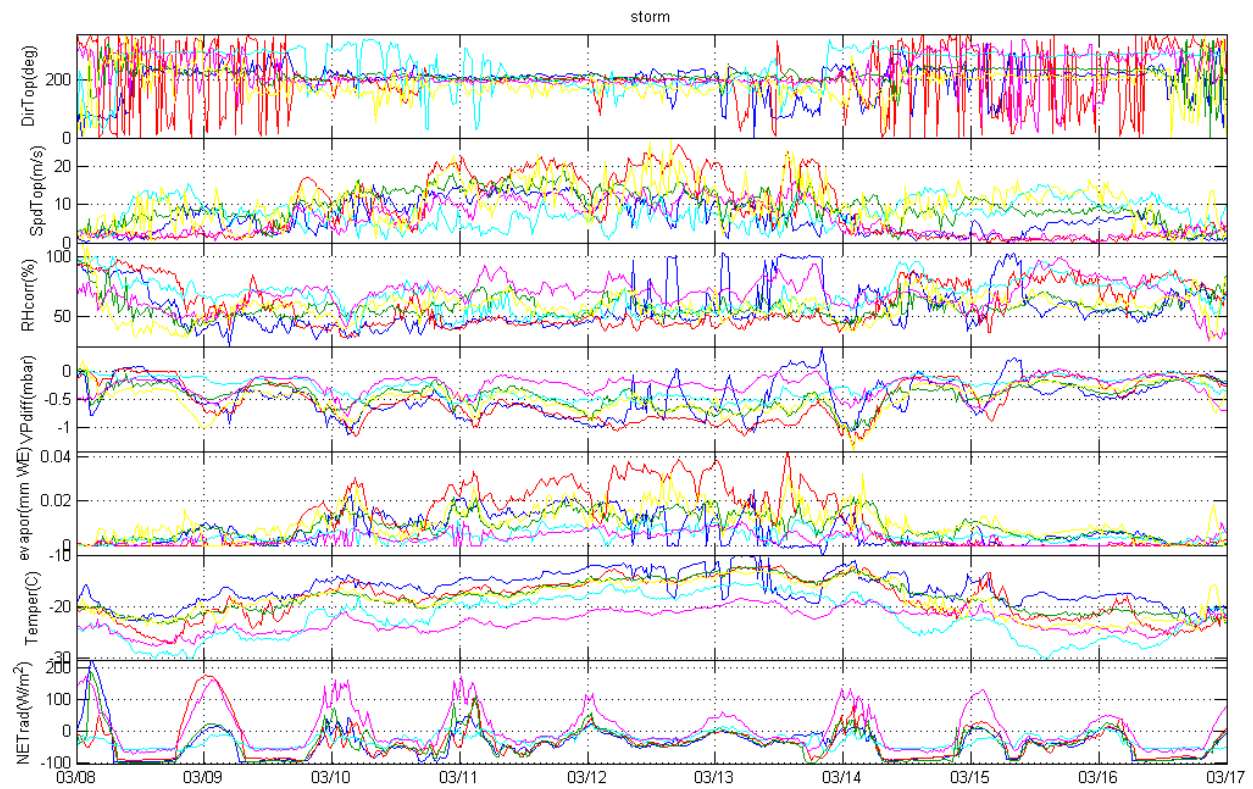


Figure 6.19. Another way of looking at the data from the March 2006 storm plotted above. All stations are on the same axes and are coded by color, as shown on the index map.



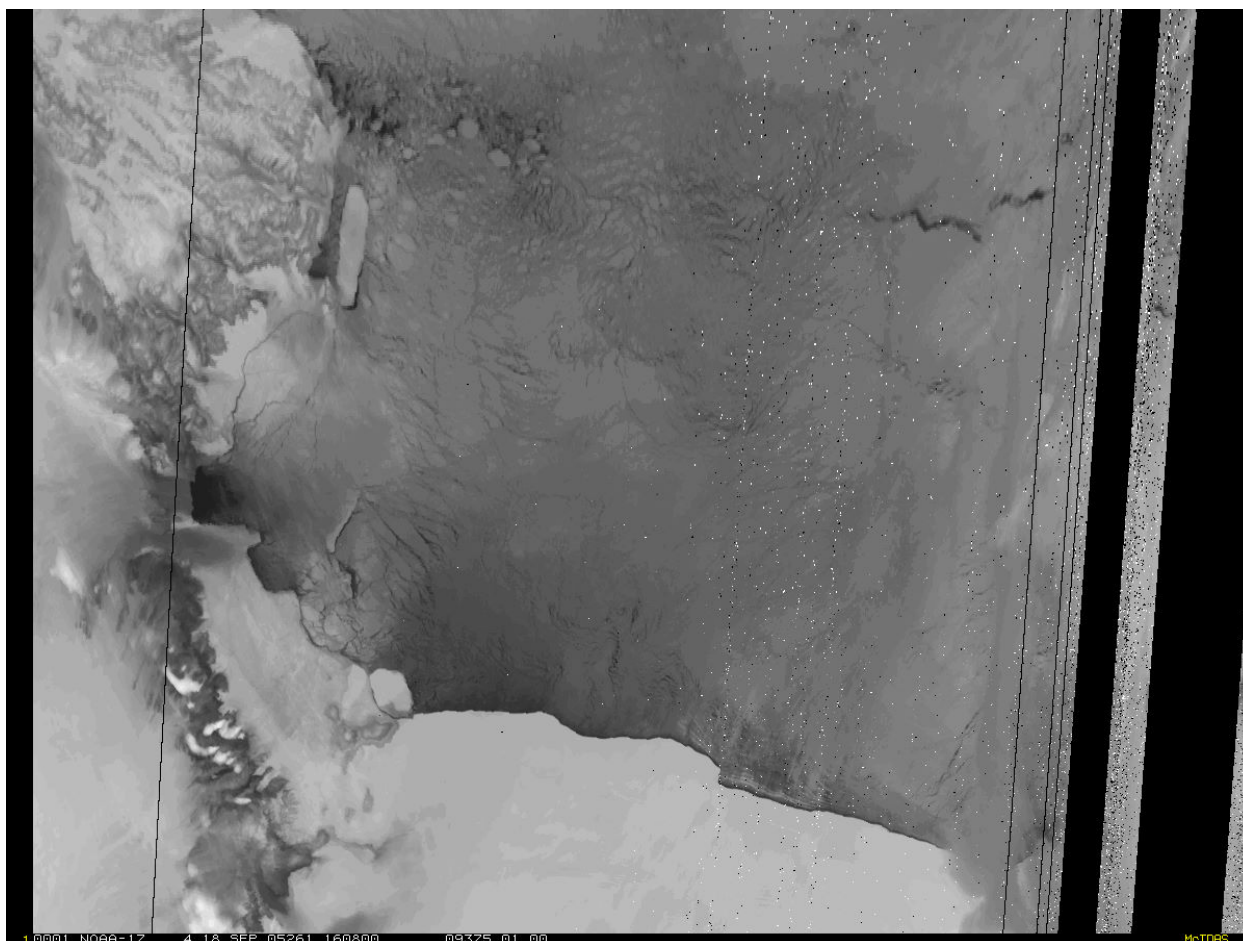


Figure 6.20. AVHRR image of a katabatic event at 16:08 UTC on September 18th, 2005. Dark areas were warm (the Dry Valleys and Transantarctic Mountains along the left side of the image). Drainage winds from the continent were evident by the sea ice they cleared from Terra Nova Bay (dark spot of ocean in the left center).

### 6.2.2 September 2005: katabatic/foehn

A big storm swept over the Ross Ice Shelf and Sea on the September 16th, 2005, followed by a strengthening of the katabatic/foehn winds on the 17-19th, as seen in figure 6.20. The event brought incredibly warm temperatures – up to 0°C at Wx 4 (1012 m elevation), fast winds, and dry air which combined to produce the highest ablation rates of the spring (figure 6.21). Wx 3 was the first to experience an increase in wind speed and maintained the fastest wind speeds throughout the event. The event started gradually at most stations, with temperatures rising 15 or 20 degrees in 24 hours. However, stations Bo, T, and 4 experienced especially rapid warming at the onset (16° in one hour at station T, ). The event passed almost as quickly as it arrived, with temperatures decreasing to their former levels within a day following the event. This contrasts with the findings of *Nylen et al.* [2004] who observed temperatures decreases that took multiple days.

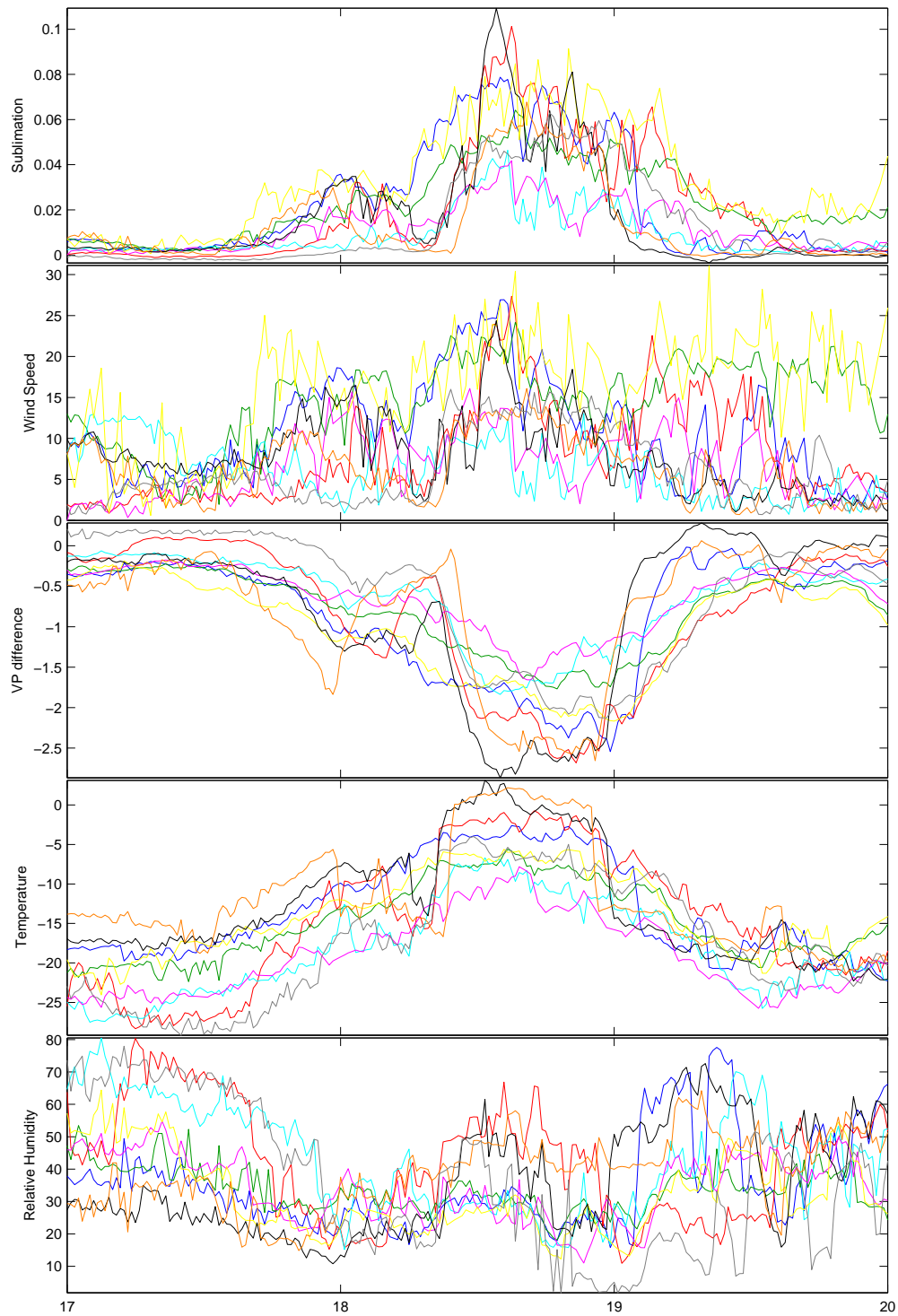


Figure 6.21. Ablation variables example for All Stations – September 17-20, 2005. Refer to figure 6.19 for an index map with the station color coding.

# Chapter 7

## Conclusions and Future Work

### 7.1 Concluding Remarks

The turbulent heat-flux methods used here are similar to those used on other blue-ice areas of Antarctica. Our surface temperature correction procedure is unique and may benefit other studies, because surface temperature is one of the important unknowns in the equations.

Our finding that the stability correction did not drastically affect the calculated sublimation may prove useful for extrapolation to other regions, climates, or time periods with unknown stability conditions. Future work (see below) will investigate this further.

The magnitude-frequency analysis may also aid extrapolation. Since the extreme events, which are inherently difficult to predict, are significantly less important than the “regular” low sublimation times, a climate forecast or hindcast may allow a reasonably accurate estimation of sublimation conditions. In the case of past Taylor Glacier climates, this may be used as input to an ice flow model to test our understanding of the glacier dynamics that led to the observed glacial deposits at various times within the last few hundred thousand years.

Once we are confident that we understand the present and past variations in sublimation on Taylor Glacier, we may have some confidence in our ability to predict what will happen to sublimation in the future, as the anthropogenically-modified climate continues to change. From an understanding of sublimation, we can predict the glacier’s likely response to the surface forcing and ultimately establish Taylor Glacier’s place in the bigger picture context of the entire Antarctic ice sheet.

### 7.2 Future Work

My next paper will attempt to find a relationship between sublimation and broader climate variables, instead of just the micro-meteorological data that we used here. We will

start by comparing our ablation data to the sublimation predicted from the simplest form of the equations discussed above. Then we will decompose the input data (vapor pressure difference and wind speed) into their climatologies and perturbations about the climatologies, excising any terms that are not significant. Assuming these approximations still are able to predict present-day sublimation with some accuracy, we will then adjust the climatologies to fit a variety of past and future scenarios.

A list of other things that I would like to try follows, ordered from big-picture important things to small-scale curiosities.

- Investigate the applicability of the methods described here to other glaciers in Antarctica and Greenland.
- Use MODIS and AVHRR satellite imagery, reanalysis data, and mesoscale modeling to better understand the synoptic conditions that affect the weather on Taylor Glacier. The AMPS model has a storm tracks field that may be interesting.
- Use empirical orthogonal functions to create a regional summary of the weather from our network of station data. Also try this with LTER data to put our data into the context of a longer time period.
- “Follow” a parcel of air as it moves down Taylor Glacier and see how its temperature and humidity change depending on the wind speed or synoptic conditions. The discussion of lapse rates in section 3.3.5 gets at this, but at a larger scale. Compare moisture changes in the parcel to sublimation from the glacier.
- Explore other methods to find the surface temperature appropriate for the energy flux calculations. This could be either measurements or modeling.
- Understand the spatial and temporal variability of surface roughness across the glacier, and the mechanisms that create the roughness (ablation hollows).
- Make use of the LIDAR elevation survey of the Taylor Glacier terminus to understand how the melt processes there interact with the sublimation processes described here.



Figure 7.1. A cliff above Plummet Glacier in the Kukri Hills. Plummet Glacier is a minor tributary to Taylor Glacier. Photo by Andy Bliss.

# Bibliography

- Aciego, S. M., K. M. Cuffey, J. L. Kavanaugh, D. L. Morse, and J. P. Severinghaus, Pleistocene ice and paleo-strain rates at Taylor Glacier, Antarctica, *Quaternary Research*, 68, 303–313, doi:10.1016/j.yqres.2007.07.013, 2007.
- Bintanja, R., On the glaciological, meteorological, and climatological significance of Antarctic blue ice areas, *Reviews Of Geophysics*, 37(3), 337–359, 1999.
- Bintanja, R., Surface heat budget of Antarctic snow and blue ice: Interpretation of spatial and temporal variability, *Journal of Geophysical Research*, 105, 24,387–24,408, doi:10.1029/2000JD900356, 2000.
- Bintanja, R., and C. H. Reijmer, Meteorological conditions over Antarctic blue-ice areas and their influence on the local surface mass balance, *Journal of Glaciology*, 47(156), 37–50, 2001.
- Box, J. E., and K. Steffen, Sublimation on the Greenland ice sheet from automated weather station observations, *Journal of Geophysical Research (Atmospheres)*, 106(D24), 33,965 – 33,981, 2001.
- Brock, B. W., and N. S. Arnold, A spreadsheet-based (Microsoft Excel) point surface energy balance model for glacier and snow melt studies, *Earth Surface Processes and Landforms*, 25(6), 649–658, 2000.
- Brook, E., Chronology of Taylor Glacier Advances in Arena Valley, Antarctica, Using in Situ Cosmogenic  $^3\text{He}$  and  $^{10}\text{Be}$ , *Quaternary Research*, 39, 11–23, doi:10.1006/qres.1993.1002, 1993.
- Clow, G. D., C. P. McKay, G. M. Simmons, and R. A. Wharton, Climatological Observations and Predicted Sublimation Rates at Lake Hoare, Antarctica, *Journal of Climate*, 1(7), 715–728, 1988.
- Cuffey, K. M., and W. S. B. Paterson, *The Physics of Glaciers*, 4th ed., 693 pp., Elsevier, 2010.
- Doran, P. T., C. P. McKay, G. D. Clow, G. L. Dana, A. G. Fountain, T. Nylen, and W. B. Lyons, Valley floor climate observations from the McMurdo dry valleys, Antarctica, 1986-2000, *Journal of Geophysical Research (Atmospheres)*, 107, 4772, doi: 10.1029/2001JD002045, 2002.

- Doran, P. T., et al., Antarctic climate cooling and terrestrial ecosystem response, *Nature*, *415*(6871), 517–520, 2002.
- Fountain, A. G., T. H. Nylén, K. L. Macclune, and G. L. Dana, Glacier mass balances (1993–2001), Taylor Valley, McMurdo Dry Valleys, Antarctica, *Journal of Glaciology*, *52*, 451–462, doi:10.3189/172756506781828511, 2006.
- Fountain, A. G., T. H. Nylén, A. Monaghan, H. J. Basagic, and D. Bromwich, Snow in the McMurdo Dry Valleys, Antarctica, *Int. J. Climatol.*, *30*(5), 633–642, 2009.
- Higgins, S. M., G. H. Denton, and C. H. Hendy, Glacial Geomorphology of Bonney Drift, Taylor Valley, Antarctica, *Geografiska Annaler. Series A, Physical Geography*, *82*(2/3), 365–389, 2000a.
- Higgins, S. M., C. H. Hendy, and G. H. Denton, Geochronology of Bonney Drift, Taylor Valley, Antarctica: Evidence for Interglacial Expansions of Taylor Glacier, *Geografiska Annaler. Series A, Physical Geography*, *82*(2/3), 391–409, 2000b.
- Hoffman, M. J., A. G. Fountain, and G. E. Liston, Surface energy balance and melt thresholds over 11 years at Taylor Glacier, Antarctica, *Journal of Geophysical Research (Earth Surface)*, *113*(F04014), 4014, doi:10.1029/2008JF001029, 2008.
- Holt, J. W., M. E. Peters, S. D. Kempf, D. L. Morse, and D. D. Blankenship, Echo source discrimination in single-pass airborne radar sounding data from the Dry Valleys, Antarctica: Implications for orbital sounding of Mars, *Journal of Geophysical Research (Planets)*, *111*(E06S24), 6, doi:10.1029/2005JE002525, 2006.
- Hubbard, A., W. Lawson, B. Anderson, B. Hubbard, and H. Blatter, Evidence for sub-glacial ponding across Taylor Glacier, Dry Valleys, Antarctica, *Annals of Glaciology*, *39*, 79–84, 2004.
- Iqbal, M., *An Introduction to Solar Radiation*, Academic Press, Toronto, Canada, 1983.
- Johnston, R. R., A. G. Fountain, and T. H. Nylén, The origin of channels on lower Taylor Glacier, McMurdo Dry Valleys, Antarctica, and their implication for water runoff, *Annals of Glaciology*, *40*, 1–7, 2005.
- Kavanaugh, J. L., and K. M. Cuffey, Dynamics and mass balance of Taylor Glacier, Antarctica: 2. Force balance and longitudinal coupling, *Journal of Geophysical Research (Earth Surface)*, *114*(F04010), 4011, doi:10.1029/2009JF001329, 2009.
- Kavanaugh, J. L., K. M. Cuffey, D. L. Morse, A. K. Bliss, and S. M. Aciego, Dynamics and mass balance of Taylor Glacier, Antarctica: 3. State of mass balance, *Journal of Geophysical Research (Earth Surface)*, *114*(F04010), 4012, doi:10.1029/2009JF001331, 2009a.
- Kavanaugh, J. L., K. M. Cuffey, D. L. Morse, H. Conway, and E. Rignot, Dynamics and mass balance of Taylor Glacier, Antarctica: 1. Geometry and surface velocities, *Journal of Geophysical Research (Earth Surface)*, *114*(F04010), 4010, doi:10.1029/2009JF001309, 2009b.

- Lenaerts, J. T. M., M. R. van den Broeke, S. J. Déry, G. König-Langlo, J. Ettema, and P. K. Munneke, Modelling snowdrift sublimation on an Antarctic ice shelf, *The Cryosphere*, 4(2), 179–190, 2010.
- Lewis, K. J., A. G. Fountain, and G. L. Dana, Surface energy balance and meltwater production for a Dry Valley glacier, Taylor Valley, Antarctica, *Annals of Glaciology*, 27, 603–609, 1998.
- Liu, H., K. Jezek, B. Li, and Z. Zhao, Radarsat Antarctic Mapping Project digital elevation model version 2, Digital media, 2001.
- Lythe, M. B., and D. G. Vaughan the BEDMAP Consortium, BEDMAP: A new ice thickness and subglacial topographic model of Antarctica, *Journal of Geophysical Research*, 106, 11,335–11,352, doi:10.1029/2000JB900449, 2001.
- Marchant, D. R., G. H. Denton, and I. Swisher, Carl C., Miocene-Pliocene-Pleistocene Glacial History of Arena Valley, Quartermain Mountains, Antarctica, *Geografiska Annaler. Series A, Physical Geography*, 75(4), 269–302, 1993.
- Monaghan, A. J., D. H. Bromwich, J. G. Powers, and K. W. Manning, The climate of the McMurdo, Antarctica, region as represented by one year of forecasts from the Antarctic Mesoscale Prediction System, *Journal Of Climate*, 18(8), 1174–1189, 2005.
- Morse, D. L., E. D. Waddington, and E. J. Steig, Ice age storm trajectories inferred from radar stratigraphy at Taylor Dome, Antarctica, *Geophysical Research Letters*, 25, 3383–3386, doi:10.1029/98GL52486, 1998.
- Morse, D. L., E. D. Waddington, H.-P. Marshall, T. A. Neumann, E. J. Steig, J. E. Dibb, D. P. Winebrenner, and R. J. Arthern, Accumulation Rate Measurements at Taylor Dome, East Antarctica: Techniques and Strategies for Mass Balance Measurements in Polar Environments, *Geografiska Annaler. Series A, Physical Geography*, 81(4), 683–694, 1999.
- Morse, D. L., E. D. Waddington, and L. A. Rasmussen, Ice deformation in the vicinity of the ice-core site at Taylor Dome, Antarctica, and a derived accumulation rate history, *Journal of Glaciology*, 53, 449–460, doi:10.3189/002214307783258530, 2007.
- Nylen, T. H., A. G. Fountain, and P. T. Doran, Climatology of katabatic winds in the McMurdo dry valleys, southern Victoria Land, Antarctica, *Journal of Geophysical Research (Atmospheres)*, 109, 3114, doi:10.1029/2003JD003937, 2004.
- Parish, T. R., and J. J. Cassano, Forcing of the Wintertime Antarctic Boundary Layer Winds from the NCEP-NCAR Global Reanalysis., *Journal of Applied Meteorology*, 40, 810–821, doi:10.1175/1520-0450(2001)040<0810:FOTWAB>2.0.CO;2, 2001.
- Peck, L., Temporal and spatial fluctuations in ground cover surface temperature at a northern New England site, *Atmospheric Research*, 41(2), 131–160, 1996.
- Pickup, G., and W. A. Rieger, A conceptual model of the relationship between channel characteristics and discharge, *Earth Surf. Process.*, 4(1), 37–42, 1979.



- Priscu, J. C., Life in the Valley of the "Dead", *BioScience*, 49(12), 959–959, doi:10.1525/bisi.1999.49.12.959, 1999.
- Robinson, P. H., Ice dynamics and thermal regime of Taylor Glacier, South Victoria Land, Antarctica, *Journal of Glaciology*, 30, 153–160, 1984.
- Smeets, C. J. P. P., and M. R. van den Broeke, Temporal and Spatial Variations of the Aerodynamic Roughness Length in the Ablation Zone of the Greenland Ice Sheet, *Boundary-Layer Meteorology*, 128, 315–338, doi:10.1007/s10546-008-9291-0, 2008.
- Speirs, J. C., D. F. Steinhoff, H. A. McGowan, D. H. Bromwich, and A. J. Monaghan, Foehn Winds in the McMurdo Dry Valleys, Antarctica: The Origin of Extreme Warming Events\*, *Journal of Climate*, 23, 3577–3598, doi:10.1175/2010JCLI3382.1, 2010.
- Steig, E. J., D. L. Morse, E. D. Waddington, M. Stuiver, P. M. Grootes, P. A. Mayewski, M. S. Twickler, and S. I. Whitlow, Wisconsinan and Holocene Climate History from an Ice Core at Taylor Dome, Western Ross Embayment, Antarctica, *Geografiska Annaler: Series A, Physical Geography*, 82(2-3), 213–235, 2000.
- Van de Berg, W. J., M. R. Van den Broeke, C. H. Reijmer, and E. Van Meijgaard, Characteristics of the Antarctic surface mass balance, 1958-2002, using a regional atmospheric climate model, in *Annals of Glaciology, Vol 41, 2005*, vol. 41, pp. 97–104, Int Glaciological Soc, Cambridge, 2005.
- van den Broeke, M. R., Spatial and temporal variation of sublimation on Antarctica: Results of a high-resolution general circulation model, *Journal of Geophysical Research*, 102, 29,765–29,778, doi:10.1029/97JD01862, 1997.
- Wolman, M. G., and J. P. Miller, Magnitude and Frequency of Forces in Geomorphic Processes, *Journal of Geology*, 68, 54–74, doi:10.1086/626637, 1960.